Ionization impact on molecular clouds and star formation Numerical simulations and observations

Pascal Tremblin

To cite this version:

Pascal Tremblin. Ionization impact on molecular clouds and star formation Numerical simulations and observations. Solar and Stellar Astrophysics [astro-ph.SR]. Université Paris-Diderot - Paris VII, 2012. English. NNT : . tel-00786668v2

HAL Id: tel-00786668

https://theses.hal.science/tel-00786668v2

Submitted on 9 May 2013

École doctorale d'astronomie et d'astrophysique d'Ile-de-France
Université Paris-Diderot

Thèse de doctorat

présentée pour obtenir le grade de

docteur de l'Université Paris-Diderot
Spécialité : Astronomie et Astrophysique

par

Pascal Tremblin

Ionization impact on molecular clouds and star formation
Numerical simulations and observations

Thèse dirigée par Edouard Audit et Vincent Minier
Soutenue le 9 novembre 2012

Jury composé de :

Pr. Jacques Le bourlot	Président
Pr. Ian Bonnell	Rapporteur
Dr. Mark Thompson	Rapporteur
Pr. Edouard Audit	Directeur de thèse
Dr. Vincent Minier	co-Directeur de thèse
Pr. Rolf Walder	Examinateur
Dr. Annie Zavagno	Examinatrice

Laboratoire AIM Paris-Saclay (CEA/Irfu - Uni. Paris Diderot - CNRS/INSU), Centre d'études de Saclay, 91191 Gif-Sur-Yvette, France
pascal.tremblin@cea.fr
Ingénieur des mines, Conseil général de l'économie, de l'industrie et des technologies, Ministère de l'économie et des finances, 120 rue de Bercy, 75572 Paris cedex 12, France
pascal.tremblin@mines.org

Abstract

At all the scales of Astrophysics, the impact of the ionization from massive stars is a crucial issue. At the galactic scale, the ionization can regulate star formation by supporting molecular clouds against gravitational collapse and at the stellar scale, indications point toward a possible birth place of the Solar System close to massive stars. At the molecular cloud scale, it is clear that the hot ionized gas compresses the surrounding cold gas, leading to the formation of pillars, globules, and shells of dense gas in which some young stellar objects are observed. What are the formation mechanisms of these structures? Are the formation of these young stellar objects triggered or would have they formed anyway? Do massive stars have an impact on the distribution of the surrounding gas? Do they have an impact on the mass distribution of stars (the initial mass function, IMF)?

This thesis aims at shedding some light on these questions, by focusing especially on the formation of the structures between the cold and the ionized gas. We present the state of the art of the theoretical and observational works on ionized regions (H II regions) and we introduce the numerical tools that have been developed to model the ionization in the hydrodynamic simulations with turbulence performed with the HERACLES code. Thanks to the simulations, we present a new model for the formation of pillars based on the curvature and collapse of the dense shell on itself and a new model for the formations of cometary globules based on the turbulence of the cold gas. Several diagnostics have been developed to test these new models in the observations. If pillars are formed by the collapse of the dense shell on itself, the velocity spectrum of a nascent pillar presents a large spectra with a red-shifted and a blue-shifted components that are caused by the foreground and background parts of the shell that collapse along the line of sight. If cometary globules emerge because of the turbulence of the molecular cloud, the velocity spectrum of these globules is shifted at different velocities than the velocity of the shell, pillars and clumps that follow the global expansion of the H II region. An other diagnostic is the impact of the compression on the probability density function (PDF) of the cold gas. The distribution is double peaked when the turbulent ram pressure is low compared to the ionized-gas pressure. This is the signature of the compression caused by the expansion of the ionized bubble. When the turbulence is high, the two peaks merge and the compression can still be identified although the signature is less clear.

We have used *Herschel* column density maps and molecular-line data to characterize the density and velocity structures of the interface between the ionized and the cold gas in several regions: RCW 120, RCW 36, Cygnus X, the Rosette and Eagle Nebulae. In addition to the diagnostics derived from the simulations, analytical predictions of the shell and pillar parameters was tested and confronted to the observations. In all the regions, we have seen that there is a good agreement with the analytical models and with the simulation diagnostics. The velocity structure of a nascent pillar in the Rosette Nebula suggests that it has been formed by the collapse of the shell on itself and the bulk velocity of cometary globules in Cygnus X and in the Rosette Nebula tends to confirm their turbulent origin. The compression caused by the ionized gas can be seen on the PDF of the cold gas in most of the regions studied. This result is important for the link between the IMF and the global properties of the cloud. If the IMF can be derived from the PDF of a cloud, the impact of the massive stars on the PDF has to be taken in account. Furthermore, we present dedicated simulations of RCW 36 that suggest that the dense clumps at the edge of the ionized gas are not pre-existing, it is likely that their formation was triggered by the compression caused by the ionization. Therefore the ionization from the massive stars is a

key process that has to be taken into account for the understanding of the IMF.

We also present in appendix other works that have been done in parallel of this thesis: the charge exchange in colliding planetary and stellar winds in collaboration with Prof. E. Chiang during the ISIMA summer school 2011 in Beijing; and the sub-millimeter site testing at the Concordia station in Antarctica with the CAMISTIC team (PI: G. Durand).

Résumé

À toutes les échelles de l'Astrophysique, l'impact de l'ionisation venant des étoiles massives est une question cruciale. A l'échelle galactique, l'ionisation peut réguler la formation des étoiles en soutenant les nuages moléculaires contre l'effondrement gravitationnel et à l'échelle stellaire, diverses indications pointent vers une naissance possible du système solaire à proximité des étoiles massives. À l'échelle du nuage moléculaire, il est clair que le gaz chaud et ionisé comprime le gaz froid qui l'entoure, conduisant à la formation des piliers, des globules, et des coquilles de gaz dense dans lesquelles des coeurs pré-stellaires sont observés. Quels sont les mécanismes de formation de ces structures ? La formation de ces coeurs pré-stellaires est-elle déclenchée par l'ionisation ou préexistante ? Les étoiles massives ont-elles un impact sur la distribution en densité du gaz environnant ? Ont-elles un impact sur la distribution des étoiles en fonction de leur masse (la fonction de masse initiale, IMF) ?

Cette thèse vise à apporter des éléments de réponse à ces questions, en se concentrant en particulier sur la compréhension de la formation des structures entre le gaz froid et ionisé. Nous présentons, dans un premier temps, l'état de l'art des travaux théoriques et des observations des régions ionisées (régions H II). Cela comprend l'étude théorique des fronts d'ionisation ainsi que des modèles existants de formation de structures : le modèle d'accumulation de matière et effondrement, le modèle d'implosion radiative et les modèles incluant la turbulence du nuage moléculaire. Nous introduisons ensuite les outils numériques qui ont été développés pour modéliser l'ionisation dans les simulations d'hydrodynamique turbulente effectuées avec le code HERACLES. L'étude des structures qui se développent à l'interface entre les régions H II et les nuages moléculaires nécessite la modélisation de trois phénomènes : la dynamique du gaz moléculaire, la propagation des photons ionisants et l'interaction entre les deux. Les outils développés pour modéliser ces éléments comprennent un module résolvant la gravité et l'auto-gravité du gaz couplé à sa dynamique et un module résolvant les équations d'ionisation/recombinaison du gaz avec la propagation des photons ionisants. Ces outils sont testés dans des situations simples ou les solutions analytiques du problème sont disponibles.

Grâce aux simulations numériques éffectuées avec ces nouveaux outils, nous présentons un nouveau modèle pour la formation des piliers basés sur la courbure et l'effondrement de la coquille dense sur elle-même. Lorsque la coquille de gaz dense rencontre un obstacle (par exemple une surdensité dans le nuage moléculaire), le ralentissement provoque une déformation de la coquille qui se courbe autour de l'obstacle. Si la courbure provoquée est suffisamment importante, la coquille va ensuite s'éffondrer sur elle-même pour former un pilier de gaz. Dans le cas ou la courbure est relativement faible, le gaz dans la coquille converge vers la perturbation pour former une surdensité qui est accélérée avec la coquille et reste dans la coquille. Ce procédé est illustré en Fig.1, les vues de gauche présentent une simulation où la courbure n'est pas suffisante pour former un pilier. Seule une surdensité est formée car la perturbation provoque des mouvements de gaz dans la coquille qui convergent vers le centre. Dans l'autre cas (vues de droite), la coquille est assez déformée pour s'effondrer sur elle-même et former un pilier. Avant l'effondrement, le spectre en vitesse d'un pilier en formation présente une composante décalée vers le rouge et une composante décalée vers le bleu correspondant aux parties de la coquille en avant-plan et en arrière-plan qui entrent en collision sur la ligne de visée. Après l'effondrement, le spectre a une seule composante de vitesse, centrée sur la vitesse moyenne de la coquille (projetée sur la ligne de visée pour les observations).

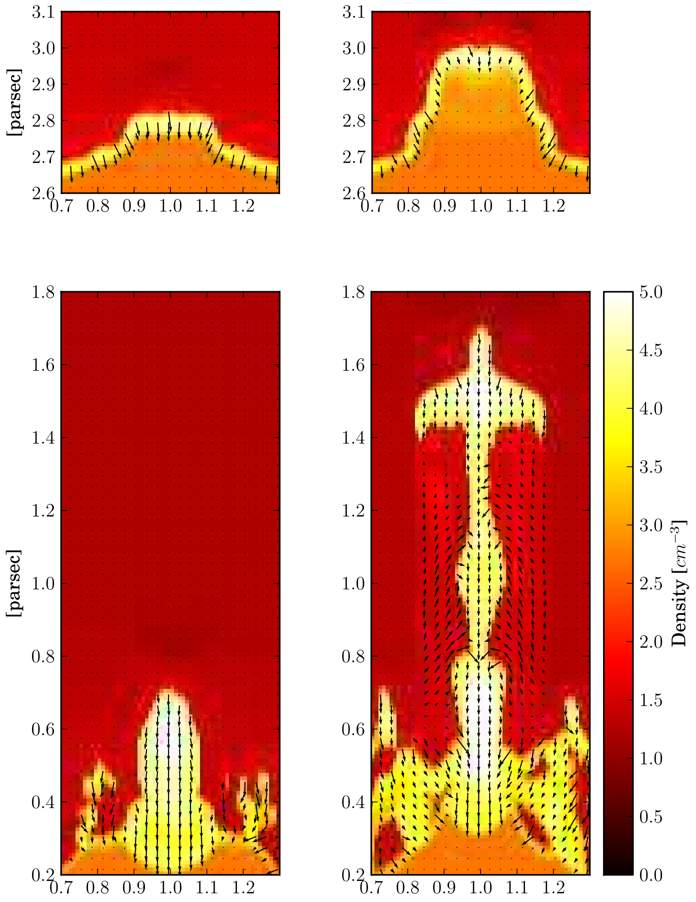

Figure 1 – Coupe en densité de deux simulations d'ionisation d'une surdensité dans un milieu homogène. Le champ de flèches noires représente le champ de vitesse du gaz non-ionisé. Le flux ionisant est introduit par le haut de la boite en $y = 4$ pc. La densité de la surdensité est deux fois (gauche) et cinq fois (droite) plus importante que la densité du milieu homogène. Les coupes en haut sont faites 220 kans après le début de la simulation et illustrent la courbure de la coquille provoquée par la surdensité. Les coupes du bas sont faites 1 Man après le début de la simulation et représentent l'état final des structures : une surdensité lorsque la courbure est faible (gauche) et un pilier de gaz lorsque la coquille a été suffisamment courbée (droite).

Lorsque la turbulence du gaz froid est prise en compte, deux principaux cas émergent. Si la pression du gaz ionisé est plus importante que la pression dynamique de la turbulence, les structures formées sont similaires aux cas précedemment étudiés sans turbulence, i.e. on forme essentiellement des piliers et des surdensités dans la coquille en fonction du degré de courbure de la coquille. Les perturbations de la coquille sont provoquées par la turbulence initiale du gaz froid. Lorsque la courbure de la coquille est suffisante, elle s'effondre sur elle-même pour former des piliers et la même signature est observée dans les spectres en vitesse : pics décalés vers le rouge et le bleu avant effondrement et pic simple après effondrement.

Lorsque la pression dynamique de la turbulence est plus importante que la pression du gaz ionisé, la situation est assez différente : des parties du gaz froid vont avoir assez d'énergie cinétique pour pénétrer dans le gaz ionisé. La vitesse de ces bulles de gaz est aléatoire car elle a pour origine la turbulence initiale du gaz froid. Elle aura donc très probablement une composante perpendiculaire à la propagation de la coquille. Ces bulles

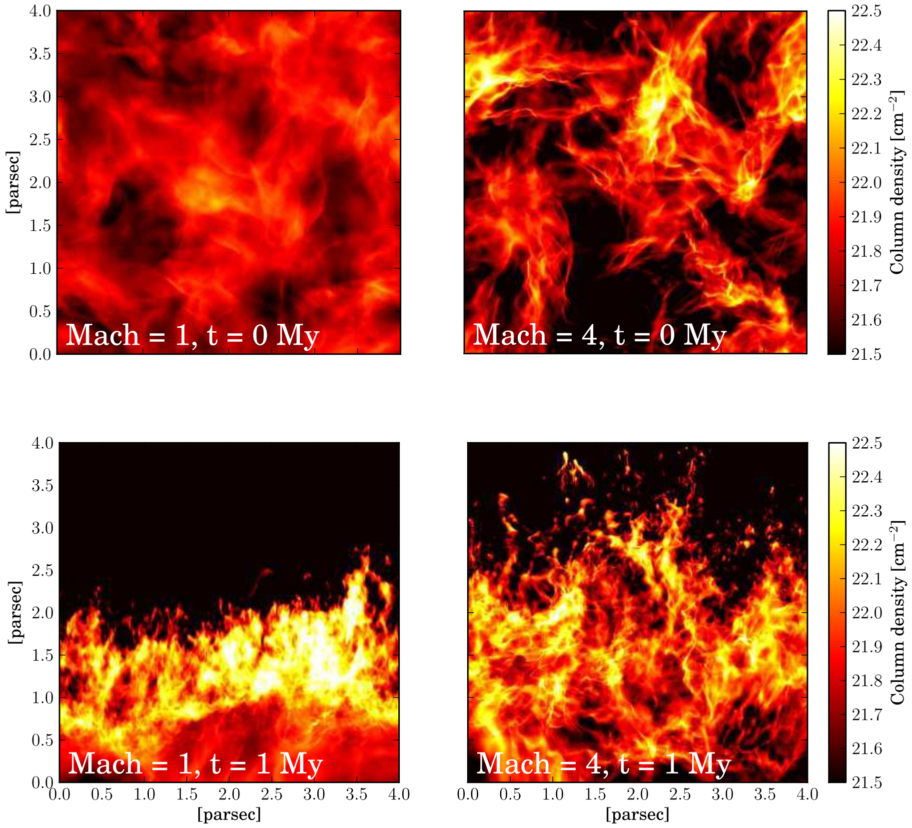

FIGURE 2 – Vues de la densité de colonne d'une simulation de l'ionisation d'un nuage moléculaire turbulent à Mach 1 (gauche) et à Mach 4 (droite). La première ligne correpond à des vues prises avant que l'ionisation du milieu soit lancée, la deuxième 1 Man après.

de gaz vont donc se détacher du nuage moléculaire et former des globules de gaz froid. Le mouvement turbulent du globule conduit à un spectre en vitesse qui sera centré sur une vitesse complétement différente de la vitesse d'expansion de la région H II. Cette conséquence peut être directement étudiée dans les observations pour vérifier le lien entre turbulence et formation des globules.

Une autre conséquence de l'interaction entre turbulence et ionisation est l'impact de la compression sur la fonction de densité de probabilité (PDF) du gaz froid. La distribution a un double pic lorsque la pression dynamique turbulente est faible par rapport à la pression du gaz ionisé. Il s'agit de la signature de la compression causée par l'expansion de la bulle ionisée. Quand la turbulence est élevée, les deux pics fusionnent et la compression peut encore être identifiée, mais la signature est moins claire. La conséquence principale est un élargissement de la PDF du gaz tout en gardant des nombres de Mach relativement faibles pour le nuage initial. Ce résultat pourrait être important pour les théories dérivant la fonction de masse initiale (IMF) des étoiles à partir des PDFs des nuages moléculaires. En effet, pour produire une IMF conforme aux observations dans le cas isotherme, il faut prendre des PDFs relativement larges qui correspondent à des nombres de Mach irréalistes pour le nuage initial. En prenant en compte la compression due à l'ionisation, la PDF est naturellement élargie tout en conservant des nombres de Mach faibles. Dès lors, l'ionisation pourrait jouer un rôle important pour une théorie expliquant la formation des étoiles dans son ensemble.

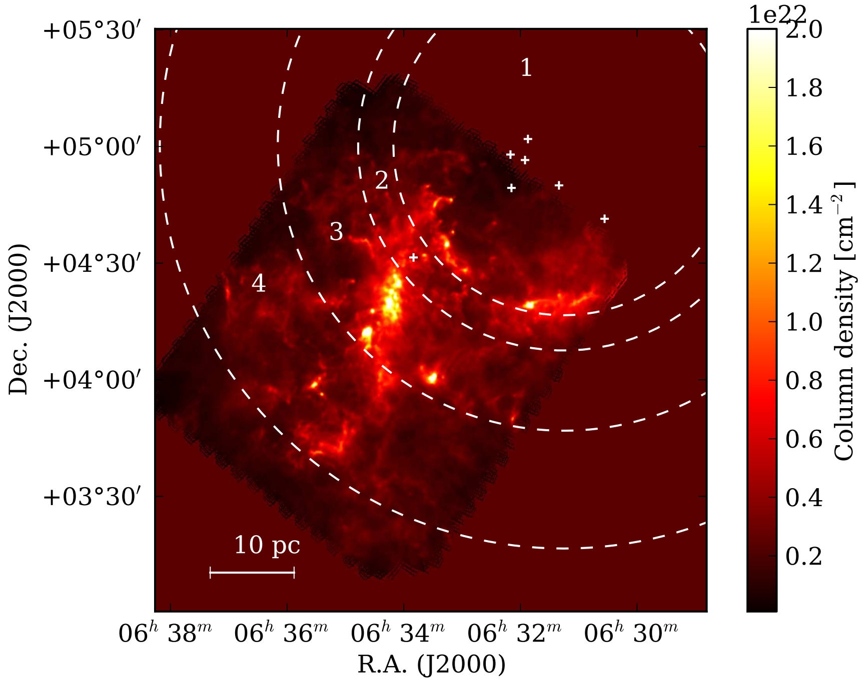

FIGURE 3 – Carte de densité de colonne de la nébuleuse de la Rosette observée par *Herschel*. Les croix blanches indiquent la position des sources principales d'ionisation. Les cercles sont les différentes régions dans lesquelles les PDFs sont calculées.

Les observations du télescope *Herschel* ont révélé la structure de beaucoup d'objets à l'interface des régions H II et des nuages moléculaires et parmi eux, les piliers et les globules sont les plus connus et étudiés. Ils sont présents dans beaucoup de régions de formation d'étoiles massives telles que la nébuleuse de l'aigle et de la rosette, localisés près des coquilles denses induites par l'expansion des régions H II. Grâce aux nouvelles observations obtenues dans le cadre du programme HOBYS de *Herschel*, il est possible de tester les diagnostics dérivés à partir des simulations numériques. Il est possible de caractériser les profils des coquilles et des piliers grâce à l'algorithme DisPerSe qui permet de suivre les crêtes denses dans les cartes de densité de colonne. La dynamique du gaz est caractérisée grâce à des données de traceurs moléculaires ce qui permet la comparaison avec les simulations numériques. Les observations utilisées comprennent des régions ionisées très larges telles que la nébuleuse de la rosette, de l'aigle et Cygnus X ainsi que des régions à plus petites échelles telles que RCW 120 et RCW 36. En plus des diagnostics issus des simulations, des prédictions analytiques des paramètres de la coquille et des piliers ont été testées et confrontées aux observations. Dans toutes ces régions, les modèles analytiques et les diagnostics issus des simulations donnent des résultats concluants. La structure en vitesse d'un pilier en formation dans la nébuleuse de la Rosette suggère qu'il a été formé par l'effondrement de la coquille sur elle-même et la dispersion des vitesses moyennes des globules dans Cygnus X et dans la Nébuleuse de la Rosette tend à confirmer leur origine turbulente.

Le gaz ionizé chaud compresse le gaz froid du nuage moléculaire dans la coquille autour de la région H II. Cette région devient plus dense que le reste du nuage et devrait avoir un impact sur la PDF en densité de colonne autour du gaz ionisé. Cet effet peut maintenant être quantifié grâce aux nouvelles observations de *Herschel*. Nous avons calculé la PDF en densité de colonne du gaz dans des régions concentriques autour des régions H II pour étudier l'impact de l'ionisation (e.g. Fig. 3). Les PDFs ainsi collectées présentent un double pic ; le premier correspond au gaz froid du nuage moléculaire alors que le second est la signature de la compression causée par l'expansion du gaz ionisé. A des densités plus élevées, une déviation en loi de puissance apparait et correspond à l'effet de la gravité sur le gaz. La compression permet ainsi d'obtenir des PDFs élargies telles que suggérées par les simulations numériques et cet élargissement par compression pourrait être un élément important pour obtenir une IMF réaliste à partir de la PDF du nuage initial dans les théories de la formation stellaire.

A mon attentive relectrice,

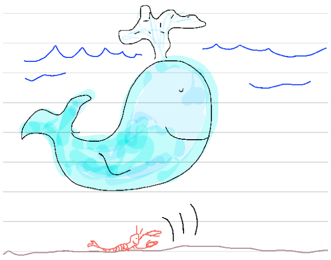

Remerciements

Je remercie Edouard et Vincent pour m'avoir guidé tout au long de cette thèse, tout en me donnant une très grande liberté. Je remercie Edouard pour son aide précieuse sur les simulations numériques et je remercie Vincent et Nicola pour leurs explications et conseils sur l'analyse des observations.

Je remercie Gilles et Vincent pour m'avoir fait confiance quand je leur ai dit que je pouvais les aider à monter une caméra en Antarctique. Je remercie Pierre-Olivier pour avoir fait confiance à Gilles et Vincent quand ils lui ont dit qu'ils pouvaient monter cette caméra en Antarctique. Je le remercie aussi ainsi que Michel Alba de me permettre d'y retourner une troisième fois pour l'installation de la caméra. Je remercie encore Nicola pour son expertise et son aide sur les modèles atmosphériques qui ont été précieux pour le projet. Je remercie tout particulièrement Yann pour les aventures partagées dans le grand froid ainsi que toutes les personnes que j'ai cotoyées pendant ces deux incroyables missions. Je remercie un peu moins ceux qui m'ont fait croire qu'il n'y avait aucun problème à marcher pieds nus sur un sol de glace par -40, et je ne me remercie pas du tout de ma crédulité.

Je remercie Matthias et Neil pour leur aide précieuse lors de nos longues séances de debuggage d'HERACLES (qui est bien évidemment bugg-free après notre passage :). Je remercie tout le groupe simulation ainsi que coast pour les séminaires/pizzaminars/journal clubs et discussions qui ont rendu ses trois années très enrichissantes. Je remercie tout particulièrement Sébastien pour leur organisation et je le remercie ainsi que Thierry pour leurs innombrables conseils et explications.

Je remercie astrugar, o(l)docao et jfaure pour tout le temps partagé en pièce 232, pour tous les raccourcis emacs un peu "touchy", les commandes latex très "fancy", les astuces pythons (qu'idl n'arrivera jamais à égaler) et pour toutes les autres geekeries joyeusement partagées.

Je remercie Eugene pour son aide et ses conseils sur notre étude des interactions entre vents stellaires et Jupiters chaudes. Je remercie aussi Patrick, Nicolas, Eva, Subu, Matthias, Marina, Pascale et toutes les personnes ayant contribué à faire d'ISIMA 2011 une école d'été particulièrement réussie.

Je remercie tous les membres du jury pour avoir accepté de lire et évaluer le travail que j'ai effectué durant ces trois années au Service d'Astrophysique du CEA et je remercie ma famille de m'avoir supporté pendant toute cette période.

Enfin, je tiens à souligner mon admiration pour les astrophysiciens des années 60 et 70, qui par leur talent et leur compréhension fine de la physique, ont obtenu tant de résultats sans ordinateur, alors que de nos jours, nous avons tant de mal à nous en passer.

Contents

Chapter 1

Context and perspectives of this work

> *I'm astounded by people who want to 'know' the universe when it's hard enough to find your way around Chinatown.*
> *Woody Allen*

1.1 Star formation at the galactic scale

Understanding star formation in the Milky Way and in other galaxies has been a major driver of Astrophysics for decades. Stars form from the turbulent gas contained in molecular clouds (the stellar nurseries) by gravitational collapse. The low-mass stars like the Sun, will spend most of their lifetime (10 billion years) burning the hydrogen in their center before turning Red Giant and exploding in a planetary nebula that will return heavier materials (carbon, oxygen, calcium) to the interstellar medium (see *Gurzadyan*, 2010). The stars more massive than the Sun will strongly impact the interstellar medium (ISM) even during their short lifetime (about 1-10 million years), because of their winds and their strong ultra-violet emission that heats and ionizes the surrounding gas. At the end of their life they will explode in supernovae that will enrich the interstellar medium with the heavy elements (up to iron) they have produced. New stars will form from this enriched ISM perpetuating the life cycle of stars. A key achievement in the field of star formation was to link the star formation rate (SFR) of galaxies to their gas content. *Schmidt* (1959) was the first to propose that the rate of star formation varies as a power law of the density of the interstellar gas i.e.:

$$\Sigma_{\rm SFR} \propto (\Sigma_{\rm gas})^n \tag{1.1}$$

where $\Sigma_{\rm SFR}$ is the SFR surface density usually expressed in $\rm M_\odot\ yr^{-1}\ pc^{-2}$ and $\Sigma_{\rm gas}$ the gas surface density. Based on observations in the Milky Way, Schmidt derived a value of $\rm n = 2$ for the power law. More recently, *Kennicutt* (1998) combined Hα, H I, CO and far-infrared (FIR) data over almost a hundred of galaxies to derive the form of the global star formation law and found a value of $\rm n = 1.4 \pm 0.15$ (see Fig. 1.1). In the study of Kennicutt, the star formation rate is linked to the Hα luminosity coming from the stars through

$$\rm SFR(M_\odot\ yr^{-1}) = \frac{L(H\alpha)}{1.26 \times 10^{41} erg\ s^{-1}} \tag{1.2}$$

This relation provides the amount of stars that are formed in function of the Hα emission that principally comes from massive stars. Therefore an important assumption is made in order to derive this relation: the global amount of stars can be determined when only the number of massive stars is known, i. e. the distribution of stars in function of their

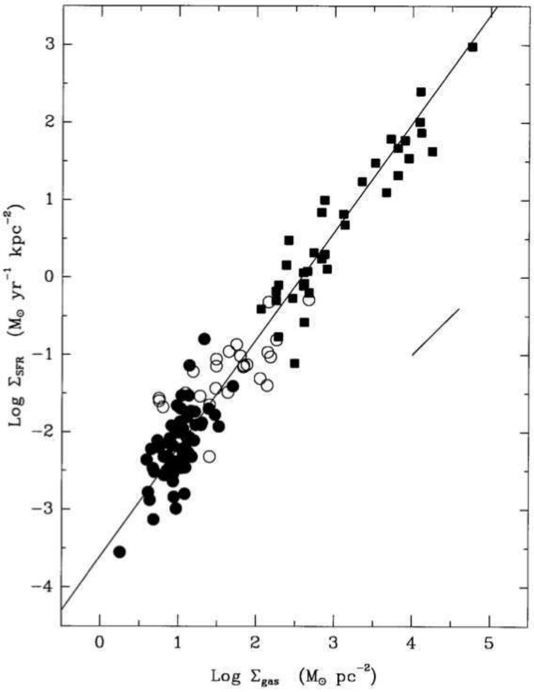

Figure 1.1: Schmidt-Kennicutt law from *Kennicutt* (1998). The power law fit gives an exponent of 1.4 ± 0.15.

mass is the same from one galaxy to another. This distribution is called the initial mass function (IMF) and is assumed universal although *Cappellari et al.* (2012) recently showed it was not the case. Note also that recent works (*Daddi et al.*, 2010; *Genzel et al.*, 2010) presented evidence of two different star formation regimes: a low-rate mode for isolated disks and a high-rate one for starbursts (probably occurring during mergers).

1.2 The regulation of star formation

Giant molecular clouds (GMCs) have a typical mass of 10^4-10^6 M$_\odot$, a size of 10-100 parsecs and a density of 10^2-10^3 particles per cm^3 (see *Lada et al.*, 2010, for estimations in various GMCs). Their surface density is typically of the order of 100 M$_\odot$ pc^{-2}, which gives a SFR surface density of the order of 10^{-1} M$_\odot$ yr^{-1} kpc^{-2} from the Schmidt-Kennicutt law and a SFR of the order of 10^{-1} M$_\odot$ yr^{-1} for a cloud with a size around 30 pc. This rate is quite low, the lifetime of a typical molecular cloud is 10 million years, therefore a giant cloud will form up to 1000 solar mass of stars. This corresponds only to 1 % of the mass of the cloud, meaning that star formation has a poor efficiency in molecular clouds. This low efficiency is unexpected when only self-gravity is considered. The typical free-fall time of a molecular cloud is given by $1/\sqrt{G\rho}$ with ρ the density of the cloud. It is of the order of 10 million years for densities around 100 cm^{-3}. If the cloud was globally collapsing under its own gravity, it will convert all its mass into stars leading to a star formation rate of 10^{-2} M$_\odot$ yr^{-1}, which is two orders of magnitude higher than the observed star formation rate. Therefore star formation has to be regulated by some kind of processes, e.g. the cloud pressure, its magnetic energy, its internal turbulence, or the feedback processes of massive stars (see *Ballesteros-Paredes et al.*, 2007).

- The pressure support is described by the Jeans length

$$\lambda_J = \frac{c_s}{\sqrt{G\rho}} \approx 0.6 \text{ pc} \left(\frac{c_s}{0.25 \text{ km/s}}\right) \left(\frac{n}{10^3 \text{ cm}^{-3}}\right)^{-1/2} \tag{1.3}$$

All scales smaller than the Jeans length are stabilized by the pressure. However molecular clouds have a much larger scale than their Jeans length, their pressure is not high enough to prevent the gas from collapsing.

- The virial theorem for magnetized clouds states that clouds with a mass smaller than the critical mass

  $$M_\Phi = \frac{\Phi}{2\pi\sqrt{G}} \approx 10^4 M_\odot \left(\frac{B}{20\ \mu\mathrm{G}}\right)\left(\frac{R}{10\ \mathrm{pc}}\right)^2 \tag{1.4}$$

  are stabilized by the magnetic field of flux Φ (see *Nakano and Nakamura*, 1978). Even if magnetic fields are difficult to measure in molecular clouds (Zeeman effect, projection of the field on the line of sight...), current estimations tend to show that the magnetic field in a molecular cloud cannot prevent the collapse. The clouds are marginally supercritical with a mass $\mathrm{M} \approx 2{\times}\mathrm{M}_\Phi$ (see *Troland et al.*, 1996; *Crutcher et al.*, 1999; *Troland and Crutcher*, 2008).

- The level of turbulence in a molecular cloud can be estimated by the Larson law (see *Larson*, 1981; *Blitz*, 1993; *Heyer and Brunt*, 2004)

  $$\Delta v \approx 3\ \mathrm{km/s}\left(\frac{R}{10\ \mathrm{pc}}\right)^\alpha \tag{1.5}$$

  with α between 0.38 and 0.5. This relation gives a typical RMS Mach number of 10 for molecular clouds (at a temperature of 10 K). The turbulent ram pressure is then

  $$P_{\mathrm{turb}} = \rho(\Delta v)^2 \approx 1.5 \times 10^{-11}\ \mathrm{Pa} > G\rho M/R \tag{1.6}$$

  and dominates over the gravitational potential energy of the cloud. The turbulence is therefore sufficient to prevent the cloud from collapsing. However such a high turbulence in the interstellar medium dissipates quickly, in one crossing time of the driving scale. The turbulence is thought to be injected at the scale of the cloud, i.e. $\mathrm{t}_{\mathrm{diss.}} \approx R/\Delta v \approx$ few millions years. Therefore the turbulence cannot prevent the collapse on a long time scale unless it is maintained.

After the early stage of star formation in the cloud, the feedback of the newly-formed massive stars will become important, first through ionization and stellar winds and finally through supernovae explosions (see *McKee and Ostriker*, 1977; *Matzner*, 2002). These processes will prevent the cloud from collapsing and in fact are even responsible for its destruction. According to *Whitworth* (1979), only 4 % of the cloud needs to be converted into stars to get - with a standard IMF - enough massive stars that will completely ionize the rest of the cloud. The fact that we got even a lower star formation efficiency may indicate the role of stellar winds and supernova explosions. This result was also confirmed by numerical simulations *Yorke et al.* (1989).

Observationally, this picture is supported by the fact that molecular clouds have short lifetimes comparable to the lifetime of massive stars: of the order of 10 million years (see *Ballesteros-Paredes et al.*, 1999; *Hartmann et al.*, 2001; *Hartmann*, 2003). On this timescale, the turbulence (and marginally, the magnetic fields) is sufficient to prevent the cloud from collapsing under its own gravity, until the feedback from massive stars destroys the cloud and set the final star-formation efficiency.

Recent simulations of galaxy formation have now sufficient resolution to resolve the GMCs (e.g. *Bournaud et al.*, 2010) and to treat with ad hoc models the feedback from massive stars. *Hopkins et al.* (2011) and a series of following papers developed an implementation of the different kind of feedbacks: winds, ionization, radiation pressure and supernova. On the scale of the galaxy, they found a typical Schmidt-Kennicutt law that only depends on the feedback and not on the implementation of the star-formation process (i.e. density threshold, high-density star formation efficiency...). This result suggests that the star-formation rate is regulated only by the feedback processes. Which of these processes is dominant for the regulation? *Fall et al.* (2010) calculated the different impact of these feedbacks and found that the radiation pressure is important for massive molecular cloud while at low mass the ionization is dominant. *Hopkins et al.* (2011) found that the feedback from stellar winds and supernova is inefficient to regulate star formation because the cooling of the gas is strong enough to evacuate the absorbed energy. On the other hand, the radiation pressure from the absorption of UV/IR photons by the dust and the photo-ionization of the gas are able to disrupt the cloud and prevent the collapse of MCs and GMCs (radiation pressure at high densities for starbursts and galaxies at high redshift and photo-ionization at low densities for the Milky Way and dwarf galaxies, similarly to the results of *Fall et al.* (2010). Note that these studies do not take in account the destruction of the dust by the ionization. Therefore, it is still difficult to know if the ionization can be neglected when the radiation pressure seems dominant. A full treatment of the photo-ionization/radiation-pressure physics on a gas/dust mixture is needed to treat that question. Anyway, in the Milky Way, H II regions are commonly observed in molecular clouds and are probably the dominant process in this range of densities.

1.3 The initial mass function in the Milky Way

As we have seen in Sect. 1.1, an important issue, in order to compute the star formation rate of a galaxy, is to know the distribution of the stars in function of their mass, i. e. the initial mass function (IMF). *Salpeter* (1955) proposed that this distribution is described by a power law:

$$dN = \xi(log_{10}(m))dlog_{10}(m) = \xi(m)dm \propto m^{-\alpha}dm \tag{1.7}$$

with α = -2.35 for a mass range between 0.5 $M_\odot$ and 10 $M_\odot$. This work has been extended for low mass stars where the distribution flattens by *Miller and Scalo* (1979) and *Kroupa* (2001). More recently, *Chabrier* (2003) proposed that the low-mass part of the logarithmic IMF is well described by a log-normal distribution (see Fig. 1.2) and suggested a link with the compressible MHD turbulence inside molecular clouds. According to *Chabrier* (2003), the IMF cannot be obtained by Jeans-type mechanisms where gravity is the only source of fragmentation. These theories cannot predict a large number of sub-stellar objects and match the constraints on star formation. On the other hand, star formation in compressible turbulence will be induced by the dissipation of the large-scale modes to smaller scales thanks to radiative MHD shocks. The dense structures formed by these shocks will eventually collapse by gravitational instability to form bound objects. The log-normal shape of the IMF is then a direct consequence of the log-normal distribution of the turbulent gas while the power law tail at high mass is caused by the gravitational instability. This result is supported observationally in many different types of environments and also by studies of the pre-stellar clump mass function (CMF) (e.g. *Motte et al.*, 1998; *Alves et al.*, 2007). In that picture, the shape of the IMF is set by the CMF and the peak is shifted to lower mass depending on the efficiency of clumps to turn into stars (in *Alves et al.* (2007) the efficiency factor is typically of 25 %). The log-normal shape of the CMF with a high-mass power law tail is thought to originate from the turbulence of the cloud and the gravitational instability and is now strongly supported by theoretical studies (*Hennebelle and Chabrier*, 2008,0) and numerical studies (*Schmidt et al.*, 2010). The IMF is then set at the early stage of the clump formation, by the global properties of the cloud (i.e. mean density, temperature and level of turbulence) and does not depend much on the local environmental factors.

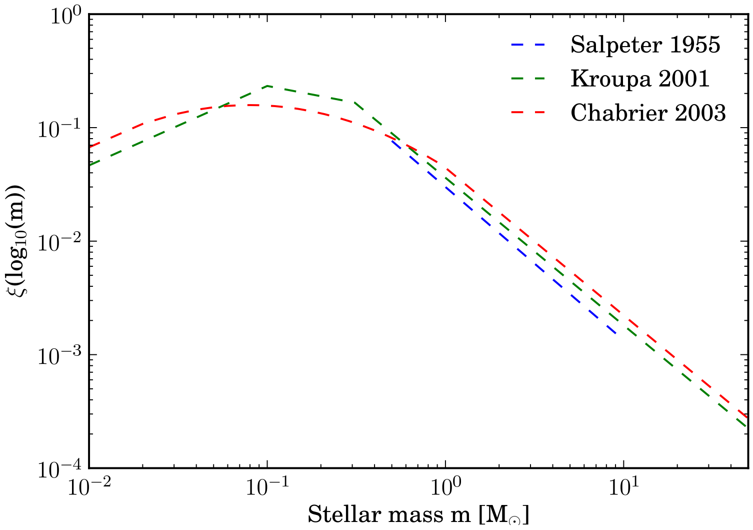

Figure 1.2: Initial mass functions from *Salpeter* (1955), *Kroupa* (2001) and *Chabrier* (2003)

1.4 The turbulence in the interstellar medium

Molecular clouds have turbulent motions driven at large scale since they are observed to be self-similar up to the largest scale traced by molecules (see *Heyer and Brunt*, 2004, and references therein). The turbulence is driven by the large-scale compression coming from gravitational instabilities at the galactic scale (see *Toomre*, 1964; *Goldreich and Lynden-Bell*, 1965) or from the shear caused by the differential rotation of the galaxy. The compression is also caused by the expansion of superbubble shells such as H II regions and supernova remnants (see *McCray and Kafatos* (1987) and recent simulations from *Ntormousi et al.* (2011)). Then, various instabilities in the flow are responsible for the development of the turbulence and for the compression and fragmentation of the gas leading to molecular clouds. *Vishniac* (1994) showed that a cold slab bounded by accretion shocks is subject to non-linear instabilities (often called the non-linear thin shell instability). *Pikel'Ner* (1968); *Field et al.* (1969); *Wolfire et al.* (1995) showed that the neutral ISM was subject to a thermal instability caused by the UV heating of the gas and the cooling by radiation. The turbulence and the gas fragmentation caused by these dynamical and thermal instabilities have been well studied in various conditions thanks to numerical simulations (see *Koyama and Inutsuka*, 2002; *Audit and Hennebelle*, 2005; *Heitsch et al.*, 2005; *Vázquez-Semadeni et al.*, 2006; *Hennebelle and Audit*, 2007; *Hennebelle et al.*, 2007; *Audit and Hennebelle*, 2010). All these simulations have adapted cooling and heating functions for the ISM (see *Wolfire et al.*, 2003) and they showed that the ISM is a turbulent two-phase medium because of the thermal instability. Shocked gas is fragmenting into cold dense clumps at a typical temperature of 10-100 K embedded into a warm phase at 10,000 K. The clumps have a velocity dispersion of a few kilometers per second and therefore are supersonic with respect to their internal sound speed. These condensations can be seen in Fig.1.3, a snapshot of the 3D bistable simulation of *Audit and Hennebelle* (2010). The probability density function (PDF) of the gas is showed in Fig. 1.4 (left) with the mass distribution of the gas in function of its density and pressure (right). The black solid curve (right) indicates the thermal equilibrium (see *Wolfire et al.*, 2003). In the pressure/density plane, the two-phase medium is separated by the thermally unstable region in between the two black-dashed lines where $dp/d\rho \leq 0$. In this region, an increase of density ($d\rho \geq 0$) leads to a decrease of pressure ($dp \leq 0$) that will enhance the decrease of density and trigger

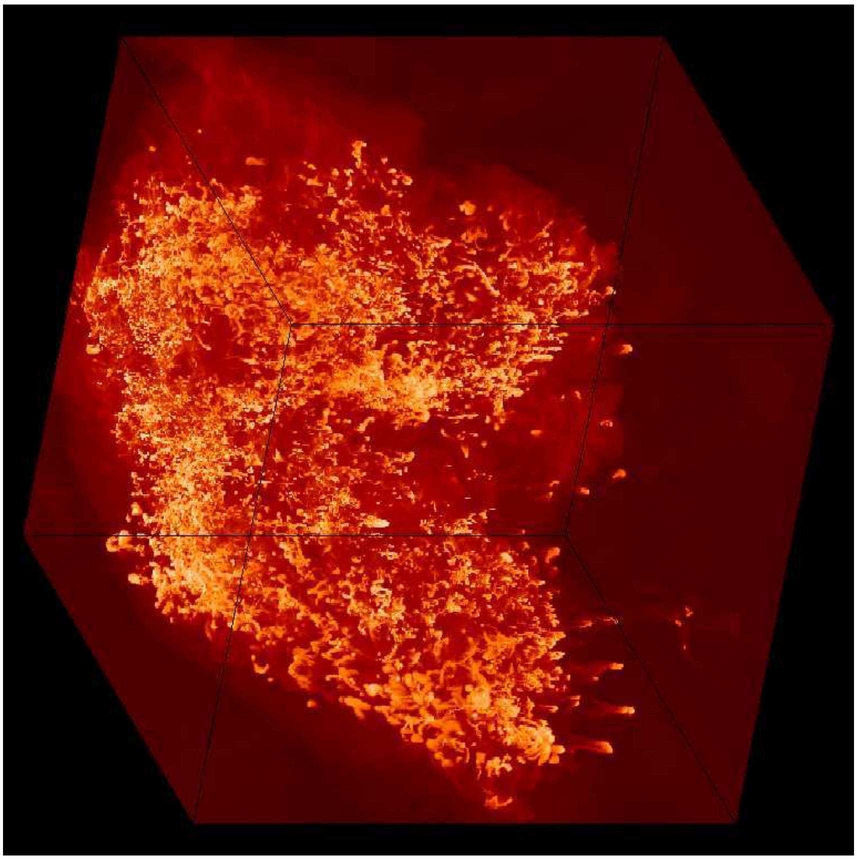

Figure 1.3: 3D simulations of colliding flows subject to the thermal instability from *Audit and Hennebelle* (2010). A two-phase ISM is formed with dense and cold condensations embedded into a warm phase.

the instability. Note that the turbulence is responsible for keeping a fraction of the gas in the unstable region (i.e. in between the two black-dashed lines). The high-density part of the PDF (left) is fitted with a log-normal distribution

$$P(n) = \frac{a}{\sqrt{2\pi\sigma}} \exp\left(-\frac{(\ln(n) - \ln(\bar{n}) - 0.5\sigma^2)}{2\sigma^2}\right) \tag{1.8}$$

with $\sigma = \ln(1 + b^2 M^2)$. n is the density of the gas, M the mean Mach number of the turbulence and b a parameter that links the width of the log-normal to the level of turbulence in the cloud. The parameters used for the fit in Fig. 1.4 are $\bar{n} = 280$ cm^{-3}, $M = 2.48$ and $b = 0.26$. The log-normal shape of the dense phase and the value of b are in agreement with previous works on compressible isothermal turbulence (see *Passot and Vázquez-Semadeni*, 1998; *Federrath et al.*, 2008). Therefore the cold phase has a behaviour relatively close to isothermal turbulence. However, note that the physical properties of the clumps are quite different in a simulation with heating and cooling compared to an isothermal simulation. When the gas is isothermal, an over-density (as a clump) implies necessarily a local over-pressure that will disperse the over-density. Therefore isothermal clumps are transient while it is not the case for clumps in a simulation with an explicit heating and cooling function for the gas. The simulation in *Audit and Hennebelle* (2010) is a large scale simulation (40 parsecs). The same type of simulations can be applied at smaller scale to study the turbulence inside a molecular cloud and the distribution of the gas also follows a log-normal distribution (see Chapter 5). The densest parts of the cloud will eventually reach densities sufficiently high to trigger their gravitational collapse. This will lead to a power law distribution of the gas at high densities that sets, with the log-normal distribution,

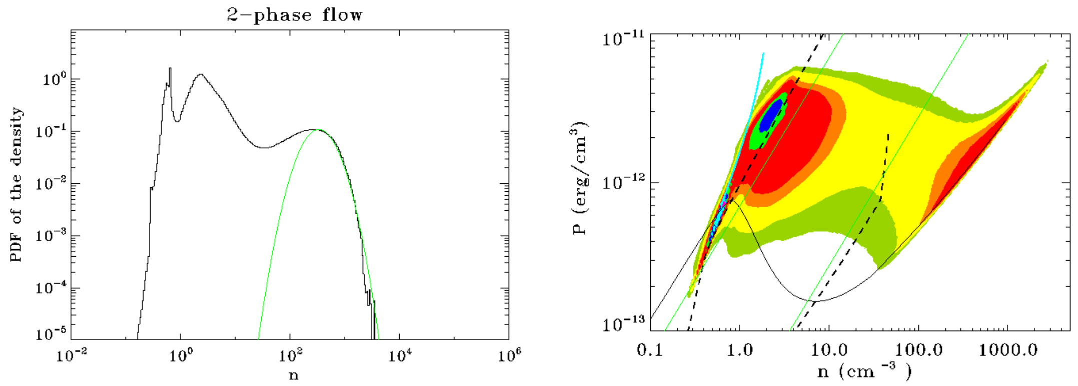

Figure 1.4: Left: Mass fraction distribution in function of the density of the gas (i.e. PDF) from *Audit and Hennebelle* (2010). Right: Mass fraction distribution in function of the density and the pressure of the gas. The mass fraction is indicated by the color scale from yellow to cyan. The thermal equilibrium is indicated by the black curve (see also *Wolfire et al.*, 2003) and the thermally unstable region is in between the green-dashed lines.

the shape of the CMF and then the IMF inside molecular clouds in the gravo-turbulent scenario of *Hennebelle and Chabrier* (2008).

However the question remains how this scenario is affected by the feedback from massive stars. *Ebert* (1955) was first to demonstrate that high pressures in the interstellar medium could squeeze a pre-existing cloud and trigger its collapse. Observations from *Blaauw* (1964) showed that there was a spatial age sequence of stars around OB associations leading to the idea of (*Elmegreen and Lada*, 1977) that star formation could be triggered by the expansion of H II regions (for supernova see *Ogelman and Maran* (1976) and following works). The pressure from H II regions inside molecular clouds can sufficiently compress the surrounding gas to trigger the gravitational instability and therefore star formation (the triggering scenarii will be reviewed in Sect. 2.1). There is now a lot of observations showing that ionization shapes the edge of molecular clouds, forming globules of gas, pillars and dense layers. In all these structures, star formation is commonly observed, suggesting their formation was triggered (the observations will be reviewed in sect. 2.2). However in order to quantify the effect of triggering, a major issue is to know if the apparent triggered sources would have collapse or not without the presence of the trigger. This question is of great importance to tell how the massive stars impact the IMF and to make the balance between the large-scale regulation and the small-scale triggering of star formation.

1.5 The origin of the Solar System

The impact of massive stars on their environment became of great interests when some indications showed that the Solar System was probably formed in their direct neighborhood. *Lee et al.* (1977) discovered the presence of a Short-Lived Radionucleus (SLR) isotope of the aluminium (^{26}Al: $T_{1/2}$=0.74 Myr) in a Ca-Al rich inclusion (CAI) of the Allende meteorite. The presence of such a SLR at the early time of the Solar System implies the local injection of freshly synthesized materials from massive stars in a phase of intense activity of the Sun. The discovery of an isotope of iron in CAIs (^{60}Fe: $T_{1/2}$= 1.5 Myr) definitely support an extra-solar origin since it cannot be produce locally in the Solar System (see *Lee et al.*, 1998). *Cameron and Truran* (1977) was the first to propose that a triggered-formation of the Solar System by a type II supernova explosion could explain the observed SLRs. Since then, two scenarii have been developed: the injection of SLRs into the solar protoplanetary disk (see *Ouellette et al.*, 2007) or into the pre-stellar core progenitor of the solar system (see *Cameron et al.*, 1995). However both possibilities are rather unlikely. For the first scenario, *Gounelle and Meibom* (2008) showed that the probability for the disk to be close enough (≈ 0.3 pc), to survive the photo-evaporation of the massive star, and to capture the SLRs from the supernova was less than 1 %. For the second scenario, the pre-stellar core does not need to be so close to the supernova since it has a bigger area cross section with the blast wave. However efficient mixing seems to be possible only in specific initial conditions (e.g. *Boss et al.*, 2008; *Gritschneder et al.*, 2012) and a correct ratio between the different SLRs is only possible for a special kind of supernova, a faint one with an ad-hoc fall back (see *Takigawa et al.*, 2008). The requirement for the correct ratio and the efficient mixing impose very strong constraints on the scenario that are also rather unlikely to happen. Furthermore, these models are based on nucleo-synthesis calculations that are promising but still suffer large discrepancies with current *INTEGRAL* observations (see *Woosley and Heger*, 2007).

An interesting new point of view was introduced by *Gounelle et al.* (2009). They proposed a scenario in which the abundance of iron-60 is coming from the ISM of the parent molecular cloud that has been enriched by several supernova explosions. This scenario is very appealing because it does not need to give a special position to the Solar System. Moreover, it naturally comes in the picture of dynamic molecular clouds dispersed by massive stars that was described in Sect. 1.4 for the regulation of star formation. *Gounelle et al.* (2009) used a stochastic model for the explosion of supernovae in a molecular cloud with a standard IMF and they were able to reproduce the abundance of iron-60 present in the ISM at the beginning of the Solar System. Note that this is an estimate of the steady state iron-60 abundance in the ISM that previous supernova models did not take into account. Aluminum-26 could also come from the ISM but current estimates from observations gives a ratio ^{26}Al/^{60}Fe of 3-4 while the ratio is of the order of 9 in the early Solar System. This suggests that the Solar System was enriched in ^{26}Al and a possible explanation is the wind from massive stars, at the edge of the H II region (reviewed by *Hester and Desch* (2005)). A series of issues could also be explained by this scenario, such as the properties of organic compounds in carbonaceous chondrites (see *Bernstein et al.*, 1999), the observed anomalies in the relative abundances of ^{16}O, ^{17}O, and ^{18}O (see *Clayton*, 2003). The early Solar System would also have formed in a photo-evaporated protoplanetary disk (proplyd) that can explained the observed 50 AU outer edge of the Kuiper Belt (*Chiang and Brown*, 1999) and the relatively low masses of Uranus and Neptune (see *Shu et al.*, 1993). Although it could be argued that the edge of a H II region is a special location, it is much more probable for a star to be formed by triggering at the edge (that could be in big H II regions up to 100 pc) than to be close to a supernova (e.g. *Gritschneder et al.*, 2012, less than 5 pc). Furthermore current estimations of young stellar objects that have been formed by triggering in the Milky Way are in between 25-50 % (see *Snider et al.*, 2009; *Thompson et al.*, 2011).

At all the scales of Astrophysics, the impact of the ionization from massive stars is a crucial issue.

- At the galactic scale: H II regions regulate star formation by supporting molecular clouds against gravitational collapse. However the detail repartition between thermal, turbulent and kinetic transferred energy is not known and is of great importance for galaxy simulations.
- At the molecular cloud scale: It is clear that H II regions compress the surrounding gas, form pillars, globules, and dense layers in which proto-stars are observed. What are the formation mechanisms of these structures? Are the formation of these proto-stars triggered or would they have formed anyway? Do massive stars have an impact of the PDF on the surrounding gas? Do they have an impact on the IMF? Do we need to complete the gravo-turbulent scenario?
- At the stellar and solar scale: indications point to a possible birth place of the Solar System at the edge of an H II region. What is the impact of the ionization on a proto-planetary disk? Would a stellar wind be able to enrich in aluminum-26 an early Solar System at the edge of a H II region?

The present work aims at answering some of these questions, by focusing especially on the formation of the structures at the edge of the H II *regions and on the impact of ionization on the molecular gas.*

We will present in Chap. 2 the state of the art of the theoretical and observational works on H II *regions. In Chap. 3, we present the numerical tools that have been developed to model the ionization in a hydrodynamic simulation. The main results on the formation of pillars and on the formation of globules are presented in Chap. 4 and 5. Finally we compare the new models developed in these chapters with a multi-wavelength study of* H II *regions with ground-based observations and recent Herschel observations.*

We present in appendix other works that have been done in parallel of this PhD: the charge exchange in colliding planetary and stellar winds in collaboration with Prof. E. Chiang during the ISIMA summer school 2011 in Beijing; and the sub-millimeter site testing at the Concordia station in Antarctica with the CAMISTIC team (PI: G. Durand).

Bibliography

Alves, J., M. Lombardi, and C. J. Lada (2007), The mass function of dense molecular cores and the origin of the IMF, *A&A*, *462*(1), L17–L21. 10

Audit, E., and P. Hennebelle (2005), Thermal condensation in a turbulent atomic hydrogen flow, *A&A*, *433*(1), 1–13. 11

Audit, E., and P. Hennebelle (2010), On the structure of the turbulent interstellar clouds . Influence of the equation of state on the dynamics of 3D compressible flows, *A&A*, *511*, 76. 11, 12, 13

Ballesteros-Paredes, J., L. Hartmann, and E. Vázquez-Semadeni (1999), Turbulent Flow-driven Molecular Cloud Formation: A Solution to the Post-T Tauri Problem?, *ApJ*, *527*(1), 285–297. 9

Ballesteros-Paredes, J., R. S. Klessen, M.-M. Mac Low, and E. Vázquez-Semadeni (2007), Molecular Cloud Turbulence and Star Formation, *Protostars and Planets V*, pp. 63–80. 8

Bernstein, M. P., S. A. Sandford, L. J. Allamandola, J. S. B. Gillette, S. J. Clemett, and R. N. Zare (1999), UV Irradiation of Polycyclic Aromatic Hydrocarbons in Ices: Production of Alcohols, Quinones, and Ethers, *Science*, *283*, 1135. 14

Blaauw, A. (1964), The O Associations in the Solar Neighborhood, *Annual Review of Astronomy and Astrophysics*, *2*, 213. 13

Blitz, L. (1993), Giant molecular clouds, *In: Protostars and planets III (A93-42937 17-90)*, pp. 125–161. 9

Boss, A. P., S. I. Ipatov, S. A. Keiser, E. A. Myhill, and H. A. T. Vanhala (2008), Simultaneous Triggered Collapse of the Presolar Dense Cloud Core and Injection of Short-Lived Radioisotopes by a Supernova Shock Wave, *ApJ*, *686*(2), L119–L122. 14

Bournaud, F., B. G. Elmegreen, R. Teyssier, D. L. Block, and I. Puerari (2010), ISM properties in hydrodynamic galaxy simulations: turbulence cascades, cloud formation, role of gravity and feedback, *MNRAS*, *409*(3), 1088–1099. 9

Cameron, A. G. W., and J. W. Truran (1977), The supernova trigger for formation of the solar system, *Icarus*, *30*, 447–461. 13

Cameron, A. G. W., P. Hoeflich, Myers, P. C., and D. D. Clayton (1995), Massive Supernovae, Orion Gamma Rays, and the Formation of the Solar System, *Astrophysical Journal Letters v.447*, *447*, L53. 14

Cappellari, M., et al. (2012), Systematic variation of the stellar initial mass function in early-type galaxies, *Nature*, *484*(7), 485–488. 8

Chabrier, G. (2003), Galactic Stellar and Substellar Initial Mass Function, *PASP*, *115*(8), 763–795. 10, 11

Chiang, E. I., and M. E. Brown (1999), Keck Pencil-Beam Survey for Faint Kuiper Belt Objects, *The Astronomical Journal*, *118*(3), 1411–1422. 14

Clayton, R. N. (2003), Oxygen Isotopes in the Solar System, *Space Science Reviews*, *106*(1), 19–32. 14

Crutcher, R. M., D. A. Roberts, T. H. Troland, and W. M. Goss (1999), The Magnetic Field of the NGC 2024 Molecular Cloud, *ApJ*, *515*(1), 275–285. 9

Daddi, E., et al. (2010), Different Star Formation Laws for Disks Versus Starbursts at Low and High Redshifts, *ApJ*, *714*(1), L118–L122. 8

Ebert, R. (1955), Über die Verdichtung von H I-Gebieten. Mit 5 Textabbildungen, *Zeitschrift für Astrophysik*, *37*, 217. 13

Elmegreen, B. G., and C. J. Lada (1977), Sequential formation of subgroups in OB associations, *ApJ*, *214*, 725–741. 13

Fall, S. M., M. R. Krumholz, and C. D. Matzner (2010), Stellar Feedback in Molecular Clouds and its Influence on the Mass Function of Young Star Clusters, *ApJ*, *710*(2), L142–L146. 10

Federrath, C., R. S. Klessen, and W. Schmidt (2008), The Density Probability Distribution in Compressible Isothermal Turbulence: Solenoidal versus Compressive Forcing, *ApJ*, *688*(2), L79–L82. 12

Field, G. B., D. W. Goldsmith, and H. J. Habing (1969), Cosmic-Ray Heating of the Interstellar Gas, *ApJ*, *155*, L149. 11

Genzel, R., et al. (2010), A study of the gas-star formation relation over cosmic time, *MNRAS*, *407*(4), 2091–2108. 8

Goldreich, P., and D. Lynden-Bell (1965), II. Spiral arms as sheared gravitational instabilities, *MNRAS*, *130*, 125. 11

Gounelle, M., and A. Meibom (2008), The Origin of Short-lived Radionuclides and the Astrophysical Environment of Solar System Formation, *ApJ*, *680*(1), 781–792. 14

Gounelle, M., A. Meibom, P. Hennebelle, and S.-i. Inutsuka (2009), Supernova Propagation and Cloud Enrichment: A New Model for the Origin of 60Fe in the Early Solar System, *ApJ*, *694*(1), L1–L5. 14

Gritschneder, M., D. N. C. Lin, S. D. Murray, Q.-Z. Yin, and M.-N. Gong (2012), The Supernova Triggered Formation and Enrichment of Our Solar System, *ApJ*, *745*(1), 22. 14

Gurzadyan, G. A. (2010), *The Physics and Dynamics of Planetary Nebulae*, Springer Verlag. 7

Hartmann, L. (2003), Comments on Inferences of Star Formation Histories and Birth Lines, *ApJ*, *585*(1), 398–405. 9

Hartmann, L., J. Ballesteros-Paredes, and E. A. Bergin (2001), Rapid Formation of Molecular Clouds and Stars in the Solar Neighborhood, *ApJ*, *562*(2), 852–868. 9

Heitsch, F., A. Burkert, L. W. Hartmann, A. D. Slyz, and J. E. G. Devriendt (2005), Formation of Structure in Molecular Clouds: A Case Study, *ApJ*, *633*(2), L113–L116. 11

Hennebelle, P., and E. Audit (2007), On the structure of the turbulent interstellar atomic hydrogen. I. Physical characteristics. Influence and nature of turbulence in a thermally bistable flow, *A&A*, *465*(2), 431–443. 11

Hennebelle, P., and G. Chabrier (2008), Analytical Theory for the Initial Mass Function: CO Clumps and Prestellar Cores, *ApJ*, *684*(1), 395–410. 10, 13

Hennebelle, P., and G. Chabrier (2009), Analytical Theory for the Initial Mass Function. II. Properties of the Flow, *ApJ*, *702*(2), 1428–1442. 10

Hennebelle, P., E. Audit, and M.-A. Miville-Deschênes (2007), On the structure of the turbulent interstellar atomic hydrogen. II. First comparison between observation and theory. Are the characteristics of molecular clouds determined early in the turbulent 2-phase atomic gas?, *A&A*, *465*(2), 445–456. 11

Hester, J. J., and S. J. Desch (2005), Understanding Our Origins: Star Formation in HII Region Environments, *Chondrites and the Protoplanetary Disk*, *341*, 107. 14

Heyer, M. H., and C. M. Brunt (2004), The Universality of Turbulence in Galactic Molecular Clouds, *ApJ*, *615*(1), L45–L48. 9, 11

Hopkins, P. F., E. Quataert, and N. Murray (2011), Self-regulated star formation in galaxies via momentum input from massive stars, *MNRAS*, *417*(2), 950–973. 9, 10

Kennicutt, R. C. J. (1998), The Global Schmidt Law in Star-forming Galaxies, *Astrophysical Journal v.498*, *498*, 541. 7, 8

Koyama, H., and S.-i. Inutsuka (2002), An Origin of Supersonic Motions in Interstellar Clouds, *ApJ*, *564*(2), L97–L100. 11

Kroupa, P. (2001), On the variation of the initial mass function, *MNRAS*, *322*(2), 231–246. 10, 11

Lada, C. J., M. Lombardi, and J. F. Alves (2010), On the Star Formation Rates in Molecular Clouds, *ApJ*, *724*(1), 687–693. 8

Larson, R. B. (1981), Turbulence and star formation in molecular clouds, *MNRAS*, *194*, 809–826. 9

Lee, T., D. A. Papanastassiou, and G. J. Wasserburg (1977), Aluminum-26 in the early solar system - Fossil or fuel, *ApJ*, *211*, L107–L110. 13

Lee, T., F. H. Shu, H. Shang, A. E. Glassgold, and K. E. Rehm (1998), Protostellar Cosmic Rays and Extinct Radioactivities in Meteorites, *ApJ*, *506*(2), 898–912. 13

Matzner, C. D. (2002), On the Role of Massive Stars in the Support and Destruction of Giant Molecular Clouds, *ApJ*, *566*(1), 302–314. 9

McCray, R., and M. Kafatos (1987), Supershells and propagating star formation, *ApJ*, *317*, 190–196. 11

McKee, C. F., and J. P. Ostriker (1977), A theory of the interstellar medium - Three components regulated by supernova explosions in an inhomogeneous substrate, *ApJ*, *218*, 148–169. 9

Miller, G. E., and J. M. Scalo (1979), The initial mass function and stellar birthrate in the solar neighborhood, *and J. M. Scalo. Astrophysical Journal Supplement Series*, *41*, 513–547. 10

Motte, F., P. André, and R. Neri (1998), The initial conditions of star formation in the rho Ophiuchi main cloud: wide-field millimeter continuum mapping, *A&A*, *336*, 150–172. 10

Nakano, T., and T. Nakamura (1978), Gravitational Instability of Magnetized Gaseous Disks 6, *Publications of the Astronomical Society of Japan*, *30*, 671–680. 9

Ntormousi, E., A. Burkert, K. Fierlinger, and F. Heitsch (2011), Formation of Cold Filamentary Structure from Wind-blown Superbubbles, *ApJ*, *731*(1), 13. 11

Ogelman, H. B., and S. P. Maran (1976), The origin of OB associations and extended regions of high-energy activity in the Galaxy through supernova cascade processes, *ApJ*, *209*, 124–129. 13

Ouellette, N., S. J. Desch, and J. J. Hester (2007), Interaction of Supernova Ejecta with Nearby Protoplanetary Disks, *ApJ*, *662*(2), 1268–1281. 13

Passot, T., and E. Vázquez-Semadeni (1998), Density probability distribution in one-dimensional polytropic gas dynamics, *Physical Review E (Statistical Physics*, *58*(4), 4501–4510. 12

Pikel'Ner, S. B. (1968), Heating of the Interstellar Gas by Subcosmic Rays, and the Formation of Clouds., *Soviet Astronomy*, *11*, 737. 11

Salpeter, E. E. (1955), The Luminosity Function and Stellar Evolution., *ApJ*, *121*, 161. 10, 11

Schmidt, M. (1959), The Rate of Star Formation., *ApJ*, *129*, 243. 7

Schmidt, W., S. A. W. Kern, C. Federrath, and R. S. Klessen (2010), Numerical and semi-analytic core mass distributions in supersonic isothermal turbulence, *A&A*, *516*, 25. 10

Shu, F. H., D. Johnstone, and D. Hollenbach (1993), Photoevaporation of the solar nebula and the formation of the giant planets, *Icarus*, *106*, 92. 14

Snider, K. D., J. J. Hester, S. J. Desch, K. R. Healy, and J. Bally (2009), Spitzer Observations of The H II Region NGC 2467: An Analysis of Triggered Star Formation, *ApJ*, *700*(1), 506–522. 14

Takigawa, A., J. Miki, S. Tachibana, G. R. Huss, N. Tominaga, H. Umeda, and K. Nomoto (2008), Injection of Short-Lived Radionuclides into the Early Solar System from a Faint Supernova with Mixing Fallback, *ApJ*, *688*(2), 1382–1387. 14

Thompson, M. A., J. S. Urquhart, T. J. T. Moore, and L. K. Morgan (2011), The statistics of triggered star formation: an overdensity of massive YSOs around Spitzer bubbles, *arXiv*, *astro-ph.GA*. 14

Toomre, A. (1964), On the gravitational stability of a disk of stars, *ApJ*, *139*, 1217–1238. 11

Troland, T. H., and R. M. Crutcher (2008), Magnetic Fields in Dark Cloud Cores: Arecibo OH Zeeman Observations, *ApJ*, *680*(1), 457–465. 9

Troland, T. H., R. M. Crutcher, A. A. Goodman, C. Heiles, I. Kazes, and Myers, P. C. (1996), The Magnetic Fields in the Ophiuchus and Taurus Molecular Clouds, *Astrophysical Journal v.471*, *471*, 302. 9

Vázquez-Semadeni, E., D. Ryu, T. Passot, R. F. González, and A. Gazol (2006), Molecular Cloud Evolution. I. Molecular Cloud and Thin Cold Neutral Medium Sheet Formation, *ApJ*, *643*(1), 245–259. 11

Vishniac, E. T. (1994), Nonlinear instabilities in shock-bounded slabs, *ApJ*, *428*, 186–208. 11

Whitworth, A. P. (1979), The erosion and dispersal of massive molecular clouds by young stars, *MNRAS*, *186*, 59–67. 9

Wolfire, M. G., D. Hollenbach, C. F. McKee, A. G. G. M. Tielens, and E. L. O. Bakes (1995), The neutral atomic phases of the interstellar medium, *ApJ*, *443*, 152–168. 11

Wolfire, M. G., C. F. McKee, D. Hollenbach, and A. G. G. M. Tielens (2003), Neutral Atomic Phases of the Interstellar Medium in the Galaxy, *ApJ*, *587*(1), 278–311, doi: 10.1086/368016. 11, 13

Woosley, S. E., and A. Heger (2007), Nucleosynthesis and remnants in massive stars of solar metallicity, *Physics Reports*, *442*(1), 269–283. 14

Yorke, H. W., G. Tenorio-Tagle, P. Bodenheimer, and M. Rozyczka (1989), The combined role of ionization and supernova explosions in the destruction of molecular clouds, *A&A*, *216*, 207–214. 9

Chapter 2

State of the art of the study of H II regions

Experience without theory is blind, but theory without experience is mere intellectual play.
Immanuel Kant

In this chapter, we review the theoretical and observational works (relevant for this thesis) that has been done on H II regions and present the state of the art of the models used to describe the formation and evolution of the structures around these H II regions. We shall review the theory of ionization fronts, the collect and collapse model, the radiation-driven implosion model, and the recent turbulent models. We also present (non-exhaustively) the observations of pillars, globules, dense shells around H II regions.

2.1 Theory and numerical simulations

2.1.1 Ionization fronts

Struve and Elvey (1939) were the first to observe strong and extended Hα emissions in the Milky Way. Based on these observations, *Strömgren* (1939) proposed that the emission was coming from ionized gas around O stars and demonstrated that the emission could be extended up to hundreds of parsecs. Let us take an O star emitting S_* ionizing photons per second, surrounded by a homogeneous gas of density n and temperature T. The gas surrounding the stars will be subject to ionization and recombination reactions

$$H^0 + \gamma \leftrightarrow H^+ + e^- \tag{2.1}$$

The star will ionize the gas around but recombination will also take place in the ionized gas. Therefore the star ionizes the surroundings until all the emitted photons are used to compensate the recombination reactions along the path. The number of recombination in a volume V is given by

$$r = \beta n_{H^+} n_{e^-} V = \beta X^2 n_H^2 V \tag{2.2}$$

in which β is taken from *Black* (1981) and is equal to 2×10^{-10} $\mathrm{T}^{-0.75}$ cm^3 s^{-1}. X is the ionization fraction, and local neutrality of the ionized gas was assumed ($\mathrm{n}_H^+ = \mathrm{n}_e^- = \mathrm{X}\mathrm{n}_H$). In the ionized gas, $X = 1$ and the ionization will stop at the location where all the photons are used for the recombinations, i.e. when $S_* = r$. Assuming that the ionized region is spherical, the limit of the ionized sphere is given by the Strömgren radius

$$R_s = \left(\frac{3S_*}{4\pi\beta n_H^2}\right)^{1/3} \tag{2.3}$$

This is the limit of the ionization front (I-front hereafter). The thickness of the front can be estimated by $1/n_H\sigma$ with σ the cross section of ionization ($\sigma \approx 6.8{\times}10^{-18}$ cm^2 see Sect. 3.3 for details). For an O4 star emitting 10^{50} photons per second and a hot phase of the ISM with $n_H = 1$ cm^{-3} and $T = 8{,}000$ K, the Strömgren radius is typically of the order of 100-200 parsecs as estimated by *Strömgren* (1939) and the thickness of the I-front is 10^{-2} pc. Therefore the transition between ionized and neutral gas in the I-front is very thin even for low densities, compared to the size of the H II region. When massive stars start to ionize their surroundings, they are embedded in a molecular cloud that is much denser and colder. For an O4 star emitting 10^{50} photons per second in a molecular cloud at $n_H = 500$ cm^{-3} and $T = 25$ K, the Strömgren radius is 0.56 parsec. However the ionized gas will be heated up to 8,000 K by the energetic electrons pulled off by the ionizing photons (see Sect. ?? for the detailed calculation). The recombination rate will decrease because of the increase of temperature and therefore the I-front will propagate further inside the cold medium up to 2.4 parsec. The typical timescale for the propagation is given by the ionization timescale $t_{\rm io} = 1/\sigma n_H c$ of the order of 10^4 seconds that is much shorter than the hydrodynamic timescale $\mathrm{t_{dyn}} \approx R_s/c_0 \approx 10^{13}$ s with c_0 the sound speed in the cold gas. Therefore the propagation of the I-front is very fast and the gas is "frozen" during that stage. When the I-front reaches the new limit of $R_s = 2.4$ pc for T = 8,000 K, the ionized sphere is small, dense, and very hot. This ionized sphere is therefore at very high pressure, 300 times the pressure of the surrounding gas and will expand in the cold medium. The equilibrium between the pressure of the ionized gas and the cold gas is achieved when

$$P_{II} = 2n_{II}k_bT_{II} \approx P_0 = n_0k_bT_0 \tag{2.4}$$

where subscript II refers to the quantity in the ionized gas and subscript 0 to the quantity in the cold medium. The density to reach the hydrostatic equilibrium is then $\mathrm{n}_{II} \approx 1$ cm^{-3} that implies an expansion for the sphere from a Strömgren radius of 2.4 pc up to 175 pc. All the quantities here are taken from the conditions in the Rosette Nebula (see *Schneider et al.*, 1998). Note that at such densities, there is not much recombination in the H II region and most of them occurs at the I-front in the transition between the low-density gas to the cold dense medium, before hydrostatic equilibrium is reached. This is also in agreement with the observations in which not much Hα emission is seen at the proximity of the ionization sources but most of it come from the surface of the cold gas that is exposed to the radiation ("bright rims").

When the I-front expands the flux that is arriving at the I-front is the initial flux minus the amount of recombination between the star and the I-front, and each photons that cross the I-front ionizes one atom

$$F_\gamma = \frac{S_*}{4\pi R_I^2}\left(1 - \frac{R_I^3}{R_s^3}\right) = n_0V_I \tag{2.5}$$

with R_I and V_I the position and velocity of the I-front and F_γ the flux at the I-front. We assumed a constant density in the ionized region. We can use the Rankine-Hugoniot conditions for isothermal gas in the referential of the I-front (see *Kahn*, 1954; *Spitzer*, 1978)

$$\begin{aligned} n_0u_0 &= n_{II}u_{II} = F_\gamma \\ n_0(u_0^2 + c_0^2) &= n_{II}(u_{II}^2 + c_{II}^2) \end{aligned} \tag{2.6}$$

with u_0 the velocity of the unionized gas relative to the I-front(therefore equal to the velocity of the I-front) and u_{II} the velocity of the ionized gas relative to the I-front. We can compute the density jump across the I-front with (see *Spitzer*, 1978)

$$\frac{n_{II}}{n_0} = \frac{u_0}{u_{II}} = \frac{c_0^2 + u_0^2 \pm \sqrt{(u_0^2 - u_D^2)(u_0^2 - u_R^2)}}{2c_{II}^2} \tag{2.7}$$

$u_0 = F_\gamma/n_0$	I-front type	S-front
$u_0 > u_R$	R-type	no
$u_0 = u_R$	R-critical	no
$u_R > u_0 > u_D$	M-type	yes $\rightarrow$ D-type
$u_0 = u_D$	D-critical	yes if M-type before
$u_0 < u_D$	D-type	yes if M-type before

Table 2.1: Conditions that define the different types of I-front and the creation of the S-front.

with

$$\begin{aligned} u_R &= c_{II} + \sqrt{c_{II}^2 - c_0^2} \approx 2c_{II} \\ u_D &= c_{II} - \sqrt{c_{II}^2 - c_0^2} \approx c_0^2/2c_{II} \end{aligned} \tag{2.8}$$

when $c_{II} \gg c_0$. As explained above, at the beginning, the I-front propagates very fast in the cold medium, when F_γ tends to infinity close to the star. Therefore at the beginning $u_0 \gg u_R$ and the I-front is defined to be of "R type". Note that the condition $n_{II} = n_0$ in the hydro-frozen phase with $u_0 \gg u_R$ impose to choose the minus sign in Eq. 2.7 (weak "R type" in *Spitzer* (1978)). When the recombinations in the ionized gas have taken enough ionizing photons, the I-front decelerates and becomes "R critical" when $u_0 = u_R$. When $u_R \geq u_0 \geq u_D$, there is no solution to Eq. 2.7 and the I-front is defined as M-type. A shock front (S-front hereafter) has to precede the I-front in order to get a denser and slower gas with $u_0 \leq u_D$. In that situation the I-front is of "D type" (D critical when $u_0 = u_D$). When the I-front is D critical then the density jump is given by $n_{II}/n_0 = c_0^2/2c_{II}^2$ and for the whole D-type phase $n_{II} \leq n_0$, this corresponds to the expansion phase of the H II region. When the front is D critical, $u_{II} = c_{II}$ and then u_{II} decreases during the D-type phase (i.e. minus sign in Eq. 2.7, weak D type in *Spitzer* (1978)). All these conditions are resumed in Tab. 2.1.

The expansion of the hot gas into the cold medium can be estimated to be at a velocity of the order of the sound speed of the hot gas $\mathrm{c}_{II} \approx 10$ km/s. The expansion will be highly supersonic relative to the cold gas with a Mach number around 25. Assuming that the S-front reaches a constant velocity, in its own referential the Rankine-Hugoniot conditions can be applied to get an idea of the compression. Assuming an isothermal equation of state in the cold gas, the density jump will be the square of the Mach number. Therefore a dense layer of gas will be formed between the I-front and S-front in the D-type phase at a density of the order of 3×10^5 cm^{-3}.

2.1.2 Collect and collapse

Elmegreen and Lada (1977) proposed that this dense layer could get sufficiently dense to reach the gravitational instability and trigger the formation of a second generation of stars. This could explain the age sequence observed by *Blaauw* (1964) around OB associations. This scenario is called "collect and collapse" (CCS). An outline of the model is given in Fig. 2.1. Based on the works of *Elmegreen and Lada* (1977) and *Spitzer* (1978), we derive in this section an analytical expression for the different parameters of the shell, its velocity V_{shell}, its density n_c, its thickness L_{shell} and its radius r_{shell}. These expressions will be tested with the observations in Chap. 6.

For simplicity we suppose that the velocity of the I-front and S-front are the same and are equaled to V_{shell}. The cold medium (n_0, v_0=0) is separated from the compressed shell (n_c,v_c) by the S-front. The compressed shell is separated from the ionized gas (n_{II},v_{II}) by the I-front. The isothermal Rankine-Hugoniot conditions in the referential of the cold gas

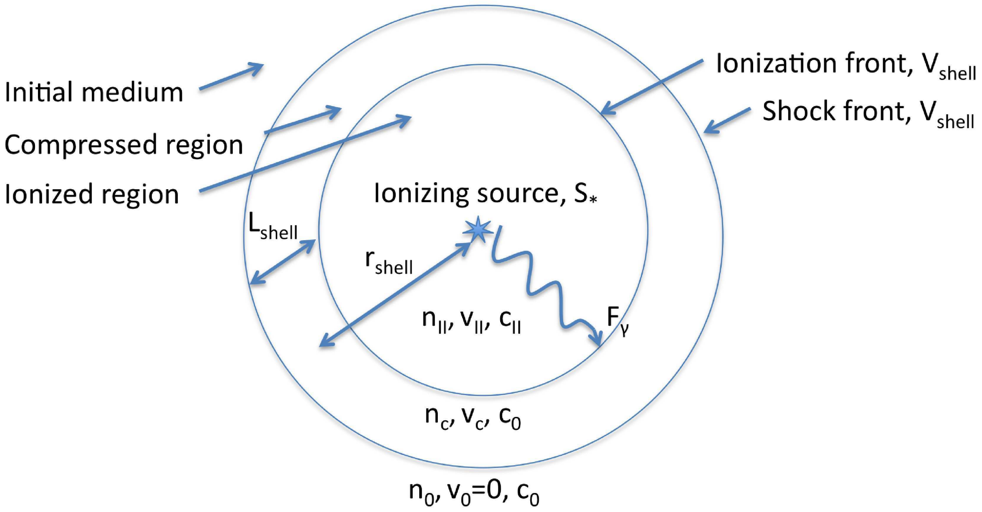

Figure 2.1: Outline of the collect and collapse scenario with the different variables used in the analytical model.

gives

$$\begin{aligned} -n_0 V_{\rm shell} &= n_c(v_c - V_{\rm shell}) = n_{II}(v_{II} - V_{\rm shell}) = -F_\gamma \\ n_0(V_{\rm shell}^2 + c_0^2) &= n_c((v_c - V_{\rm shell})^2 + c_0^2) = n_{II}((v_{II} - V_{\rm shell})^2 + c_{II}^2) \end{aligned} \tag{2.9}$$

with F_γ the ionization flux at the I-front (taking in account the recombination in the ionized gas). These relations are local and we neglect the curvature of the fronts, besides the shell is assumed stationary in the referential of the cold gas. Since the shock is strongly supersonic, the second equation can be approximated by

$$n_0 V_{\rm shell}^2 \approx n_c c_0^2 \approx n_{II} \zeta c_{II}^2 \tag{2.10}$$

with $\zeta = 2$ for a D-critical I-front ($V_{\rm shell} - v_{II} = c_{II}$) and ζ varies from 2 to 1 in the weak D phase. The time-scale of the expansion of the shell is much longer than the ionization time-scale, therefore the equilibrium between ionization and recombination holds during the expansion

$$S_* = \beta n_0^2 4\pi R_s^3/3 = \beta n_{II}^2 4\pi r_{\rm shell}^3/3 \tag{2.11}$$

with R_s the strömgren radius at the end of the R-type phase and $r_{\rm shell}$ the position of the shell at a time t in the D-type phase. Therefore from Eq. 2.10 and Eq. 2.11, we get

$$V_{\rm shell} = \frac{dr_{\rm shell}}{dt} = \sqrt{\zeta} c_{II} \left(\frac{n_{II}}{n_0}\right)^{1/2} = \sqrt{\zeta} c_{II} \left(\frac{R_s}{r_{\rm shell}}\right)^{3/4} \tag{2.12}$$

By integration we get the position of the shell and we set ζ to 1 (weak D-type I-front) to get back the result from *Spitzer* (1978)

$$r_{\rm shell} = R_s \left(1 + \frac{7}{4}\frac{c_{II}}{R_s} t\right)^{4/7} \approx R_s \left(\frac{7}{4}\frac{c_{II}}{R_s} t\right)^{4/7}$$

$$\approx \quad 20\ \mathrm{pc} \left(\frac{t}{5\ \mathrm{My}}\right)^{4/7} \left(\frac{S_*}{10^{50}\ \mathrm{s}^{-1}}\right)^{1/7} \left(\frac{n_0}{500\ \mathrm{cm}^{-3}}\right)^{-2/7} \tag{2.13}$$

This is the quickest way to obtain the position of the shell that was obtained by *Spitzer* (1978). The numerical estimation is done in the conditions of the Rosette Nebula and we get the observed radius of the H II region. Note that the hydrostatic radius of the H II region, i.e. 175 parsecs cannot be reached in the lifetime of the O star ($\leq$ 10 million years). The velocity of the shell can be obtained with Eq. 2.12

$$\begin{aligned} V_{\mathrm{shell}} &\approx c_{II} \left(1 + \frac{7}{4}\frac{c_{II}}{R_s} t\right)^{-3/7} \approx c_{II} \left(\frac{7}{4}\frac{c_{II}}{R_s} t\right)^{-3/7} \\ &\approx 2\ \mathrm{km/s} \left(\frac{t}{5\ \mathrm{My}}\right)^{-3/7} \left(\frac{S_*}{10^{50}\ \mathrm{s}^{-1}}\right)^{1/7} \left(\frac{n_0}{500\ \mathrm{cm}^{-3}}\right)^{-2/7} \end{aligned} \tag{2.14}$$

The relation gives a shell with a Mach number of 5 that is again what is observed in the region. The density in the shell n_c can be obtained with Eq. 2.10

$$\begin{aligned} n_c &\approx n_0 \frac{V_{\mathrm{shell}}^2}{c_0^2} \approx n_0 \frac{c_{II}^2}{c_0^2} \left(1 + \frac{7}{4}\frac{c_{II}}{R_s} t\right)^{-6/7} \\ &\approx 10^4\ \mathrm{cm}^{-3} \left(\frac{c_0}{0.4\ \mathrm{km/s}}\right)^{-2} \left(\frac{t}{5\ \mathrm{My}}\right)^{-3/7} \left(\frac{S_*}{10^{50}\ \mathrm{s}^{-1}}\right)^{1/7} \left(\frac{n_0}{500\ \mathrm{cm}^{-3}}\right)^{-2/7} \end{aligned} \tag{2.15}$$

It is interesting to note that the compression decreases with time, from $3{\times}10^5$ cm^3 to 10^4 cm^3 after 5 million years. The column density N in the shell is equal to what has been accumulated during the collect phase: $\mathrm{n}_0\mathrm{r}_{\mathrm{shell}}/3$, minus what remains in the H II region: $\mathrm{n}_{II}\mathrm{r}_{\mathrm{shell}}/3$

$$N = \frac{1}{3} n_0 r_{\mathrm{shell}} \left(1 - \left(\frac{R_s}{r_{\mathrm{shell}}}\right)^{3/2}\right) \tag{2.16}$$

The thickness of the shell $\mathrm{L}_{\mathrm{shell}}$ is then given by N/n_c

$$\begin{aligned} L_{\mathrm{shell}} &= \frac{1}{3} r_{\mathrm{shell}} \frac{c_0^2}{c_{II}^2} \left(\frac{R_s}{r_{\mathrm{shell}}}\right)^{-3/2} \left(1 - \left(\frac{R_s}{r_{\mathrm{shell}}}\right)^{3/2}\right) \approx \frac{1}{3} r_{\mathrm{shell}} \frac{c_0^2}{c_{II}^2} \left(\frac{R_s}{r_{\mathrm{shell}}}\right)^{-3/2} \\ &\approx 0.24\ \mathrm{pc} \left(\frac{t}{5\ \mathrm{My}}\right)^{6/7} \left(\frac{S_*}{10^{50}\ \mathrm{s}^{-1}}\right)^{-2/7} \left(\frac{n_0}{500\ \mathrm{cm}^{-1}}\right)^{4/7} \left(\frac{c_0}{0.4\ \mathrm{km/s}}\right)^{2} \end{aligned} \tag{2.17}$$

The condition for gravitational instability in an expanding shell was determined by *Elmegreen* (1994)

$$\frac{\pi G \rho_0}{3 c_0} > \frac{8^{1/2} V_{\mathrm{shell}}}{r_{\mathrm{shell}}^2} \tag{2.18}$$

Using Eq. 2.12, the condition becomes that r_{shell} should be greater than a characteristic size r_{Jeans} defined by

$$\begin{aligned} r_{\mathrm{Jeans}} &= R_s \left(\frac{3\sqrt{8} c_{II} c_0}{\pi G \rho_0 R_s^2}\right)^{4/11} \\ &= 8\ \mathrm{pc} \left(\frac{S_*}{10^{50}\ \mathrm{s}^{-1}}\right)^{1/11} \left(\frac{n_0}{500\ \mathrm{cm}^{-3}}\right)^{-6/11} \left(\frac{c_0}{0.4\ \mathrm{km/s}}\right)^{4/11} \end{aligned} \tag{2.19}$$

The shell around NGC2244 in the Rosette Nebula is therefore gravitationally unstable since the H II region has a size of 20 parsecs. Indeed, there are clumps in the shell that could have been formed by the collect and collapse scenario.

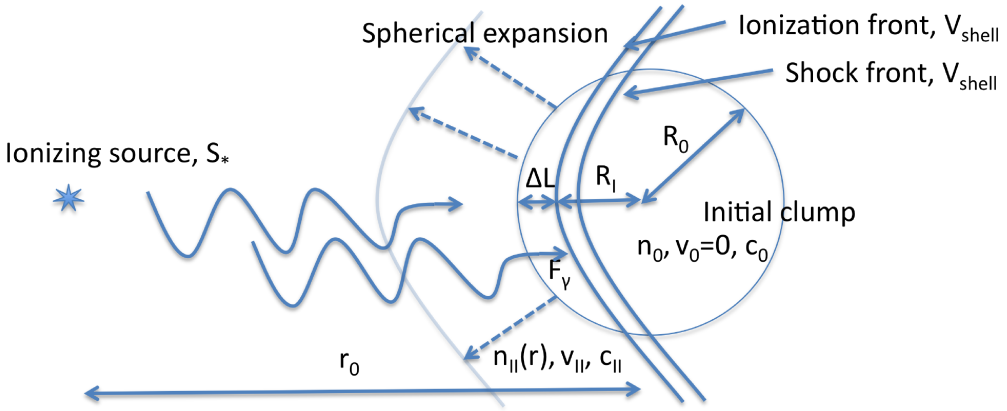

Figure 2.2: Outline of the radiation driven implosion scenario with the different variables used in the analytical model.

The gravitational collapse of an expanding shell around a H II region has been studied for years both theoretically and numerically. Among those studies, *Elmegreen and Elmegreen* (1978); *Elmegreen* (1994) studied the growth rate of the instability; *Whitworth et al.* (1994) the fragmentation of the shell and *Elmegreen* (1998) did a complete review of the various models based and the idea of collect and collapse. Recent numerical studies by *Dale et al.* (2007b,0) were able to form self-gravitating fragments in the shell, showing that they did achieve the collapse phase after the collect phase. *Dale et al.* (2009); *Wünsch et al.* (2010) did a numerical study of the fragmentation and found a good agreement with the analysis of *Whitworth et al.* (1994) in the limit of the thin-shell approximation (when the shell is confined by the pressure of the H II region). *Lora et al.* (2009) studied the angular momentum of the fragments thanks to numerical simulations and showed that it tends to be perpendicular to the ionizing radiation. The effect of magnetic fields was studied by *Krumholz et al.* (2007); *Arthur et al.* (2011) and they showed that the magnetic field does not alter the global morphology of the H II region, but tends to suppress the fragmentation at small scale because of the magnetic support.

However, the radius of the shell can only be greater than its Jeans radius at late time ($\approx$ a few million years), when the H II region is well developed. Lots of structures are already observed at the earliest time of the evolution of H II regions. Therefore other processes are needed to explain such structures (e.g. *Hester et al.*, 1996, for the Pillars of Creation).

2.1.3 Radiation-driven implosion

The collect and collapse cannot explain the structures seen at the earliest time of the expansion of an H II region ($\approx$ less than one million year). This fact with the observations of globules and pillars in these early H II regions lead to the conclusion that the initial structures of the molecular cloud should be of importance. The ionization of isolated small clouds was studied by *Oort and Spitzer* (1955); *Spitzer* (1978) and *Bertoldi* (1989); *Bertoldi and McKee* (1990) performed a detailed analysis of the profiles and evolution of these objects. They showed how the radiation-driven implosion (RDI) of the clump could result in structures like cometary globules in H II region (e.g. Rosette Nebula (*Herbig*, 1974) and Gump Nebula (*Hawarden and Brand*, 1976) and following studies). In this section, we will develop simple analytical expressions of the duration of the implosion $t_{\rm imp}$, the velocity of the cometary globule V_g and its radius R_g. These quantities can be compared with numerical simulations and the radius and velocity of the globule can be compared with observations.

The ionizing flux impacting an isolated homogeneous spherical cloud (density $\rm n_0$, sound speed $\rm c_0$ and radius $\rm R_0$) at a distance r_0 of a star is given by

$$F_0 = \frac{S_*}{4\pi r_0^2} \tag{2.20}$$

in which we neglected the absorption by the gas between the cloud and the star. As in Eq. 2.5, the velocity of the I-front is given by $V_I = F_0/n_0$. As before, if $V_I \geq u_R = 2c_{II}$ then the I-front is of type R, if $u_R \geq V_I \geq u_D = c_0^2/2c_{II}$, a shock front is created and $\rm n_0$ is increased so that the I-front becomes of D-type: $V_I \leq u_D$ (see Tab. 2.1 for the different conditions and types of I-front). If the density of the cloud is high enough, the I-front will start in the D phase. We will suppose first that we start in the R phase since at the end of the R phase, we will also study the D phase. In the R phase, the photons will ionize a layer of gas on the face of the cloud facing the star. We take as origin the centre of the cloud and we call $\rm R_s$ the position of the I-front at the end of the R-phase. The thickness of the layer ΔL is set by the number of recombination in the layer that will absorb all the incoming photons (very similar to Strömgren analysis)

$$\begin{aligned} \Delta L &= \frac{F_0}{\beta n_0^2} \\ &\approx 0.001 \text{ pc} \left(\frac{S_*}{10^{50}\text{ s}^{-1}}\right)\left(\frac{r_0}{20\text{ pc}}\right)^{-2}\left(\frac{n_0}{1500\text{ cm}^{-3}}\right)^{-2} \end{aligned} \tag{2.21}$$

A first condition arises, the cloud is completely ionized if $\Delta L \geq 2\rm R_0$. This could happen for example for a cloud of density 100 $\rm cm^{-3}$ and radius 0.5 pc at 10 pc of an O4 star. In this case, the cloud is completely heated up to 8,000 K and destroyed by this huge increase of thermal pressure.

When ΔL is small compared to the size of the cloud, the ionization progresses rapidly inside the cloud before reaching this limit. When the limit is reached, the I-front is at the end of the R-type phase and a shock will be created to get to the D-critical condition at I-front. If the I-front remains in this condition, the velocity of the ionized gas relative to the I-front will be $\rm c_{\it II}$ (i.e. $V_I - v_{II} = c_{II}$. The velocity of the I-front can be estimated by the Rankine-Hugoniot relations from Eq. 2.9

$$\begin{aligned} n_{II}c_{II} &\approx F_\gamma \\ n_0 V_I^2 &\approx 2n_{II}c_{II}^2 \end{aligned} \tag{2.22}$$

with $\rm F_\gamma$ the photon flux at the I-front. Substituting in the second equation $\rm n_{\it II}c_{\it II}$ by $\rm F_\gamma$, we get $\rm V_{\it I}$ for the D-critical I-front

$$V_I = \left(\frac{2F_\gamma c_{II}}{n_0}\right)^{1/2} \tag{2.23}$$

In the weak D-type phase, the relation holds but the photon flux at the I-front will vary. The ionized gas will expand from the face of the cloud in direction of the star. Since its density decreases, the number of recombinations inside the gas will decrease and the photon flux will increase. However, the propagation of the I-front will increase the quantity of the ionized gas and therefore lower the photon flux at the front. The balance between the two is difficult to determine but it can be estimated if we suppose that the velocity of the ionized gas relative to the I-front stays at its D-critical value (i.e. c_{II}). The mass conservation imposes a r^{-2} profile for the density in the ionized gas

$$n(r) = n_{II}\frac{R_I^2}{r^2} \tag{2.24}$$

in which n_{II} is the density at the I-front in the ionized gas and R_I the distance of the I-front from the centre of the cloud. Note that this expression suppose that we are not D-critical anymore (even if the velocity is kept at its D-critical value), because the gas had time to expand in front of the cloud. Then the number of photons reaching the I-front F_γ is just the initial flux F_0 minus the recombination in the ionized gas

$$F_0 - F_\gamma = \int_{R_I}^{\infty} \beta n(r)^2 dr = \beta n_{II}^2 R_I/3 \tag{2.25}$$

This relation is valid close to the axis joining the star and the centre of the cloud. Away from it, the profile of recombination that absorbs the photons is more complicated (see *Bertoldi*, 1989). We can substitute n_{II} by F_γ/c_{II} in Eq. 2.25 to obtain F_γ

$$F_\gamma = F_I\left(\sqrt{1+2\frac{F_0}{F_I}}-1\right) \approx \sqrt{2F_0F_I} \tag{2.26}$$

with $F_I = 3c_{II}^2/2\beta R_I$. The approximation is valid when $F_I \ll F_0$ which is the case in the D phase ($F_0 \approx 2{\times}10^9$ s^{-1}cm^{-2} and $F_I \approx 10^6$ s^{-1}cm^{-2} at the end of the R phase). With Eq. 2.23 and Eq. 2.26

$$V_I = c_{II}\left(12\frac{\Delta L}{R_I}\right)^{1/4} \tag{2.27}$$

from which we can get by integration

$$R_I = R_s\left(1-\frac{5}{4}\left(12\frac{\Delta L}{R_s}\right)^{1/4}\frac{c_{II}t}{R_s}\right)^{4/5} \tag{2.28}$$

The implosion of the cloud will be almost complete when the I-front gets through the whole cloud, i.e. approximately twice the time it takes to reach the centre (when $R_I \approx 0$).

$$\begin{aligned} t_{\mathrm{imp}} &= \frac{8}{5}\frac{R_s}{c_{II}}\left(\frac{R_s}{12\Delta L}\right)^{1/4} \\ &\approx 200\ \mathrm{ky}\left(\frac{R_0}{0.5\ \mathrm{pc}}\right)^{5/4}\left(\frac{n_0}{1500\ \mathrm{cm}^{-3}}\right)^{1/2}\left(\frac{r_0}{20\ \mathrm{pc}}\right)^{1/2}\left(\frac{S_*}{10^{50}\ \mathrm{s}^{-1}}\right)^{-1/4} \end{aligned} \tag{2.29}$$

The estimation of the time of the collapse is very close to what is observed in the simulations of *Lefloch and Lazareff* (1994) and *Bisbas et al.* (2009). From Eq. 2.28, the progression of the I-front is almost linear with time, therefore we can get the average velocity of the globule with

$$\begin{aligned} V_g &\approx 2R_0/t_{\mathrm{imp}} \\ &\approx 5\ \mathrm{km/s}\left(\frac{R_0}{0.5\ \mathrm{pc}}\right)^{-1/4}\left(\frac{n_0}{1500\ \mathrm{cm}^{-3}}\right)^{-1/2}\left(\frac{r_0}{20\ \mathrm{pc}}\right)^{-1/2}\left(\frac{S_*}{10^{50}\ \mathrm{s}^{-1}}\right)^{1/4} \end{aligned} \tag{2.30}$$

The change of M per unit time is equal to the rate at which gas is ionized at the I-front

$$\frac{dM}{dt} = -\pi R_I^2 F_\gamma \mu m_H \tag{2.31}$$

with μ the mean molecular weight. We assumed that the whole cloud is a collapsing sphere of radius R_I. Using Eq. 2.26

$$\begin{aligned}\left|\frac{\dot{M}}{\mu}\right| &\approx m_H \pi R_I^2 \sqrt{2F_0F_I} \\ &\approx 25 M_\odot My^{-1} \left(\frac{S_*}{10^{50}\ \mathrm{s}^{-1}}\right)^{1/4} \left(\frac{r_0}{20\ \mathrm{pc}}\right)^{-1/2} \left(\frac{R_I}{0.5\ \mathrm{pc}}\right)^{3/2} \end{aligned} \quad (2.32)$$

If we assume a constant mass loss during the collapse phase, the total evaporated mass is of the order of 5 $\mathrm{M}_\odot$ during $\mathrm{t}_{\mathrm{imp}}$ that is also what is evaporated in the simulation of *Lefloch and Lazareff* (1994).

At the end of the collapse phase, the resulting dense globule is in a quasi-steady state called the cometary phase. We can estimate its velocity gained by the effect of the Rocket motion (see *Oort and Spitzer*, 1955). If M is the mass of the cloud and v the velocity of the cloud

$$M\frac{dv}{dt} = -V\frac{dM}{dt} \quad (2.33)$$

with V the velocity (relative to the cloud) of the gas streaming out of the cloud. The solution is then

$$M = M_0 e^{-v/V} \quad (2.34)$$

with M_0, the initial mass of the cloud that is supposed to be at rest at the beginning. We supposed that the gas was streaming out at the sound speed, therefore the velocity kick received by the globule at the end of the collapse phase is $\ln(M_0/M)c_{II}$ and is of the order of 3 km/s in our case. The quasi-steady state imposes that the pressure of the globule is in equilibrium with the acceleration received from the ionized gas (see *Lefloch and Lazareff*, 1994), therefore

$$\begin{aligned} P_g &= \rho_g c_0^2 = \rho_g R_g dv/dt \\ dv/dt &= dM/dt \times c_{II}/M_g = \mu m_H \pi R_g^2 \sqrt{2F_0F_I} c_{II}/M_g \end{aligned} \quad (2.35)$$

We can extract the radius of the globule R_g

$$\begin{aligned} R_g &\approx \left(\frac{M_g c_0^2}{\pi \mu m_H \sqrt{3F_0/\beta} c_{II}^2}\right)^{2/5} \\ &\approx 0.15 - 0.20\ \mathrm{pc} \left(\frac{S_*}{10^{50}\ \mathrm{s}^{-1}}\right)^{-1/5} \left(\frac{r_0}{20\ \mathrm{pc}}\right)^{2/5} \left(\frac{M_g}{15\ \mathrm{M}_\odot}\right)^{2/5} \left(\frac{c_0}{0.8\ \mathrm{km/s}}\right)^{4/5} \end{aligned} \quad (2.36)$$

The estimation is made with the values for the parameters at the beginning of the cometary phase. This estimation is in good agreement with the simulations (see *Lefloch and Lazareff*, 1994; *Bisbas et al.*, 2009, and Fig. 2.3). The mass-loss rate corresponding to a width of 0.2 pc is of the order of 6 $\mathrm{M}_\odot$ My^{-1}, that gives a life time for the cometary globule of 2.4 My. That is also in very good agreement with the simulated life time in *Lefloch and Lazareff* (1994); *Bisbas et al.* (2009). The density in the globule can be estimated by $\mathrm{M}_g/(4/3\pi \mathrm{R}_g^3)$ and is of the order of 2×10^4 cm^{-3}. The Jeans length associated is 0.6 parsec, therefore the globule is not subject to gravitational instabilities in the cometary phase.

The radiation driven implosion of a cloud has been studied numerically by *Sandford et al.* (1982); *Lefloch and Lazareff* (1994); *Kessel-Deynet and Burkert* (2003); *Bisbas et al.* (2011) among many other studies. They confirmed the above estimations and the detailed analytical work of *Bertoldi* (1989). *Kessel-Deynet and Burkert* (2003) did the first 3D RDI simulation with self-gravity included and found that the RDI process could also be efficient to inject turbulent motions into molecular clouds. *Bisbas et al.* (2011) followed the collapse

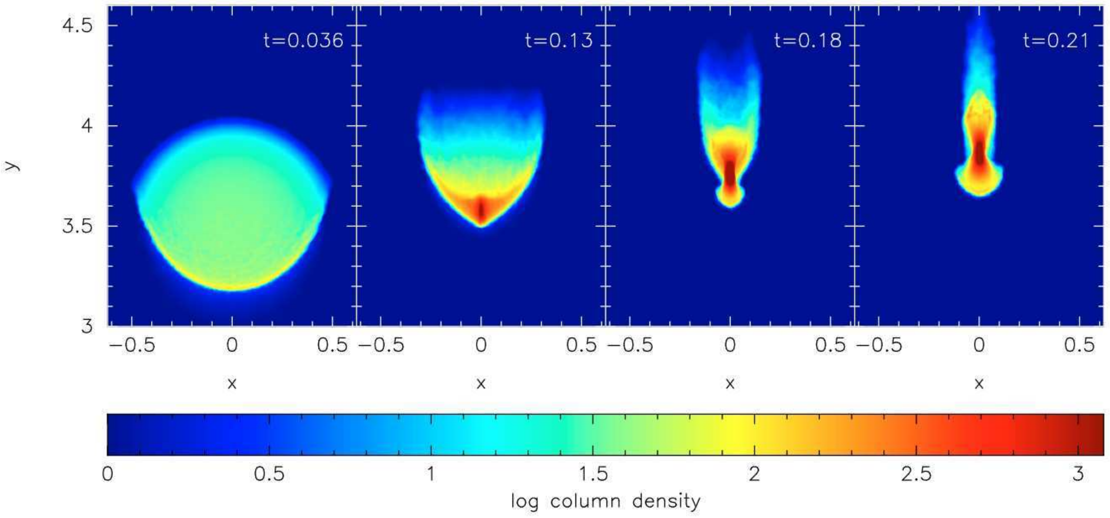

Figure 2.3: Radiation driven implosion from *Bisbas et al.* (2009) with the same parameters as *Lefloch and Lazareff* (1994) for the cloud.

with SPH (Smooth Particle Hydrodynamic, *Monaghan*, 1992) and the star formation with sink particles. They found that the time at which star formation occurs is proportional to the flux at the power -1/3 and that the pattern of star formation is similar to the one observed in bright-rimmed clouds.

2.1.4 Turbulent model

The CCS and RDI models are simple ideas of what is observed in H II regions. A more realistic set up is to consider the impact of the ionization on a turbulent molecular cloud and see whether these models are also representative of what is happening in a turbulent medium. Two ways have been investigated so far, the large-scale study of a molecular cloud (see *Dale and Bonnell*, 2011,0; *Dale et al.*, 2012) and small-scale study of a turbulent medium (see *Elmegreen et al.*, 1995; *Mellema et al.*, 2006; *Gritschneder et al.*, 2010; *Arthur et al.*, 2011).

On large scale, *Dale and Bonnell* (2011) studied with SPH simulations, the evolution of a dense molecular cloud ($M_c \approx 10^6$ $M_\odot$, $R_c \approx 50$ pc) subject to self-gravity, turbulence and the ionization from the massive stars that are formed. They found that the dense gas formed by the gravitational collapse resists ionization and prevent the radiation from eroding the filaments in which star formation occurs. They concluded that ionized gas fill pre-existing voids and impacts the cloud marginally in this simulation. This result is linked to the fact that the escape velocity of this very massive cloud $\sqrt{GM_c/R_c}$ is of the order of the sound speed of the ionized gas. Therefore, the ionization is not strong enough to disperse the cloud and the radiation pressure should be the dominant process for the regulation of star formation for such clouds (see Chap. 1). In *Dale et al.* (2012), they also studied less massive clouds (10^{4-5} $M_\odot$) and found that they are strongly impacted by the ionization up to their destruction. They found in these kind of simulations that the resulting IMF is biased to solar-mass stars because of the ionization feedback. These less-massive molecular clouds are more representative of the ones in the Milky Way (as already seen in Chap. 1 for the feedback processes in galaxy simulations).

On smaller scales, the early study by *Elmegreen et al.* (1995) showed that the clumps formed by the initial turbulence are squeezed by the ionization compression and merge in the post-shock gas to form dense cores. *Mellema et al.* (2006) presented simulations of the

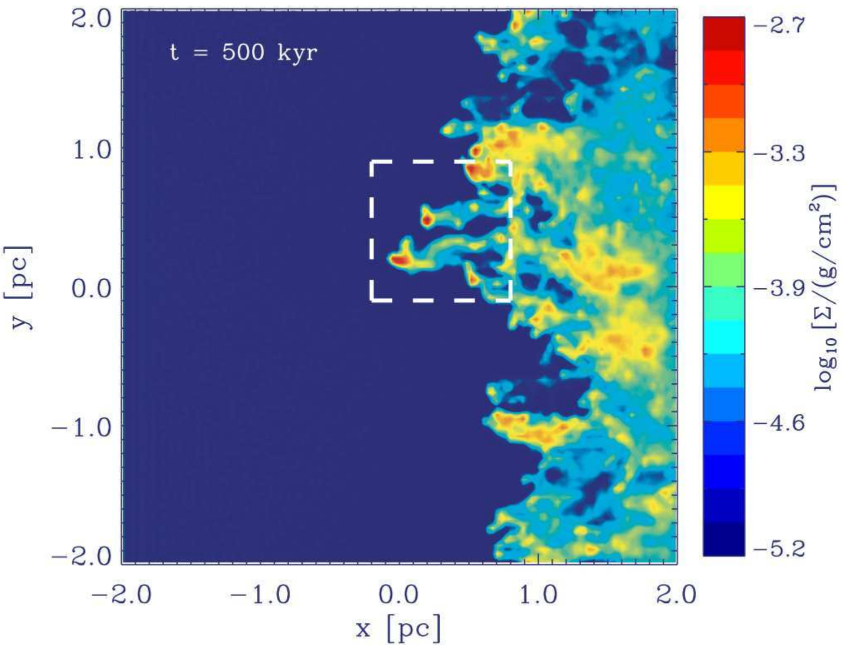

Figure 2.4: Formation of pillars in turbulent simulations of *Gritschneder et al.* (2009).

expansion of spherical H II regions in a turbulent medium. They showed that the expansion of the sphere can be highly asymmetric and the morphology of the structures are in a good agreement with observations. *Arthur et al.* (2011) did the same kind of simulations but adding magnetic fields. They found that the global morphology was similar but on small scales, the magnetic fields prevent the fragmentation of the shell. *Gritschneder et al.* (2010) used SPH simulation coupled to ionization that is solved at equilibrium and with a very simple prescription for the thermal processes (isothermal gas at a temperature function of the ionization fraction). They found that pillars form preferentially at high turbulence level (Mach 5 in their simulation, see Fig. 2.4).

2.1.5 The formation of pillars

Early studies of the formation of "elephant trunk" at the edge of H II regions proposed that the Rayleigh-Taylor instability could be at work (see *Frieman*, 1954). The linear growth rate of the instability is given by

$$\sigma_{RT} = \sqrt{g\frac{2\pi}{\lambda}\frac{\rho_c - \rho_{II}}{\rho_c + \rho_{II}}} \tag{2.37}$$

with g the acceleration of the gas in the compressed shell of density ρ_c, ρ_{II} the density in the H II region, and λ the wavelength of the disturbance at the origin of the pillar. The time-scale of the linear growth is $1/\sigma_{RT}$. Because the pillar in this model is in free fall, the velocity along the pillar should be

$$v(x) - v_0 = \sqrt{g(x - x_0)} \tag{2.38}$$

Pound (1998) showed that the velocity gradients along the Pillars of Creation in M16 were not compatible with this relation and therefore excluded the Rayleigh-Taylor instability as a formation mechanism for the pillars.

Williams (1999) showed that the shell is subject to an instability when a part of the I-front receives less flux because of a shadowing object in the ionized gas. This instability could form pillars and in *Williams et al.* (2001) they also proposed a series of different set-ups that are able to reproduce elongated structures similar to the Pillars of the Creation. They concluded that there is no unambiguous way to determine how these structures form.

Miao et al. (2006) used RDI simulations of a cloud and argued that the initial structure was only subject to UV radiation for 400 ky. They also concluded that the shock has not pass the head of the pillar and also that the compression layer is still present at the top of the structure. Therefore it seems they did not reach the cometary phase of the RDI scenario. However the velocity profiles do indicate that the whole cloud is in motion suggesting that they have passed the compression phase. The fact that the shock has probably travel through the head of the pillar was also addressed in *Williams et al.* (2001).

Mackey and Lim (2010) proposed that only the shadowing of clumps in a low-dense medium is sufficient to form elongated structures that look like pillars without self-gravity, cooling instabilities or I-fronts. They studied in *Mackey and Lim* (2011) the effect of magnetic fields and found that the field has to be strong in order to change the dynamic, otherwise the input of energy from the ionization remains the main driver.

Recently *Gritschneder et al.* (2009,0) compared the formation of elongated structures from RDI and turbulent models. They found that the velocity pattern of pillars from turbulent models is peaked around a central value whereas in RDI models the velocity pattern is large. They concluded that the turbulent model is closer to the observations than the RDI one. Note that in their RDI model it is not clear that they have reach the cometary phase, the large velocity pattern could be the result of the shocked gas still converging at the centre. A cometary globule does not present such large velocity structures.

2.2 Observations

2.2.1 H II regions

H II regions are observed for a very long time. The most luminous ones are visible to the naked eye, although the first observation of the Orion Nebula (see Fig. 2.5 for recent observations) was only reported by the French astronomer Nicolas-Claude Fabri de Peiresc in 1610, the same nebula that was described 150 years later by William Herschel as “an unformed fiery mist, the chaotic material of future suns”.

? compiled the data from several catalogs in order to build a database of 1442 H II regions in the Galaxy. The vast majority of the sources are located between -2 and +2 degrees in Galactic latitude and between -100 and +100 degrees in Galactic longitude. The catalog gathers the flux density, diameter and velocity at 2.7 GHz and should be complete down to flux density of 1 Jy.

After the suggestion of the collect and collapse process by *Elmegreen and Lada* (1977), many observational studies looked for the age sequences resulting from this scenario. *Sargent* (1979) observed a clear sequence of star formation in the molecular cloud associated with Cepheus OB3 while the signatures are less clear around Perseus OB2. *Blaauw* (1991) studied the sequential star formation around the H II region created by Orion OB1 and *Phelps and Lada* (1997) looked at age sequences in the Rosette Nebula. See *Elmegreen* (1998) for other works.

More recently, these H II regions are seen in many massive molecular clouds and are the object of a great number of observational studies: in the Rosette nebula (*Schneider et al.*, 2010), M16 (*Andersen et al.*, 2004), 30 Doradus (*Walborn et al.*, 2002), Carina nebula (*Smith et al.*, 2000), the Elephant Trunk nebula (*Reach et al.*, 2004), the Trifid nebula (*Lefloch et al.*, 2002), M17 (*Jiang et al.*, 2002), or the Horsehead nebula (*Bowler et al.*, 2009).

Figure 2.5: Orion Nebula (M42) observed with the Wide Field Imager camera on the MPG/ESO 2.2-metre telescope at the La Silla Observatory, Chile. This image is a composite of several exposures taken through a total of five different filters. Light that passed through a red filter, as well as light from a filter that shows the glowing hydrogen gas, is coloured red. Light in the yellow–green part of the spectrum is coloured green, blue light is coloured blue and light that passed through an ultraviolet filter has been coloured purple. Credit: ESO/Igor Chekalin.

Spitzer observations also provide a wide range of H II regions, which were cataloged and studied in detail by *Churchwell et al.* (2006,0). They observed 322 partial and closed rings, 1.5 bubbles per square degree. One quarter of the bubbles is associated with observed H II regions in radio, and 13 % contain known star clusters. *Churchwell et al.* (2006) estimated that three-quarters of the bubbles may be produced by B4-B9 stars, that are too cool to produce detectable radio H II regions. In *Churchwell et al.* (2007), they showed that the typical eccentricity of the bubbles is between 0.6 and 0.8 and more than 50 % showed evidence for blow-outs. *Deharveng et al.* (2010) pushed further this analysis and found that 86 % of the bubbles contain ionized gas that is seen in the radio-continuum. This corrected the first results of *Churchwell et al.* (2006) and showed that most of the bubbles are formed by O-B2 clusters. They also showed that 40 % are surrounded by cold gas and 28 % contain interacting condensations. If the formation of these condensations are triggered, more than one quarter of the bubbles may have triggered the formation of massive objects that could form stars. *Thompson et al.* (2011) used the Churchwell catalog and looked for the correlation between the edge of the bubbles and the position of Young Stellar Objects (YSOs) from the RMS survey. They showed that there is a clear statistically significant over-density of YSOs at the edge of the bubbles. They suggested that it is likely that the YSOs were triggered by the expansion of the bubbles and estimate that the fraction of massive stars in the Milky Way formed by this process could be between 14 and 30 %.

In addition to eccentricity, H II regions can differ from the classical spherical shape by having a complex geometry. Many star-forming regions exhibit similar morphological properties: a H II region, a star cluster inside, and a dust lane that crosses the cavity and sometimes partly hides the ionizing stars. S 106 (*Bally et al.*, 1998), IRS16/Vela D (*Strafella et al.*, 2010), NGC 3576 (*Purcell et al.*, 2009), NGC 2024 (*Mezger et al.*, 1992),

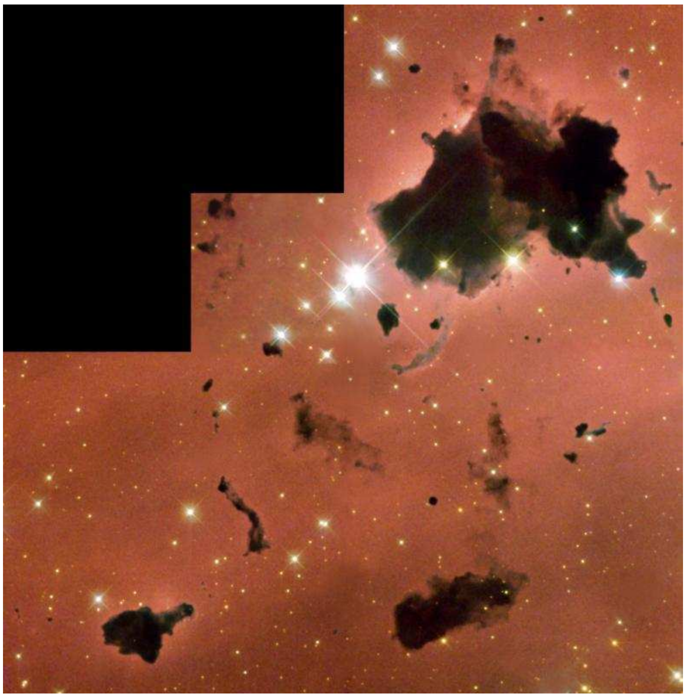

Figure 2.6: Thackeray's Globules in IC2944 observed with the *Hubble* space telescope. The hydrogen-emission image that clearly shows the outline of the dark globules was taken in February 1999 with Hubble's Wide Field Planetary Camera 2 (WFPC2). Credit: NASA, The Hubble Heritage Team (STScI/AURA) and Bo Reipurth.

S88 (*White and Fridlund*, 1992) and S 201 (*Mampaso et al.*, 1987), for instance, are among this type of H II regions, and these could be referred as being hourglass-shaped nebulae, bipolar nebulae, or bi-lobed appearance nebulae (e.g. *Staude and Elsasser*, 1993). Note also that H II regions are also often observed at the edge of molecular clouds (see *Israel*, 1978). Therefore the ionized gas can expand almost freely in the vacuum, that is at the edge of the cloud. These type of H II regions are highly asymmetric and they are called "blister-type" (see *Israel*, 1978; *Icke et al.*, 1980). Whatever the morphology, these cavities of ionized gas are also surrounded by complex molecular gas structures such as globules, proplyds and pillars and will be discussed in the two following sections.

2.2.2 Globules and proplyds

Many globules are found in H II regions (e.g. Fig. 2.6) and were first observed by *Bok and Reilly* (1947) in the Lagoon Nebula (M8). They have a typical mass between 1 and 100 $M_{\odot}$. In their original paper, *Bok and Reilly* (1947) suggested that these globules were undergoing gravitational collapse to form new stars. *Dyson* (1968) proposed their existence in the Orion Nebula to explain the observation of turbulence in the ionized gas. It took ten years before the globules were actually observed by *Laques and Vidal* (1978). Many globules were also observed in other H II regions, e.g. *Herbig* (1974) in the Rosette Nebula *Hawarden and Brand* (1976) in the Gum Nebula. A review of the observations of globules can be found in *Elmegreen* (1998). When the compression is one-sided, the globules can get a characteristic cometary shape. Catalogs of such objects can be found in *Hawarden and Brand* (1976) and *Reipurth* (1983). Note that such cometary shapes can also emerge from the interaction with stellar winds or supernovae. Another common structure is the observation of bright rims in which neutral globules are found to be embedded. A catalog of such bright-rimmed clouds can be found in *Sugitani et al.* (1991).

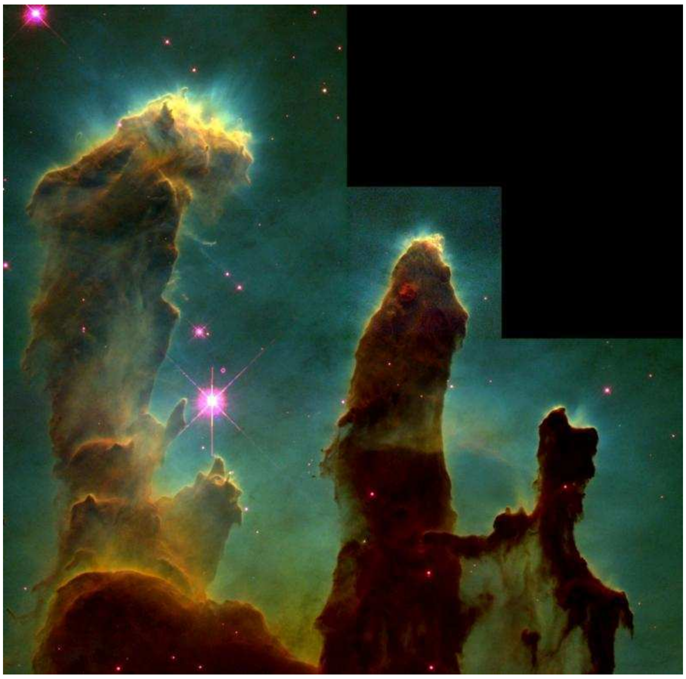

Figure 2.7: The Pillars of Creation in the Eagle Nebula (M16). Credit: NASA, ESA, STScI, J. Hester and P. Scowen (Arizona State University)

Solar-system size globules were first observed by *Hubble* in Orion (*Hester et al.*, 1991; *O'dell et al.*, 1993), in M16 (*Hester et al.*, 1996), in M8 (*Caulet*, 1997). Some of these small-size globules can be protostellar disks, in which case they are called proplyds (see *Wright et al.*, 2012, for recent examples in Cygnus).

Young embedded stellar objects or nearby stars are often seen in association with these globules. However in most cases, it is rather uncertain that the star formation was triggered by the compression. It is probable that these stars would have formed anyway and that the ionization only revealed the embedded on-going star formation. However *Sugitani et al.* (1995) and *Chandler and Carlstrom* (1996) observed the age sequence of stars in bright-rimmed clouds that suggests the triggered origin.

2.2.3 Pillars

Elephant trunk globules are a sort of cometary globules with a tail that connect them to the molecular cloud (see *Elmegreen*, 1998). Early examples of such structures can be found in *Minkowski* (1949) and *Pottasch* (1956). After the iconic image of the "Pillars of Creation" in the Eagle Nebula by *Hubble* (see *Hester et al.*, 1996, and Fig. 2.7), these structures are now often called pillars. Recent observations can be found in *Gahm et al.* (2006); *Schuller et al.* (2006); *Guzmán et al.* (2012). Pillars have typically a size between 1 and 4 pc, a width between 0.1 and 0.7 pc (see *Gahm et al.*, 2006). They have an internal structure with a dense cold head often surrounded by a bright rim and a tail that is connected to the molecular cloud. They also have a complex velocity structure (rotational and helical) that has been studied in details by *Carlqvist et al.* (1998, 2003); *Gahm et al.* (2006). They showed that pillars can have rotation periods between 1 and 7 My. Combined with a velocity along the pillar, the rotational motion turns into a helical motion with characteristic filaments that run in the diagonal of the pillars (corkscrew rotation). Star formation has been observed for many years in the dense head of the pillars (see *Sugitani et al.*, 1989) and can lead to spectacular jets from proto-stars escaping of the head (e.g. HH901/902 in the Carina nebula). Despite these signatures, it is often unclear whether the star formation is triggered or not in these structures. For instance, *Sugitani et al.* (2002) found Type I proto-stars near the heads of the pillars of Creation, suggesting an age sequence within the pillar. However, *Indebetouw et al.* (2007) found that young stellar objects in M16 were randomly distributed without a clear pattern in ages. Therefore the possible triggering effect in M16 remains an open question.

Bibliography

Andersen, M., J. Knude, B. Reipurth, A. Castets, L. A. Nyman, M. J. McCaughrean, and S. Heathcote (2004), Molecular cloud structure and star formation near HH 216 in M 16, *A&A*, *414*, 969–978. 32

Anderson, L. D., et al. (2010), The physical properties of the dust in the RCW 120 H II region as seen by Herschel, *A&A*, *518*, L99.

André, P., et al. (2010), From filamentary clouds to prestellar cores to the stellar IMF: Initial highlights from the Herschel Gould Belt Survey, *A&A*, *518*, L102.

Arthur, S. J., W. J. Henney, G. Mellema, F. De Colle, and E. Vázquez-Semadeni (2011), Radiation-magnetohydrodynamic simulations of H II regions and their associated PDRs in turbulent molecular clouds, *MNRAS*, *414*(2), 1747–1768. 26, 30, 31

Arzoumanian, D., et al. (2011), Characterizing interstellar filaments with Herschel in IC 5146, *A&A*, *529*, L6.

Bally, J., K. C. Yu, J. Rayner, and H. Zinnecker (1998), Hubble Space Telescope Wide Field Planetary Camera 2 Observations of the Young Bipolar H II Region S106, *The Astronomical Journal*, *116*(4), 1868–1881. 33

Bertoldi, F. (1989), The photoevaporation of interstellar clouds. I - Radiation-driven implosion, *ApJ*, *346*, 735–755. 26, 28, 29

Bertoldi, F., and C. F. McKee (1990), The photoevaporation of interstellar clouds. II - Equilibrium cometary clouds, *ApJ*, *354*, 529–548. 26

Bisbas, T. G., R. Wünsch, A. P. Whitworth, and D. A. Hubber (2009), Smoothed particle hydrodynamics simulations of expanding H II regions. I. Numerical method and applications, *A&A*, *497*(2), 649–659. 28, 29, 30

Bisbas, T. G., R. Wünsch, A. P. Whitworth, D. A. Hubber, and S. Walch (2011), Radiation-driven Implosion and Triggered Star Formation, *ApJ*, *736*(2), 142. 29

Blaauw, A. (1964), The O Associations in the Solar Neighborhood, *Annual Review of Astronomy and Astrophysics*, *2*, 213. 23

Blaauw, A. (1991), OB Associations and the Fossil Record of Star Formation, *The Physics of Star Formation and Early Stellar Evolution*, p. 125. 32

Black, J. H. (1981), The physical state of primordial intergalactic clouds, *MNRAS*, *197*, 553–563. 21

Bok, B. J., and E. F. Reilly (1947), Small Dark Nebulae., *ApJ*, *105*, 255. 34

Bontemps, S., et al. (2010), The Herschel first look at protostars in the Aquila rift, *A&A*, *518*, L85.

Bowler, B. P., W. H. Waller, S. T. Megeath, B. M. Patten, and M. Tamura (2009), An Infrared Census of Star Formation in the Horsehead Nebula, *The Astronomical Journal*, *137*(3), 3685–3699. 32

Carlqvist, P., H. Kristen, and G. F. Gahm (1998), Helical structures in a Rosette elephant trunk, *A&A*, *332*, L5–L8. 35

Carlqvist, P., G. F. Gahm, and H. Kristen (2003), Theory of twisted trunks, *A&A*, *403*, 399–412. 35

Caulet, A. (1997), The Lagoon Saga goes on: Proplyds and other remarkable Objects seen in WFPC2 Images of the Lagoon Nebula, *American Astronomical Society*, *190*, 834. 35

Chandler, C. J., and J. E. Carlstrom (1996), Star Formation in the NGC 2024 Molecular Ridge, *Astrophysical Journal v.466*, *466*, 338. 35

Churchwell, E., D. F. Watson, M. S. Povich, M. G. Taylor, B. L. Babler, M. R. Meade, R. A. Benjamin, R. Indebetouw, and B. A. Whitney (2007), The Bubbling Galactic Disk. II. The Inner 20 °, *ApJ*, *670*(1), 428–441. 33

Churchwell, E., et al. (2006), The Bubbling Galactic Disk, *ApJ*, *649*(2), 759–778. 33

Dale, J. E., and I. Bonnell (2011), Ionizing feedback from massive stars in massive clusters: fake bubbles and untriggered star formation, *MNRAS*, *414*(1), 321–328. 30

Dale, J. E., and I. A. Bonnell (2012), Ionization-induced star formation - III. Effects of external triggering on the initial mass function in clusters, *MNRAS*, *422*(2), 1352–1362. 30

Dale, J. E., I. A. Bonnell, and A. P. Whitworth (2007a), Ionization-induced star formation - I. The collect-and-collapse model, *MNRAS*, *375*(4), 1291–1298. 26

Dale, J. E., P. C. Clark, and I. A. Bonnell (2007b), Ionization-induced star formation - II. External irradiation of a turbulent molecular cloud, *MNRAS*, *377*(2), 535–544. 26

Dale, J. E., R. Wünsch, A. Whitworth, and J. Palouš (2009), The fragmentation of expanding shells - I. Limitations of the thin-shell approximation, *MNRAS*, *398*(3), 1537–1548. 26

Dale, J. E., B. Ercolano, and I. A. Bonnell (2012), Massive stars in massive clusters II: Disruption of bound clusters by photoionization, *arXiv*, *astro-ph.GA*, 360. 30

de Graauw, T., et al. (2010), The Herschel-Heterodyne Instrument for the Far-Infrared (HIFI), *A&A*, *518*, L6.

Deharveng, L., et al. (2010), A gallery of bubbles. The nature of the bubbles observed by Spitzer and what ATLASGAL tells us about the surrounding neutral material, *A&A*, *523*, 6. 33

Di Francesco, J., et al. (2010), Small-scale structure in the Rosette molecular cloud revealed by Herschel, *A&A*, *518*, L91.

Dyson, J. E. (1968), Dynamics of the Orion Nebula. II: Shock Waves in an H II Region, *Astrophysics and Space Science*, *2*(4), 461–473. 34

Elmegreen, B. G. (1994), A Q condition for long-range propagating star formation, *ApJ*, *427*, 384–387. 25, 26

Elmegreen, B. G. (1998), Observations and Theory of Dynamical Triggers for Star Formation, *Origins*, *148*, 150. 26, 32, 34, 35

Elmegreen, B. G., and D. M. Elmegreen (1978), Star formation in shock-compressed layers, *ApJ*, *220*, 1051–1062. 26

Elmegreen, B. G., and C. J. Lada (1977), Sequential formation of subgroups in OB associations, *ApJ*, *214*, 725–741. 23, 32

Elmegreen, B. G., T. Kimura, and M. Tosa (1995), Sequential Star Formation in OB Associations: The Role of Molecular Cloud Turbulence, *ApJ*, *451*, 675. 30

Frieman, E. A. (1954), On Elephant-Trunk Structures in the Region of O Associations., *ApJ*, *120*, 18. 31

Gahm, G. F., P. Carlqvist, L. E. B. Johansson, and S. Nikolić (2006), Rotating elephant trunks, *A&A*, *454*(1), 201–212. 35

Giannini, T., et al. (2012), The Herschel view of the on-going star formation in the Vela-C molecular cloud, *A&A*, *539*, 156.

Griffin, M. J., et al. (2010), The Herschel-SPIRE instrument and its in-flight performance, *A&A*, *518*, L3.

Gritschneder, M., T. Naab, S. Walch, A. Burkert, and F. Heitsch (2009), Driving Turbulence and Triggering Star Formation by Ionizing Radiation, *ApJ*, *694*(1), L26–L30. 31, 32

Gritschneder, M., A. Burkert, T. Naab, and S. Walch (2010), Detailed Numerical Simulations on the Formation of Pillars Around H II Regions, *ApJ*, *723*(2), 971–984. 30, 31, 32

Guzmán, V., J. Pety, P. Gratier, J. R. Goicoechea, M. Gerin, E. Roueff, and D. Teyssier (2012), The IRAM-30m line survey of the Horsehead PDR. I. CF+ as a tracer of C+ and as a measure of the fluorine abundance, *A&A*, *543*, L1. 35

Hawarden, T. G., and P. W. J. L. Brand (1976), "Cometary" globules and the structure of the Gum nebula., *MNRAS*, *175*, 19P–22P. 27, 34

Hennemann, M., et al. (2010), Herschel observations of embedded protostellar clusters in the Rosette molecular cloud, *A&A*, *518*, L84.

Hennemann, M., et al. (2012), The spine of the swan: a Herschel study of the DR21 ridge and filaments in Cygnus X, *A&A*, *543*, L3.

Herbig, G. H. (1974), On the nature of the small dark globules in the Rosette Nebula, *Astronomical Society of the Pacific*, *86*, 604–608. 27, 34

Hester, J. J., et al. (1991), Ionization fronts and shocked flows - The structure of the Orion Nebula at 0.1 arcsec, *ApJ*, *369*, L75–L78. 35

Hester, J. J., et al. (1996), Hubble Space Telescope WFPC2 Imaging of M16: Photoevaporation and Emerging Young Stellar Objects, *Astronomical Journal v.111*, *111*, 2349. 26, 35

Hill, T., et al. (2011), Filaments and ridges in Vela C revealed by Herschel: from low-mass to high-mass star-forming sites, *A&A*, *533*, 94.

Hill, T., et al. (2012), The M 16 molecular complex under the influence of NGC 6611. Herschel's perspective of the heating effect on the Eagle Nebula, *A&A*, *542*, 114.

Icke, V., I. Gatley, and F. P. Israel (1980), The appearance of dusty H II blisters at radio and infrared wavelengths, *ApJ*, *236*, 808–822. 34

Indebetouw, R., T. P. Robitaille, B. A. Whitney, E. Churchwell, B. Babler, M. Meade, C. Watson, and M. Wolfire (2007), Embedded Star Formation in the Eagle Nebula with Spitzer GLIMPSE, *The Astrophysical Journal*, *666*(1), 321–338. 36

Israel, F. P. (1978), H II regions and CO clouds - The blister model, *A&A*, *70*, 769–775. 34

Jiang, Z., et al. (2002), Deep Near-Infrared Survey toward the M17 Region, *ApJ*, *577*(1), 245–259. 32

Kahn, F. D. (1954), The acceleration of interstellar clouds, *Bulletin of the Astronomical Institutes of the Netherlands*, *12*, 187. 22

Kessel-Deynet, O., and A. Burkert (2003), Radiation-driven implosion of molecular cloud cores, *Monthly Notice of the Royal Astronomical Society*, *338*(3), 545–554. 29

Könyves, V., et al. (2010), The Aquila prestellar core population revealed by Herschel, *A&A*, *518*, L106.

Krumholz, M. R., J. M. Stone, and T. A. Gardiner (2007), Magnetohydrodynamic Evolution of H II Regions in Molecular Clouds: Simulation Methodology, Tests, and Uniform Media, *ApJ*, *671*(1), 518–535. 26

Laques, P., and J.-L. Vidal (1978), A new kind of condensations in the core of the Orion nebula., *Stars and star systems*. 34

Lefloch, B., and B. Lazareff (1994), Cometary globules. 1: Formation, evolution and morphology, *A&A*, *289*, 559–578. 28, 29, 30

Lefloch, B., J. Cernicharo, L. F. Rodríguez, M.-A. Miville-Deschênes, D. Cesarsky, and A. Heras (2002), The Photoionization of a Star-forming Core in the Trifid Nebula, *ApJ*, *581*(1), 335–356. 32

Lora, V., A. C. Raga, and A. Esquivel (2009), The angular momentum of condensations within elephant trunks, *A&A*, *503*(2), 477–482. 26

Mackey, J., and A. J. Lim (2010), Dynamical models for the formation of elephant trunks in HII regions, *MNRAS*, *403*(2), 714–730. 32

Mackey, J., and A. J. Lim (2011), Effects of magnetic fields on photoionized pillars and globules, *MNRAS*, *412*(3), 2079–2094. 32

Mampaso, A., J. M. Vilchez, P. Pismis, and J. P. Phillips (1987), The bipolar H II region S 201, *(IAU*, *14*, 474–478. 34

Mellema, G., S. J. Arthur, W. J. Henney, I. T. Iliev, and P. R. Shapiro (2006), Dynamical H II Region Evolution in Turbulent Molecular Clouds, *ApJ*, *647*(1), 397–403. 30

Men'shchikov, A., et al. (2010), Filamentary structures and compact objects in the Aquila and Polaris clouds observed by Herschel, *A&A*, *518*, L103.

Mezger, P. G., A. W. Sievers, C. G. T. Haslam, E. Kreysa, R. Lemke, R. Mauersberger, and T. L. Wilson (1992), Dust emission from star forming regions. II - The NGC 2024 cloud core: Revisited, *A&A*, *256*, 631–639. 33

Miao, J., G. J. White, R. Nelson, M. Thompson, and L. Morgan (2006), Triggered star formation in bright-rimmed clouds: the Eagle nebula revisited, *MNRAS*, *369*(1), 143–155. 32

Minkowski, R. (1949), The Diffuse Nebula in Monoceros, *PASP*, *61*, 151. 35

Miville-Deschênes, M.-A., et al. (2010), Herschel-SPIRE observations of the Polaris flare: Structure of the diffuse interstellar medium at the sub-parsec scale, *A&A*, *518*, L104.

Monaghan, J. J. (1992), Smoothed particle hydrodynamics, *In: Annual review of astronomy and astrophysics. Vol. 30 (A93-25826 09-90)*, *30*, 543–574. 30

Motte, F., et al. (2010), Initial highlights of the HOBYS key program, the Herschel imaging survey of OB young stellar objects, *A&A*, *518*, L77.

Nguyen-Luong, Q., et al. (2011), The Herschel view of massive star formation in G035.39-00.33: dense and cold filament of W48 undergoing a mini-starburst, *A&A*, *535*, 76.

O'dell, C. R., Z. Wen, and X. Hu (1993), Discovery of new objects in the Orion nebula on HST images - Shocks, compact sources, and protoplanetary disks, *ApJ*, *410*, 696–700. 35

Oort, J. H., and L. J. Spitzer (1955), Acceleration of Interstellar Clouds by O-Type Stars., *ApJ*, *121*, 6. 26, 29

Peretto, N., et al. (2012), The Pipe Nebula as seen with Herschel: formation of filamentary structures by large-scale compression?, *A&A*, *541*, 63.

Phelps, R. L., and E. A. Lada (1997), Spatial Distribution of Embedded Clusters in the Rosette Molecular Cloud: Implications for Cluster Formation, *Astrophysical Journal v.477*, *477*, 176. 32

Pilbratt, G. L., et al. (2010), Herschel Space Observatory. An ESA facility for far-infrared and submillimetre astronomy, *A&A*, *518*, L1.

Poglitsch, A., et al. (2010), The Photodetector Array Camera and Spectrometer (PACS) on the Herschel Space Observatory, *A&A*, *518*, L2.

Pottasch, S. R. (1956), A study of bright rims in diffuse nebulae, *Bulletin of the Astronomical Institutes of the Netherlands*, *13*, 77. 35

Pound, M. W. (1998), Molecular Gas in the Eagle Nebula, *Astrophysical Journal Letters v.493*, *493*, L113. 31

Purcell, C. R., et al. (2009), Multi-generation massive star-formation in NGC 3576, *A&A*, *504*(1), 139–159. 33

Reach, W. T., et al. (2004), Protostars in the Elephant Trunk Nebula, *The Astrophysical Journal Supplement Series*, *154*(1), 385–390. 32

Reipurth, B. (1983), Star formation in BOK globules and low-mass clouds. I - The cometary globules in the GUM Nebula, *A&A*, *117*, 183–198. 34

Sadavoy, S. I., et al. (2012), Herschel observations of a potential core-forming clump: Perseus B1-E, *Astronomy & Astrophysics*, *540*, 10.

Sandford, M. T. I., R. W. Whitaker, and R. I. Klein (1982), Radiation-driven implosions in molecular clouds, *ApJ*, *260*, 183–201. 29

Sargent, A. I. (1979), Molecular clouds and star formation. II - Star formation in the Cepheus OB3 and Perseus OB2 molecular clouds, *ApJ*, *233*, 163–181. 32

Schneider, N., J. Stutzki, G. Winnewisser, A. Poglitsch, and S. Madden (1998), The Rosette molecular complex. II. [CII] 158 MU M observations, *A&A*, *338*, 262–272. 22

Schneider, N., et al. (2010), The Herschel view of star formation in the Rosette molecular cloud under the influence of NGC 2244, *A&A*, *518*, L83. 32

Schneider, N., et al. (2012), Cluster-formation in the Rosette molecular cloud at the junctions of filaments, *A&A*, *540*, L11.

Schuller, F., S. Leurini, C. Hieret, K. M. Menten, S. D. Philipp, R. Güsten, P. Schilke, and L. A. Nyman (2006), Molecular excitation in the Eagle nebula's fingers, *A&A*, *454*(2), L87–L90. 35

Smith, N., M. P. Egan, S. Carey, S. D. Price, J. A. Morse, and P. A. Price (2000), Large-Scale Structure of the Carina Nebula, *ApJ*, *532*(2), L145–L148. 32

Spitzer, L. (1978), *Physical processes in the interstellar medium*, New York Wiley-Interscience, Princeton University, New Observatory, Princeton, N.J. 22, 23, 24, 25, 26

Staude, H. J., and H. Elsasser (1993), Young bipolar nebulae, *Astronomy and Astrophysics Review (ISSN 0935-4956)*, *5*, 165–238. 34

Strafella, F., et al. (2010), The Spitzer-IRAC Point-source Catalog of the Vela-D Cloud, *ApJ*, *719*(1), 9–27. 33

Strömgren, B. (1939), The Physical State of Interstellar Hydrogen., *ApJ*, *89*, 526. 21, 22

Struve, O., and C. T. Elvey (1939), Observations Made with the Nebular Spectrograph of the Mcdonald Observatory., *ApJ*, *89*, 119. 21

Sugitani, K., Y. Fukui, A. Mizuni, and N. Ohashi (1989), Star formation in bright-rimmed globules - Evidence for radiation-driven implosion, *ApJ*, *342*, L87–L90. 35

Sugitani, K., Y. Fukui, and K. Ogura (1991), A catalog of bright-rimmed clouds with IRAS point sources: Candidates for star formation by radiation-driven implosion. I - The Northern Hemisphere, *Astrophysical Journal Supplement Series (ISSN 0067-0049)*, *77*, 59–66. 34

Sugitani, K., M. Tamura, and K. Ogura (1995), Young Star Clusters in Bright-rimmed Clouds: Small-Scale Sequential Star Formation?, *Astrophysical Journal Letters v.455*, *455*, L39. 35

Sugitani, K., et al. (2002), Near-Infrared Study of M16: Star Formation in the Elephant Trunks, *ApJ*, *565*(1), L25–L28. 36

Thompson, M. A., J. S. Urquhart, T. J. T. Moore, and L. K. Morgan (2011), The statistics of triggered star formation: an overdensity of massive YSOs around Spitzer bubbles, *arXiv*, *astro-ph.GA*. 33

Walborn, N. R., J. Maíz-Apellániz, and R. H. Barbá (2002), Further Insights into the Structure of 30 Doradus from the Hubble Space Telescope Instruments, *The Astronomical Journal*, *124*(3), 1601–1624. 32

Ward-Thompson, D., et al. (2010), A Herschel study of the properties of starless cores in the Polaris Flare dark cloud region using PACS and SPIRE, *A&A*, *518*, L92.

White, G., and C. V. M. Fridlund (1992), High resolution CO observations of S88-B, *A&A*, *266*, 452–456. 34

Whitworth, A. P., A. S. Bhattal, S. J. Chapman, M. J. Disney, and J. A. Turner (1994), Fragmentation of shocked interstellar gas layers., *Astronomy and Astrophysics 290*, *290*, 421–427. 26

Williams, R. J. R. (1999), Shadowing instabilities of ionization fronts, *MNRAS*, *310*(3), 789–796. 31

Williams, R. J. R., D. Ward-Thompson, and A. P. Whitworth (2001), Hydrodynamics of photoionized columns in the Eagle Nebula, M 16, *MNRAS*, *327*(3), 788–798. 32

Wright, N. J., J. J. Drake, J. E. Drew, M. G. Guarcello, R. A. Gutermuth, J. L. Hora, and K. E. Kraemer (2012), Photoevaporating Proplyd-like Objects in Cygnus OB2, *ApJ*, *746*(2), L21. 35

Wünsch, R., J. E. Dale, J. Palouš, and A. P. Whitworth (2010), The fragmentation of expanding shells - II. Thickness matters, *MNRAS*, *407*(3), 1963–1971. 26

Zavagno, A., et al. (2010), Star formation triggered by the Galactic H II region RCW 120. First results from the Herschel Space Observatory, *A&A*, *518*, L81.

Chapter 3

Numerical methods

> *Computers are useless. They can only give you answers.*
> *Pablo Picasso*

The study of the structures that develop at the interface between H II regions and molecular clouds requires the modeling of three components: the dynamics of the molecular gas, the propagation of the ionizing photons and the interaction between the two. In this chapter, we present the tools that we have developed to study the ionization of the gas in hydrodynamic simulations performed with the HERACLES code. We have implemented a method to solve gravity and self-gravity coupled to hydrodynamics to model the molecular cloud and a method to solve the ionization/recombination physics inside the gas. These tools are tested in simple situations in which the results can be compared to analytical solutions. We investigate the role of gravity and ionization in a first application on pillar formation.

3.1 Hydrodynamics & Gravity

The dynamics of a molecular cloud can be described by the Euler equations in a gravitational field **g**:

$$\begin{aligned}\frac{\partial \rho}{\partial t} + \nabla \cdot (\rho \mathbf{V}) &= 0 \quad , \\ \frac{\partial \rho \mathbf{V}}{\partial t} + \nabla \cdot [\rho \mathbf{V} \otimes \mathbf{V} + pI] &= \rho \mathbf{g} \quad , \\ \frac{\partial E}{\partial t} + \nabla \cdot [(E+p)\mathbf{V}] &= \rho(\mathbf{V}\cdot\mathbf{g}) \quad . \end{aligned} \tag{3.1}$$

with ρ the density of the gas, **V**, its velocity, E its total energy equals to $e + \rho \mathbf{V}^2/2$. e is the internal energy and is linked to the pressure p by $p = e(\gamma - 1)$ with $\gamma = 5/3$ for an ideal gas. HERACLES[1] (*González et al.*, 2007) is a 3D RMHD code that solves these equations in finite volume and on fixed grids (Cartesian, cylindric, spheric... multi-grid in progress). The code is based on Godunov methods, solving Riemann problems at the interfaces between cells. Equation 3.1 is in terms of conservative variables ρ, $\rho\mathbf{V}$ and E.

$$\frac{\partial \mathbf{U}}{\partial t} + \nabla \cdot (\mathbf{F}(\mathbf{U})) = S_g(\mathbf{U}) \tag{3.2}$$

with

$$\mathbf{U} = (\rho \quad \rho\mathbf{V} \quad E)^T$$

---

[1] `http://irfu.cea.fr/Projets/Site_heracles/index.html`

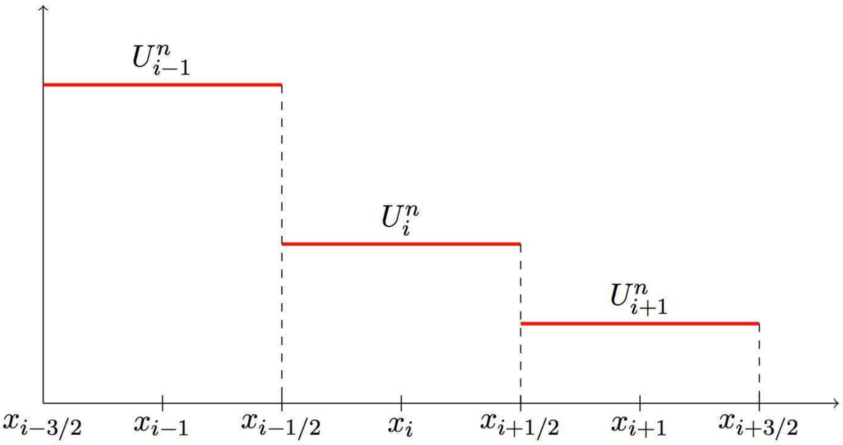

Figure 3.1: Discretization in finite volumes

$$\begin{aligned} \mathbf{F}(\mathbf{U}) &= (\rho\mathbf{V} \quad \rho\mathbf{V}\otimes\mathbf{V}+pI \quad (E+p)\mathbf{V})^T \\ S_g(\mathbf{U}) &= (0 \quad \rho\mathbf{g} \quad \rho(\mathbf{V}\cdot\mathbf{g}))^T \end{aligned} \tag{3.3}$$

To illustrate the way HERACLES works, we simplify 3.2 considering only a 1D equation without gravity : $\partial_t\mathbf{U}+\partial_x\mathbf{F}(\mathbf{U})=0$. In finite volumes, on a lattice, we define

$$\mathbf{U}^n_i = \frac{1}{\Delta x}\int_{x_{i-1/2}}^{x_{i+1/2}} \mathbf{U}(x,t^n)dx \tag{3.4}$$

and we get the situation described in Fig. 3.1. Using the integral form of the conservation law

$$\int_{x_{i-1/2}}^{x_{i+1/2}}\int_{t^n}^{t^{n+1}} \partial_t\mathbf{U}+\partial_x\mathbf{F}(\mathbf{U})=0 \tag{3.5}$$

we get

$$\frac{\mathbf{U}^{n+1}_i-\mathbf{U}^n_i}{\Delta t}+\frac{\mathbf{F}^{n+1/2}_{i+1/2}-\mathbf{F}^{n+1/2}_{i-1/2}}{\Delta x}=0 \tag{3.6}$$

where

$$\mathbf{F}^{n+1/2}_{i+1/2} = \int_{t^n}^{t^{n+1}} \mathbf{F}(\mathbf{U}(x_{i+1/2},t)) \tag{3.7}$$

Godunov scheme consists in taking for fluxes, the flux function evaluated on $\mathbf{U}$ at the interfaces between cells. The problem is then to evaluate $\mathbf{F}$ at the interfaces ($x_{i-1/2}$, $x_{i+1/2}$ ...). This can be done by solving the Riemann problem between cells, i.e finding the solution of 3.2 for a piecewise constant initial data set, $\mathbf{U}_L$ at the left of the interface and $\mathbf{U}_R$ at the right of the interface. The solution to this problem is known and can be computed, it consists in the propagation from the initial discontinuity of three waves (seven for MHD), always a contact discontinuity and rarefaction waves or shocks depending on the initial states. A solution to the problem is drawn on figure 3.2, a contact discontinuity at the center, we put here a rarefaction wave at left and a shock at right. The solution is self similar, it means that at any time the solution is just an homothetic transformation around the initial interface, therefore the value of $\mathbf{U}$ remains constant on the interface: $\mathbf{U}(x_{i+1/2},t)=\mathbf{U}(x_{i+1/2},0)=\mathbf{U}^*_{i+1/2}$. Then we take $\mathbf{F}^{n+1/2}_{i+1/2}=\mathbf{F}(\mathbf{U}^*_{i+1/2})$ which allows us to compute $\mathbf{U}^{n+1}_i$ from Eq. 3.6.

Using an exact solver to find the solution of Riemann problems can be numerically costly. There exist lots of other solvers to get approximate solutions which can be rapidly computed (linear solvers, HLL solvers... *Toro* (2001)).

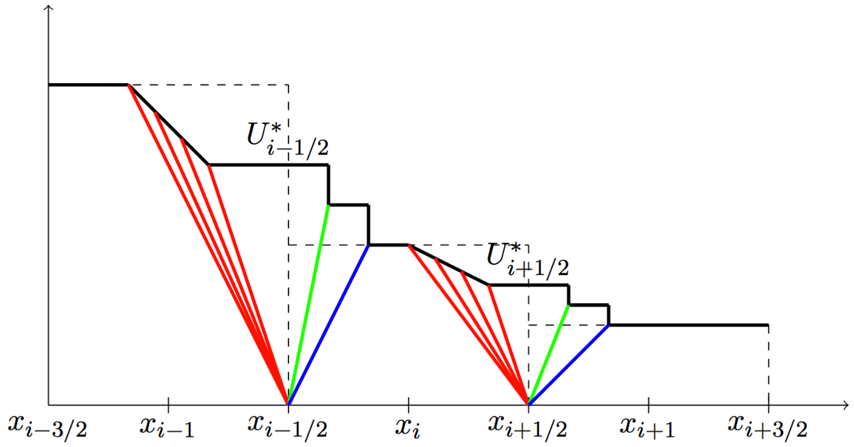

Figure 3.2: Solutions of the Riemann problems $\mathcal{RP}(U^n_{i-1}, U^n_i)$ and $\mathcal{RP}(U^n_i, U^n_{i+1})$
Green: contact discontinuities, red: rarefaction waves and blue: shocks.

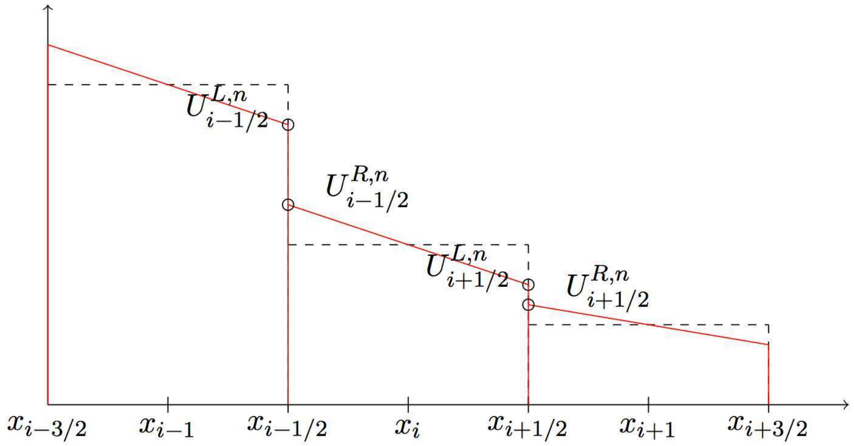

Figure 3.3: Second order Godunov scheme

For the moment we have presented first order scheme which is stable but very diffusive. In the 80's, high order schemes were developed (see *van Leer*, 1979). Second order Godunov scheme consists in taking piecewise linear approximation of the initial states before solving Riemann problems at interfaces. An example is shown in figure 3.3. For second order, we use the neighbours of a cell to build the slopes. The linear approximation gives left and right states, from which we compute fluxes to evolve (tilde) states at $\Delta t/2$. This is called the predictor step. We take now these tilde states to solve Riemann problems and compute fluxes to make the final Δt step. Therefore, we have

$$\begin{aligned}
\frac{\tilde{\mathbf{U}}_i(\Delta t/2) - \mathbf{U}^n_i}{\Delta t/2} &= -\frac{\mathbf{F}(U^{L,n}_{i+1/2}) - \mathbf{F}(U^{R,n}_{i-1/2})}{\Delta x} \\
\mathbf{U}^*_{i+1/2}\left(\frac{\Delta t}{2}\right) &= \mathbf{U}^{*,n+1/2}_{i+1/2} = \mathcal{RP}(\tilde{\mathbf{U}}^{n+1/2}_i, \tilde{\mathbf{U}}^{n+1/2}_{i+1}) \\
\frac{\mathbf{U}^{n+1}_i - \mathbf{U}^n_i}{\Delta t} &= -\frac{\mathbf{F}(U^{*,n+1/2}_{i+1/2}) - \mathbf{F}(U^{*,n+1/2}_{i-1/2})}{\Delta x} \qquad (3.8)
\end{aligned}$$

The use of second order Godunov scheme with a predictor step is called a MUSCL scheme. If slopes are too strong, the scheme may become unstable. Therefore, slope limiters are needed. There exists a whole class of such tools (minmod, moncen,superbee...).

Coupling gravity to hydrodynamic can be done by splitting the problem in two step:

the hydrodynamic evolution and then the update with the gravity source term. First, it is necessary to include the source term S_g in the predictor step (first equation of 3.8), then to add it in the last Δt step evolution (third equation of 3.8). The new tilde states are used to compute stars states by solving Riemann problems. From stars states we compute states at t^{n+1}, which we update with the gravity source term at $t^{n+1/2}$, $S^{g,n+1/2}$ which can be evaluated by $(S^g(\mathbf{U}_i^n) + S^g(\mathbf{U}_i^{n+1}))/2$ (see equations 3.9).

$$\begin{array}{rcl} \tilde{\mathbf{U}}_i^g(\Delta t/2) & = & \tilde{\mathbf{U}}_i(\Delta t/2) + S^g(\mathbf{U}_i^n) \times \Delta t/2 \\ \mathbf{U}_i^{g,n+1} & = & \mathbf{U}_i^{n+1} + (S^g(\mathbf{U}_i^n) + S^g(\mathbf{U}_i^{n+1}))/2 \times \Delta t \end{array} \tag{3.9}$$

The update can be done directly when the gravitational force is a known external force. However, in the case of the self-gravity of the medium, the Poisson equation has to be solved in order to find the gravitational potential.

3.2 Gravitational Potential Computation

For the self-gravity, it is needed to solve the Poisson equation for the gravitational potential Φ.

$$\begin{array}{rcl} \mathbf{g} & = & -\nabla \cdot \Phi \quad , \\ \triangle\Phi & = & 4\pi G\rho \quad . \end{array} \tag{3.10}$$

with $\Phi = \Phi^l$ on the boundary of the box. In finite volumes, the equation becomes

$$\frac{1}{\Delta x_i}\left(\frac{\Phi_{(i+1)jk} - \Phi_{ijk}}{\Delta x_{i+1}^c} - \frac{\Phi_{ijk} - \Phi_{(i-1)jk}}{\Delta x_i^c}\right) + \cdots = 4\pi G\rho_{ijk} \tag{3.11}$$

which can be written in the form $A\Phi = B$. Knowing B, the problem is reduced to the inversion of the symmetric matrix A. This can be done by a conjugate gradient method. We will take isolated boundary conditions, which are approximated by the potential created by a multi-polar development of the mass distribution at the boundary. Considering that the box is large enough, we take at first order the potential created by a punctual mass which is at the barycentre of the distribution, concentrating all the mass of the system.

Punctual Mass The first test is the computation of the potential created by a punctual mass. The results are given in Fig. 3.4 in which the computed potential of a one-solar-mass point is plotted against the analytic solution. Figure 3.5 shows the potential of two punctual masses and the potential computed with one CPU against the potential computed with eight CPUs. The maximum of the difference between the 1-CPU and 8-CPUs computation is 2.9×10^{-14}. Therefore the parallelization of the algorithm is correct. However, it is visible that there is a little difference between computed and analytical potentials for a punctual object. The difference is going up to 175 % close to the pixel in which the mass lies. In the neighborhood of the pixel containing the mass, the distribution is never punctual, which causes this difference. A single cell is not a very good test therefore a better solution is to compute the potential created by a sphere. Higher the resolution, smoother the spherical shape.

Homogeneous Sphere, test of the discretization of the Poisson equation Fig. 3.6 shows the computed potential and the analytic solution of a homogeneous sphere of total mass $M_\odot$ along the x axis direction and along the direction defined by $y = x/3$ and $z = 0$. As said before, the shape of the sphere is smooth at high resolution. The difference

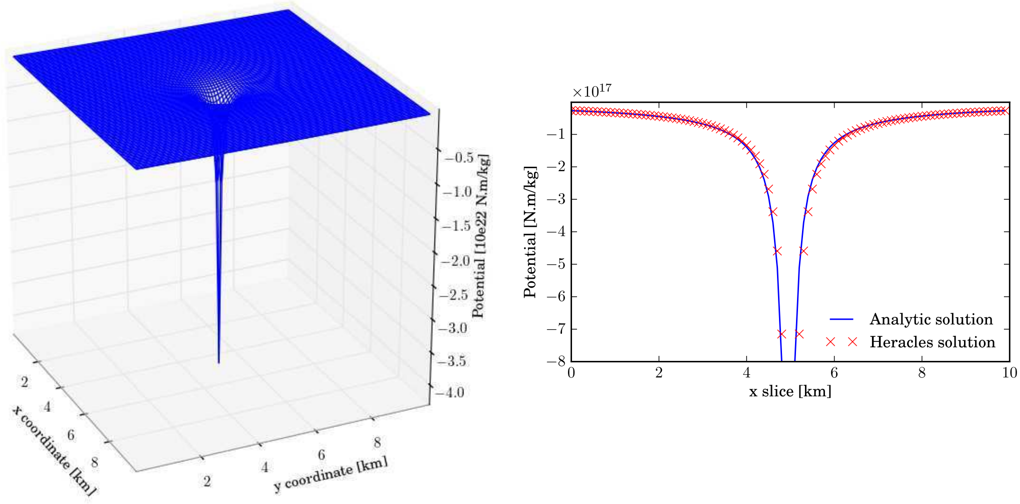

Figure 3.4: Potential of a punctual mass ($m = M_\odot$) at the center of a ten-kilometer box

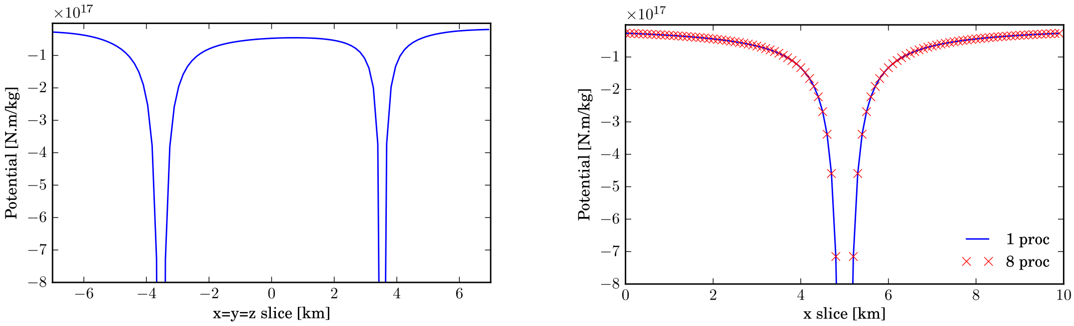

Figure 3.5: Potential of two points with different masses in the diagonal of the box and Potentials computed with one and eight processors

between the two solutions is 0.14 % along the x axis. However along the other direction, the difference with the analytical solution is 2.83 %. This is caused by the fact that we have a Cartesian mesh, this difference would disappear for a spherical mesh but note that in general, the mesh introduces some anisotropies in the force field.

Homogeneous Spheroid, test of the boundary conditions We now compare the computed and analytic potential of a homogeneous oblate spheroid of big half-axis a (in x-y plane) and small half-axis c (in z axis), to test the isolated boundary conditions. We can degenerate the small axis to end up with a disk and test how the numerical approximation of isolated boundary conditions behaves in function of a and c. Since the distribution is not anymore spherical, the solution computed is not converging to the analytic solution. Figure 3.7 shows the worst case, the spheroid is extremely degenerated and is big compare to the box.

The difference between the analytic solution and the computed one is 15 %. Table 3.1 contains all the results of the comparisons we have made. It shows that, if the object is small enough compared to the box size, the potential computed at the edge is well approximated by the potential of a punctual mass independently of its shape. The difference is less than 1% if the object is ten times smaller than the box.

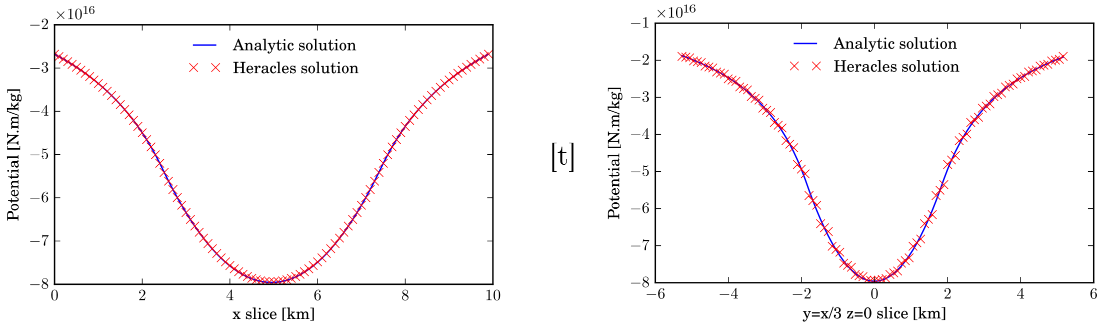

Figure 3.6: Potential created by a homogeneous sphere of mass $M_\odot$ in two different directions

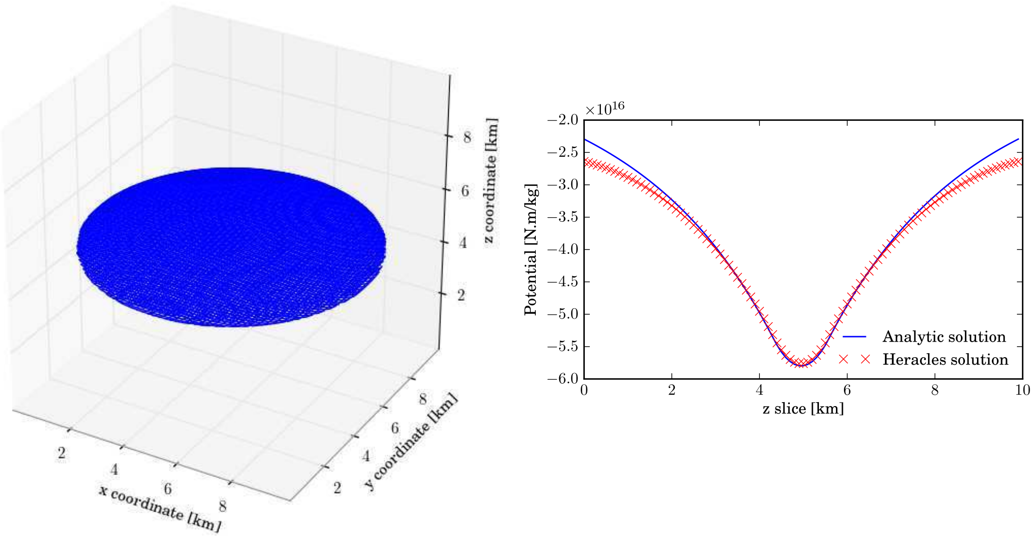

Figure 3.7: Oblate spheroid distribution and Analytic and computed potential in isolated boundary conditions

Homegenous Medium Collapse A simple test to see if gravity is well couple to hydrodynamics is to see the free-fall collapse of a homogeneous medium by self-gravity. Starting from a homogeneous medium with $\rho_i = 5.42 \times 10^{-22}$ g/cm^3, the collapse of the medium should take a time around the free-fall time $1/\sqrt{G\rho_i} = 2.85 \times 10^6$ years. It is approximately the time when the density diverges in the simulation (see Fig. 3.8). We took the initial values as imposed values at the boundaries for the hydrodynamics variables, and isolated boundary conditions for gravity.

Rayleigh Taylor Instability In a gravitational field, when a dense fluid lies on a less dense one, the interface in between is unstable. This is known as the Rayleigh-Taylor instability, which can also be used to test the coupling between gravitation and hydrodynamic. Let us take a situation in which we have a dense fluid with $\rho = 2$ g/cm^3 on a fluid with $\rho = 1$ g/cm^3 in a gravitational field with $g = 0.1$ cm/s^2 pointing down the light fluid. If we perturb slightly the interface between the two fluids, the separation is unstable and the dense fluid starts to sink in the light one as well as the light one goes up into the dense one. For the test we will take a single mode perturbation:

$$u_y(x, y) = 0.01(1 + \cos(4\pi x))(1 + \cos(3\pi y))/4 \tag{3.12}$$

The growth of the instability is in a linear regime at the beginning and then becomes nonlinear when structures are developing because of Kelvin-Helmholtz instabilities. Figure 3.9

	a=lbox/8	a=lbox/4	a=lbox/2
c=a/8	1.15	4.20	15.1
c=a/4	1.10	4.00	14.5
c=a/2	0.881	3.22	11.9

Table 3.1: Maximum (in percentage) of the difference between computed and analytic solutions for homogeneous oblate spheroid of half-axes a and c

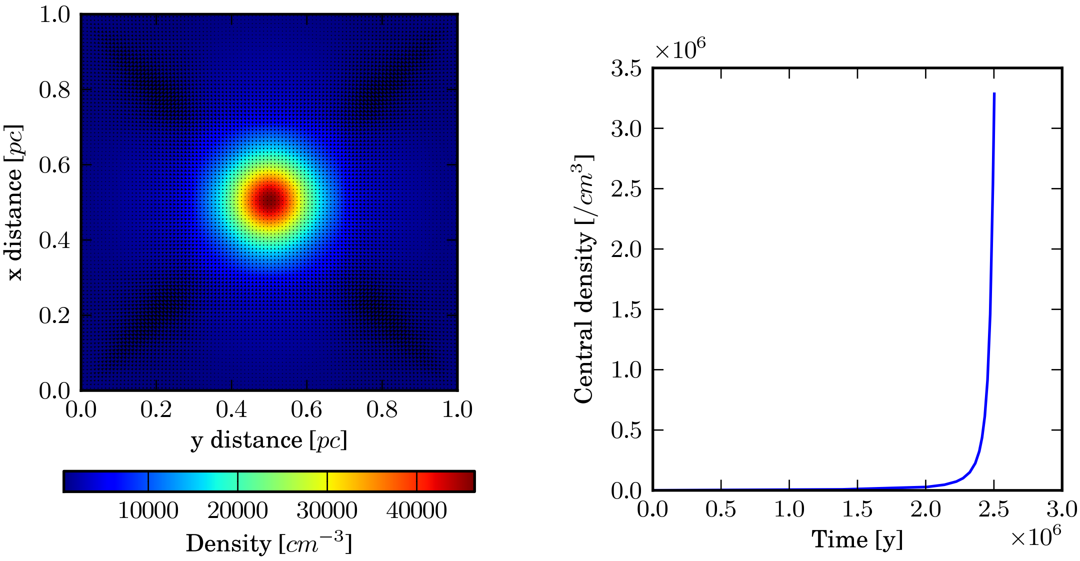

Figure 3.8: Collapse of a homogeneous medium ($\rho_i = 5.42 \times 10^{-22}$ g/cm^3) at $t = 2.1$ My and evolution of the central density in function of time

shows this instability computed with two different codes, HERACLES and ATHENA (see *Stone et al.*, 2008). The resolution for both computations is 200 x 600 cells. It can be seen on these plots that structures are quite different. This is caused by the fact that there is no cutoff to turbulence at small scales. Down to the size of a few cells, structures are very dependent on the scheme and are not physical. Therefore such simulations have to be compared at larger scale. The height and width of the instability are in good agreement in this two simulations. A movie is available online[2].

3.3 Photo-Chemistry Computation

The simulation of the development of H II regions requires the introduction of radiative transfer, in order to follow the ionizing photons and their interactions with the gas through heating and cooling processes. This can be decomposed in three steps:

1. The radiative transfer, to follow the photons
2. The photo-chemistry
    - Ionization : $H + \gamma \rightarrow e^- + H^+$
    - Recombination : $e^- + H^+ \rightarrow H + \gamma$

---

[2] `https://sites.google.com/site/astrohep/movies/rayleigh-taylor`

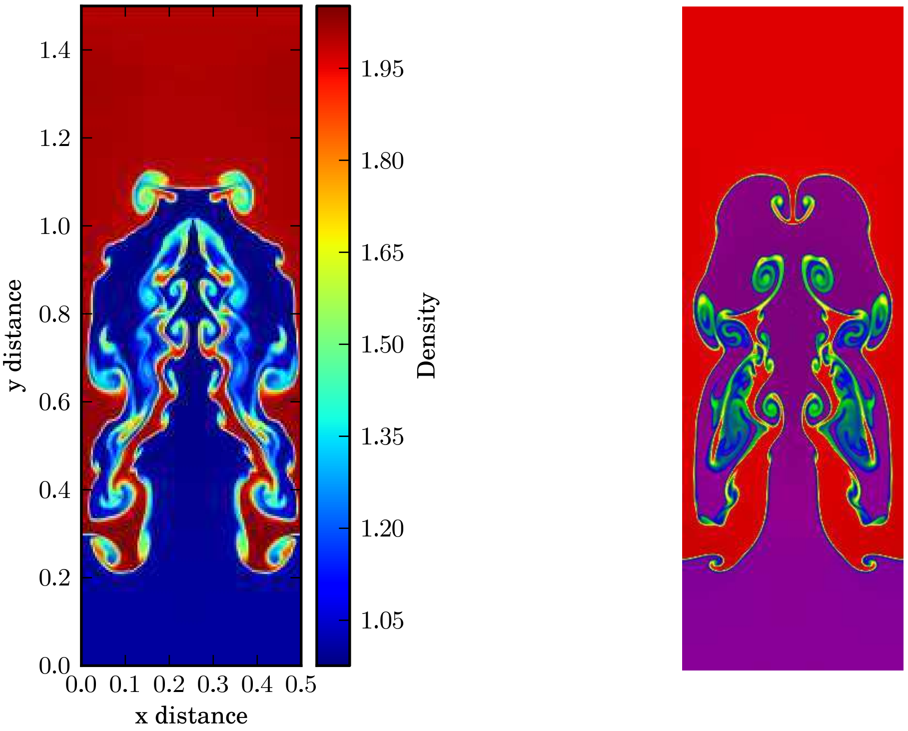

Figure 3.9: Expansion of a Rayleigh Taylor instability (grid 200x600), left HERACLES (second order, exact solver, slope positively preserving); right ATHENA (third order, HLLC solver) (see *Stone et al.*, 2008)

3. The heating and cooling
    - Heating by ionization, ionizing photons give kinetic energy to electrons
    - Cooling by recombination, thermal energy of electrons is lost by recombination

Radiative Transfer The equation governing radiative transfer is

$$\frac{1}{c}\frac{\partial I_\nu}{\partial t} + \vec{n} \cdot \vec{\nabla} I_\nu = -\kappa_\nu I_\nu + \eta_\nu \tag{3.13}$$

where $I_\nu(\vec{x}, t, \nu, \vec{n})$ is the spectral intensity, $\kappa_\nu(\vec{x}, \nu, \vec{n})$ is the absorption coefficient and $\eta_\nu(\vec{x}, t, \nu, \vec{n})$ is the source term.

The typical size of our simulations is about tens of parsecs, it takes only tens of year for light to travel this distance, we can consider that photon transport is instantaneous $c \to \infty$. We consider that photons are coming from only one direction (from the central O star) so that $\vec{n} = (1, 0, 0)$. On a Cartesian mesh, it means that we are dealing with a plane-parallel simulation far away from the central star so that we can consider the flux to be parallel. In spherical coordinates, it means that photons are traveling only on the radial direction, from the central star to the ISM which can be used in the close neighborhood of the star. Therefore we can start our simulations by a 1D case keeping only the x direction in the transfer equation. Equation 3.13 becomes

$$\frac{\partial I_\nu(x, t, \nu) ds}{\partial x} = -\kappa_\nu(x, \nu) I_\nu(x, t, \nu) ds + \eta_\nu(x, t, \nu) ds \tag{3.14}$$

If we are in Cartesian coordinates, ds is constant and disappear in the previous equation, in spherical coordinates $ds = r^2 d\Omega$ and depends on $x = r$. The use of ds allows us to take into account dilution factors along the propagation. The source term can be decomposed in two parts; a term coming from the star which we assume to be a Planckian distribution diluted at the distance we start our simulation, and a term coming from the recombination. We make the so-called **on the spot approximation**, in considering that photons from recombination which have enough energy to ionize another hydrogen atom, are instantaneously re-absorbed. This approximation is valid if the density is high enough to have a high probability for photons to interact with an atom. The remaining photons cannot ionize hydrogen anymore, therefore they escape from the system and they only contribute to the cooling of the gas. That is why we can consider that the source term due to recombination is zero.

$$\begin{aligned}\eta_\nu(x,t,\nu) &= S_*(\nu)\delta_0(x) + S_{rec}(x,t,\nu) \\ S_*(\nu) &= \pi(r_*^2/r_0^2)B_\nu(T_*) \\ S_{rec}(x,t,\nu) &= 0 \end{aligned} \tag{3.15}$$

The absorption coefficient is given by

$$\kappa_\nu(x,\nu) = \sigma n_{H_0}(x)\frac{\nu_1^3}{\nu^3} \tag{3.16}$$

where $h\nu_1 = 13.6eV$, σ is the ionizing cross section for photons at frequency ν_1 and $n_{H_0}(x)$ the density of neutral hydrogen atoms.

We can divide Eq. 3.14 by $h\nu$ to have an equation on the number of photons rather than on radiative energy. We then average Eq. 3.14 on the frequencies and since we are only interested in the ionizing photons, we average ν between ν_1 and $+\infty$.

$$\begin{aligned}F_\gamma(x,t) &= \int_{\nu_1}^{\infty} I_\nu(x,t,\nu)/(h\nu) \\ \sigma_\gamma(T_*) &= \left(\int_{\nu_1}^{\infty} \sigma(\nu_1^3/\nu^3)(B_\nu(T_*)/h\nu)\right) / \int_{\nu_1}^{\infty}(B_\nu(T_*)/h\nu) \\ S_*(T_*,r_*,r_0) &= \pi\int_{\nu_1}^{\infty}(r_*^2/r_0^2)B_\nu(T_*)/(h\nu) \end{aligned} \tag{3.17}$$

Such that equation 3.14 becomes

$$\frac{\partial F_\gamma ds}{\partial x} \approx -n_{H_0}\sigma_\gamma F_\gamma ds + n_{H_0}\sigma_\gamma\delta_0(x)S_* ds \tag{3.18}$$

where F_γ is just now the number of photons per unit of surface and time arriving in the x direction and σ_γ is the average cross-section over a typical Planckian source at the temperature of the star.

Photo-Chemistry We now compute the equations for photo-chemistry. We set X to be the fraction of ionization $X = n_{H^+}/n_H$ where $n_H = n_{H^+} + n_{H^0}$. The variation of H^+ atoms is just the number of incoming photons, which are going to interact, minus the number of ionized atoms, which will recombine. The number of interacting photons is given by the number of incoming photons multiplied by the probability of interaction given by the cross-section $dP = \sigma_\gamma n_{H^0} dx$. Therefore

$$\begin{aligned}d(Xn_H) &= dn_{\gamma_{int}} - dn_{H_{rec}} \\ dn_{H_{rec}} &= \beta n_{H^+}n_{e^-}dt = \beta X^2 n_H^2 dt \\ dn_{\gamma_{int}} &= F_\gamma(x,t)ds_{in}dtdP/dv_{cell} = \sigma_\gamma F_\gamma n_H(1-X)\omega dt \end{aligned} \tag{3.19}$$

The term $\omega = (ds_{in}dx/dv_{cell})$ is equal to 1 in Cartesian coordinates and is equal to the dilution factor r_{in}^2/r_{cell}^2 in spherical coordinates (r_{in} is the position of the interface of the cell while r_{cell} is the position of the centre of the cell). β gives the rate of recombination and is equal to $2 \times 10^{-10} T^{-0.75}$ cm^3/s where T is the temperature of thermodynamic equilibrium between all the species (see *Black*, 1981).

Thermal balance The thermal balance is the balance between the heating and cooling rate

$$\frac{de}{dt} = \mathcal{H} - \mathcal{L} \tag{3.20}$$

whith $e = k_b n_{tot} T/(\gamma - 1)$ is the internal energy of the gas, $\mathcal{H}$ the heating rate and $\mathcal{L}$ the cooling rate. The heating during ionization comes only by the extra-energy that absorbed photons give to the kinetic energy of electrons. This can be computed at a given wavelength by

$$\begin{aligned} d\mathcal{Q}^e(\nu) &= (I_\nu/h\nu \times ds_{in}dt/dv_{cell})(\kappa_\nu dx)\delta e_\gamma(\nu) \\ &= n_{H^0}\omega dt(I_\nu/h\nu)(\sigma\frac{\nu_1^3}{\nu^3})(h\nu - h\nu_1) \end{aligned} \tag{3.21}$$

With a single group approach, we need to sum this quantity over ν. Like before we take a typical Planckian distribution at the star temperature for the radiation.

$$e_\gamma(T_*) = \left(\int_{\nu_1}^{\infty} (B_\nu(T_*)/h\nu)(h\nu - h\nu_1)\right) / \int_{\nu_1}^{\infty} (B_\nu(T_*)/h\nu) \tag{3.22}$$

Therefore,

$$\begin{aligned} d\mathcal{Q}^e &\approx n_{H^0}\omega dt F_\gamma \sigma_\gamma e_\gamma \\ \mathcal{H} &= d\mathcal{Q}^e/dt \approx \omega(1-X)n_H F_\gamma \sigma_\gamma e_\gamma \end{aligned} \tag{3.23}$$

The cooling term is just the loss of the thermal energy of electrons used by recombination.

$$\begin{aligned} d\mathcal{Q}^{rec} &= dn_{H_{rec}} \times k_b T/(\gamma - 1) = \beta X^2 n_H^2 dt \times k_b T/(\gamma - 1) \\ \mathcal{L} &= d\mathcal{Q}^{rec}/dt = \beta X^2 n_H^2 k_b T/(\gamma - 1) \end{aligned} \tag{3.24}$$

Algorithm To resume, the three equations we have to solve are

$$\begin{aligned} \partial F_\gamma ds/\partial x &= n_H(1-X)\sigma_\gamma(\delta_0(x)S_* - F_\gamma)ds \\ d(Xn_H)/dt &= n_H(1-X)\sigma_\gamma F_\gamma \omega - \beta X^2 n_H^2 \\ de/dt &= n_H(1-X)\sigma_\gamma F_\gamma \omega e_\gamma - \beta X^2 n_H^2 k_b T/(\gamma - 1) \end{aligned} \tag{3.25}$$

The strategy we adopt is to solve the first two equations implicitly and then the thermal transfer a posteriori, implicitly, with sub-cycling.

- First step: Initialization

Knowing the characteristics of the O star: T_*, r_* and r_0 the distance between the boundary of the box and the star, we can compute the initial parameters of the simulation: the source term $S_*(T_*, r_*, r_0)$, the average cross section $\sigma_\gamma(T_*)$ and the average electron energy $e_\gamma(T_*)$.

At the boundary, we impose a constant flux equal to the source term $F_{0-1/2}^n = S_*$ for all n. Then we just have two solve $\partial F_\gamma ds/\partial x = -n_H(1-X)\sigma_\gamma F_\gamma ds$ on the rest of the mesh.

- Second step: Radiative transfer & photo-chemistry

We can consider that the photo-chemistry is done much faster than the hydrodynamic evolution, so that we can consider hydrodynamics quantities, such as n_H, to be constant during the chemistry step. The first two equations of 3.25 become

$$\begin{aligned} F^n_{i+1/2}\Delta s_{i+1/2} - F^n_{i-1/2}\Delta s_{i-1/2} &= -n_{Hi}(1-X^n_i)\sigma_\gamma F^n_{i+1/2}\Delta s_{i+1/2}\Delta x \\ X^{n+1}_i - X^n_i &= (1-X^{n+1}_i)\sigma_\gamma F^{n+1}_{i+1/2}\Delta t(\Delta s_{i+1/2}\Delta x)/\Delta v_i - \beta(X^{n+1}_i)^2 n_{Hi}\Delta t \end{aligned} \tag{3.26}$$

To simplify these expressions, we set

$$\begin{aligned} N^n_{i+1/2} &= \sigma_\gamma F^n_{i+1/2}\Delta t(\Delta s_{i+1/2}\Delta x)/\Delta v_i \\ p &= n_{Hi}\sigma_\gamma\Delta x \\ r &= \beta n_{Hi}\Delta t \end{aligned} \tag{3.27}$$

Therefore, equations 3.26 become

$$\begin{aligned} N^n_{i+1/2} - N^n_{i-1/2} &= -p(1-X^n_i)N^n_{i+1/2} \\ X^{n+1}_i - X^n_i &= (1-X^{n+1}_i)N^{n+1}_{i+1/2} - r(X^{n+1}_i)^2 \end{aligned} \tag{3.28}$$

Since our source term is at the left of our simulation we have to compute from 3.28 $N^{n+1}_{i+1/2}$ and X^{n+1}_i, knowing $N^{n+1}_{i-1/2}$ and X^n_i.

$$\begin{aligned} 0 &= a(X^{n+1}_i)^3 + b(X^{n+1}_i)^2 + cX^{n+1}_i + d \\ N^{n+1}_{i+1/2} &= N^{n+1}_{i-1/2}/(1+p(1-X^{n+1}_i)) \end{aligned} \tag{3.29}$$

with

$$\begin{aligned} a &= rp \\ b &= p - r(1+p) \\ c &= -N^{n+1}_{i-1/2} - (1+p) - pX^n_i \\ d &= N^{n+1}_{i-1/2} + (1+p)X^n_i \end{aligned} \tag{3.30}$$

The solution of the third degree polynom in the first equation of 3.29 gives us X^{p+1}_i from which we can compute $N^{n+1}_{i+1/2}$ and then $F^{n+1}_{i+1/2}$ with the second equation of 3.29.

- Third step: Thermal transfer

The third equation of 3.25 becomes

$$k_b n_H/(\gamma-1)\times((1+X)dT/dt + TdX/dt) = n_H(1-X)\sigma_\gamma F_\gamma \omega e_\gamma - \beta X^2 n_H^2 k_b T/(\gamma-1) \tag{3.31}$$

From Eq. 3.19 we can extract $d(n_H X)/dt = \sigma_\gamma F_\gamma n_H(1-X)\omega - \beta X^2 n_H^2$:

$$n_{Hi}k(1+X^{n+1}_i)(T^{n+1}_i - T^n_i) = (e_\gamma - kT^{n+1}_i)n_{Hi}(1-X^{n+1}_i)N^{n+1}_{i+1/2} \tag{3.32}$$

with $k = kb/(\gamma-1)$. Knowing T^n_i, X^{n+1}_i and $N^{n+1}_{i+1/2}$ we can sub-cycle this equation to obtain T^{n+1}_i.

Note that these equations do not suppose the equilibrium between the ionization and the recombination. This assumption is often made in the study of H II regions. We will see in Chap. 5, that it is crucial to treat the out-of-equilibrium physics when the turbulence of the cold gas is included.

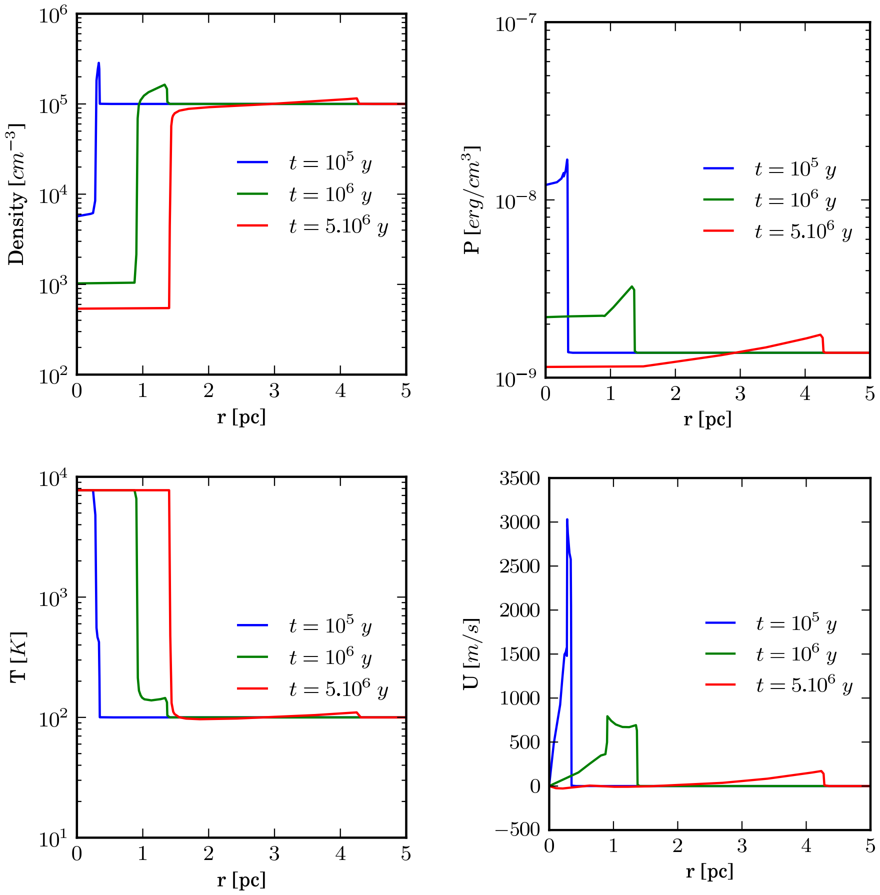

Figure 3.10: H II region expansion: profiles of density, temperature, pressure and velocity.

3.4 H II region expansion

We make a 1D spherical simulation of a H II region expansion. Starting from a dense medium with $n_H = 10^5$ cm^{-3} and $T = 20$ K, we switch on a photon flux coming from a typically O4 star with a ionizing flux of $S_* = 1.9 \times 10^{50}\ s^{-1}$. The simulation domain extend from 10^{-4} pc to 0.1 pc with 400 mesh point with logarithmic spacing. The gas is ideal with $\gamma = 5/3$ and $\mu = 1.4$. After ionization the medium is at a temperature corresponding to 1 eV i.e. 7723 K. The sound speed in the medium is given by $c_s = \sqrt{\gamma P/\rho}$ such that the typical time scale for hydrodynamics $\tau_h = \Delta x/a$ is of order 20 years. Evolution of the ionization front is only controlled by the recombination term whose time scale is $\tau_r = 1/\beta n_H$ which is of the order of one year, much shorter than τ_h. Therefore there is a first phase of development where there are only two regions both at the same density but one is ionized and the other neutral i.e. the R phase in Sect. 2.1. The ionized sphere expands until all the incoming photons are used to compensate recombinations inside the sphere. Recall that the radius is given by Strömgren radius $R_S = (3S_*/4\pi\beta(T)n_H^2)^{1/3}$, *Strömgren* (1939). In our example $R_s = 0.086$ pc. Figure 3.11 (left) shows the development of the ionized sphere before hydrodynamics starts to matter at the end of the R phase. The time evolution of the ionization front can be easily estimated when we made the approximation of immediate heating of the medium, the formula is given by (see *Spitzer*, 1978)

$$R_I(t) = R_S(1 - e^{t/\tau_r})^{1/3} \tag{3.33}$$

After this first step the energy deposed by the ionizing photons creates a shock front ahead the ionized front, i.e. the D phase. This shock creates a ionized cavity and a

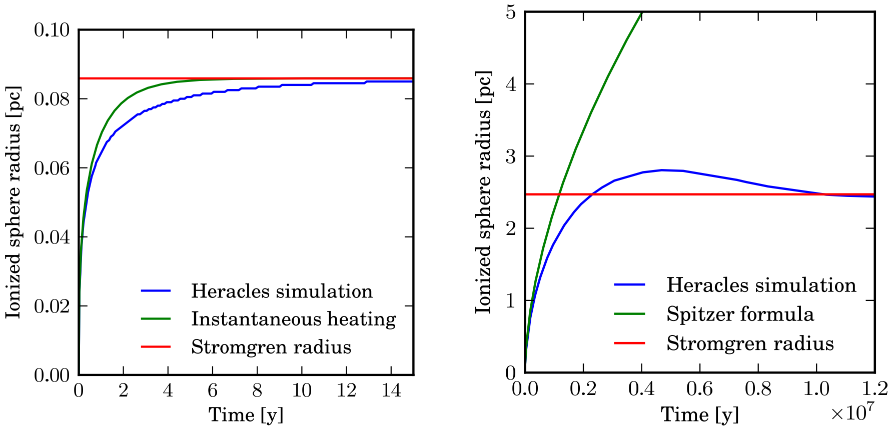

Figure 3.11: Expansion of an H II region from a homogeneous medium ($n_H = 10^5$ cm^{-3}, $T = 20$ K, $S_* = 1.9 \times 10^{50}$ s^{-1}): Left, while hydro is static in the R phase. The Strömgren radius is computed with the initial density. Right: while hydrodynamics is in the D phase. The Strm̈gren radius is computed with the density reached in the hydrostatic limit.

zone of compressed gas.The shock propagates until hydrostatic equilibrium between the ionized gas inside the sphere and the exterior medium. From hydrostatic equilibrium we can compute the density inside the hydrostatic Strömgren sphere and then the radius with the Strömgren formula. In our example $R_{\rm hs} = 2.47$ pc at the hydrostatic equilibrium. The time evolution of the ionization front can be evaluated by the formula computed by *Spitzer* (1978) given by Eq. 2.13. This formula is an approximation only valid at the beginning of the shock propagation. The evolution of the ionized front is shown in Fig. 3.11. Note that the medium is very dense, therefore we reach hydrostatic equilibrium in a relatively short time. For standard ISM densities in molecular clouds of the Milky Way, the hydrodynamic equilibrium is not reached during the life-time of the clouds (see Sect. 2.1).

The profiles of density, temperature, pressure and velocity are shown in Fig. 3.10. At t= 0.1 My, the shell is dense and thin. Because of the adiabatic condition in the cold gas, the compression cannot exceed a factor 4 in the shell. Since there is no cooling, the shock is accelerated by a gradient of pressure and the shell gets thicker and thicker. At t = 5 My, the shock becomes weak and hydrostatic equilibrium is nearly reached at that time. In the next chapter, we will investigate the effect of the cooling in the molecular cloud on the structure of the shell.

3.5 Test on the formation of pillars

A application is to test if pillars (e.g. Pillars of Creation *Hester et al.*, 1996) can emerge only from gravitational forces from a star cluster on a clump or if ionization is needed. A clump in a homogeneous medium will be heavier that the surrounding gas and therefore, will "sink" into the H II region. Taking a cluster of 500 $M_\odot$ at 5 pc gives a gravitational acceleration of 10^{10} cm s^{-2}. We compare this situation to a clump in homogeneous medium at 5 pc of a B star that gives a flux of $8{\times}10^9$ cm^{-2} s^{-1}. The outcome of the simulations are shown in Fig. 3.12. The simulations are stopped when the final structure is around 2 parsecs long. It takes 15 My for the gravitational force to stretch the pillar up to that size, longer than the typical life-time of massive stars. It is therefore not plausible that the gravitational force is responsible for the formation of these structures. Furthermore the pillar is in free fall, therefore the velocity profile along the pillar should vary as the square root of the position. As seen in Chap. 2, this was ruled out by the observations of *Pound*

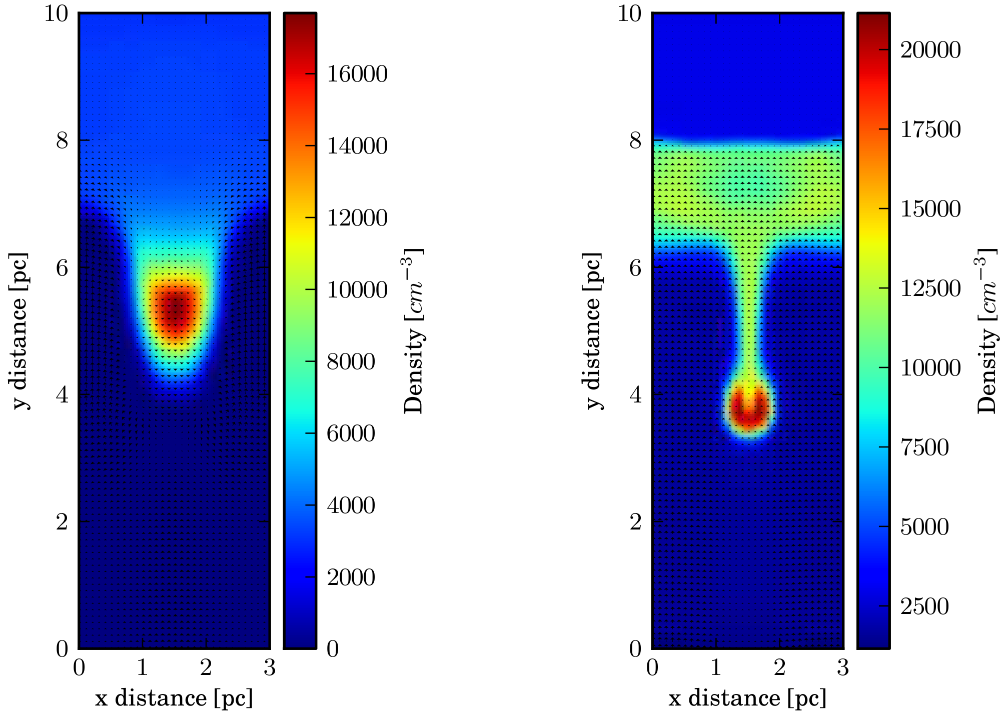

Figure 3.12: Clump in a homogeneous medium; left: $t = 15$ My under a gravitational acceleration of 10^{10} cm s^{-2}, right: $t = 1$ My under a ionization flux of $8{\times}10^{9}$ cm^{-2} s^{-1}.

(1998). With ionization, it takes only 1 My to form a 2-pc pillar. This time-scale is much more compatible with the observational constraints. In the next chapter, we will further investigate how the pillars form in the context of the deformation of the shell around the H II region.

Bibliography

Black, J. H. (1981), The physical state of primordial intergalactic clouds, *MNRAS*, *197*, 553–563. 52

González, M., E. Audit, and P. Huynh (2007), HERACLES: a three-dimensional radiation hydrodynamics code, *A&A*, *464* (2), 429–435. 43

Hester, J. J., et al. (1996), Hubble Space Telescope WFPC2 Imaging of M16: Photoevaporation and Emerging Young Stellar Objects, *Astronomical Journal v.111*, *111*, 2349. 55

Pound, M. W. (1998), Molecular Gas in the Eagle Nebula, *Astrophysical Journal Letters v.493*, *493*, L113. 55

Spitzer, L. (1978), *Physical processes in the interstellar medium*, New York Wiley-Interscience, Princeton University, New Observatory, Princeton, N.J. 54, 55

Stone, J. M., T. A. Gardiner, P. Teuben, J. F. Hawley, and J. B. Simon (2008), Athena: A New Code for Astrophysical MHD, *The Astrophysical Journal Supplement Series*, *178* (1), 137–177. 49, 50

Strömgren, B. (1939), The Physical State of Interstellar Hydrogen., *ApJ*, *89*, 526. 54

Toro, E. F. (2001), *Godunov Methods*, Theory and Applications, Springer. 44

van Leer, B. (1979), Towards the ultimate conservative difference scheme. V - A second-order sequel to Godunov's method, *Journal of Computational Physics*, *32*, 101–136. 45

Chapter 4

Shell collapse and pillar formation

> *A complex system that works is invariably found to have evolved from a simple system that works.*
> *John Gaule*

The present chapter focuses on "simple" situations to highlight the key mechanisms at work in the interaction between a H II region and a cloud. We present the numerical methods needed for this study, followed by two different set-ups, cloud-H II region interface modulation and density modulation inside the cloud. Finally we present a study of the different stages of evolution of the resulting pillars.

UV radiation creates a dense shell compressed between an ionization front and a shock ahead. Interface modulations produce a curved shock that collapses on itself, which leads to stable growing pillar-like structures. The narrower the initial interface modulation, the longer the resulting pillar. We interpret pillars resulting from density modulations in terms of the ability of these density modulations to curve the shock ahead of the ionization front.

The shock curvature is a key process for understanding the formation of structures at the edge of H II regions. Interface and density modulations at the edge of the cloud have a direct impact on the morphology of the dense shell during its formation.

4.1 Thermal processes in the molecular cloud

We considered a molecular cloud impacted by the UV radiation of an OB cluster to study how structures develop at the interface between the resulting H II region and the cloud. The method used to simulate gas hydrodynamics in the molecular cloud and the UV radiation from the OB cluster were presented in Chap. 3. We will present now the heating and cooling rates used in the molecular cloud. Thermal processes are taken in account by adding the heating and cooling rate $\Lambda(\rho, T)$ in the equation of energy conservation in Eq. 3.1.

In the ionized phase, we considered in Chap 3 two processes that have a major impact on the thermodynamics of the gas. The photoelectric heating caused by the massive star UV flux and the cooling through recombination of electrons onto protons. At the equilibrium between ionization and recombination, the recombination rate is equal to the ionization rate $dn_{\gamma_{int}} = dn_{H_{rec}}$. Therefore the temperature is given by $(\gamma - 1)e_\gamma/k_b$ when thermodynamic equilibrium is achieved in the ionized phase, which is equal to 7736 Kelvin. The corresponding isothermal curve in the pressure-density plane is drawn in Fig. 4.1.

In the weakly ionized phase, we simulate the radiative heating and cooling of the interstellar medium (ISM) by adding five major processes following the work of *Audit and Hennebelle* (2005) and *Wolfire et al.* (1995, 2003):

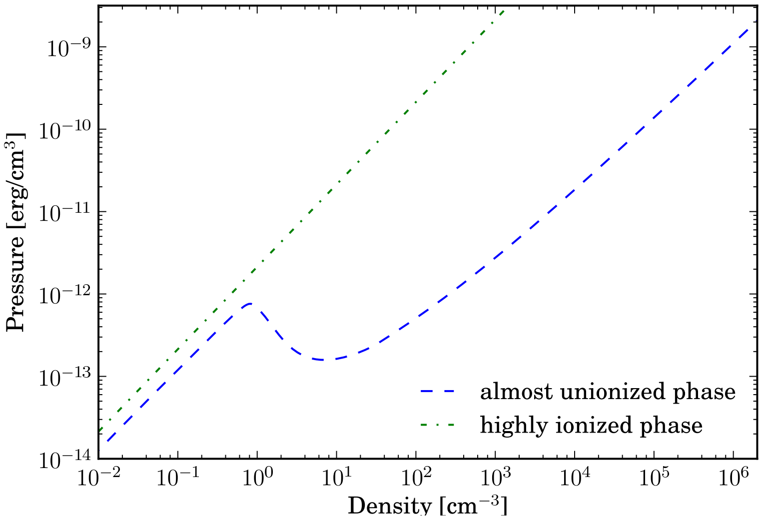

Figure 4.1: Thermodynamic equilibrium in the pressure-density plane for the highly and weakly ionized phases

- photoelectric heating by UV radiation with a flux equal to $G_0/1.7$, in which G_0 is the Habing flux
- cooling by atomic fine-structure lines of C II
- cooling by atomic fine-structure lines of O I
- cooling by H (Lyα)
- cooling by electron recombination onto positively charged grains.

The UV flux used in this phase is an ambient low flux, additional to the UV flux F_γ from the massive stars, which is used in our ionization process described in subsect. 3.3. This heating and cooling function is only valid for the dense cold and weakly ionized phase. Therefore these processes are weighted by $1-X$ and contribute only in the weakly ionized phase. In this phase, the ionization fraction used for the thermal processes is a function of the temperature and is given by *Wolfire et al.* (2003) (typically around 10^{-4}). The thermodynamic equilibrium in the pressure-density plane is given in Fig. 4.1.

The transition at the ionization front is very sharp as it can be seen on the 1D test below. Therefore the fraction of the gas in between the two phases is small and is not dynamically significant.

We take now a homogeneous medium with n_H=500 cm^{-3}, T≈25 K, S_*=10^{50} s^{-1}. After the R phase, the energy deposited by the ionizing photons creates a spherical region with a high pressure. The radius of the sphere is given by the Strömgren radius $R_s = 2.4$ pc. This region will therefore start expanding and pushes the surrounding interstellar matter away, creating a shock front ahead of the ionization front. This process creates an expanding ionized cavity and a shell of compressed gas. Typical density and temperature profiles are given in Fig. 4.2. Solid lines correspond to the adiabatic case for the cold gas and the dashed lines to the cooling function described in Subsect. 4.1. The shock front is cooled down by the thermal processes and the shell is compressed up to two orders of magnitude. This phenomenon is at the origin of the idea of the collect-and-collapse scenario for triggered star formation around H II regions, proposed by *Elmegreen and Lada* (1977).

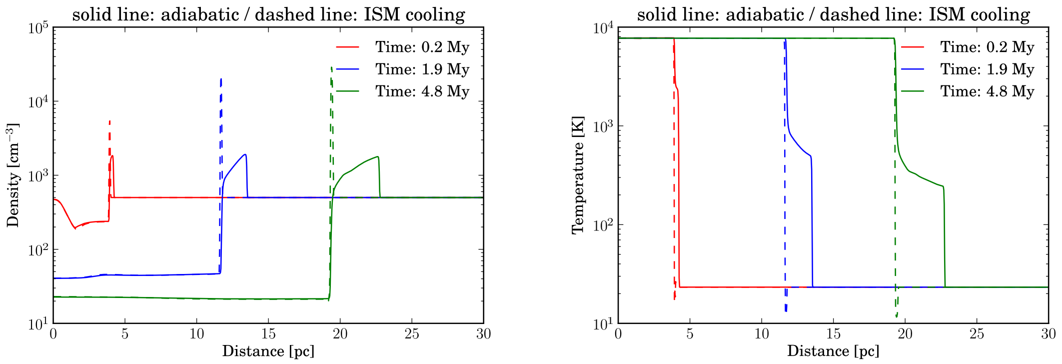

Figure 4.2: Density (left) and temperature (right) profiles of the expansion of an H II region in a homogenous medium (n_H=500 cm^{-3}, T≈25 K, S_*=10^{50} s^{-1}). Solid lines correspond to an adiabatic cold phase and dashed lines to a cooled cold phase with the cooling described in Subsect. 4.1.

We can derive the equations governing the density, the speed and the thickness of the shell in the approximation of an isothermal weak D-type shock following *Elmegreen and Lada* (1977) and *Spitzer* (1978) (see Sect. 2.1)

$$\begin{aligned} v_{\text{shell}} &= c_{II}(R_s/r_{\text{shell}})^{3/4} \\ n_{\text{shell}} &= n_0/\gamma \times (v_{\text{shell}}^2/c_{\text{shell}}^2) \\ l_{\text{shell}} &\approx r_{\text{shell}}\gamma \times (c_{\text{shell}}^2/v_{\text{shell}}^2) \end{aligned} \tag{4.1}$$

The velocity and position of the shell are determined exactly in the same way as in Sect. 2.1 and corresponds very well to the simulation, i.e. $r_{\text{shell}} = 19.5$ pc and $v_{\text{shell}} = 2.3$ km/s at t = 4.8 My. However, the density and thickness of the shell differ because the simulation is not isothermal. That is why we corrected the formula from Sect. 2.1 with the use of γ and c_{shell} in Eq. 4.1. Assuming a temperature in the shell of 10 Kelvin and with $\gamma = 5/3$, we obtain a shell density of 2.8×10^4 cm^{-3}, and a width of 0.34 parsec. These values agree well with the shell parameters we obtained in the 1D simulation in Fig. 4.2, the maximum density is 2.9×10^4 cm^{-3} and the shell width is 0.27 parsec. We can see that our code can follow the ionization front and the subsequent evolution of the dense shell. As a consequence, we will now turn our attention to more interesting 3D cases.

4.2 Forming pillars

The interstellar medium has a very complex structure with considerable inhomogeneities and high density fluctuations. The passage from 1D to 3D brings many new degrees of freedom. It allows us to study how the shell resulting from the collect and collapse scenario, may be perturbed. The possibility to have localized density gradients has been extensively studied with the RDI scenario (*Mackey and Lim*, 2010; *Bisbas et al.*, 2011; *Gritschneder et al.*, 2009) and more recently within a turbulent media (*Gritschneder et al.*, 2010) (see Chap. 2). Here, we first want to focus on more simple and schematic situations in which the physical processes at work can be identified and studied more easily. We will therefore study two idealized cases. First, we will look at the interaction of the ionization front with a medium of constant density having a modulated interface. Then, we will consider a flat interface with overdense clumps in the medium.

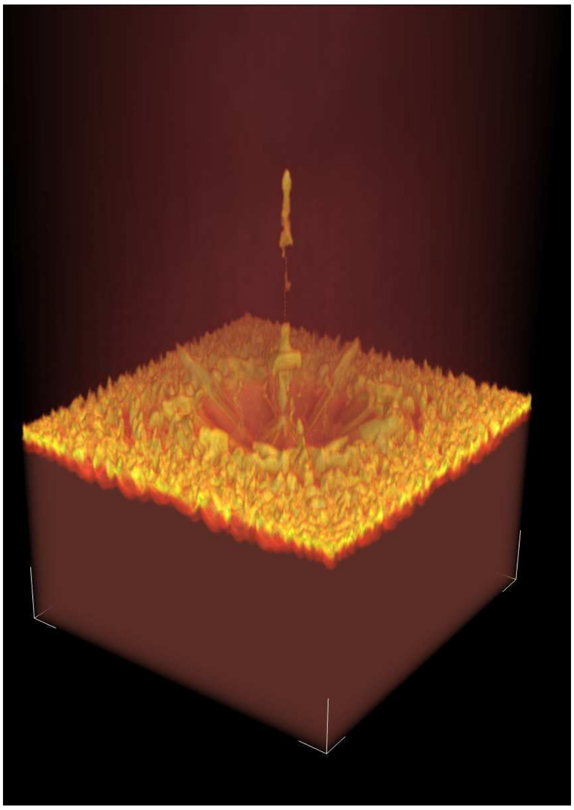

Figure 4.3: Three-dimensional snapshot of density at 500 ky of an ionization front propagation with a modulated interface. The UV flux at the top of the box is 10^9 photons per second per square centimetre, the box is 4x2x2 pc^3. The dense gas is initially at 500 $\mathrm{H/cm}^3$ at a temperature around 25 K (thermal equilibrium from Fig. 4.1). The (base width)/height ratios (w/h ratios hereafter) of the modulation is w/h=0.9.

4.2.1 From interface modulations to pillars

We first studied the interaction between the ionization front and an interface modulated by an axisymmetric sinus mode with constant heigh (amplitude of 0.5 parsec) and four different base widths (see Fig. 4.3 and Fig. 4.4). The size of the computational domain was adapted to the typical observed length scale of pillars, $4 \times 2 \times 2$ pc^3, at a resolution of $400 \times 200 \times 200$ corresponding to a spatial resolution of 10^{-2} pc. The boundary conditions were periodic in the directions perpendicular to the ionization propagation direction, imposed where the flux is incoming and free flow at the opposite. Ionization processes introduced in subsect. 3.3 were taken in the plane-parallel limit. A movie of the time evolution of case (c) (see Fig. 4.4) is available online[1]. The snapshots around 500 ky show that the narrower the initial structures, the longer the resulting pillars. With a (base width)/heigh ratio (w/h ratio hereafter) of 0.5, we obtained a structure whose size was almost multiplied by 3.5 in 500 ky. In addition to this, the initial structures have less and less mass with decreasing widths and still manage to form longer pillars, as can be seen in Fig. 4.4. High densities, or high initial mass, are not needed to form structures that are going to resist the ionization. The important factor here is how matter is distributed in space and interacts with the propagating shock. Very little and low-density material, well distributed in space, can result in a long pillar-like structure. We will call these structures pillars hereafter, but a detailed comparison with observations is needed to see whether these structures emerging from idealized scenarii are a good approximation of the reality or not.

---

[1] `https://sites.google.com/site/astrohep/movies/pillar`

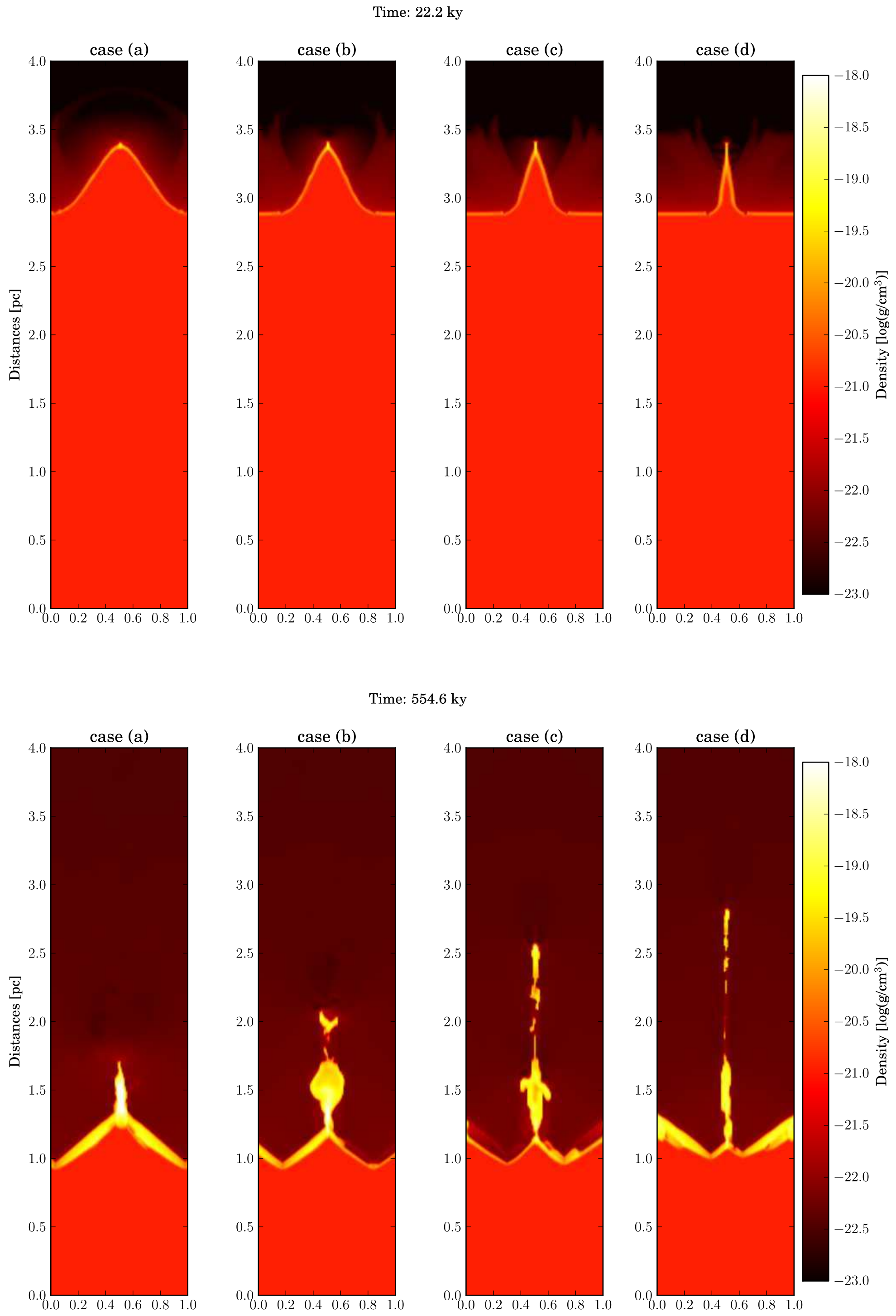

Figure 4.4: Density cuts of four simulations of an ionization front propagation with a modulated interface. The UV flux at the top of the box is 10^9 photons per second per square centimetre, the box is 4x2x2 pc^3 (half of the cut is shown). The dense gas is initially at 500 $\mathrm{H/cm}^3$ at a temperature around 25 K (thermal equilibrium from Fig. 4.1). The (base width)/(height) ratios of the modulations are respectively 2 for case (a), 1.4 for case (b), 0.9 for case (c) and 0.5 for case (d).

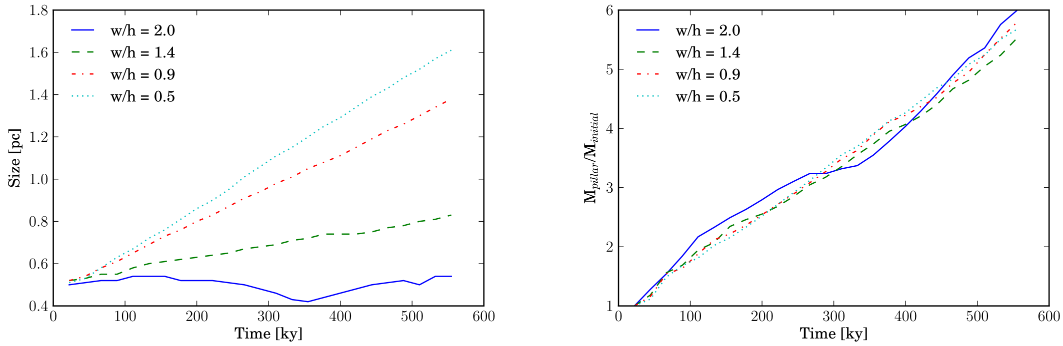

Figure 4.5: Monitoring of the size (left) and the mass (right) of pillars identified in Fig. 4.4. The size is calculated by the difference of the average position of the ionization front and its position at the centre of the y-z plane (head of the initial structure). The mass is calculated in a box between the two vertical positions that are defined to calculate the size and whose width is defined by the width of the initial structure and is normalized by the mass in the initial modulation.

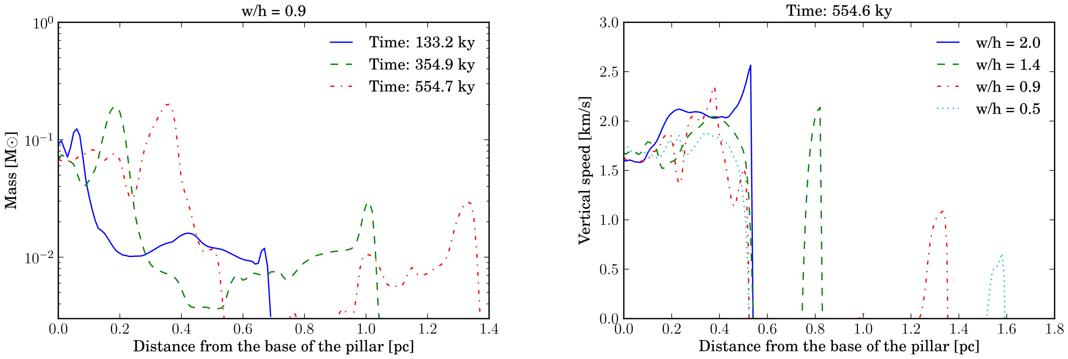

Figure 4.6: Mass profiles (left) and vertical velocity profiles (right) at three different times of the pillar in the w/h = 0.9 simulation. These profiles were obtained within the boxes defined in Fig. 4.5

.

To study the properties of the pillars, we monitor their sizes and masses in Fig. 4.5. The size gain identified previously is a continuous process in time at an almost constant speed which depends very strongly on the width/heigh ratio. Narrow initial modulation have a very fast growth while larger one grow slowly, if at all. The mass increase relative to the initial mass of the structure is almost the same in all simulations and does not seems to depend on the initial w/h ratio. It reaches a factor of 5-6 in 500 ky.

Vertical profiles of the mass in the pillars (see Fig. 4.6) show that the mass gain identified in Fig. 4.5 is accumulated at the base. The mass of the head of the pillar slightly increases and then remains stable during the simulation while the central part connecting the head and the base is stretched and its mass decreases. The profiles of the vertical speed show that the bases of the pillars have a roughly constant speed and that the size variations are caused by the vertical speed difference of the heads. The differences between the size of the pillars can be directly deduced from the velocity differences of the heads: a velocity difference of 0.5 km/s during 500 ky gives a spatial difference of 0.25 pc, which is approximatively the differences observed between the simulations with a width/heigh ratio of 2 and the one with a ratio of 1.4.

A closer look at the simulations (see Fig. 4.7) shows that the motions perpendicular

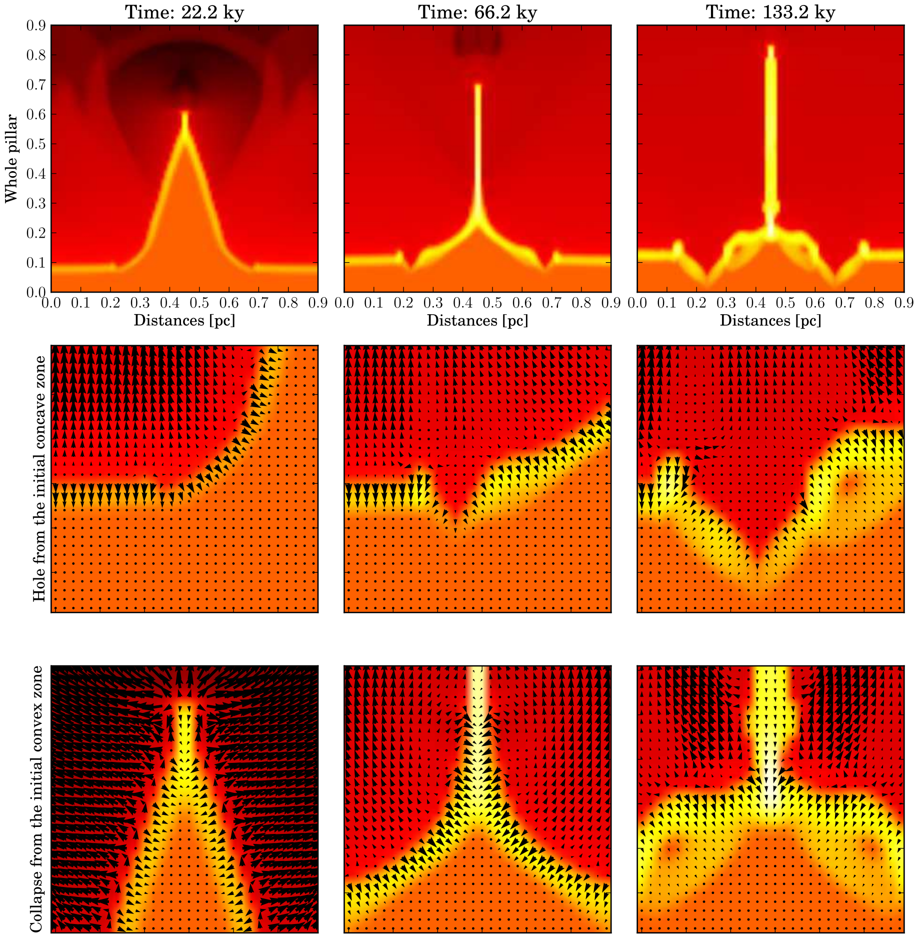

Figure 4.7: Zoom on the ionization of convex and concave zone in the w/h = 0.9 simulation between 22 and 132 ky. Arrows represent the velocity field projected in the x-y plane.

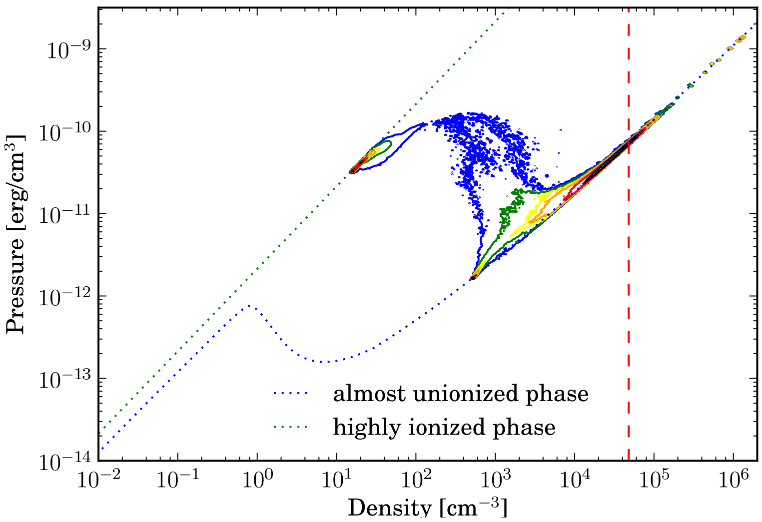

Figure 4.8: Two-dimensional plot of the mass fraction at a given density and pressure for the w/h = 0.9 simulation at the end of the simulation (554 ky). Blue to black contours are increasing mass fraction contours (blue: 1E-6, green: 1E-5, yellow: 5E-5, orange: 1E-4, red: 5E-4, black: 2E-3). The dashed red line is the maximum density achieved in a plan-parallel 1D simulation : 4.8×10^4 cm^3. The total mass at a density above this limit is around 10 solar masses.

to the propagation direction are shaping the structures. These motions are triggered by the initial curvature of the structure, two cases are distinguished, an initially convex zone and a initially concave zone. A shock front in a convex zone will trigger its collapse; this is the phenomenon that takes place in the radiation-driven-implosion scenario and here at the head of the initial structure. The curvature of the initial structure leads to lateral converging shocks that collide with themselves. However, the ionization of a concave zone is quite different, it will dig a hole in the medium, and the gas is pushed away lateraly. The velocity fields in Fig. 4.7 illustrate these phenomena; for an initially convex zone the velocities point inwards and lead to the collapse of the central structure, whereas in the initially concave zone at the base, they point outwards and dig a hole in the media. These phenomena are at the origin of the size and mass increase. Indeed, the collapse of the structure takes more time if the structure is wide, therefore it will be accelerated longer, which explain the difference of the vertical speed of the pillar heads seen in Fig. 4.6. Additionally, the holes in each side of the pillar (see Fig. 4.7) gather the gas at the base of the pillar, which explains the mass increase in Fig. 4.6.

In addition to the mass increase there is an important density gain. The mass histogram in the pressure-density plane in Fig. 4.8 shows that the compression caused by the heating from UV radiation increases the pressure by one order of magnitude from the initial state, which is at a density of 500 cm^3 and at a pressure of 10^{-12} erg/cm^3. The gas is then distributed in two phases at equilibrium, hot-ionized in the green-dashed straight line and cold-dense-unionized in the blue dashed curve. The gas in transition between them is depicted with the blue contour. A 1D simulation of the collect-and-collapse process can increase the density by up to 5×10^4 cm^3; this limit is drawn with the red dashed line in Fig. 4.8. The mass at the base of the pillar, caused by the holes from the initial concave parts and from the collapse of the lateral shocks, leads to a density enhancement of 1-2 orders of magnitude. Although the structures in our simulations are still slightly below their Jeans lengths, this process has a better chance to trigger star formation at the base of the pillars than the simple collect-and-collapse scenario.

4.2.2 From density modulations to pillars

Clouds have irregular shapes, but they also have unhomogeneities. Therefore, after this study of interface modulations, we considered density modulations that we call clumps hereafter (with no reference to an observational definition). We define them as regions of constant overdensity. Figure 4.9 shows the different cases we studied. The three first cases are clumps in a homogeneous cold cloud, with a density contrast of 2, 3.5 and 5 respectively. The last one corresponds to the radiation-driven-implosion scenario, where the clump is "isolated" in a hot low-density medium so that the shock forms directly in the structure. The density in the clump is the same as the one with a density contrast of 5. In all cases the clumps are at pressure equilibrium with the surrounding matter.

In the isolated case the shock forms at the surface of the clump and the shell is therefore initially curved by the shape of the clump with a w/h ratio of 2. This roughly corresponds to the wider case studied in sect. 4.2.1. Because the shock is curved, it will collapse on itself and form a pillar-like structure. This case was studied in detail by *Mackey and Lim* (2010); *Gritschneder et al.* (2009). However, with a width/heigh ratio of 2 the structure is quite small and looks quite similar to the w/h=2 case of the previous section. However, because it is isolated, the accumulation of mass process at the base identified in the previous section cannot take place.

In the three other cases, the shell is flat when it is formed, therefore the outcomes of the simulations are not as clear. When the clump is not sufficiently dense (first case $nH_{clump}/nH_{cloud}=2$), it does not curve the shell enough to trigger lateral colliding shocks. Therefore there is no head in the final structure in this case, which is very small (i.e comparable to the initial clump size). In the two other simulations ($nH_{clump}/nH_{cloud}=3.5$ and 5) the clumps curve the shell enough to trigger the collision of vertical shocks, thereby forming an elongated pillar. This is very close to what we observed previously in interface modulations. Besides, we can identify a base for the pillar-structures in the final snapshots that is formed by lateral holes in the cloud and the associated accretion mass process discussed previously.

The importance of the curvature effect can be emphasized by comparing the isolated case and the $nH_{clump}/nH_{cloud}=5$ case. In both cases the density of the clump is the same, but when the shell is formed flat on a homogeneous medium, the dense clump will resist the shock to form an elongated modulation on the shock surface. In the isolated case, the shock is formed instantaneously curved on the structure with a w/h ratio of 2. Furthermore, contrary to the isolated case, the structures will grow in mass and size because of the connection with the cloud. These effects result in a final 0.5-parsec-long pillar for the isolated case, whereas the final structure in the $nH_{clump}/nH_{cloud}=5$ case is 1.5 parsec long. The driving process to form a pillar is the ability of the matter distribution to first curve the shell and then to feed the base of the pillar by the hole mechanism identified in sect. 4.2.1 (the holes are clearly visible in the final snapshots in Fig. 4.9).

The size evolution and the mass evolution of the pillars are comparable to the modulated-interface case. However, the evolution is not linear because of the initial conditions. Indeed, there is a first phase in which the ionization front is curved and stretched vertically around the clump when its propagation is slowed down by the overdensity. At this point (around 200 ky) the physical situation is comparable to the interface-modulated case, the ionization front is curved around a "hill". It also explains why we chose to do a longer simulation for the density-modulated case, it allows us to compare both cases at a "physically equivalent" state at the end. When the lateral shocks collide around the hill, the pillar captures slightly more than the mass of the initial clump and its mass increase slows down. This phase occurs around 300 ky and can be clearly identified in Fig. 4.10. Then the mass

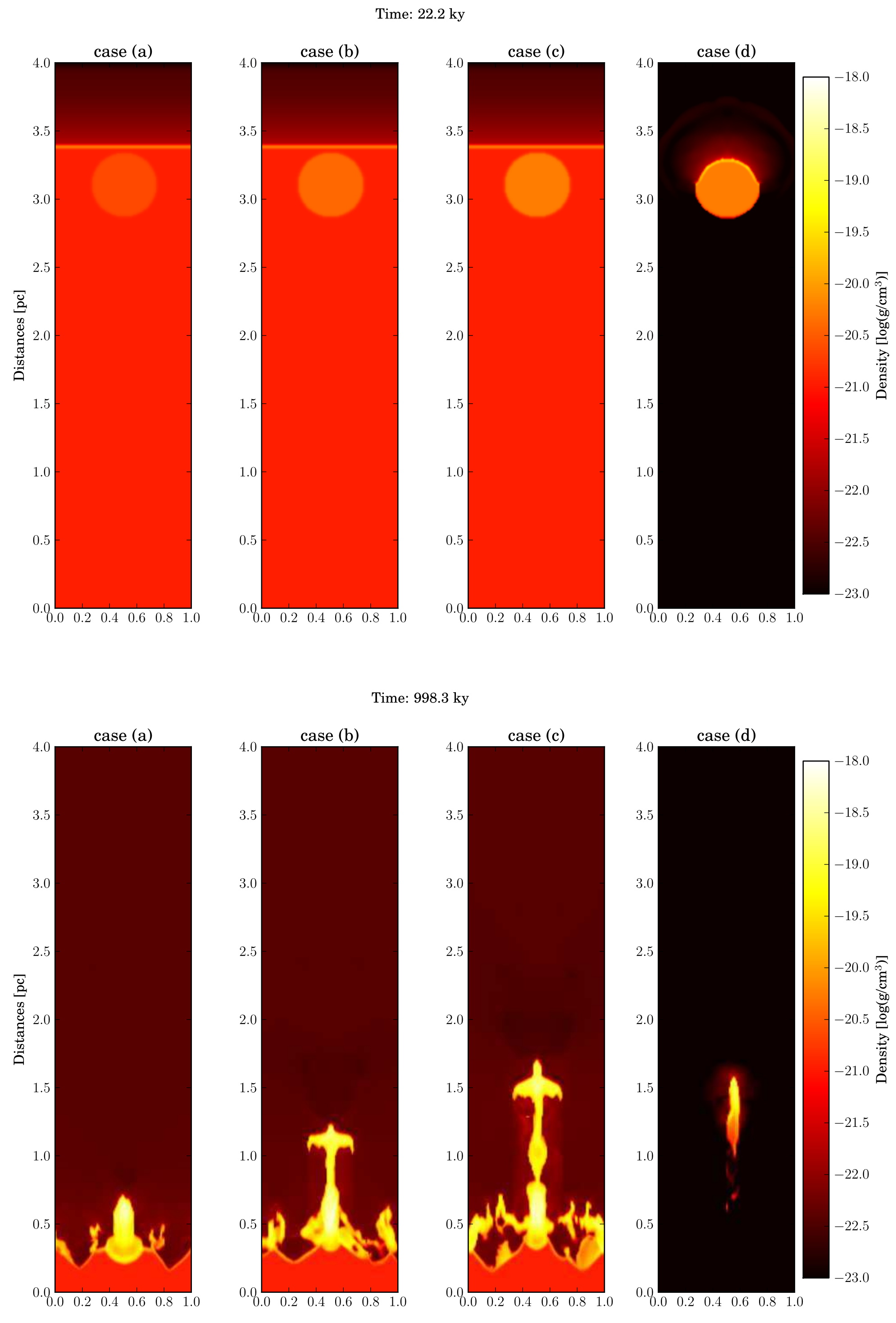
Time: 22.2 ky

Time: 998.3 ky

Figure 4.9: Density cuts of four simulations of an ionization front propagation on clumps (0.5 parsec in diameter). The UV flux at the top of the box is 10^9 photons per second per square centimetre, the box is 4x2x2 pc^3 (half of the cut is shown, only the central parsec of the simulation box). The last simulation (case(d)) is an isolated spherical clump of constant density 1000 cm^3, the three others are clumps in a homogeneous medium of density 500 cm^3. The clumps have densities of 1000 for case (a), 1750 for case (b) and 2500 cm^3 for case (d).

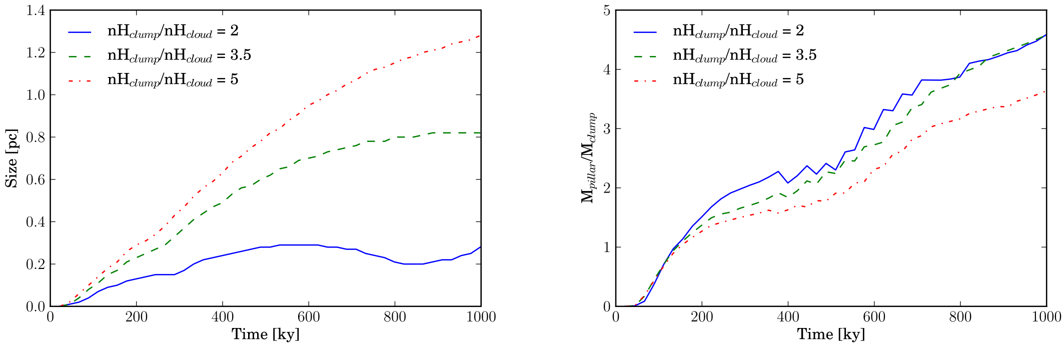

Figure 4.10: Monitoring of the size (left) and the mass (right) of pillars identified in Fig. 4.9. The size is calculated by the difference of the average position of the ionization front and its position at the centre of the y-z plane (head of the initial structure). The mass is calculated in a box between the two vertical positions that are defined to calculated the size and whose width is defined by the width of the initial structure and is normalized by the mass of the initial clump.

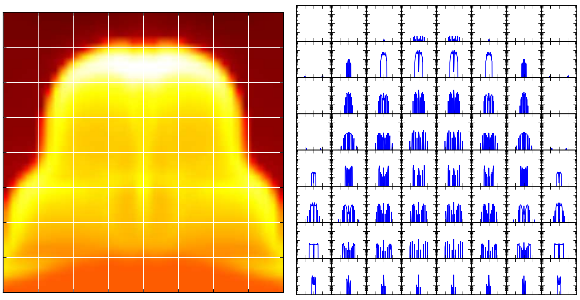

Figure 4.11: nH$_{clump}$/nH$_{cloud}$=5 simulation at t=222 ky. Left: column density on a 0.4x0.4x0.4 pc^3 box around the pillar structure in a face-on geometry. Right: mass-weighted histogram of the line-of-sight velocity in the same box (similar to optically-thin observational line spectra). Each spectrum is made on a square of 0.05x0.05 pc^2 drawn on the column density map. The spectra are drawn between -4 and 4 km/s in 80 bins (horizontal axis) and the mass between 10^{-4} and 1 solar mass (vertical axis in log scale). The lateral shocks can be clearly identified in the double wing spectra, which leads to a very broad line width.

increases because of the accumulation of matter at the base of the pillar. The process is less linear than in the interface-modulated case.

4.3 Observational signature

The two sections above present how pillars can be formed in a density- or interface- modulated region of the molecular cloud. These pillars are connected to the cloud, increasing in size and mass with time. However, these variations cannot be observed. A potentially observational signature to study is the structure of the line-of-sight velocity. We used the same method as *Gritschneder et al.* (2010). We defined a grid of squares of 0.05x0.05 pc^2 along the pillar and binned the line-of-sight velocity in each square (see Fig. 4.11, 4.12 and 4.13). We used the simulation with the densest clump to study the line-of-sight velocity structure, but the following results are generic. At t=222 ky (Fig. 4.11), the lateral shocks can be clearly identified in the broad line spectrum. There are two components, a positive one coming towards us and a negative one going away. At this time the

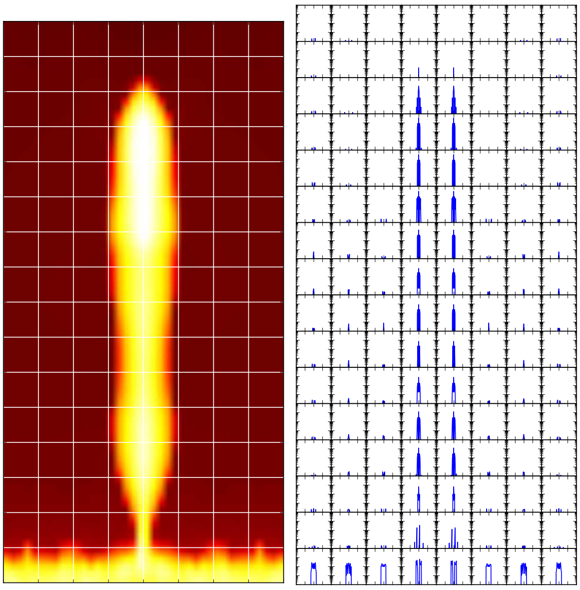

Figure 4.12: nH_{clump}/nH_{cloud}=5 simulation at t=444 ky. Same plots as Fig. 4.11. The lateral shocks collided and cannot been identified anymore.

shell is curved around a hill, which is comparable to the situation we encountered in the interface-modulated scenario after a short time.

At t=444 ky (Fig. 4.12) the lateral shocks have collided, which results in a narrow line width for the histograms. The whole pillar is narrow and evacuates the pressure through radiative cooling and expansion to reach the equilibrium defined for the cold phase in Fig. 4.8. There are two dense parts in the pillar: the head in which the matter of the clump has been accumulated and the base at the point where the lateral shocks have closed. It will resist the ionization because it is dense enough and matter is starting to accumulate at the base.

At t= 998 ky (Fig. 4.13) matter has accumulated at the base of the pillar based on the process that was identified in Fig. 4.7. The line-of-sight velocity histograms still have a narrow line width compared to Fig.4.11. This phenomenon is not specific to clump simulations, the same analysis on the interface modulated simulation (aspect ratio of 0.9) in Fig. 4.14 and Fig. 4.15 shows similar results but at an earlier stage. The interface modulated simulation presents double-wing velocity spectra around t=22.2 ky, whereas the clumpy simulation presents these spectra around t=222 ky when the shock is curved around a hill. The double-wing structure of the velocity spectra is therefore a signature of the lateral shocks that are going to collide and a signature of the early stage of a forming pillar.

The previous analysis can be applied to the different simulations presented in this paper without noticable change to our conclusion. We also changed some physical conditions and parameters. We added a constant external gravitational field, included self-gravity, doubled the resolution without general changes in the morphology of the final structures. We also changed the flux to a higher value (from 10^9 to 5×10^9 photons/s/cm^2) and the structures are similar, but evolve faster, as seen by *Gritschneder et al.* (2009). The shell speed c_{shell} is proportional to $F_\gamma^{1/4}$ (see Eq. 4.1), therefore when the flux is multiplied by five the shell increases speed by 50%, and the whole simulation evolves faster by 50%. In all these situations, pillars form through the lateral collision of a curved shocked surface, and the double-wing spectrum is always visible before the shocks collide.

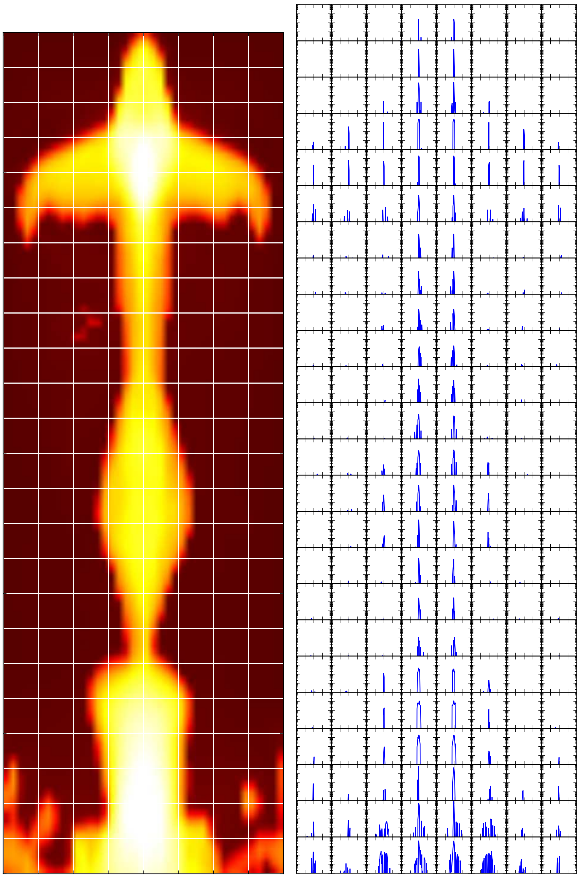

Figure 4.13: nH_{clump}/nH_{cloud}=5 simulation at t=998 ky. Same plots as Fig. 4.11. The line width is very narrow compared to the snapshots at t=222 ky.

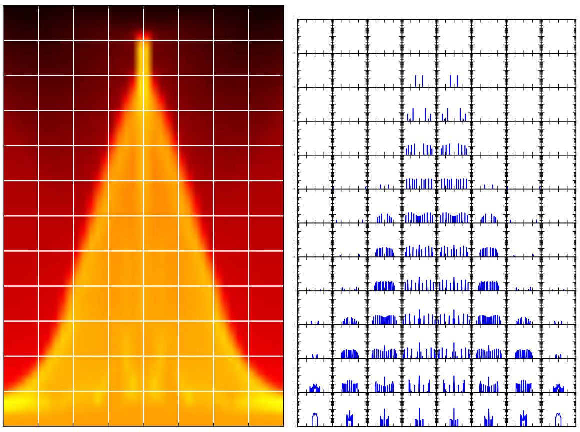

Figure 4.14: w/h=0.9 simulation at t=22.2 ky (first column in Fig. 4.7). The shock just formed on the modulation, the line width and the double-wing structure is comparable to Fig. 4.11

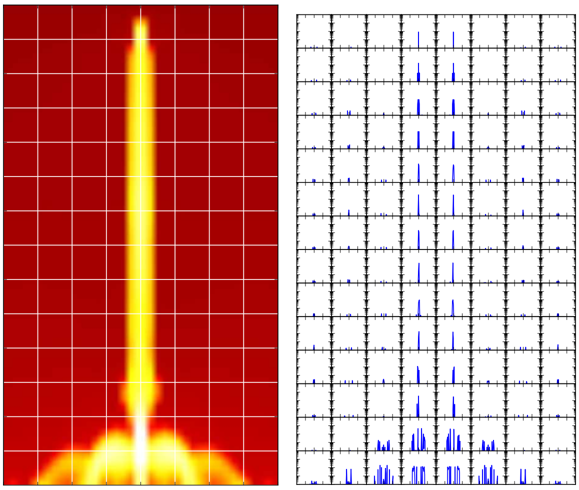

Figure 4.15: w/h=0.9 simulation at t=133.2 ky (third column in Fig. 4.7). The shock collided laterally and the line width is narrow as in Fig. 4.12

4.4 Conlusion and discussion

We have presented a new scenario for the formation of structures at the edge of H II regions and have shown that

i A curved shock ahead of an ionization front can lead to a pillar if it is sufficiently curved to collide laterally with itself.

ii This pocess is very efficient for forming stable growing pillars, and the narrower the initial structure, the more curved the front and the longer the pillar.

iii Lateral gas flows can result in a density enhancement at the base of the pillars of 1-2 orders of magnitude compared to the-collect and-collapse scenario.

iv When the shock is first formed flat, it can be curved by sufficiently dense clumps and leads to pillars. In isolated clumps (radiation-driven implosion) the shock is naturally curved by the form of the clump, but the resulting structure has a constant size and mass.

v The double-wing line spectra of the line-of-sight velocity is a signature of the lateral collision of the shock, and hence is a signature of the early stage of a pillar formation. It can be used as an observational signature for this new scenario.

Various aspects of shocks orientation have been considered by other authors. Oblique shocks have previously been studied by *Chevalier and Theys* (1975) and cylindrical shocks by *Kimura, Toshiya and Tosa* (1990). These effects have also been explored in the context of 2D turbulent simulations (see *Elmegreen et al.*, 1995). However, these studies focused on the effects of curvature on clump enhancement. In this work, we have shown that shocks need to be sufficiently curved to collide with themselves in order to form a pillar-like structure.

At the edge of H II regions the structure of the line-of-sight velocity can be investigated using radiotelescopes and suitable molecules that trace the dynamic to detect the double-wing spectra on gas hills and thus nascent pillars. If a gas overdensity is detected at the top of the hill (e.g. using Herschel data), the shock curvature could be attributed to the presence of an initial clump, if not to the curvature of an initial interface.

We generated curved shocks using either density or interface modulations on a parsec scale and in a very simplified situation. However, we expect that the physical processes discussed in this chapter can also be applied to more realistic situations where the ionization front interacts with a turbulent interstellar medium. In this case the density fluctuations are much more complex, but the same mechanism should be at work to describe pillar formation. These turbulent situations will be studied in the next chapter in which we will study the interplay between shock curvature and turbulence to see its impact on star-formation rates at the edge of H II regions.

Bibliography

Audit, E., and P. Hennebelle (2005), Thermal condensation in a turbulent atomic hydrogen flow, *A&A*, *433*(1), 1–13, doi:10.1051/0004-6361:20041474. 58

Bisbas, T. G., R. Wünsch, A. P. Whitworth, D. A. Hubber, and S. Walch (2011), Radiation-driven Implosion and Triggered Star Formation, *ApJ*, *736*, 142, doi:10.1088/0004-637X/736/2/142. 60

Chevalier, R. A., and J. C. Theys (1975), Optically thin radiating shock waves and the formation of density inhomogeneities, *ApJ*, *195*, 53, doi:10.1086/153303. 71

Elmegreen, B. G., and C. J. Lada (1977), Sequential formation of subgroups in OB associations, *ApJ*, *214*, 725, doi:10.1086/155302. 59, 60

Elmegreen, B. G., T. Kimura, and M. Tosa (1995), Sequential Star Formation in OB Associations: The Role of Molecular Cloud Turbulence, *ApJ*, *451*, 675, doi:10.1086/176253. 71

Gritschneder, M., T. Naab, A. Burkert, S. Walch, F. Heitsch, and M. Wetzstein (2009), iVINE - Ionization in the parallel tree/sph code VINE: first results on the observed age-spread around O-stars, *MNRAS*, *393*(1), 21–31, doi:10.1111/j.1365-2966.2008.14185.x. 60, 66, 69

Gritschneder, M., A. Burkert, T. Naab, and S. Walch (2010), Detailed Numerical Simulations on the Formation of Pillars Around H ii Regions, *ApJ*, *723*(2), 971–984, doi:10.1088/0004-637X/723/2/971. 60, 68

Kimura, Toshiya, and M. Tosa (1990), Fragmentation of a converging shock, *MNRAS*, *245*, 365–369. 71

Mackey, J., and A. J. Lim (2010), Dynamical models for the formation of elephant trunks in H II regions, *MNRAS*, *403*, 714–730, doi:10.1111/j.1365-2966.2009.16181.x. 60, 66

Spitzer, L. (1978), *Physical Processes in the Interstellar Medium*, Wiley-VCH. 60

Wolfire, M. G., D. Hollenbach, C. F. McKee, A. G. G. M. Tielens, and E. L. O. Bakes (1995), The neutral atomic phases of the interstellar medium, *ApJ*, *443*, 152, doi:10.1086/175510. 58

Wolfire, M. G., C. F. McKee, D. Hollenbach, and A. G. G. M. Tielens (2003), Neutral Atomic Phases of the Interstellar Medium in the Galaxy, *ApJ*, *587*(1), 278–311, doi:10.1086/368016. 58, 59

Chapter 5

Turbulence and globule formation

> *Man muß noch Chaos in sich haben, um einen tanzenden Stern gebären zu können.*
> *Also sprach Zarathustra, Friedrich Nietzsche*
> *Translation: You need chaos in your soul to give birth to a dancing star.*

In this chapter, we investigate the interplay between the ionization radiation from massive stars and the turbulence inside the surrounding molecular gas. We used HERACLES to model an initial turbulent medium that is ionized and heated by an ionizing source. Three different simulations are performed with different mean Mach numbers (1, 2 and 4). We used the non-equilibirum model for the ionization and the associated thermal processes presented in Chap 3. This revealed to be crucial when turbulent ram pressure is of the same order as the ionized-gas pressure.

The density structures initiated by the turbulence cause local curvatures of the dense shell formed by the ionization compression. When the curvature of the shell is sufficient, the shell collapse on itself to form a pillar while smaller curvature leads to the formation of dense clumps that are accelerated with the shell and therefore remain in the shell during the simulation. When the turbulent ram pressure of the cold gas is sufficient to balance the ionized-gas pressure, some dense-gas bubbles have enough kinetic energy to penetrate inside the ionized medium, forming cometary globules. This suggests a direct relation in the observations between the presence of globules and the relative importance of the turbulence compared to the ionized-gas pressure. The probability density functions present a double peak structure when the turbulence is low relative to the ionized-gas pressure. This could be used in observations as an indication of the turbulence inside molecular clouds.

5.1 Numerical methods

We used the numerical methods described in Chap. 3 and 4 to model the molecular cloud and the ionization coming from the OB cluster. In addition to the physics Chap. 4, the turbulence in the cloud is modeled using the turbulence module described in *Schmidt et al.* (2006) and *Schmidt et al.* (2009). Gravity is an important ingredient for ultra-compact H II region (e.g. *Peters et al.*, 2010), however we are interested in large scale H II regions (e.g. the Rosette Molecular cloud, *Schneider et al.* (2010). Self-gravity and the gravity from the ionizing source were considered in Chap. 4 without noticeable change on the formation of the structures. Therefore we do not consider gravity in the present study.

First, recall the model we used for ionization is an out-of-equilibrium model solving the equations

$$d(F_\gamma)/dx = -n_H(1-X)\sigma_\gamma F_\gamma + \delta_0(x)S_*$$

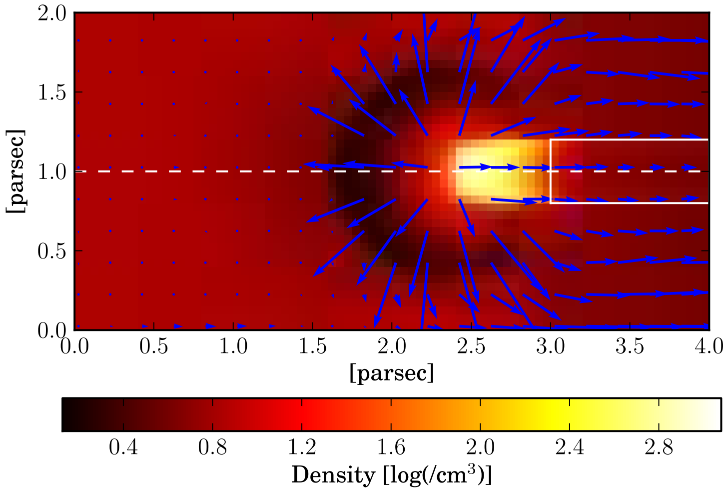

Figure 5.1: Cut of the density field and velocity field in the radiation driven implosion of a clump inside an ionized medium. The gas behind the clump in the white box is out of equilibrium and recombines slowly. The gas at the front of the clump is escaping by the rocket effect and is cooled down by the strong expansion.

$$\begin{aligned} d(Xn_H)/dt &= I - R = n_H(1-X)\sigma_\gamma F_\gamma - \beta X^2 n_H^2 \\ de/dt &= I \times e_\gamma - R \times k_b T/(\gamma - 1) \end{aligned} \tag{5.1}$$

in which X is the ionization fraction (advected with the hydrodynamic), F_γ is the photon flux, S_* the source term, n_H the total hydrogen density, σ_γ the cross-section for ionization, I the ionization rate, R the recombination rate, β is given by $2 \times 10^{-10} T^{-0.75}\text{cm}^3/\text{s}$, e is the internal energy of the gas, e_γ the energy transferred from the ionizing photons to the electrons and T the temperature of thermal equilibrium between all the species. The first equation is the ray tracing of the ionizing photons coming from the source. The second one is the ionization/recombination photo-chemistry evolution and the third one is the thermodynamic evolution associated. 1D and 3D tests of the out-of-equilibrium ionization and recombination processes are performed in Sect. 5.2.

The turbulent forcing is modeled by an Ornstein-Uhlenbeck process in Fourier space. For each mode of the force field, random increments with a Gaussian distribution are added after each time step. The wave-numbers of the forcing modes are in the interval $[0, 2k_0]$, where k_0 is given by the typical length scale of the forcing, $L = 2\pi/k_0$ with $L = 4$ pc, the size of the box in our case. By projecting the modes in transversal and longitudinal directions with regard to the wave vectors, divergence-free and rotation-free components are produced in physical space. The resulting force field is statistically homogeneous, isotropic, and stationary. The RMS magnitude is of the order of V^2/L, where V is the characteristic velocity of the flow. We will perform three simulations with V resulting in stationary transonic and supersonic velocity: Mach 1, 2 and 4. The turbulence used is solenoidal with a ratio of compressive forcing power to the total forcing power of 10 %.

Three turbulent scenarii are investigated in Sect. 5.3, a transonic turbulent molecular cloud (mean Mach number around 1) and two supersonic cases (mean Mach number of 2 and 4). The box is a cube of 4 parsecs at a resolution of 0.01 pc (400^3), the mean density is 500 cm^{-3} and the temperature is initially at 25 Kelvin. During the turbulent evolution, the boundary conditions are periodic. The simulations are run until a statistically steady state is obtained, i.e. a constant mean Mach number in the box. Then, we turn on the ionization with a flux of 10^9 photons per second per squared centimeter, which is the typical flux of

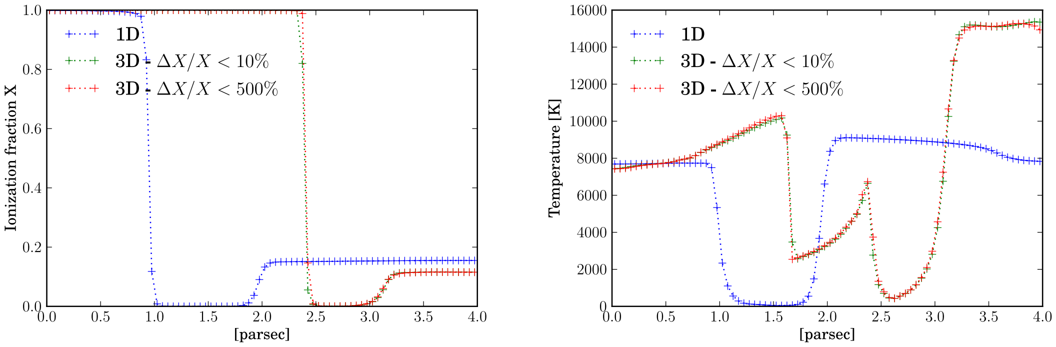

Figure 5.2: 1D and 3D simulations of an isolated clump inside a completely ionized medium exposed to an ionization flux of 10^9 photons per second per squared centimeter. Note that in the 1D simulation the clump is in fact an infinite slab. Top: ionization profile through the middle of the box at t = 500 ky. Bottom Temperature profile at T = 500ky. The ionization source is at x = 0 parsec. In the 1D simulation the clump is located at x = 1.5 parsec while in the 3D simulations it is at 2.75 parsec. The two 3D simulations show that it is not needed to limit too much the variation of the ionization fraction. The gas behind the clump is in the shadow and is therefore being recombined. Its recombination time is long and is not at equilibrium. These simulations also show the importance of the 3D effects on the temperature structure.

an O4 star at 30 parsecs. The ionization is coming from the top of the box and this face is changed to reflexive boundary condition for the hydrodynamics while the opposite side is set to free flow. The turbulent stirring is kept during the ionization phase. Some runs were done without the turbulence maintained without noticeable change, the large-scale modes do not have time to influence the small scales during the ionization phase. In Sect. 5.3, we investigate the interplay between turbulence and ionization for the three different simulations.

5.2 Tests of the out-of-equilibrium ionization and recombination processes

When turbulence is included in an ionization simulation, the main difference is the possibility that some ionized gas gets into the shadow of the dense unionized gas because of the mixing. This is typically an out-of-equilibrium state for the ionized gas that will begin to recombine. To study this state, we investigate simplified set-ups in which hot ionized gas is put in the shadow of dense cold gas and therefore will be out of equilibrium. We simulate the impact of ionization on a clump (D_{clump}=0.5 parsec) inside an homogeneous ionized medium (see Fig. 5.1). We also perform an "equivalent" 1D simulation where the clump will be an infinite slab, to identify the effect of the geometry. The gas in the shadow of the clump/slab will start to recombine since it is out of equilibrium. The typical recombination time for the ionized gas is given by $1/\beta n$ that is of the order of 10^4-10^5 years for ionized gas at a density of 1-10/cm^3. It is of the order of the gas dynamical time: $D_{clump}/c_{io} = 10^5$ years, in which c_{io} is the sound speed of the ionized gas. Therefore an out-of-equilibrium model is needed to treat this state of the gas. We studied first the profile of the ionization fraction and the effect of the limited-variation time-stepping and then the structure of the temperature in these tests.

Our method solves the two first equations in Eq. 5.1 implicitly while the thermal balance is solved explicitly and is sub-cycled to limit the variation of T. Usually the variation

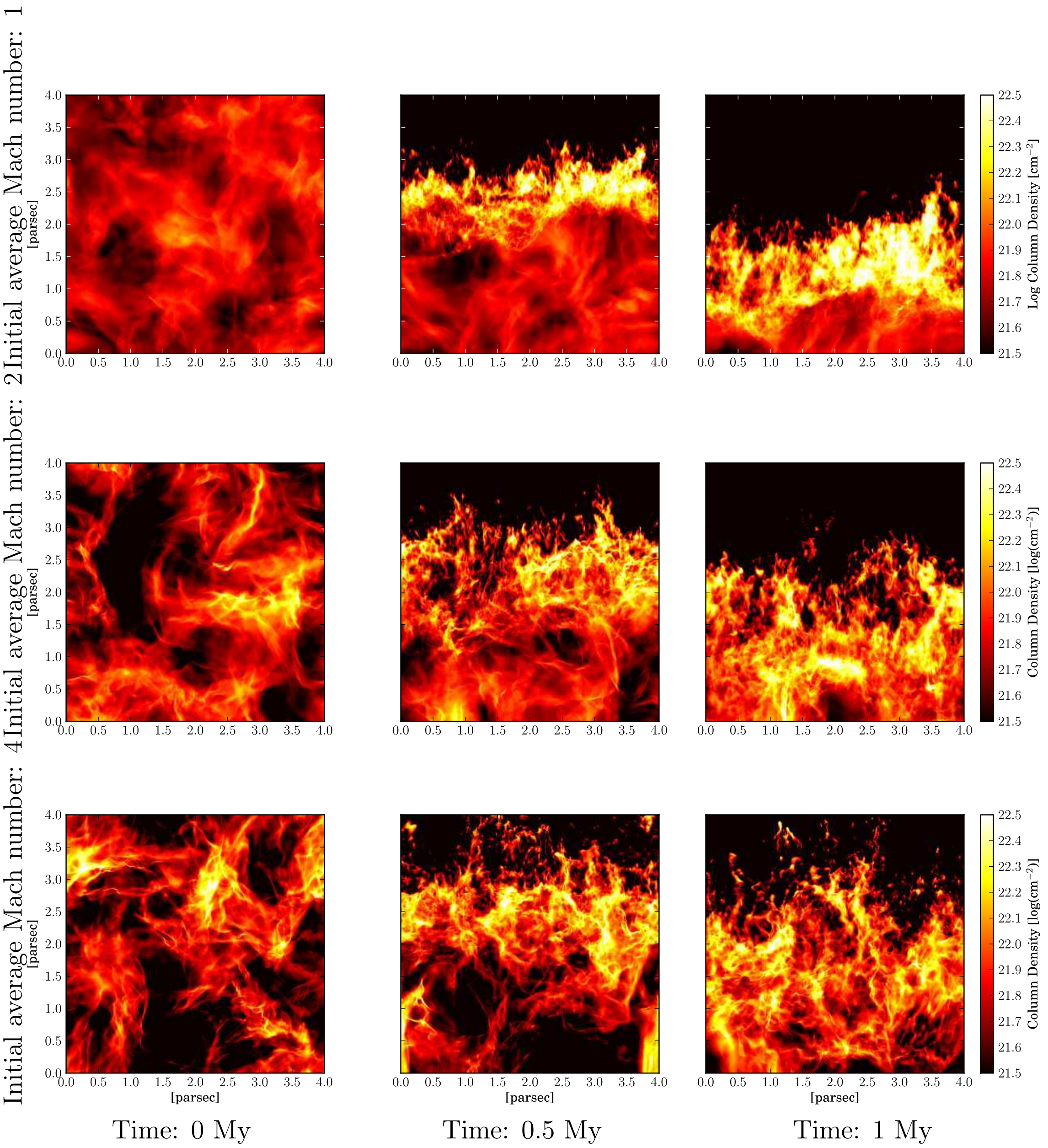

Figure 5.3: Column density snapshots of the three turbulent simulations (row 1: Mach 1, row 2: Mach 2, row 3: Mach 4) at three different times (column 1: before ionization starts, column 2: 500 ky after ionization is turned on, column 3: 1 My).

of X is limited at 10 % in the implicit step. However, it is often not needed to limit that much the variations. The ionization-fraction and the temperature profiles are plotted in Fig. 5.2, after 500 ky of evolution and for limited variations of 10 and 500 % and there is almost no difference between the two. At the front, the equilibrium for ionization is reached even with long time-step thanks to the implicit method, the ionization fraction is nearly at one. At the back, the recombination time of a hot ionized plasma is quite long. For example in our case the recombination time is of the order of 100 ky which also explains why the ionization fraction is still around 0.2 after 500 ky. Therefore it is possible to allow long time-steps.

We now investigate the temperature structure. The 3D profiles in Fig. 5.2 are taken through the middle of the box (the white-dashed line in Fig 5.1), thus through the middle of the clump, which is located between 2.5 and 3 parsecs. In the 1D case, the clump is a slab located after 500 ky between 1 and 2 parsecs. The difference of position between the two is easy to understand: in the 1D case, the ionized material cannot be evacuated on the side, the column density in front of the ionization front is higher. There are only a few ionization processes occurring at the ionization front, the dynamics is dominated by the expansion of the gas evaporating from the slab. In the 3D case, the ionized gas is escaping on the side of the clumps, therefore ionization can penetrate further inside the clump and can deposit more energy. As a consequence, the clump is pushed further away by rocket motion and the energy deposit at the surface of the clump leads to a high expansion of the ionized gas and to a shock surface that can be seen in Fig. 5.1. The ionized gas is cooled down to 3000-6000 Kelvin by the expansion at the front.

The temperature structure is also quite different behind the clump (white box in Fig. 5.1) because of the shadowed recombination. In the 1D simulation, the thermal equilibrium is reached at the front, in the HII region.Behind the slab, the gas is not at equilibrium and recombines. The ionization fraction is decreasing from 1 to 0.2. The pressure drops by nearly a factor of 2 when the ionization fraction decreases from 1 to ≈ 0.2. Moreover, most of the energy emitted during the recombination process is radiated away by the cooling, so that the temperature of the gas does not vary much, increasing only slightly, from $\approx$ 8000 K to $\approx$ 9000 K. The temperature structure is quite different in 3D as shown in Fig. 5.2. The cooling by recombination behind the clump should decrease the pressure of the gas as in the 1D case. However in 3D, it leads to lateral gas flows from the hot ionized gas, exposed to the radiation, to the hot recombined gas in the shadow. Therefore the recombination behind the clump is done more or less at constant pressure leading to an increase in temperature behind the clump, which is surprising at first sight.

This simple test shows that the equilibrium assumption for ionization is invalid when hot ionized gas gets in the shadow of dense unionized gas (Ionization fraction of 20 % instead of 0). The equilibrium assumption is usually justified by the fact that the recombination time is much shorter than the dynamical time. This is usually true in the HII region, however this is not the case at the interface between the HII region and the cold gas when turbulence is included. Indeed, especially at high level of turbulence, hot ionized gas will be mixed with cold dense gas and therefore will be in the shadow of the cold gas, exactly in the situation we studied in this simplified test. The ionization equilibrium is not reached for a non-negligible part of the ionized gas that can get in the shadow of dense unionized gas. This is especially the case when the level of turbulence is sufficient to balance the ionized-gas pressure and to mix the unionized and ionized phases as we will see in the next section.

5.3 Turbulent simulation

5.3.1 Transonic turbulence

The first line of Fig. 5.3 presents three snapshots of the column density for the transonic simulation, when ionization is turned on, 500 ky and 1 My after ionization has started. The hot ionized gas expands in the cold turbulent medium and triggers the propagation of a shock ahead of the ionization front. This is the collect part of the classical collect and collapse scenario (*Elmegreen and Lada*, 1977) and this is observed in many regions (see *Zavagno et al.*, 2010; *Thompson et al.*, 2011; *Deharveng et al.*, 2010). The 500-ky snapshot clearly shows a three-phase medium with the hot ionized gas at the top, the shocked dense region and the unperturbed cold cloud. The shocked region is apparently 0.5-1 parsec wide at 500 ky and gets wider in time, up to 1.5 parsec at 1 My. This width is a lot larger than one would expect from the collect process in a homogeneous medium. The typical width of the dense shell is 0.1 parsec in this case. However, Fig. 5.4 clearly shows that the

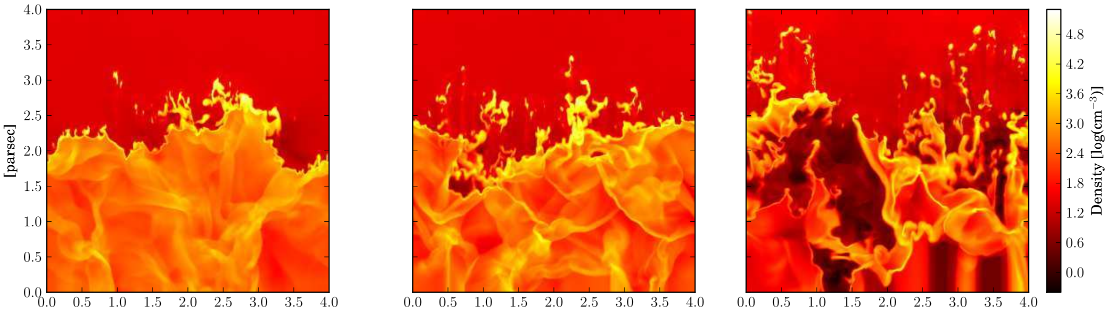

Figure 5.4: Density cuts through the three different simulations at t = 500 ky. Left: Mach 1, middle Mach 2 and right Mach 4.

real thickness of the shell is indeed of order 0.1 parsec but, contrary to the collect process in a homogeneous medium, the shell is not flat but highly curved. Therefore the column density plots show a wide shocked region just by projection effects of this highly turbulent shocked region.

The properties of these phases can be studied using the distribution of the mass fraction in the density-pressure plane or in the density-Mach number plane. Fig. 5.5 and 5.6 show the 2D plots of the mass fraction before and after ionization has been turned on. Before ionization is turned on, the distribution of the gas is at thermal equilibrium and the average Mach number is of order 1 with a dispersion of 0.48. After 1 My, the three-phase medium is formed and the three phases are well separated in the Mach number density plot. The hot ionized gas can be seen on the pressure density plot, on the isothermal equilibrium curve for the ionized gas, and on the Mach number density plot in the subsonic area. The unperturbed medium remains at the same location in the graph with respect to Fig. 5.5, while the shocked material is pushed at high Mach number and high densities. The distribution of the mass fraction is quite similar to the one found in Chap. 4, the only difference is the initial distribution of the gas, which was previously homogeneous at 500 cm^{-3} with a density or interface modulation. In both cases, the shocked region contains points with densities higher than the one corresponding to the collect and collapse scenario (red dashed line in Fig. 5.5 and 5.6), i.e. the density after the collect phase in a homogeneous medium. These points represent 3 % of the shell in mass fraction and help to achieve densities high enough to trigger the gravitational collapse.

5.3.2 Supersonic turbulence and comparison

The simulations with a mean Mach number of two and four present the same three phase structures: the ionized region, the shocked region, and the unperturbed region. However, in these cases the initial gas has more turbulent ram pressure to resist the ionized-gas expansion. The pressure of the ionized gas and the ram pressure caused by turbulence can be estimated from

$$\begin{aligned} p_{II} &= \underline{2\bar{n}_{II} k_b T_{II}} \\ p_{turb} &= \rho_0 v_0^2 \end{aligned} \tag{5.2}$$

where n_{II} and $T_{II} \approx 7700$ K are the density and the temperature in the ionized gas and where ρ_0 and v_0 the density and the mean velocity in the initial turbulent medium. The density of the ionized gas is nearly constant in time in the three simulations, and does not depend on the initial turbulence. n_{II} is around 10/cm^3. The corresponding pressure at t = 500 ky is given in Table 5.1 with the initial turbulent ram pressure. The ionized-gas pressure dominates the turbulent ram pressure for a mean Mach number of one and two.

Table 5.1: Initial turbulent ram pressure and ionized-gas pressure at t = 500 ky

Mean Mach number	1	2	4
p_{turb}/kb at t = 0 ky [K/cm^3]	3.2×10^4	1.2×10^5	4.5×10^5
p_{II}/kb at t = 500 ky [K/cm^3]	1.7×10^5	1.9×10^5	1.8×10^5

The consequent progression of the ionized-gas expansion is clearly visible in the column density plots in Fig. 5.3. However, the plots also show that this progression is nearly stopped for a mean Mach number of four. This is caused by the fact that the turbulent ram pressure dominates the ionized-gas pressure (see Table 5.1). Another interesting difference between the Mach-four case and the others is the presence of many globules. It seems that the presence of these globules in our simulations can be linked with the fact that turbulent motions dominate the ionized-gas expansion, this will be investigated in more detail in Sect. 5.4. A movie of the time evolution of the Mach-four case is available online[1].

Locally the ionization fraction changes from one in the ionized region to zero in the unionized region in a very small zone (less than 0.01 pc) when turbulence can be neglected. Therefore the position at which the fraction is less than 0.5 gives the position of the ionization front. When turbulence is high, the position of the front is difficult to find since there is mixing between ionized gas and cold gas (see Fig. 5.4). However global parameters like the mean position and apparent width of the ionizing front can still be studied thanks to the whole ionization fraction field. We used an average of the vertical profile of the ionization fraction. It transits between one in the completely ionized region and zero in the cold region. In between it slowly decreases because of the apparent width caused by the projection. We define the mean position of the ionizing front Z_X where the average profile is at 0.5 and the width ΔZ_X as the distance between the 0.95 and 0.05 positions. This corresponds to the following equations

$$\begin{aligned} Z_X &= \int_0^{L_{box}} H(\langle X(x,y,z)\rangle_{x,y} - 0.5)dz, \\ \Delta Z_X &= \int_0^{L_{box}} H(\langle X\rangle_{x,y} - 0.05) - H(\langle X\rangle_{x,y} - 0.95)dz, \\ H(x-y) &= 1, \text{ if } x \geq y \text{ or } 0, \text{ if } x < y. \end{aligned} \tag{5.3}$$

where $X(x,y,z)$ is the ionization fraction field and H the Heavy-side function. Z_X and ΔZ_X are shown in Fig. 5.7. The front progression is slowed down and its width increases as the Mach number increases. This is caused by the bigger density contrast with increasing turbulence. In the three cases, the width of the shell is mainly caused by a projection effect of the column density. The real shell is thin (see Fig. 5.4), but is very spatially disperse by the inner structures of the cloud. Therefore, it will look wider in column density.

5.3.3 Ionization and thermal equilibrium

The scheme we used (Sect. 5.1) is able to treat the ionization physics out of equilibrium. Therefore, an interesting quantity to follow is the fraction of gas which is out of equilibrium. At equilibrium, the ionization rate compensates the recombination rate. From Eq. 5.1, the ionization fraction at equilibrium is $X = (\sqrt{1+4/y}-1)y/2$ with $y = \sigma_\gamma F_\gamma / n_H \beta$. In the molecular cloud, F_γ is 0, therefore X is 0 at equilibrium. In the H II region, $y \gg 1$ so the ionization fraction tends to 1. At the ionization front, the ionization fraction can be at equilibrium and in between 0 and 1, however this region is very small and can be neglected in the simulation (less than 1 % of the box). The thickness of the ionization front is given

---

[1] `https://sites.google.com/site/astrohep/movies/turbulence`

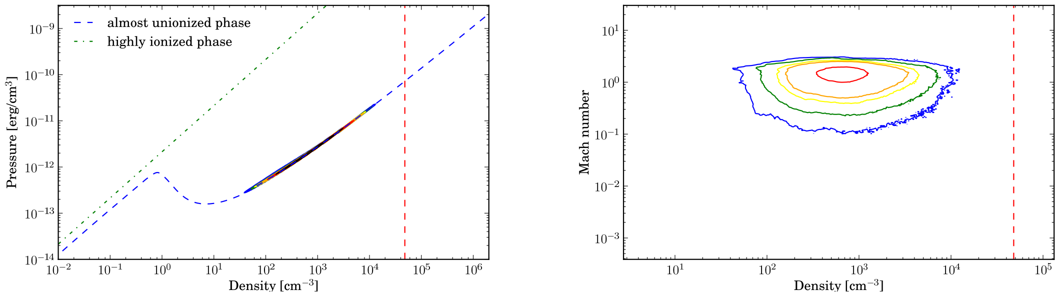

Figure 5.5: 2D plot of the mass fraction at a given density and pressure (left) and at a given density and Mach number (right), before ionization is turned on in the simulation with a mean Mach number of one. Blue to black contours are increasing mass fraction contours (blue: 1E-6, green: 1E-5, yellow: 5E-5, orange: 1E-4, red: 5E-4, black: 2E-3). The dashed-red line at $4.8{\times}10^4$ /cm^3 is the maximum density achieved in a plan-parallel 1D simulation for a homogeneous density at 500 /cm^3.

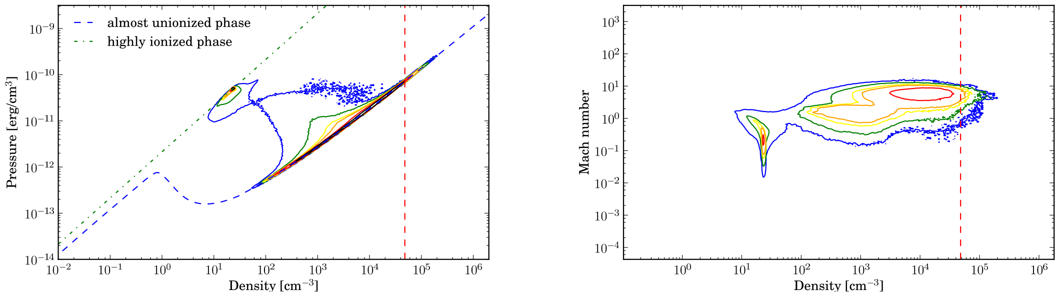

Figure 5.6: 2D plot of the mass fraction at a given density and pressure (left) and at a given density and Mach number (right), 1 My after ionization is turned on. Blue to black contours are increasing mass fraction contours (blue: 1E-6, green: 1E-5, yellow: 5E-5, orange: 1E-4, red: 5E-4, black: 2E-3). The dashed-red line is the maximum density achieved in a plan-parallel 1D simulation for a homogeneous density at 500 /cm^3: $4.8{\times}10^4$ /cm^3.

by $1/n_H\sigma_\gamma$ which is of the order of 10^{-4} pc for n_H=500/cm^3. Therefore, we define the fraction of gas out of equilibrium as the percentage of cells that have an ionization fraction between 0.05 and 0.95. The values at different times for the three simulations are given in Table 5.2. The more turbulent the medium, the more out of equilibrium. It is interesting to note that this is similar to what was observed with the thermal instability in the interstellar medium (see *Sánchez-Salcedo et al.*, 2002; *Gazol et al.*, 2005; *Audit and Hennebelle*, 2005). Almost one fifth of the simulation box at t = 1 My is out of equilibrium for a mean Mach number of four. This means that the hypothesis of an ionization equilibrium is quite bad to study the impact of ionization on a turbulent cloud. This is mainly caused by the ionized gas getting into a shadowed region. In these regions the recombination time is long, between 1 and 100 ky for densities around 1.-10. cm^{-3} and temperature around 8000 K as we have already explained in sect. 5.2.

The temperature is also an important quantity to monitor in our scheme. We solve the thermal balance between ionization and recombination and this allows the gas to be at states out of equilibrium as shown in sect. 5.1. This behavior can be identified in Fig. 5.8, the gas ahead of the dense parts facing the ionization flux is ionized but at a temperature between 2000 and 6000 K. This is caused by the 3D expansion of the dense ionized gas at the top of the structures facing the ionization radiation. Besides, the regions that are in the

Table 5.2: Percentage of cells out of ionization equilibrium.

Time	Mach 1	Mach 2	Mach 4
250 ky	1 %	7 %	8 %
500 ky	3 %	9 %	12 %
750 ky	5 %	10 %	13 %
1 My	6 %	12 %	17 %

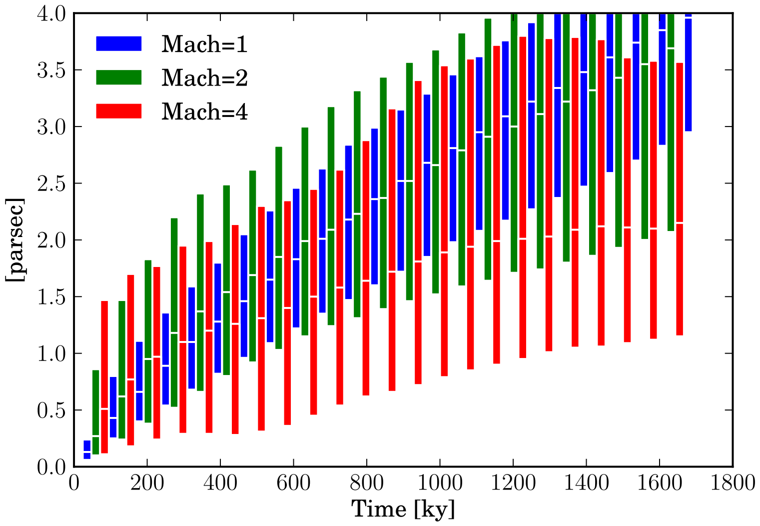

Figure 5.7: Positions of the 0.95-, 0.5- and 0.05-transition of the xy-average ionization fraction. Between 0 and the lower bound the ionization fraction of the gas is between 1 and 0.95, between the lower bound and the middle bound, between 0.95 and 0.5 and between the middle bound and the upper bound the ionization fraction is between 0.5 and 0.05.

shadow of the dense structures tend to be overheated at almost 10 000 Kelvin whereas the equilibrium temperature is around 7750 Kelvin. This is caused by the fact that the recombination process in the shadow is done at constant pressure, the pressure being imposed by the hot ionized and exposed gas surrounding the shadowed gas. Therefore, as we have demonstrated in sect. 5.1 for the simple situation of a clump shadowing parts of the hot ionized gas, the temperature behind the clump will increase. In the turbulent simulation, the cooling processes for the unionized gas is also playing a role (see Chap. 4 for details), they will cool the recombined gas so that the temperature does not reach 14 000 Kelvin but equilibrates around 10 000 Kelvin. This result is counter-intuitive since one would expect that the gas stays at 7750 Kelvin during the recombination step, the kinetic energy of the electrons being radiatively lost for the system. However, the 3D versus 1D study done in sect. 5.1 clearly show the importance of the lateral motions from the exposed gas to the shadowed gas to impose a recombination at constant pressure behind the structures.

5.4 Structures and observational signatures

5.4.1 Pillars

It is not clear how to distinguish structures on the column density maps in Fig. 5.3 because of the confusion on the line of sight. Therefore we will investigate some density cuts to

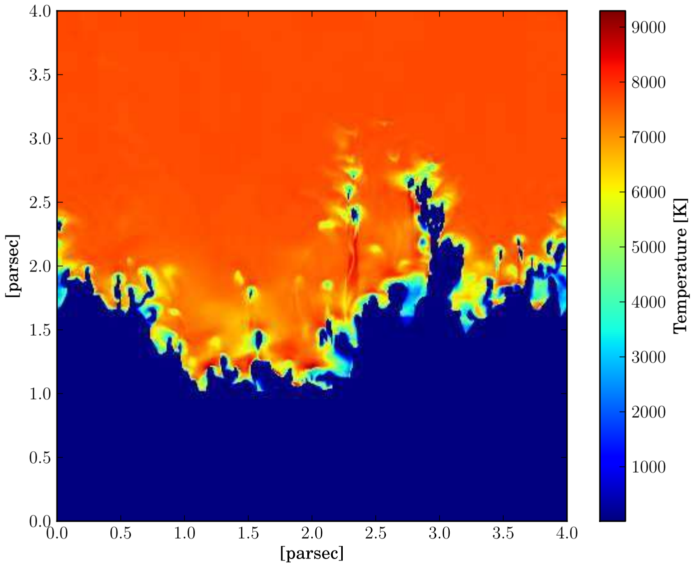

Figure 5.8: Temperature cut at t ≈ 710 ky after ionization is turned on. The 3D temperature effects studied in the clump simulation (sect. 5.1 are clearly visible through the snapshot.

identify pillars and globules. Figure 5.9 presents the formation of a pillar in the Mach 1 simulation between 200 and 700 ky. The pillar formed is one parsec long and presents a complex structure, with successive dense parts along its length. Figure 5.10 is a map along the pillar with the direction of the velocity field. The structure of the field is similar to the one already obtained in Chap. 4 for non-turbulent set-ups. The pillar has two dense heads at a vertical position of 1.4 and 1.6 parsecs, a dense base between 1.8 and 2 parsecs and two holes on the side at 2.4 parsecs. The velocity field shows that the pillar is forming at its base by the convergence of the dense parts of the shell while the holes are formed by the divergence of the dense parts created on a concave zone. This is the same configuration that was previously seen in Chap. 4, without any turbulence. This suggests that the mechanism at the origin of the formation of pillars are not too much dependent on the turbulence. Here the turbulence gives only the initial conditions in terms of density contrasts and initial structures on which pillars will form. The holes on the side of the pillars in the non-turbulent set-ups of Chap. 4 were in fact a complete annulus around the pillars caused by the symmetry of our initial conditions. The major difference with a turbulent scenario is that there is no more symmetry in the initial conditions. This leads to holes that are local and do not extend in a full annulus.

The curvature of the shell can also be seen on spectra of the line-of-sight velocity. Figures 5.11 and 5.12 show, on the left, a column density map of the pillar and on the right the mass histograms as a function of the line-of-sight velocity in squares of 0.05 parsec. Figure 5.11 is a snapshot at t ≈ 240 ky when the pillar is not yet formed and Fig. 5.12 at t ≈ 710 ky with the whole pillar. The line-of-sight velocity spectra are wide (between -2 and +2 km/s) before the pillar is formed. This was already identified in Chap. 4 as the signature of the dense shell which is curved on itself with the two components, blue-shifted and red-shifted, that are going to collide to form the pillar. When the collision has occurred, the wide spectra is no longer visible and the line-of-sight velocity spectra are peaked around a null velocity (see Fig. 5.12). This demonstrates that the scenario identified in Chap. 4 with the study of non-turbulent set-ups is also taking place in our

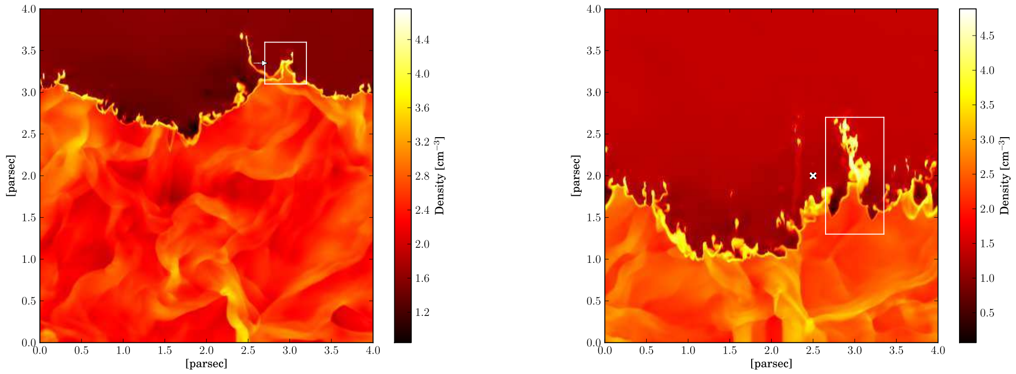

Figure 5.9: Density cut at t ≈ 240 ky and t ≈ 710 ky after ionization is turned on. The white box indicates the areas of the column density and line-of-sight velocity spectra made in Fig. 5.11 and 5.12. The arrow indicates the direction of the line of sight; for the cross, the line of sight is perpendicular to the density cut plane.

turbulent simulation.

Based on this analysis, we can infer that molecular tracers that are optically thin should reflect the same spectral structure as the line-of-sight velocity spectra of the simulations. Therefore, wide spectra could be the indication of nascent pillars whereas evolved pillars should present a spectra peaked around the velocity of the expanding bubble projected on the line of sight. This velocity is zero in our case since the line of sight is perpendicular to the direction of the expansion.

5.4.2 Dense clumps at the edge of the ionized gas

The difference between the formation mechanism of pillars and clumps inside the shell is also clearly visible in Fig. 5.9. On the first snapshot the position on which the pillar is forming can be identified as the position at which the curvature of the shell is higher. On the other parts of the shell, the curvature is not sufficient to form pillars but will rather trigger the formation of clumps inside the shell. This phenomenon was already seen in Chap. 4, the higher the curvature, the longer the pillar. If the shell is curved enough to collapse on itself it will form a pillar. At high curvature, the tip of the curved shell will be stopped by the collapse of the matter ahead of it, which leads to the formation of a pillar (Right part of Fig. 5.13, at early times the velocity field of the shocked gas shows that the shell collapses on the centre of the initial structure). The shell around the “hill” will collapse quickly on the hill, with velocities that are nearly perpendicular to the direction of the expansion. That is why the motion of the gas at the top of the hill is small. When the curvature is low, the shell collapse on the hill but with a velocity that has a component in the direction of the expansion. Therefore after the collapse, the shocked gas keeps a velocity in the direction of the expansion and propagates with the rest of the shell. The matter is accelerated with the shell and the density increases because the gas surrounding it converges smoothly at the centre (Left part of Fig. 5.13). This situation was studied and compared in the context of RCW36 in Vela C molecular cloud (see Chap. 6). The new observations from the Herschel space telescope show the presence of dense clumps around the HII region RCW36. Dedicated numerical simulations show that it is rather unlikely that these clumps were pre-existing because they would have triggered the formation of pillars. These dense clumps are located at the edge of the HII region and thus, they are formed by the lateral flows in the shell caused by curvature perturbations that are not

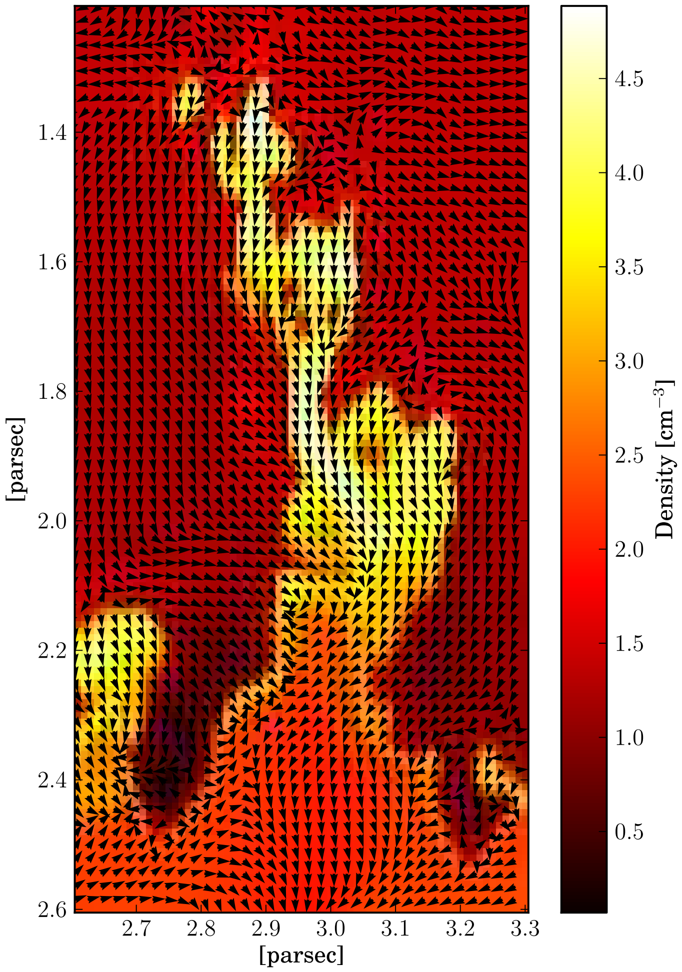

Figure 5.10: Cut of density field and velocity field orientation along the pillar at t ≈ 710 ky.

high enough to form pillars. It is exactly the same process that is at work in the present turbulent simulations. From Chap. 4, it can be estimated that the transition from clump to pillar formation is at a curvature radius between 2.5×10^{-2} and 5×10^{-2} pc in the present situation.

Thompson et al. (2011) showed that the dense clumps around HII regions are preferentially located at the interface between the ionized gas and the cold gas. We propose here a formation mechanism of these dense clumps in the shell thanks to curvature perturbations. However if the turbulent ram pressure dominates the ionized gas pressure, such dense clumps will not be present exactly at the interface. The cold gas has sufficient kinetic energy to disrupt the interface and a mixing region between the dense shocked gas and the ionized gas is present (see Fig. 5.4). Therefore the clear correlation in the observations between the position of the dense clumps and the interface suggests that in most of these regions the ionized-gas pressure dominates the turbulent ram pressure of the surrounding gas.

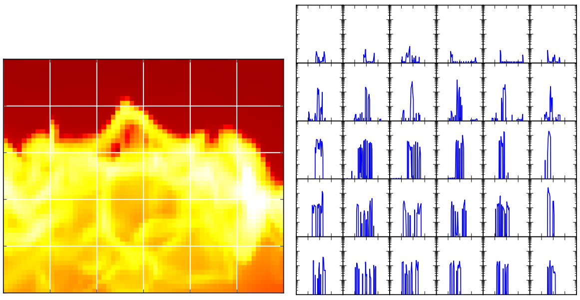

Figure 5.11: Left: column density on a 0.6x0.5x0.5 pc^3 box around the area in which the pillar will form at t≈ 240 ky. Right: mass-weighted histogram of the line of sight velocity in the same box (similar to optically-thin observational line spectra). Each spectrum is made on a square of 0.1x0.1 pc^2 drawn on the column density map. The spectra are drawn between -4 and 4 km/s in 80 bins (horizontal axis) and the mass between 10^{-4} and 1 solar mass (vertical axis in log scale). The lateral shocks can be identified in the wide spectra leading to a very broad averaged line width.

5.4.3 Globules

Contrary to the dense clumps in the shell, globules are bubbles of gas disconnected from the molecular cloud and surrounding by ionized gas. The major difference between the turbulent simulations presented in this chapter and the non-turbulent set-ups studied in Chap. 4 is the appearance of these globules in the highly turbulent case. As we have already discussed above, globules emerge because the ram pressure of turbulence dominates the pressure of the ionized gas. These bubbles of cold dense gas have enough kinetic energy to penetrate inside the H II region. An interesting consequence is that the motion of the globules is imposed by the turbulence. They could have by chance a motion aligned with the direction of expansion of the H II region but most of the time, they should have a random motion direction set by the turbulence, and it is indeed the case in our simulation. The direction of expansion of the H II region is from top to bottom in Fig. 5.3. Therefore, projected on the line of sight which is perpendicular, the velocity in the expansion direction is zero. The motion of a pillar is typically aligned with the direction of expansion of the H II region, as it can be seen on Fig. 5.12. The spectra are centered at zero. However, it is not the case for a globule. Figure 5.14 shows a typical globule in the simulation at Mach four. The line-of-sight velocity spectra are systematically shifted at a velocity of $+4$ km/s which is of the order of ten times the sound speed of the cold gas. The shift is also highlighted in Fig. 5.15. The globule does not have a motion aligned with the direction of expansion. In a region where globules and pillars are present, the velocity of a pillar is the velocity of expansion of the front projected on the line of sight, whereas the velocity of a globule will be the signature of the initial turbulence. The dense clumps that are observed in the shell also move with the expansion of the H II region. Therefore the same velocity shift between these clumps and the globules nearby can be expected. In that picture, pillars and clumps at the edge of the H II region are the result of a structure dominated by the ionization dynamics whereas globules are turbulent dominated. This is quite different from the radiation driven implosion scenario, in which there is no reason for the globules to have a velocity different from pillars.

This signature of the turbulent nature of a globule is supported by recent observations in the Cygnus X region. Thanks to Herschel Open Time and SOFIA observations (*Schneider et al.*, 2012a), 158 μm and CO maps are available and contain several pillars and globules. A pillar and a globule in this region were identified to be sufficiently close (and the H II region sufficiently big) to consider they should have the same direction of motion

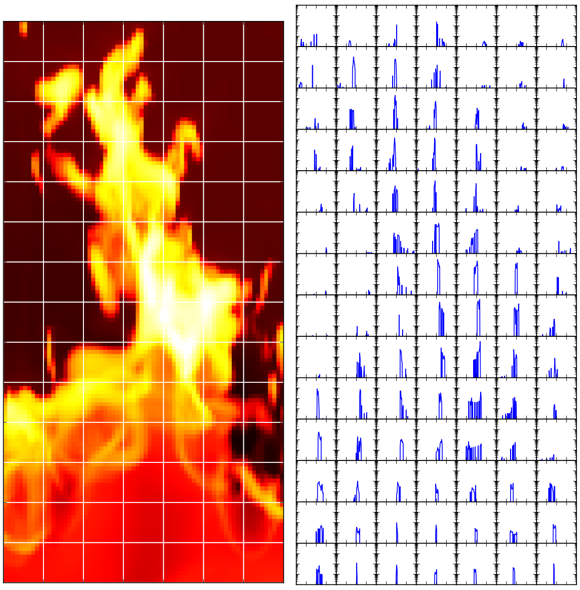

Figure 5.12: Left: column density on a 0.7x1.4x0.5 pc^3 box around the pillar structure at t ≈ 710 ky. Right: mass-weighted histogram of the line of sight velocity in the same box (similar to optically-thin observational line spectra). Each spectrum is made on a square of 0.1x0.1 pc^2 drawn on the column density map. The spectra are drawn between -4 and 4 km/s in 80 bins (horizontal axis) and the mass between 10^{-4} and 1 solar mass (vertical axis in log scale). The lateral shocks have collided to form the pillar, the spectra are now peaked around 0 km/s.

if the motion is only imposed by the H II region expansion. However the [CII] spectra show a line-of-sight velocity difference of two kilometers per second, which is clearly supporting a turbulent scenario for the formation of the globule against the radiation implosion of an isolated clump.

The difference of 2 km/s is an indication of the level of initial turbulence. For a sonic velocity of 0.4 km/s, this shift indicates typically a motion at Mach 5. In our simulation, the globule is at Mach 10 whereas the mean Mach number of the simulation is 4. Therefore the velocity of the globule is an indication of the turbulence level but not a precise measurement.

5.4.4 Probability density function

In this section, we investigate the density structure of the gas using probability density functions (PDFs). Numerical models (e.g. *Kritsuk et al.*, 2007; *Audit and Hennebelle*, 2010; *Ballesteros-Paredes et al.*, 2011) and observations of atomic and molecular gas (e.g. *Kainulainen et al.*, 2009) show that PDFs are log-normal at low densities and can have more complex shapes at higher densities. We here plot the mass fraction against the density (Fig. 5.16) from our simulations in a temporal evolution, and we obtain that the PDF shape depends on turbulence and time. At low turbulence (Mach 1) the probability density function is double-peaked because of the ionization, similarly to the bimodal PDFs caused by the thermal instability (see *Sánchez-Salcedo et al.*, 2002; *Gazol et al.*, 2005; *Audit and Hennebelle*, 2005). The dense compressed gas is forming a new peak in the distribution. At high turbulence, the probability density function is shifted toward higher densities but does not present the double peak. This directly tells that a double peak is the signature of a region dominated by the ionization, whereas a single peak is the signature that the turbulence is dominant. This signature was already observed in the Rosette nebula

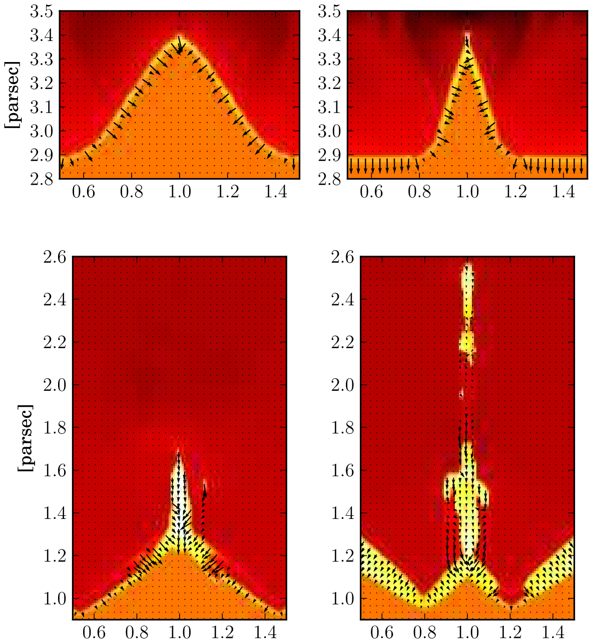

Figure 5.13: Illustration of the effect of the shell curvature on the formation of clumps and pillars. Density cut and velocity field (for the unionized gas) are taken from simulations from Chap. 4. Initial curvature radius: left: $5{\times}10^{-2}$ pc and right: $1{\times}10^{-2}$ pc. Top: 20 ky after the beginning of the simulation, the shell is formed on the curved surface. Bottom: snapshots after 550 ky. A 1.5-pc long pillar is formed at high curvature whereas a clump of the size of the initial structure is formed at low curvature.

by *Schneider et al.* (2012b). The PDFs at the edge of the H II regions present the same double-peaked signature. It suggests that, at the border of the bubble, the turbulence is low compared to the ionized-gas pressure.

Based on the PDFs of the Mach 2 simulation, it is clear that the double peak disappears when there is no more unperturbed gas in the region on which the PDFs are done. Therefore a good way to look at the PDFs around a H II region is to do concentric PDFs centered on the central ionizing cluster. By increasing the radius of the region, we will first capture the peak of the shocked region, then a double peak should appear when the unperturbed region is included. Then the first peak should disappear at some point, when the shocked region becomes negligible compared to the unperturbed region. This point could indicates on which scale the central cluster has an impact on the global PDF of the cloud and therefore on which scale, the initial mass function is impacted by the ionization. If the turbulence is high, it is possible that the shocked peak is hidden in the large peak of the turbulent cloud. In that case, no double peak will appear and this will be an indication that the turbulence in the region dominates over the ionized-gas pressure.

5.5 Conclusions

Structures at the interface between HII regions and molecular clouds can be classified mainly in three categories: pillars, globules and dense clumps. Various scenarii have been investigated in the past to explain their formation: collect & collapse, radiation driven implosion, shadowing effects and turbulence. We have presented a new model to explain the formation of clumps and pillars in Chap. 4 based on the curvature of the dense shell formed by the collect processes. High curvature leads to pillars, low curvature to

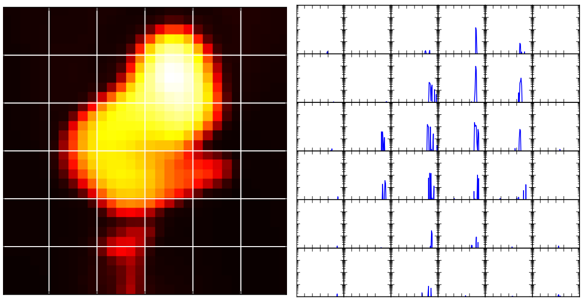

Figure 5.14: Left: column density on a 0.3x0.3x0.25 pc^3 box around a globule in the Mach 4 simulation. Right: mass-weighted histogram of the line of sight velocity in the same box (similar to optically-thin observational line spectra). Each spectrum is made on a square of 0.05x0.05 pc^2 drawn on the column density map. The spectra are drawn between -6 and 6 km/s in 80 bins (horizontal axis) and the mass between 10^{-4} and 1 solar mass (vertical axis in log scale). All the spectra are red-shifted at a velocity of +4 km/s.

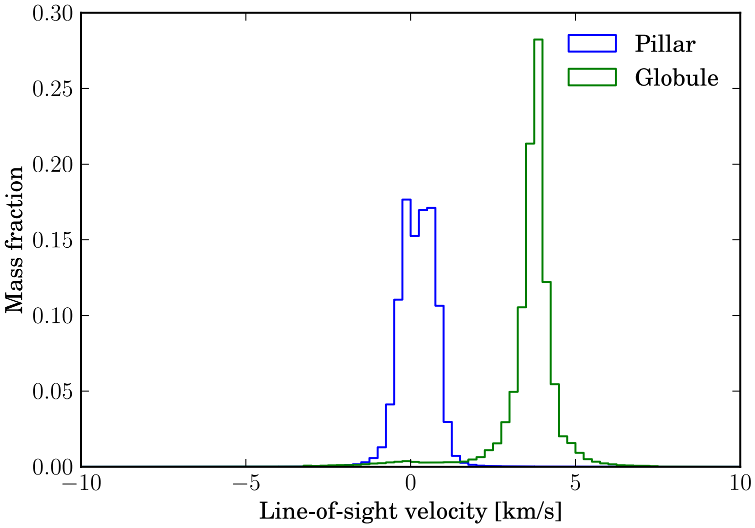

Figure 5.15: Mass fraction of the gas in the pillar and in the globule in function of the velocity. The bulk line-of-sight velocity of the pillar is at 0 km/s whereas the bulk velocity of the globule is at +4 km/s.

instabilities forming dense clumps and dips in the shell. This model was investigated using non-turbulent set-ups. In the present chapter we show that the same mechanisms are at work in simulations with a turbulent cloud. Especially the same spectral observational signatures can be identified on the formation stages of the pillars.

Furthermore we have shown that:

- Because of turbulence, hot ionized gas can get into the shadow of cold dense gas, leading to a very long recombination time for the gas. This gas can only be treated with a non-equilibrium model for ionization, up to 20 % of the box can get into that state. The equilibrium assumption is valid in situations in which the ram pressure of turbulence is not dominating the ionized-gas pressure, i.e. low turbulence levels.

- Globules are formed preferentially when the turbulence in the cold gas dominates the ionized-gas pressure. Bubbles of dense gas have sufficient kinetic energy to penetrate into the HII regions forming the globules. A signature of this scenario is the line-of-sight velocity spectrum of the globules which is either blue-shifted or red-shifted

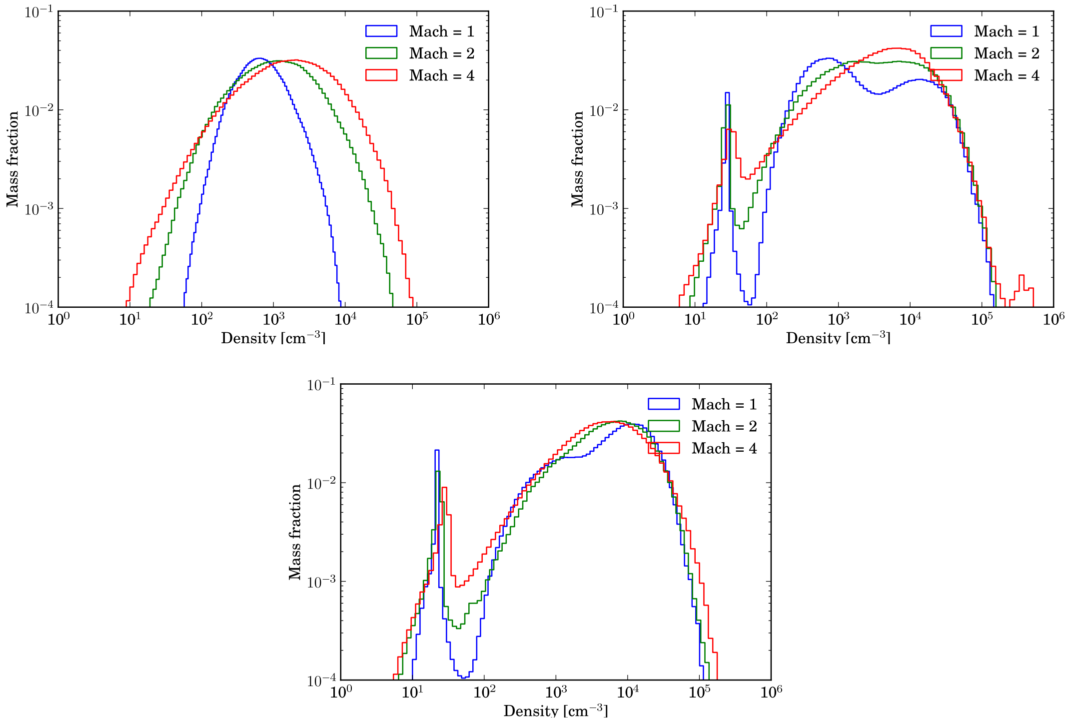

Figure 5.16: Probability density function of the gas for the three simulations. Left: t= 0 ky, middle: t = 500 ky, right: t = 1 My. The first peak is the ionized gas and therefore is not seen in the observations. At t = 500 ky, the Mach-1 simulation presents a double peak, the first one corresponds to the unperturbed turbulent gas, the second one to the shocked region. In the Mach-2 simulations, the peak is barely visible because the turbulence is higher and because the unperturbed region still present in the box becomes small. In the Mach-4 simulation, the turbulence is too high, and the second peak is hidden in the peak of the turbulent cold region.

compared to the spectrum of a pillar or a clump at the edge of the HII region. This can be directly observed in regions where pillars, clumps and globules are present.

- Probability density functions are double peaked when the turbulent ram pressure is low compared to the ionized-gas pressure. They could be used in observations as probes to determine the relative importance of the turbulence compared to the ionization.

An important step now is to do the statistics of the formation of dense structures at the edge of H II regions. It will be of great importance to conclude on the potential negative or positive effects of radiative feedback on the star-formation rates. Furthermore comparisons with observations will also tell how realistic the curvature scenario for the formation of dense clumps and pillars and the turbulent scenario for the formation of globules are.

Bibliography

Audit, E., and P. Hennebelle (2005), Thermal condensation in a turbulent atomic hydrogen flow, *A&A*, *433*(1), 1–13. 80, 86

Audit, E., and P. Hennebelle (2010), On the structure of the turbulent interstellar clouds .

Influence of the equation of state on the dynamics of 3D compressible flows, *A&A*, *511*, 76. 86

Ballesteros-Paredes, J., E. Vázquez-Semadeni, A. Gazol, L. W. Hartmann, F. Heitsch, and P. Colín (2011), Gravity or turbulence? - II. Evolving column density probability distribution functions in molecular clouds, *MNRAS*, *416*(2), 1436–1442. 86

Deharveng, L., et al. (2010), A gallery of bubbles. The nature of the bubbles observed by Spitzer and what ATLASGAL tells us about the surrounding neutral material, *A&A*, *523*, 6. 77

Elmegreen, B. G., and C. J. Lada (1977), Sequential formation of subgroups in OB associations, *ApJ*, *214*, 725–741. 77

Gazol, A., E. Vázquez-Semadeni, and J. Kim (2005), The Pressure Distribution in Thermally Bistable Turbulent Flows, *ApJ*, *630*(2), 911–924. 80, 86

Kainulainen, J., H. Beuther, T. Henning, and R. Plume (2009), Probing the evolution of molecular cloud structure. From quiescence to birth, *A&A*, *508*(3), L35–L38. 86

Kritsuk, A. G., M. L. Norman, P. Padoan, and R. Wagner (2007), The Statistics of Supersonic Isothermal Turbulence, *ApJ*, *665*(1), 416–431. 86

Peters, T., M.-M. Mac Low, R. Banerjee, R. S. Klessen, and C. P. Dullemond (2010), Understanding Spatial and Spectral Morphologies of Ultracompact H II Regions, *ApJ*, *719*(1), 831–843. 73

Sánchez-Salcedo, F. J., E. Vázquez-Semadeni, and A. Gazol (2002), The Nonlinear Development of the Thermal Instability in the Atomic Interstellar Medium and Its Interaction with Random Fluctuations, *ApJ*, *577*(2), 768–788. 80, 86

Schmidt, W., W. Hillebrandt, and J. Niemeyer (2006), Numerical dissipation and the bottleneck effect in simulations of compressible isotropic turbulence, *Computers & Fluids*, *35*(4), 353–371. 73

Schmidt, W., C. Federrath, M. Hupp, S. Kern, and J. C. Niemeyer (2009), Numerical simulations of compressively driven interstellar turbulence. I. Isothermal gas, *A&A*, *494*(1), 127–145. 73

Schneider, N., et al. (2010), The Herschel view of star formation in the Rosette molecular cloud under the influence of NGC 2244, *A&A*, *518*, L83. 73

Schneider, N., et al. (2012a), Globules and pillars seen in the [CII] 158 μm line with SOFIA, *A&A*, *542*, L18. 85

Schneider, N., et al. (2012b), Cluster-formation in the Rosette molecular cloud at the junctions of filaments, *A&A*, *540*, L11. 87

Thompson, M. A., J. S. Urquhart, T. J. T. Moore, and L. K. Morgan (2011), The statistics of triggered star formation: an overdensity of massive YSOs around Spitzer bubbles, *arXiv*, *astro-ph.GA*. 77, 84

Zavagno, A., et al. (2010), Star formation triggered by the Galactic H II region RCW 120. First results from the Herschel Space Observatory, *A&A*, *518*, L81. 77

Chapter 6

Observations of ionizing star impacts and comparisons with models

> *In the field of observation, chance favors only the prepared mind.*
> *Louis Pasteur*

Herschel observations have revealed the density structures of many objects at the interface between H II regions and molecular clouds. Among them, pillars and cometary globules are the most well-known and studied so far. They are present in many high-mass star-forming regions such as the Eagle Nebula, the Rosette, Cygnus X, and Vela C molecular clouds; located near a density-enhanced shell induced by the expansion of local H II regions.

In the previous chapters, we proposed new formation mechanisms for these structures. The initial morphology of the molecular cloud and its turbulence are of primordial importance as it induces deformations and curvature of the shell during the expansion of the H II region. Many observational diagnostics have been derived from numerical simulations to test if a pillar is formed from the collapse of the shell and if globules emerge because of the initial turbulence. Thanks to Herschel observations obtained within the HOBYS key programme, we are able to test these diagnostics on the observations of the Eagle Nebula, the Rosette, and Cygnus X molecular clouds and the H II regions RCW 36 and RCW 120. Thanks to the analytical models of the shell presented in Chap. 2, it is possible to derive the analytic expression of the initial length and age of a pillar, i.e. its length just after the collapse of the shell, and the time at which the collapse occurred.

We first resume the new observations from the Herschel space observatory. We present an analysis of the probability density function around the RCW 120 H II region, and a study of the velocity structure of globules and pillars in Cygnus X based on *Herschel* and SOFIA[1] observations. Then, we characterize the profiles of the shock fronts and pillars at the interface between the Rosette, Vela C, and Eagle Nebula and the H II regions nearby. For this purpose, we used the DisPerSe algorithm (*Sousbie*, 2011) on the *Herschel* column density maps. We investigated the velocity properties of the dense structures at the interface thanks to different molecular tracers. The combination of the density and velocity information was used to test the diagnostics derived from the numerical simulations and to test the analytical models that can predict the age and initial length of pillars.

---

[1] SOFIA (Stratospheric Observatory For Infrared Astronomy) is an airborne observatory with a 2.5-m telescope on a modified Boeing 747SP. It was developed in collaboration between NASA and DLR (German Aerospace Centre) and is in operation since the end of 2010.

Figure 6.1: *Herschel* image of the Eagle Nebula (left *Hill et al.*, 2012) and the Rosette Nebula (right *Schneider et al.*, 2010). Colour coded image: 70 microns for blue and 160 microns for green using the PACS (Photodetector Array Camera) and 250 microns for red using the SPIRE (Spectral and Photometric Imaging Receiver). Copyright: ESA/Herschel/PACS/SPIRE/HOBYS Key Programme Consortium (Motte, Zavagno, Bontemps).

6.1 Herschel Space Observatory

Herschel[2] was launched on 14 May 2009 and is now a fully operational observatory in the far-infrared and submillimetre wavelengths (see *Pilbratt et al.*, 2010). It consists in a 3.5 m telescope cooled down at 85 K whose resolution is given by $7''\times(\lambda_{\rm obs}/100\ \mu\rm m)$. Three science instruments were conceived for the telescope:

- the Photodetector Array Camera and Spectrometer (PACS *Poglitsch et al.*, 2010)
- the Spectral and Photometric Imaging REceiver (SPIRE *Griffin et al.*, 2010)
- the Heterodyne Instrument for the Far Infrared (HIFI *de Graauw et al.*, 2010)

The three instruments are complementary and give access to a broad-band photometric imagery in six bands with centered wavelengths of 70, 100, 160, 250, 350, and 500 μm as well as imaging spectroscopy and high-resolution spectroscopy.

An important part of the energy that is emitted by astrophysical sources (stars, supernovae...) has been absorbed by the dust of the interstellar medium (ISM) and re-emitted at longer wavelengths that can be observed by *Herschel*. The objectives of the mission are therefore tightly connected to the study of the ISM, in order to understand the formation of our solar system, star formation, the feedback of massive stars on the ISM, galaxy evolution, and cosmology.

The study of star formation in the Milky Way is the principal target of two guaranteed time key programmes, the Gould Belt survey (*André et al.*, 2010)[3], and the *Herschel* imaging survey of OB Young Stellar objects (HOBYS, *Motte et al.*, 2010)[4].

The Gould Belt survey focuses on the study of star formation regions that are relatively close to our solar system (less than 500 pc away). First results concentrated on the Aquila

---

[2] *Herschel* is an ESA space observatory with science instruments provided by European-led Principal Investigator consortia and with an important participation from NASA.

[3] `http://www.herschel.fr/cea/gouldbelt/en/`

[4] `http://www.herschel.fr/cea/hobys/en/`

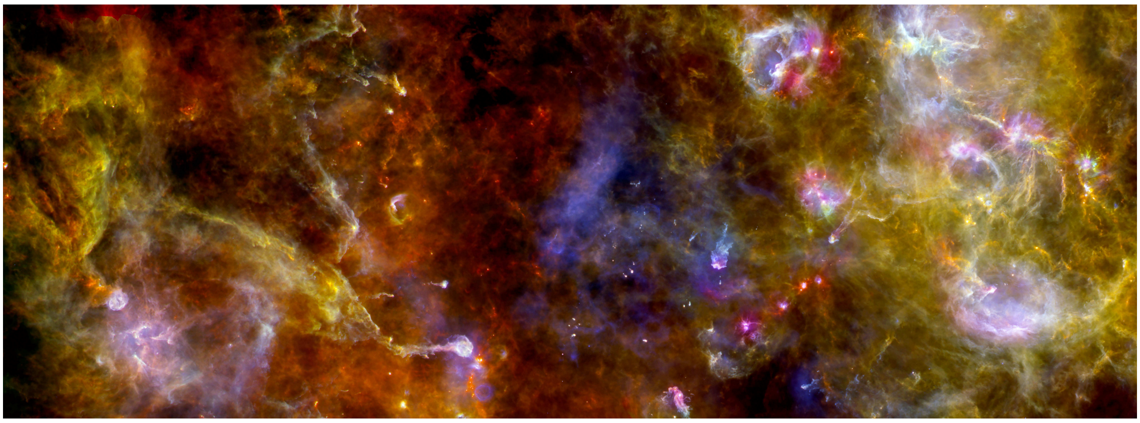

Figure 6.2: *Herschel* image of Cygnus X. Colour coded image: 70 microns for blue, 160 microns for green, and 250 microns for red. Copyright: ESA/Herschel/PACS/SPIRE/HOBYS Key Programme Consortium (Motte, Zavagno, Bontemps).

rift (*Bontemps et al.*, 2010; *Könyves et al.*, 2010) and the Polaris region (*Men'shchikov et al.*, 2010; *Miville-Deschênes et al.*, 2010; *Ward-Thompson et al.*, 2010) while more recent works studied IC5146 (*Arzoumanian et al.*, 2011), Perseus (*Sadavoy et al.*, 2012), and the Pipe nebula (*Peretto et al.*, 2012). The main result so far, is the predominance of filamentary structures in such regions whose characteristics (sub-critical, super-critical) seem to correlate with the star formation activity. An interesting result was also the discovery that the Pipe Nebula was under the influence of the stellar wind of a nearby massive star. Its filaments are asymmetric probably because of the compression from the wind (see *Peretto et al.*, 2012).

HOBYS studies star-forming regions in giant molecular clouds across the Milky Way. These regions are complex and often contain OB cluster that strongly impact their environment by the feedback from massive stars. These results are of great interests for this work and will be used in Chap. 6. The Rosette Molecular Cloud was studied in detail since the early science phase (*Schneider et al.*, 2010; *Hennemann et al.*, 2010; *Di Francesco et al.*, 2010; *Schneider et al.*, 2012a, see Fig. 6.1) with the H II region RCW 120 (*Zavagno et al.*, 2010; *Anderson et al.*, 2010). They were followed by W48 (*Nguyen-Luong et al.*, 2011), Vela C (*Hill et al.*, 2011; *Giannini et al.*, 2012, *Minier et al.* submitted), M16 (*Hill et al.*, 2012, see Fig. 6.1), and DR21 in Cygnus (*Hennemann et al.*, 2012, see Fig. 6.2). The principal results are the observations of massive proto-stars in high column-density filaments called ridges and the importance of the feedback processes of massive stars (especially ionization) for the triggered star formation. All these regions or parts of these regions are under the influence of the ionization coming from nearby massive stars. H II regions, pillars and globules can be observed and studied in great detail thanks to these new *Herschel* observations. After presenting the numerical methods and the simulations we used to study the impact of the ionization on the molecular gas, we will use the *Herschel* column density maps of Rosette, RCW 120, Vela C and M16 as well as other data sets to constrain the dynamics, in order to test the diagnostics derived from the simulations.

6.2 RCW 120

RCW 120 is a well-known H II region (see *Rodgers et al.*, 1960; *Zavagno et al.*, 2007) located at 1.3 kpc from the Sun and well studied by *Spitzer* (*Deharveng et al.*, 2009) and *Herschel* (*Zavagno et al.*, 2010; *Anderson et al.*, 2010). Although *Deharveng et al.* (2009) introduced

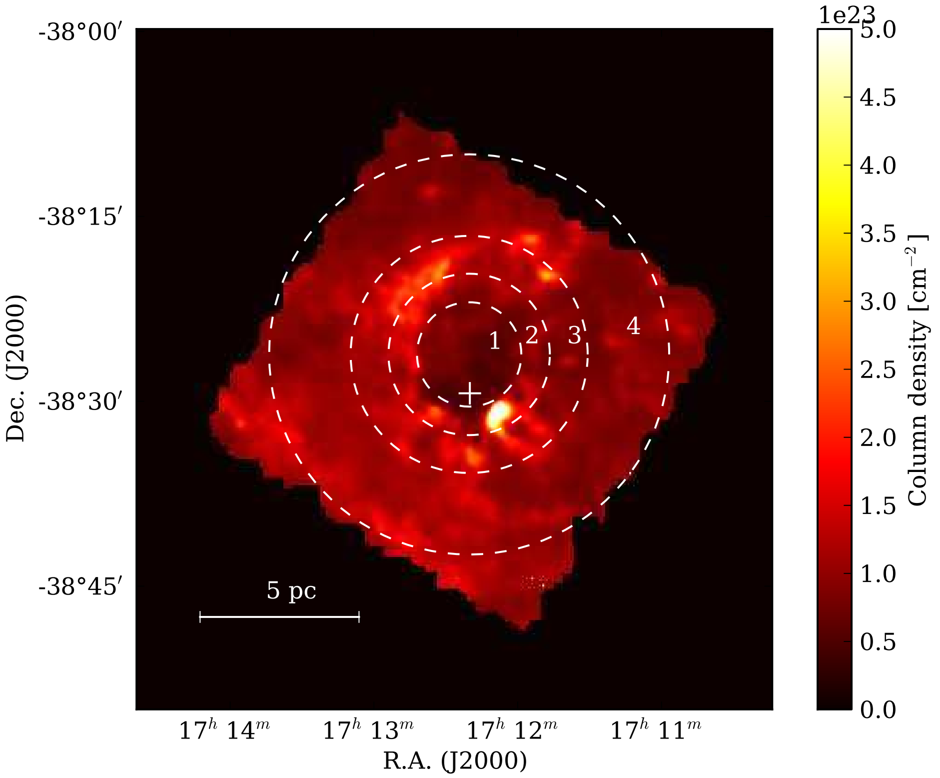

Figure 6.3: RCW 120 *Herschel* column density map. The circles indicate the different regions used for the PDFs. The white cross indicates the position of the main ionizing source (O8 star). The first region indicates the limit of the Hα emission and the limit of the H II region.

this region as the "perfect" bubble because of its nice circular shape, the ionizing source is not at the centre of the ionized sphere. The O8 star that is responsible for the ionization of the medium is indicated by the white cross in Fig. 6.3. Since the ionizing source is very close to the south part of the bubble, it is probable that the expansion is asymmetric. The molecular gas is denser at the south than the north of the bubble, as indicated by the column density (see Fig. 6.3). Because of the asymmetry, the classical model of collect and collapse is difficult to apply in the form presented in Chap. 2. Nevertheless, 1D simulations were used in *Zavagno et al.* (2007) to get a rough estimation of the parameters of the system. These simulations showed that, for an original medium at a density of 3000 cm^{-3}, the compression should be around a factor 20-30.

We will only present here a study of the probability density function (PDF) of the gas and try to extract a compression factor from the observations. Based on the simulations of Chap. 5, we study the evolution of the probability density function around an H II region by taking the distribution in concentric disk around the bubble. In Fig. 6.3, we show the four different regions that are considered for the PDFs presented in Fig. 6.4. The PDFs are fitted with log-normal distributions:

$$p(s) = \frac{p_0}{\sqrt{2\pi\sigma_0^2}} e^{\frac{-(s-s_0)^2}{2\sigma_0^2}} + \frac{p_1}{\sqrt{2\pi\sigma_1^2}} e^{\frac{-(s-s_1)^2}{2\sigma_1^2}} \qquad (6.1)$$

with $s = \ln(\Sigma/\langle\Sigma\rangle)$. Σ is the column density and $\langle\Sigma\rangle$ is the average of the column density on the whole map and not on each sub-regions (equals to 1.14×10^{23} cm^{-3}). This choice

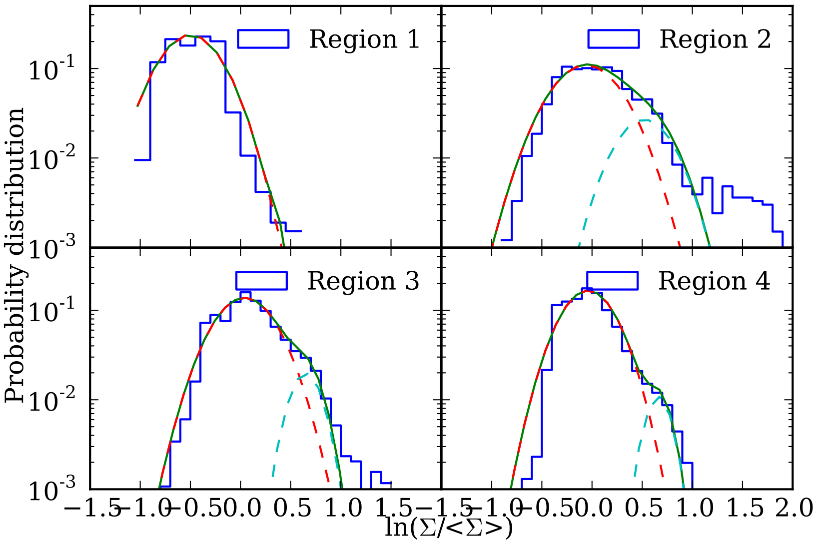

Figure 6.4: RCW 120 PDFs on the four regions indicated in Fig. 6.3. Region 4 contains region 3 and 2 but not region 1, region 3 contains region 2 but not region 1, region 2 does not contain region 1. The multi-component fit is done using log-normal distributions. The dashed curves represent the different log-normal components and the green curve is the sum ($p(s)$ in Eq.6.1).

Region	s_0	p_0	σ_0	s_1	p_1	σ_1
1	-0.5	0.16	0.28			
2	-0.06	0.08	0.31	0.52	0.017	0.26
3	0.04	0.09	0.27	0.65	0.007	0.14
4	-0.04	0.10	0.24	0.66	0.003	0.12

Table 6.1: Parameters of the log-normal fits of the PDFs in Fig. 6.4.

allows a direct comparison of the parameters between the sub-regions. s_i and σ_i are the expected value and standard deviation of each component, and p_i is the relative weight of each component. The inner part of the H II region, i.e. region 1, is fitted with a single log-normal and corresponds to the low-density cavity in which the gas has been ionized. This low-dense gas should appear as a low-density component in the other PDFs, however in order to simplify the other distribution, we exclude region 1 in the other sub-regions. This means that region 4 contains regions 3 and 2 but not region 1, region 3 contains region 2 but not region 1. The parameters of the fits are listed in Tab. 6.1. Note that the position of the peaks (i.e. s_0 and s_1) are imposed when two log-normal components are fitted.

Starting from region 2, the PDF is well fitted by a two-component log-normal. Note that on region 2 and 3, it is possible to identify the dense clump formed at the south west of the ionizing source in the dense part of the PDF. This clump is not part of the compressed component suggesting that it was not formed by the interaction of the compression and the initial turbulence of the medium. Indeed in Chap. 5, the dense parts due to the turbulence in the simulations are within the compressed component of the PDF. Therefore, it is likely that this dense clump was formed by the gravitational instability in the collect and collapse scenario as previously suggested by *Zavagno et al.* (2007).

It is also interesting to see from Tab. 6.1 that the amplitude of the compressed component decreases (from 0.017 to 0.003) when the radius of the region increases. This was

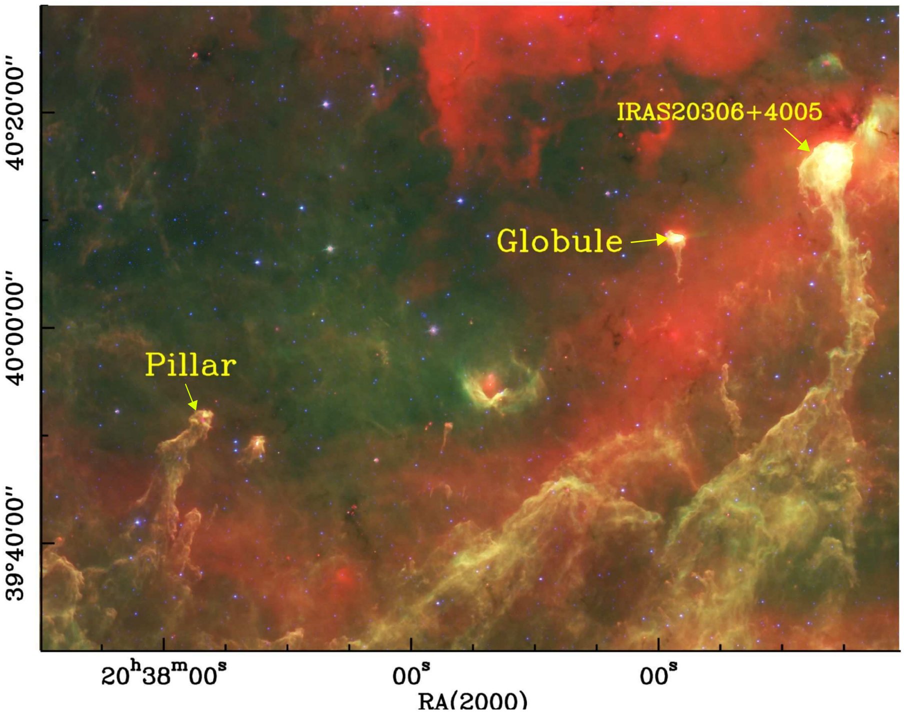

Figure 6.5: Three-color image of the southern Cygnus-X region with *Spitzer* (3.6, 8, and 24 μm) (see *Hora et al.*, 2009). The source observed with SOFIA are indicated (Pillar, globule and IRAS).

also expected: when the radius of the region increases, more and more unperturbed gas is added in the distribution while the compressed gas remains the same. Therefore the relative importance of the compressed gas decreases. The compression factor of the column density is typically of the order of 2 (given by $\exp(s_1 - s_0)$). That is rather low compared to the factor 20-30 expected from the 1D simulations in *Zavagno et al.* (2007). However the difference could be the result of a projection effect. The cloud is at a column density of 10^{23} cm^{-2} and corresponds to a density of $3{\times}10^3$ cm^{-3} on 10 pc. The compressed layer is at a column density around 2×10^{23} cm^{-2} which corresponds to a density of $6{\times}10^4$ cm^{-3} on 1 pc. Therefore we can get a compression of ≈ 20 if the line-of-sight thickness of the shell is of the order of one parsec. Considering the size of the bubble which has a radius of 1.8 pc, it seems to be a good order of magnitude for the thickness. Therefore a factor of compression of 20-30 in density can result in a factor of compression of 2 in column density.

The compression caused by the expansion of the ionized gas leads to a second component in the PDF. This component is smaller when the radius of the region on which the PDF is computed is bigger. The compression is less important than the expectation from the Collect and Collapse model, however, this is probably caused by a projection effect. We will perform this analysis on the Rosette molecular cloud, the Eagle Nebula, and RCW 36.

6.3 Cygnus-X

Cygnus-X is a large star-forming region covering about 30 square degrees in the galactic plane, located at about 1.7 kpc from the Sun. It contains a large OB association Cyg OB2, with ≈ 100 O stars (*Knödlseder*, 2000). *Reipurth and Schneider* (2008) reviewed all the observations and works on the region before 2008. Recently, thanks to *Herschel* and

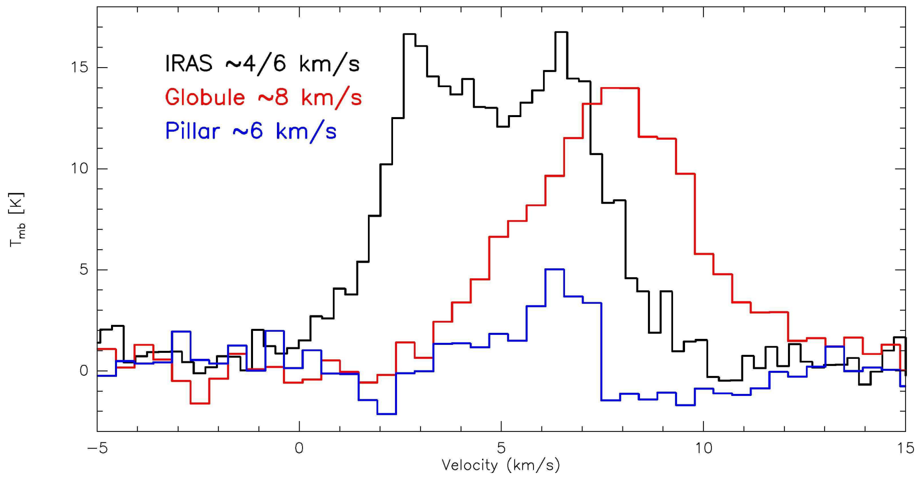

Figure 6.6: Representative C II spectra from the three observed sources (centre position with bulk emission). The double-peaked spectrum for the IRAS source is caused by two separate components at around 4 and 6 km/s. The C II spectrum of the globule (red) shows a shift of around 2 km/s with respect to the the pillar (blue) and IRAS source (black).

SOFIA new observations of the dust and C II line spectra are available (see *Hennemann et al.*, 2012; *Schneider et al.*, 2012b)[5].

The three sources that were observed are indicated in Fig. 6.5 and the corresponding C II spectra (158 μm) in Fig. 6.6. The C II spectrum of the globule (red) shows a shift of around 2 km/s with respect to the pillar (blue) and the IRAS source (black). The C II line is a PDR tracer around H II regions, therefore it is difficult to conclude that this shift corresponds to a shift of the bulk velocity of the objects. However, a study of ^{13}CO 1→0 spectra confirmed that this difference in velocity can be interpreted as a shift of the velocity of the bulk motions. The ionized region around cyg OB2 is large (around 40 pc distance from the pillars and globule) and the tail of the three structures indicate that they are relatively close compared to the size of the overall region. Therefore it can be expected that they should have the line-of-sight velocity if they follow the expansion of the bubble. It is actually the case for the two pillars that have a velocity around 6 km/s. The globule could be located in an other part of the shell and then the shift could correspond to the line-of-sight projection at two different location in the shell. However, the velocity shift of 2 km/s is relatively big compared to the typical velocity of the shell. This velocity is difficult to assess but should also be of the order of 2 km/s. Therefore, the globule should be located very far from the pillars to explain such a shift with a projection effect. We cannot completely ruled out this possibility, but the direction of the tail of the structures is in favour of a relative proximity of these structures. In that context, the shift can be interpreted as the remnant velocity of the turbulent gas that formed the globules as observed in the simulations of Chap. 5. This is an observational indication that globules are formed by the interplay between ionization and turbulence. We will give more observational evidence of this phenomenon in the Rosette nebula.

6.4 Rosette Nebula

The Rosette molecular cloud is located at 1.6 kpc from the Sun (*Williams et al.*, 1994; *Heyer et al.*, 2006). The central cluster NGC 2244 is dominated by 17 OB stars that have a total Lyman-α luminosity of 3.8×10^5 L$_\odot$ (see *Cox et al.*, 1990). Photon dominated regions

---

[5] *Schneider et al.* (2012b) was published in a A&A special issue devoted to the first SOFIA results.

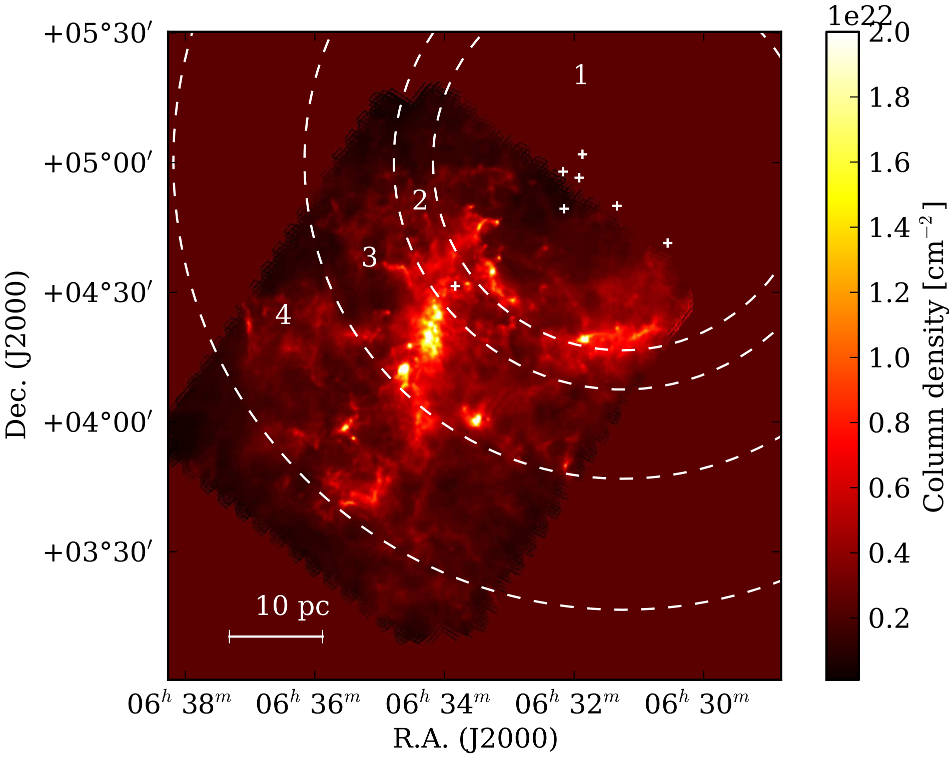

Figure 6.7: Rosette *Herschel* column density map. The circles indicate the different regions used for the PDFs. The regions are inclusive (region 2 contains region 1 ...). The white crosses indicate the position of the main ionizing sources. The second region indicates the limit of the Hα emission and the limit of the H II region.

(PDRs) are detected deep inside the cloud (see *Schneider et al.*, 1998a,9). The infrared (IR) population of the molecular cloud was investigated in Near- and mid-IR surveys (see *Poulton et al.*, 2008, and references therein). More recently, The Rosette molecular cloud was studied in far-IR thanks to *Herschel* observations (see *Schneider et al.*, 2010,0). In subsect. 6.4.1, we investigate the large-scale structure of the cloud thanks to the PDF of the gas, in function of the distance from the ionizing source. In subsect. 6.4.2, we investigate the column density structure of the edge of the molecular cloud and in subsect. 6.4.3, we concentrate on the velocity structure of three sub-regions of the interface, the pillar (east of the cavity), the globules (also east) and the south part of the shock front.

6.4.1 Probability density function

Schneider et al. (2012a) already showed that a double peak was visible in the PDF of the gas close to the border of the shell. We perform here the same analysis as in Sect. 6.2, to confirm the use of the concentric PDFs. Figure 6.9 shows the different sub-region used for the PDFs in Fig. 6.8. All the sub-regions include the inner ones, i.e. region 2 contains region 1, etc. The strategy adopted for the log-normal fit is to get a first good fit at low densities with a single log-normal and see whether the behaviour at high densities differs from the log-normal distribution. These fits are shown in black dotted lines in Fig. 6.8. In all the regions, there is a deviation from the log-normal distribution at high densities. This deviation can have two origins, the gravitational instability that generates a power-law tail at high densities, and the compression from the ionized gas as seen in Chap. 5. It can be tricky to differentiate the two. However, in the sub-regions 1, 2, and 4 the deviation is

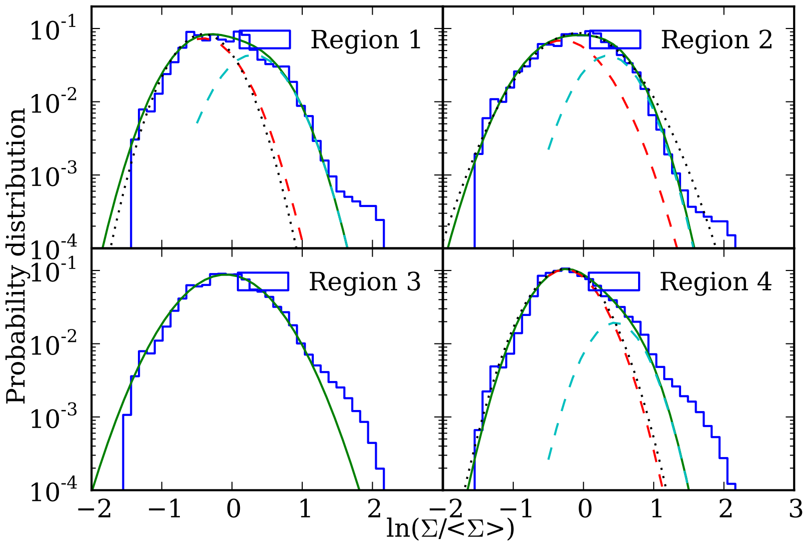

Figure 6.8: Rosette PDFs on the four regions indicated in Fig. 6.9. The multi-component fit is done using log-normal distributions.

Region	s_0	p_0	σ_0	s_1	p_1	σ_1
1	-0.41	0.07	0.39	0.30	0.04	0.38
2	-0.30	0.08	0.45	0.35	0.04	0.35
3	-0.07	0.11	0.53			
4	-0.26	0.10	0.37	0.45	0.02	0.32

Table 6.2: Parameters of the log-normal fits of the PDFs in Fig. 6.8.

at column densities close to the average column density of the cloud. If these deviations were caused by the gravitational instability, it would mean that the whole cloud is under gravitational collapse. This seems rather unlikely because of the turbulent support of the cloud (mean Mach number of the cloud around 5, Csengeri et al in prep). In region 3, the deviation from the log-normal is at $\ln(\Sigma/\langle\Sigma\rangle) = 1$. This seems coherent with a power-law tail caused by the gravity. Therefore, we fitted two-component log-normals on region 1, 2, and 4 and a single log-normal in region 3. The compression is not seen in region 3 probably because the centre of the molecular cloud is added in the distribution and is at a higher turbulence than the rest of the cloud. Therefore the compression is hidden in the turbulent-enlarged PDF (similarly to what was observed in Chap. 5 at high turbulence). When the distribution includes region 4 (almost the whole cloud), the mean turbulence decreases because of the low turbulence level of the cloud in the south-east region. The parameters of the fits are given in Tab. 6.2. The amplitude of the compressed log-normal decreases when the radius of the region has increased. This is coherent with the picture we got from RCW 120: larger the region, less important the peak, because more and more unperturbed gas is added to the distribution.

Note that in region 2, the deviation from the single log-normal fit (black dotted line) is not an excess but a deficit at high densities that is not even coherent with the effect of gravitational instabilities.

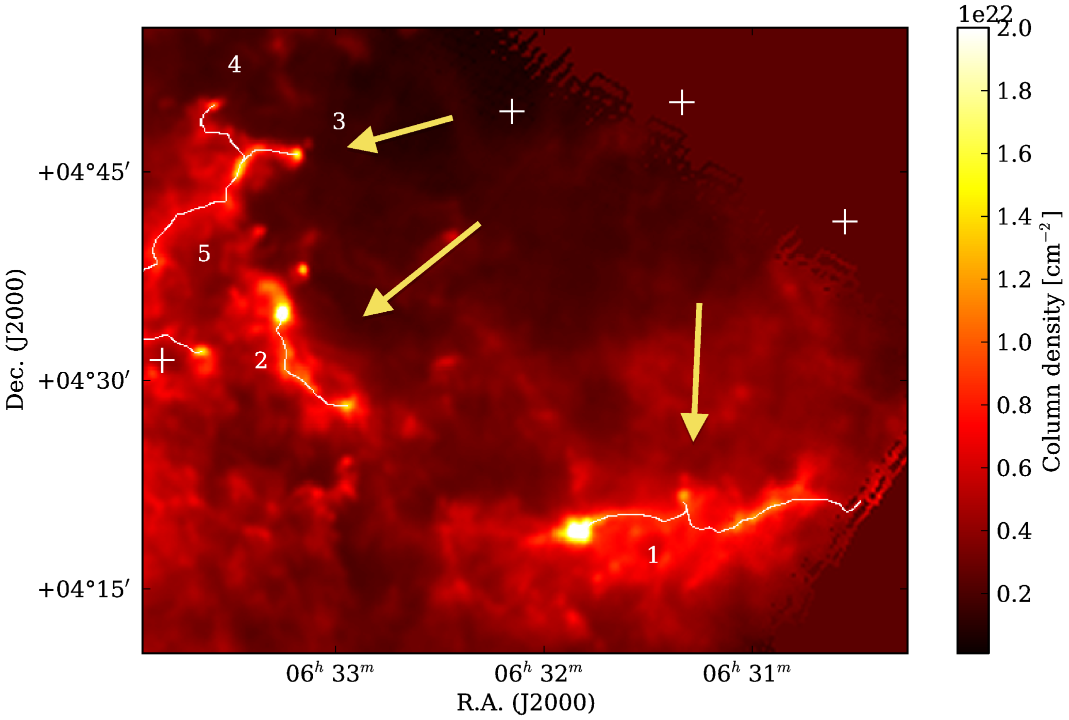

Figure 6.9: Column density map of the interface between the Rosette molecular cloud and the H II region around NGC 2244. The DisPerSe skeleton is drawn in white and each part of the shocked layer is labeled from 1 to 5. The position of the main ionizing sources (O stars) are indicated with the white crosses. The yellow arrows indicate roughly the direction of propagation of the ionizing photons.

6.4.2 Column density structure

Figure 6.9 shows the column density map of the interface between the Rosette molecular cloud and the H II region around NGC 2244. The O stars are indicated with white crosses. The DisPerSe algorithm was used with an intensity contrast level of 4×10^{21} cm^{-2} and a low-density threshold of 5×10^{21} cm^{-2}. These parameters are taken to trace the crests of the main parts of the shock front that can be identified by eye on the column density map. The shock fronts labeled 1, 2 and 4 are perpendicular to the propagation of the ionizing photons, whereas the pillar (labeled 3) and the shock front 5 are parallel to it. The pillar and the shock fronts 4 and 5 are connected together forming a triple point in the skeleton. Another triple point is appearing in the middle of the shock front 1. We performed transverse column density profiles along a piecewise linear segmentation of the DisPerSe skeleton. Figures 6.10 and 6.11 present the averaged profiles on the shock fronts and on the pillar. The extension of the parallel profiles is limited at 2 parsecs to prevent confusion with the other surrounding structures. Similarly to *Peretto et al.* (2012), we defined an asymmetric parameter as the ratio of the integrated column density on either side of the profile peak. It corresponds to the blue area over the red area in Fig. 6.10 and 6.11. The values for the different profiles are indicated in Table 6.3. The shock fronts, parallel to the propagation of the ionizing photons, tend to be more symmetric than the ones perpendicular to it.

We also fitted the inner part of the shock fronts with Gaussian functions (similarly to *Arzoumanian et al.* (2011); *Peretto et al.* (2012)) after subtracting a background set

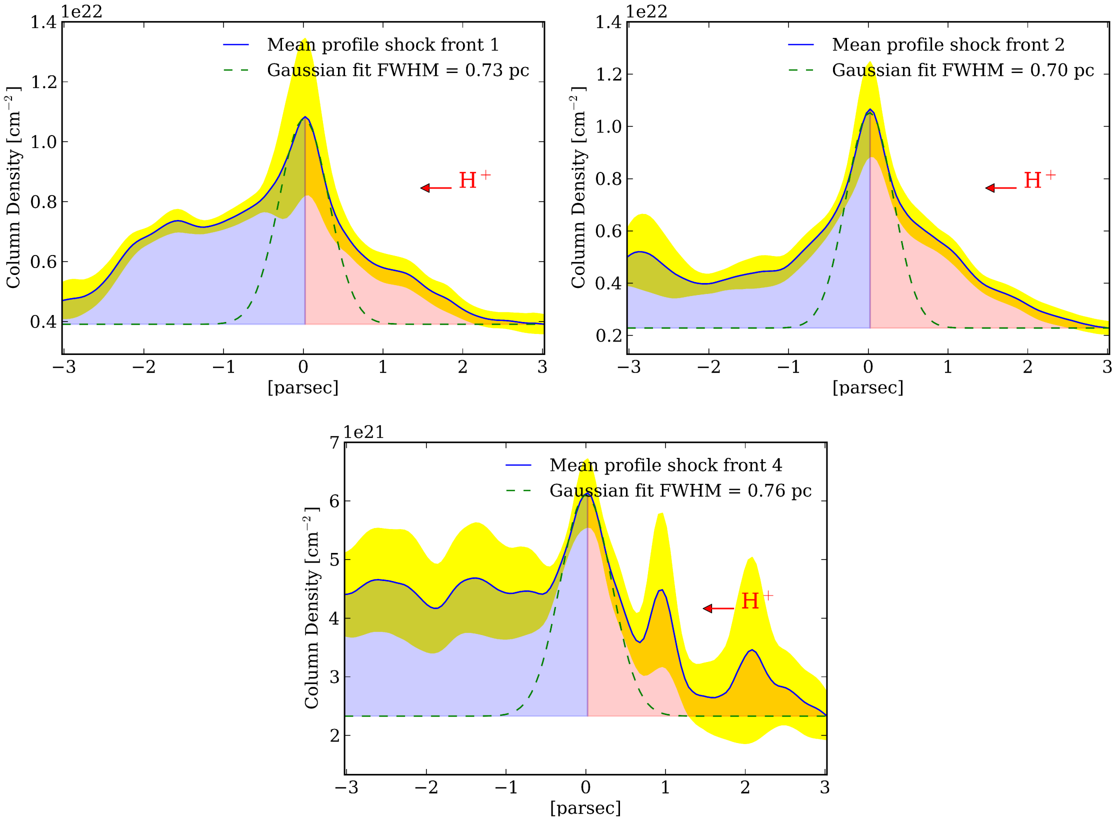

Figure 6.10: Profiles perpendicular to the shock fronts (1, 2 and 4) traced by DisPerSe. These fronts are perpendicular to the direction of propagation of the ionizing photons. The yellow shaded area represents the standard deviation of the profiles. The red arrows indicate on which side ionized gas is present (see also Fig. 6.13 and the Hα emission). The green-dashed curve is the Gaussian fit used to determinate the FWHM width.

at the minimum of the fitted profile. The level of the background does impact the width of the Gaussian profile. However, other choices of the background level only induce small variations of the width (see *Peretto et al.*, 2012). In the present study, we are only interested in comparisons of the width between shocked layers that are parallel or perpendicular to the propagation of photons within a region. This definition leads to a background around the same level in all the profiles considered. There are two possibilities to determine the full width at half maximum (FWHM), fitting Gaussian profiles at each position along the front and take the mean value or fitting a Gaussian profile on the averaged profiles in Fig. 6.10 and 6.11. We used the second strategy and the corresponding deconvolved FWHM values are given in Tab. 6.3. The indicated standard deviation of the FWHM is the standard deviation of the fit of the averaged profile. To compare with the first method, we performed Gaussian fits along the shock front 2 and the pillar. The averaged values of FWHM are 0.69 ± 0.20 pc and 0.55 ± 0.05 pc respectively (see Tab. 6.3). The mean FWHM is in good agreement with the FWHM of the averaged profile (less than 1 % for both cases). However, the standard deviation of the fit of the averaged profile is not representative of the dispersion of the FWHM along the front. In addition of being more asymmetric, the fronts perpendicular to the propagation of the photons have profiles with a higher FWHM ($\approx$ 0.7 pc) than the fronts parallel to it ($\approx$ 0.5 pc).

Comparison with the Collect and Collapse model: Using the formula we derived in Chap. 2 from the collect and collapse scenario, we can check whether this model is

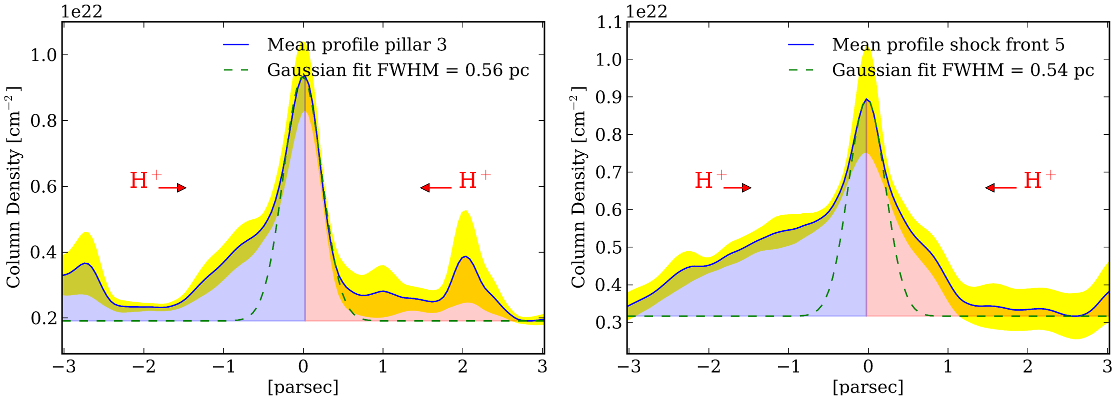

Figure 6.11: Profiles perpendicular to the shock fronts labeled 5 and the pillar labeled 3 traced by DisPerSe. These structures are parallel to the direction of propagation of the ionizing photons.

Shock front	FWHM	σ_{FWHM}	Asymmetry	σ_{asym}
1	0.75	0.29	1.84	0.43
2	0.69	0.20	1.43	0.62
3 (pillar)	0.55	0.05	1.84	0.95
4	0.76	0.23	2.20	1.38
5	0.53	0.25	1.62	0.82

Table 6.3: Deconvolved FWHM width and asymmetric parameter for the averaged profiles of the 5 shock fronts.

appropriate to describe the properties we measured on the column density. We recall quickly the formulas that can be used in function of the initial Strömgren radius R_s and the radius of the shell r_{shell}

$$\begin{aligned}
L_{\text{shell}} &= \frac{1}{3} r_{\text{shell}} \frac{c_0^2}{\zeta c_{II}^2} \left(\frac{R_s}{r_{\text{shell}}}\right)^{-3/2} \\
V_{\text{shell}} &= \sqrt{\zeta} c_{II} \left(\frac{R_s}{r_{\text{shell}}}\right)^{3/4} \\
n_{\text{shell}} &= n_0 \frac{\zeta c_{II}^2}{c_0^2} \left(\frac{R_s}{r_{\text{shell}}}\right)^{3/2} \\
t_{\text{shell}} &= \frac{4}{7} \frac{R_s}{\sqrt{\zeta} c_{II}} \left(\frac{R_s}{r_{\text{shell}}}\right)^{-7/4} \\
n_{II} &= n_0 \left(\frac{R_s}{r_{\text{shell}}}\right)^{3/2}
\end{aligned} \tag{6.2}$$

with L_{shell} the thickness of the shell, V_{shell} its velocity, n_{shell} its density, t_{shell} its age, and n_{II} the density in the H II region. Since the Rosette Nebula is an open H II region, we will suppose that the I-front is D critical, hence $\zeta = 2$.

The initial parameters that are needed for the collect and collapse model are the flux of the ionizing source S_*, the density of the initial medium n_0 and its temperature T_0. We can constrain these parameters thanks to the observations. *Celnik* (1985) estimated the temperature and the density of the ionized gas (model III), we will adopt these parameters, i.e. 15 cm^{-3} at a temperature of 6000 K. This leads to a photon number of 6.5×10^{49} s^{-1} that is in a good agreement with the ionizing flux of a 04V star. The ^{13}CO (1-0) data (see *Heyer et al.*, 2006) present two peaks, one around 10 km/s and one at 15

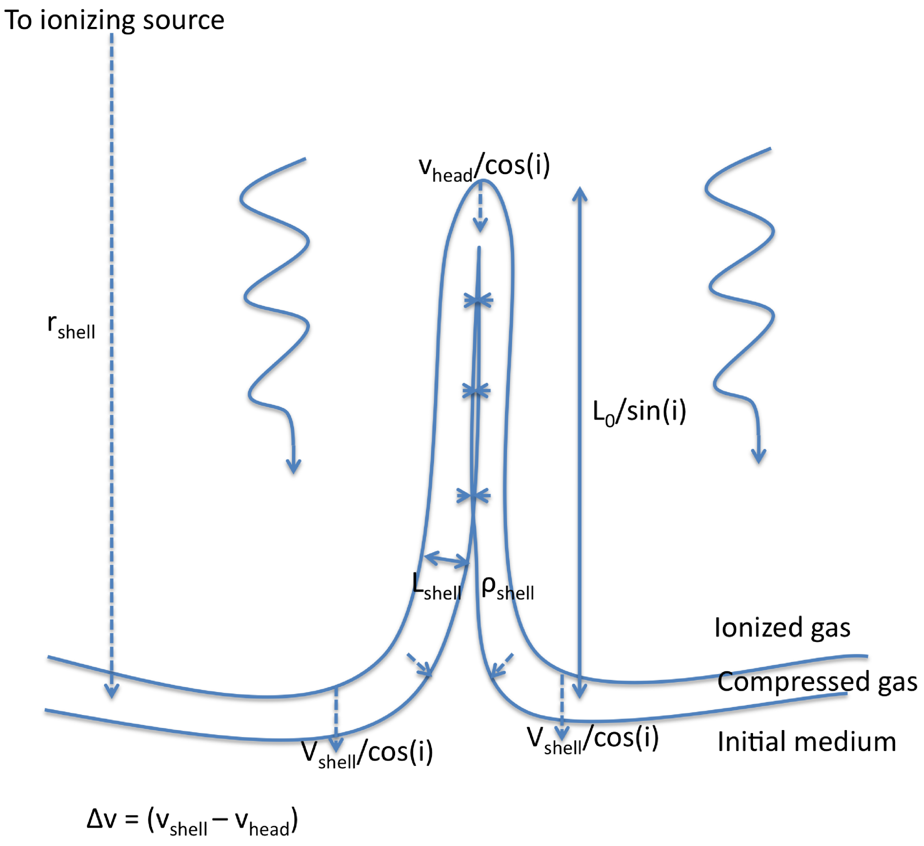

Figure 6.12: Outline of the formation of a pillar by collapse of the shell on itself, with the different variables used in the analytical model. The collapse takes place at $t = t_0$ after the beginning of the expansion of the ionized region. Without the stretching, Δv is neglected and $l_{\rm obs} = l_0$. With the stretching, Δv can be estimated thanks to the molecular line data. Note that l_0 is the initial size projected perpendicular to the line of sight and the velocities $v_{\rm head}$ and $v_{\rm shell}$ are the velocities projected along the line of sight.

km/s. We interpret these two components as the expansion of the shell on the line-of-sight and therefore leads to a shell velocity of 2.5 km/s. Thanks to Eq. 6.2 we can constraint the initial density with the equation on the shell velocity: 350 $\rm cm^{-1}$. The shell thickness is of the order of 0.75 pc and can be used to constraint the temperature in the shell at 120 K.

Now that the initial parameters have been constraint, we can compute the dynamical age of the region, 4.5 My, that is in a good agreement with the age estimation of the cluster 3± 1 My (see *Román-Zúñiga and Lada*, 2008). The H I density in the shell is $3{\times}10^3$ $\rm cm^{-3}$. If we take the half maximum column density of the shocked layer ($\approx 5{\times}10^{21}$ $\rm cm^{-2}$) and the pillar ($\approx 3{\times}10^{21}$ $\rm cm^{-2}$), the line-of-sight depth of the shock front is approximately 1.1 pc and the one of the pillar 0.65 pc. We can conclude that the shock fronts are rather 1D structures that were probably formed when the shell became gravitationally unstable (i.e., when $r_{\rm shell} \approx 8$ pc, see Chap. 2).

Age of the pillar without stretching: The pillar has a FWHM width of 0.55 pc. Its density is given by the density of the compressed shell that is at pressure equilibrium with the ionized gas, i.e. $3{\times}10^3$ $\rm cm^{-3}$ for a H I gas. Therefore, the observed mass per unit length is of the order of 100 $\rm M_\odot$ $\rm pc^{-1}$. If we neglect the stretching of the pillar, the mass per unit length is constant in time. If we assume that the pillar is formed by the collapse

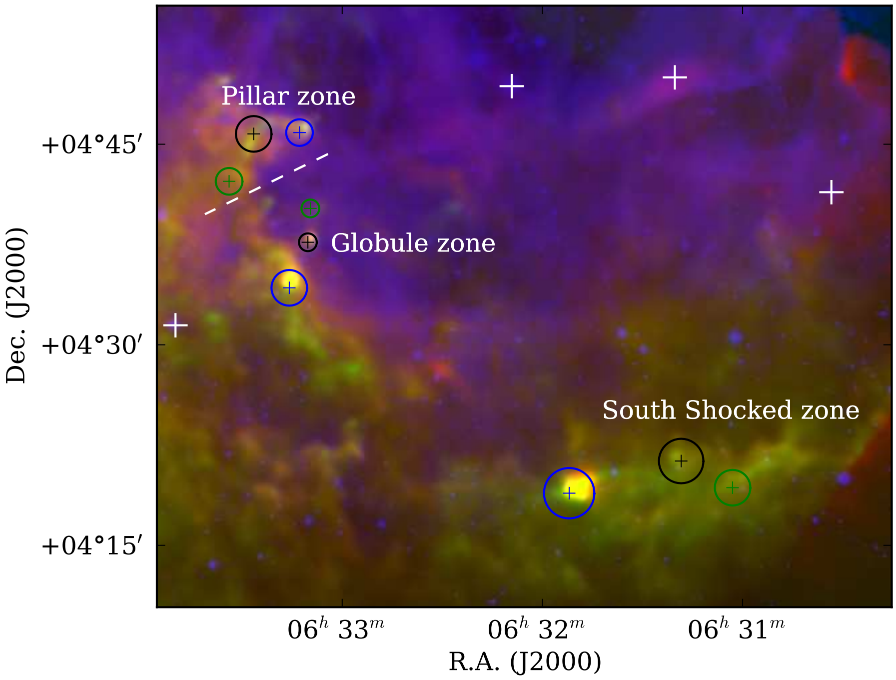

Figure 6.13: Three color image of the interface between the Rosette molecular cloud and the H II region around NGC 2244 (red: PACS 70 μm, green: SPIRE 250 μm, blue: Hα). The white crosses indicate the O stars. Each spectrum in Fig. 6.14 is integrated inside the corresponding colored circle.

of the shell (see Fig. 6.12), we can estimate the mass per unit length from Eq. 6.2

$$\begin{aligned} M_{/l} &= \rho_{\text{shell}} \pi L^2_{\text{shell}} \\ &= \frac{1}{9} \rho_0 \pi r^2_{\text{shell}} \frac{c_0^2}{\zeta c_{II}^2} \left(\frac{R_s}{r_{\text{shell}}} \right)^{-3/2} \end{aligned} \tag{6.3}$$

If we assume that the mass per unit length is constant in time, i.e. $M_{/l} \approx 100$ $M_\odot$ pc^{-1}, we can estimate from Eq. 6.3 that the pillar formed when the shell had a radius of 10.5 pc. The shell was already subject to the gravitational instability at that radius and the formation of the pillar could have been triggered by the fragmentation. However, we have to keep in mind that this result is under the assumption that the mass per unit length remains constant during the evolution of the pillar. The age of the region at the formation time of the pillar is around 3 My, meaning that the pillar could be around 1.5 My old. Note that this result is not affected by the projection: the density in the pillar is taken from a pressure balance and the width of a linear structure is not affected by the projection. We will correct this result with an estimation of the stretching thanks to velocity measurements.

6.4.3 Velocity structure

The bulk velocity of the objects in the interface is investigated thanks to a ^{13}CO 1→0 map of the Rosette molecular cloud. This map was obtained with the FCRAO[6] (see *Heyer*

---

[6] Molecular line observations were taken with the 14 m telescope of the Five College Radio Astronomy Observatory (FCRAO). The FWHM beam sizes of the antenna at the observed frequencies are 4500 (115 GHz) and 4700 (110 GHz). The ^{13}CO 1→0 observations were taken with the 32 pixel focal plane array SEQUOIA using on-the-fly mapping in which the telescope is continuously scanned across the source while rapidly reading the spectrometers.

et al., 2006), with an angular resolution of 45" and an rms noise of 0.6 K. We concentrate our study on the bulk velocity of the main components of the spectra that will be used to compare with the models. The three different regions considered are named pillar, globule and south shocked zone hereafter. The areas on which integrated spectra are performed are indicated on the three-color image in Fig. 6.13 and the corresponding spectra on Fig. 6.14.

In the south shocked zone, the blue and green spectra indicates the mean velocity of the east and west parts of the shock front, respectively. The east part has a velocity of the order of 14-15 km/s, the west part of the order of 13 km/s. These two velocity components join at the triple point that was previously identified in the DisPerSe skeleton (see Fig. 6.9), where the black spectrum is integrated. Moreover, there are also two other velocity components in the black spectrum, at 11 km/s and 19 km/s. The triple point has a complex velocity structure that can be linked to pillar formation models that we showed in Chap. 4. In that picture, the blue-shifted and red-shifted components of the black spectra are parts of the shell that are collapsing toward the central part of the front. The blue-shifted component is shifted at a velocity of -2 km/s compared to the central part that is coherent with the velocity of the shell derived from Eq. 6.2. The red-shifted part is at a higher velocity compared to the central part, +4 km/s. However, this high shift could be explained by a projection effect and a slightly higher velocity of the shell (e.g. if $\gamma = 5/3$). The multiple-component spectra is then a signature of the formation of a pillar as suggested in Chap. 4. This picture is strengthened by the triple point on the DisPerSe skeleton that also suggests the presence of a nascent pillar.

In Fig. 6.13, the blue spectrum in the globule zone is integrated around a clump in the shock front 2 and the black and green ones are integrated around the globules north of the front. The shock front 2 is used as a reference of a nearby shocked region. The globules could be close to the front only because of a projection effect. However, their Hα illumination is comparable to the one of the edge of the front, suggesting they are indeed close to the front. The shock front 2 has a mean velocity of 15 km/s, while the two globules have mean velocities around 18 and 21 km/s. Therefore, the globules have velocities red-shifted at +3 and +6 km/s relative to the nearby front whereas, a pillar has a coherent velocity with the connected fronts. This supports the turbulent origin of globules that was proposed in chap. 5. Note that a shift of +6 km/s is very high compared to the velocity of the shell. If the globule had the same velocity as the shell, such a difference could only be explained if the globule and the blue area around the clump were at two extremities of the bubble (i.e. 40 pc away) which seems rather unlikely.

In the pillar area, the blue spectrum is integrated around the head of the pillar, the black one around the triple point connecting the pillar to the shock front 4 and 5 and the green one is integrated on a part of the shock front 5. The main component of the spectra are centered around the same velocity, 10-11 km/s. The shock front 4, at the north of the pillar has a velocity also centered around the same velocity. Although the base and head of the pillar are around the same velocity (compared to the globules), there is a gradient of 1 km/s between the black and green spectrum. As the pillar appears dark in Hα, we can estimate that the pillar is between the observer and the ionizing source. The base is therefore closer to us than the head. Since the base is blue-shifted relatively to the head, it means that the pillar is stretched and its size increases in time, because of the velocity shift of 1 km/s between the head and the base.

Age and initial size of a pillar with stretching: If we assume that the pillar had an observed size l_0 when it was formed (see Fig. 6.12), we can link its age to its actual size by

$$\Delta t = t_{\text{obs}} - t_0 = \frac{l_{\text{obs}} - l_0}{\tan(i)\Delta v} \tag{6.4}$$

with i the angle between the pillar and the line of sight. Because of the velocity shift, there is a stretch of the pillar and therefore Eq. 6.3 has to be corrected by

$$\begin{aligned} M_{/l_{\text{obs}}} \times l_{\text{obs}}/\sin(i) &= \rho_{\text{shell}} l_0/\sin(i) \times \pi L^2_{\text{shell}} \\ &= \frac{1}{9}\rho_0 \pi l_0/\sin(i) \times r^2_{\text{shell}} \frac{c_0^2}{\zeta c_{II}^2} \left(\frac{R_s}{r_{\text{shell}}}\right)^{-3/2} \end{aligned} \tag{6.5}$$

with r_{shell}, the radius of the shell at the formation time of the pillar. We can extract l_0/l from Eq. 6.4 and 6.5 to get the equation

$$1 - \frac{\tan(i)\Delta v}{l_{\text{obs}}} \left(t_{\text{obs}} - \frac{4}{7} \frac{R_s}{\sqrt{\zeta} c_{II}} \left(\frac{R_s}{r_{\text{shell}}}\right)^{-7/4} \right) = \frac{9 M_{/l_{\text{obs}}} \zeta c_{II}^2}{\rho_0 \pi R_s^2 c_0^2} \left(\frac{R_s}{r_{\text{shell}}}\right)^{7/2} \tag{6.6}$$

We define the following variables

$$\begin{aligned} X &= (R_s/r_{\text{shell}})^{7/4} = t_s/t_0 \\ t_s &= 4R_s/7\sqrt{\zeta} c_{II} \\ t_v &= l_{\text{obs}}/\tan(i)\Delta v \\ \alpha &= \rho_0 \pi R_s^2 c_0^2 / 9 M_{/l_{\text{obs}}} \zeta c_{II}^2 \end{aligned} \tag{6.7}$$

The equation becomes a third-degree polynomial equation of the type $X^3 + pX + q = 0$ with

$$\begin{aligned} p &= \left(\frac{t_{\text{obs}}}{t_v} - 1\right)\alpha \\ q &= -\frac{t_s}{t_v}\alpha \end{aligned} \tag{6.8}$$

The solution can be computed thanks to the method of Cardan. We can compute the limit case, $\Delta v = 0$, that gives $X = \sqrt{\alpha}$. It is equivalent to Eq. 6.3, i.e. the no-stretching case ($l_0 = l$). For the pillar in Rosette ($\Delta v = 1$ km/s, $l_{\text{obs}} \approx 2$ pc, and $t_{\text{obs}} \approx 4.5$ My), if the angle between the pillar and the line of sight is lower than 3° then $t_{\text{obs}} \ll t_v$ (one order of magnitude). In this limit $q^2 \ll p^3$ and therefore we still have $X \approx \sqrt{\alpha}$ and no stretching. However, it is rather unlikely that $i = 3°$, it would mean that the pillar is actually 38 pc! The discriminant is given by $\Delta = q^2 + p^3 \times 4/27$. When Δ is less than zero, there are three real solutions and X is given by

$$X = X_{\Delta^-} = 2\sqrt{\frac{-p}{3}} \cos\left(\frac{1}{3} \arccos\left(\frac{-q}{2}\sqrt{\frac{27}{-p^3}}\right)\right) \tag{6.9}$$

to get back $X = \sqrt{\alpha}$ when $q = 0$. If Δ is positive

$$X = X_{\Delta^+} = \sqrt[3]{\frac{-q + \sqrt{\Delta}}{2}} + \sqrt[3]{\frac{-q - \sqrt{\Delta}}{2}} \tag{6.10}$$

If $i \geq 85°$ then $q^2 \ll \Delta$ and the solution can be approximated by

$$X = X_v = \frac{t_s}{t_0} \approx -\frac{q}{p} \approx \frac{t_s/t_v}{t_{\text{obs}}/t_v - 1} \tag{6.11}$$

If the pillar is nearly edge on (i.e. 85°), its age goes down to 170 ky. In that case, the time at which the pillar started to form t_0 is just $t_{\text{obs}} - t_v$ meaning that the pillar is completely

$i \leq 3°$	$3° \leq i \leq 75°$	$3° \leq i \leq 75°$	$i \geq 75°$	$i \to 90°$
$\Delta \leq 0$	$\Delta \leq 0$	$\Delta \geq 0$	$\Delta \geq 0$	$\Delta \geq 0$
$t_0 \approx t_s/\sqrt{\alpha}$	$t_0 = t_s/X_{\Delta-}$	$t_0 = t_s/X_{\Delta+}$	$t_0 \approx t_{\mathrm{obs}} - t_v$	$t_0 \approx t_{\mathrm{obs}}$
$l_0 \approx l_{\mathrm{obs}}$	$l_0 = X^2_{\Delta-} l_{\mathrm{obs}}/\alpha$	$l_0 = X^2_{\Delta+} l_{\mathrm{obs}}/\alpha$	$l_0 = X^2_v l_{\mathrm{obs}}/\alpha$	$l_0 \approx t^2_s l_{\mathrm{obs}}/\alpha t^2_{\mathrm{obs}}$

Table 6.4: Initial size and formation time for a pillar in function of its angle with the line of sight velocity. The limit on the angles are computed in the case of Rosette pillar.

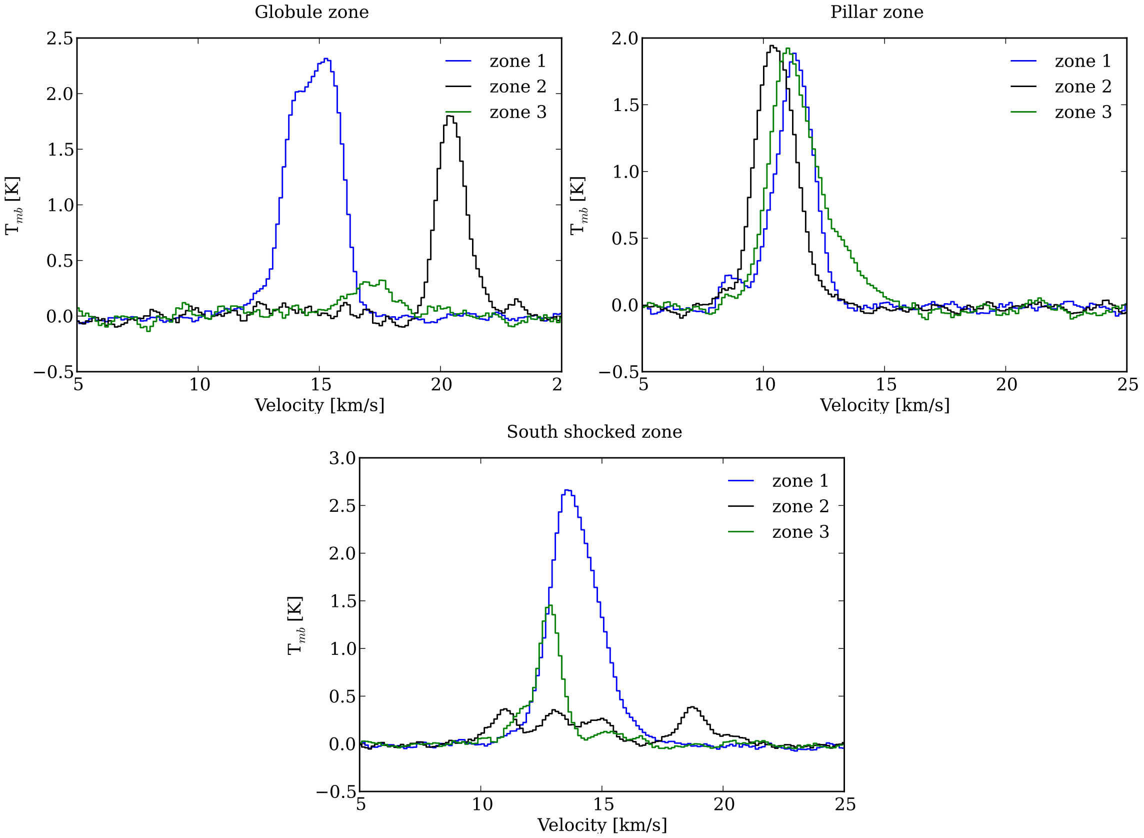

Figure 6.14: ^{13}CO 1→0 integrated spectra in the three sub-regions of the interface . The spectra are spatially integrated in the colored circles showed in Fig. 6.13.

formed by the difference of velocity. The formation time does not depend on the shell parameters. In the limit $i \to 90°$, its age tends to zero. The initial size of the pillar is always given by $l_0 = X^2 l_{\mathrm{obs}}/\alpha$. It is interesting to note that there is a limit to the initial structure, even in the case of instantaneous formation, given by $t_s^2 l_{\mathrm{obs}}/\alpha t^2_{\mathrm{obs}}$. For the pillar in Rosette, the limit of the initial size of the structure is 50 % of the observed size of the pillar. Note that this analysis makes the assumption that the mass of the pillar remains constant. This is wrong for two reasons, first we know that the head of the pillar is being evaporated by the ionization and second, the mass of the pillar increases because there is matter accumulation at its base (see Chap. 4). Nevertheless, the precedent analysis should give a good approximation of the reality. Provided that the age of the pillar is not too big, the evaporation can be neglected because we are in quasi-steady state similar to the one reached by a globule in the RDI scenario. Besides, the matter accumulation at the base changes the density but should not change the velocity shift between the head of the pillar and the rest of the shell. Therefore, the initial size and evolution is not influenced by this phenomenon.

Thanks to this analytical model, it is possible to predict the age and initial size of a pillar assuming it is formed by the collapse on the shell on itself. The result is biased by the angle between the pillar and the line of sight but other information like the illumination could be used to clear this ambiguity. This model will also be used on the Pillars of Creation in the Eagle Nebula.

6.5 Eagle Nebula

The Eagle Nebula is located in the constellation of Serpens at 1.8 kpc from the Sun (*Bonatto et al.*, 2006). A young stellar cluster NGC 6611 is ionizing the molecular gas of this star forming region. The principal ionizing sources are a O4 and O5 stars whose combined ionizing flux is of order 2×10^{50} s^{-1} (*Hester et al.*, 1996; *White et al.*, 1999). The discovery of pillars of gas by the Hubble space Telescope (*Hester et al.*, 1996) popularized this region with the name of “Pillars of Creation”. Many spectral line studies enlightened (see *Pound*, 1998; *White et al.*, 1999; *Allen et al.*, 1999; *Urquhart et al.*, 2003; *Linsky et al.*, 2007, among others). Recently, *Flagey et al.* (2011) studied dust spectral energy distribution (SED) thanks to *Spitzer* data. They show that the SED cannot be accounted by interstellar dust heating by UV radiation. An extra source of pressure is needed to match the mid IR flux. They proposed two explanations for this source of pressure: stellar winds or a supernova remnant. *Herschel* provides new observations on the region and *Hill et al.* (2012) studied in detail the impact of the ionizing source on the temperature of the molecular gas. We will use the same *Herschel* map to study the structure of the cold molecular gas at the interface with the H II region. In subsect. 6.5.1, we investigate the large-scale structure of the cloud thanks to the PDF of the gas, in function of the distance from the ionizing source. In subsect. 6.5.2, we investigate the column density structure of the edge of the molecular cloud, and in subsect. 6.5.3, we concentrate on the velocity structure of two sub-regions of the interface: the Pillars of Creation and SFO30.

6.5.1 Probability density function

We showed in the Rosette Nebula that the compression from the ionization is identifiable on the PDFs of the gas. In the Eagle Nebula, this signature is even clearer. Figure 6.15 shows the different areas on which the PDFs in Fig. 6.16 are computed. Each disk contains the smaller ones, therefore, Fig. 6.16 shows the evolution of the shape of the PDF while increasing the radius of the disk around the ionizing sources. In Rosette, a double peak was visible at small radius and only a large high-density excess was visible at bigger radius. In M16, the double peak is clearly visible even at high radius (region 4). Such a double peak is with almost no doubt, the signature of the compression from ionization. Gravitational instabilities would only give a power-law tail. This deviation with a power law can be identified at $\ln(\Sigma/\langle\Sigma\rangle) \approx 1.5$. The parameters for the fits are given in Tab. 6.5. As for RCW 120 and Rosette, the amplitude of the low-density peak increases with radius and the one of the compressed peak decreases with distance (although it is rather marginal in M16 case). This trend is coherent with a compression whose source is the ionization of the central cluster. The shift between the two peaks is of the order of 0.9. This leads to a compression factor of 2.5 in column density. This is rather low compared to the factor 10 that we got in the previous section. However, as already explained for Rosette, this difference can be explained by a projection effect. The compressed structures are rather 1D structures because of the fragmentation, therefore, in column density they do not appear as compressed as the model predicts.

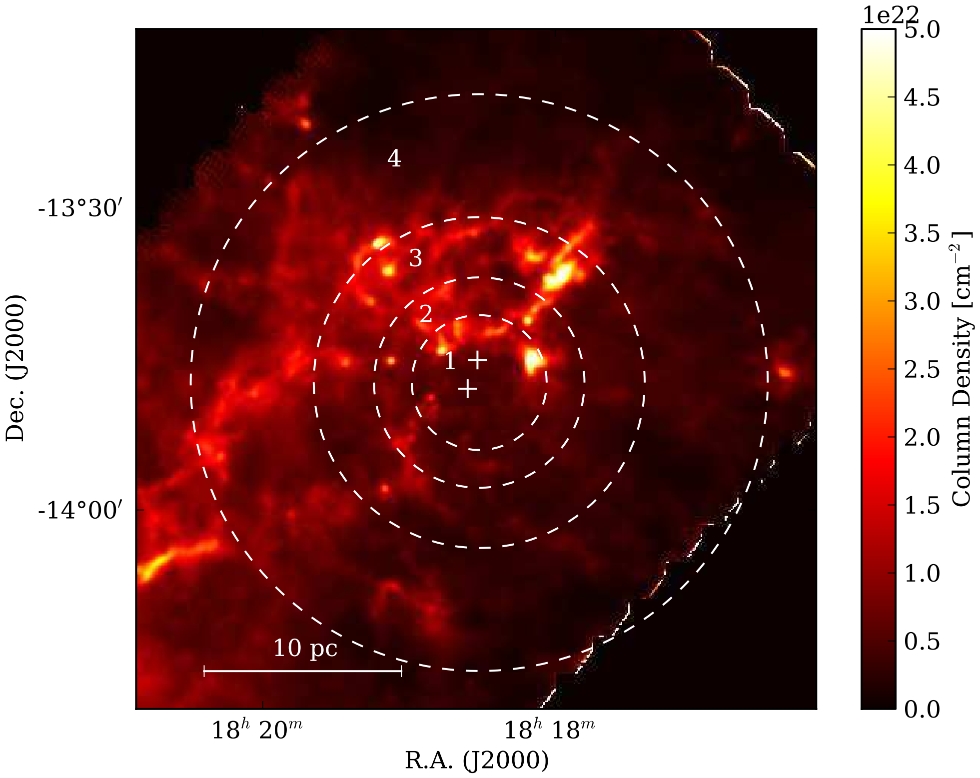

Figure 6.15: M16 *Herschel* column density map. The circles indicate the different regions used for the PDFs. The regions are inclusive (region 2 contains region 1 ...). The white crosses indicate the position of the main ionizing sources. The third region indicates the limit of the Hα emission and the limit of the H II region (although it is not a spheric H II region in M16).

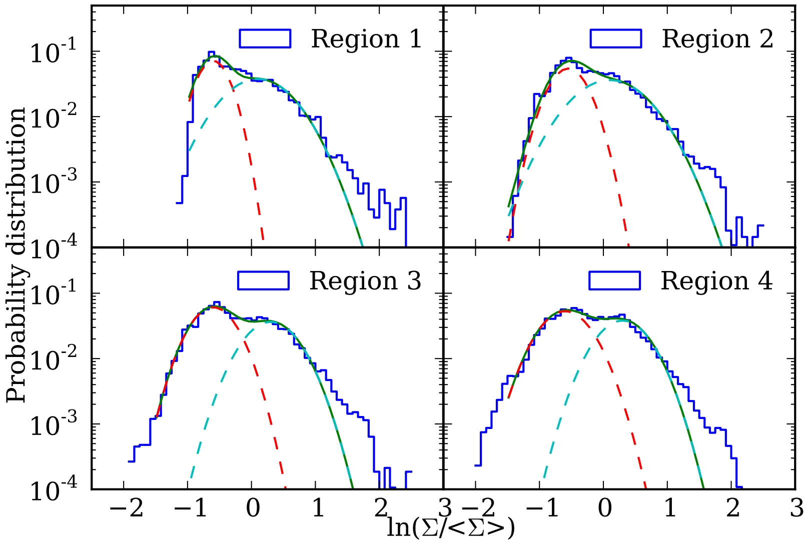

Figure 6.16: M16 PDFs on the four regions indicated in Fig. 6.15. The multi-component fit is done using log-normal distributions.

Region	s_0	p_0	σ_0	s_1	p_1	σ_1
1	-0.6	0.04	0.22	0.10	0.05	0.48
2	-0.55	0.04	0.27	0.10	0.05	0.51
3	-0.60	0.05	0.31	0.30	0.04	0.38
4	-0.60	0.05	0.36	0.30	0.04	0.37

Table 6.5: Parameters of the log-normal fits of the PDFs in Fig. 6.16.

6.5.2 Column density structure

Figure 6.17 shows the *Herschel* column density map around the main ionizing sources of NGC 6611 (white crosses). The DisPerSe Skeleton is in white and the different parts that are studied labeled from 1 to 5. The pillar 2 is usually named the "spire", while the part labeled 4 is running through the three pillars of Creation of the *Hubble* image. Note that DisPerSe connects the heads of two of the pillars of Creation. This is not physical and caused by the limited resolution of the map and the threshold used to trace the skeleton. Therefore, we used a column density map without the data at 500 μm to improve the resolution. Figure 6.18 shows that DisPerSe is able to trace correctly the pillars when the resolution is improved. Note that there is a fourth nascent pillar at the west of the pillars of creation, the triple point in the skeleton is visible on Fig. 6.18. Unfortunately, we do not have velocity information on this nascent pillar to test whether the shell is collapsing at this point (as we did in the Rosette region).

The profiles of the different parts of the DisPerSe skeleton are shown in Fig. 6.19 and 6.20. The parameters of the Gaussian fits of these profiles are indicated in Tab. 6.6. The shell width (deconvolved FWHM) is bigger than in the Rosette molecular cloud, between 0.75 and 0.9 pc. These variations between the shock fronts 1, 3, and 5 can be explained by inhomogeneities in the initial density field. Figure 6.20 presents the profiles of the pillars 2, 4a and 4b. The width of the "spire" is around 0.55 pc, while the pillars of Creation have a width of 0.36 and 0.32 pc respectively.

Comparison with the Collect and Collapse model: We can estimate the different theoretical properties of the shell from the collect in a homogeneous medium. We will take here an average width for the shell around 0.8 pc. We estimate the radius of the ionized bubble thanks to the distance of the ionizing stars to the base of the Spire pillar. This is the maximum extension of the ionized gas from the central source. In other direction the extension of the ionized gas is smaller but this could be an effect of the line of sight. Therefore we make the assumption that the bubble is spherical in 3D with a radius around 7 pc. From Eq. 6.2, we can estimate the initial Strömgren radius and density from the width of the shell and the size of the bubble. They are respectively 0.13 pc and 5.5×10^4 cm^{-3}. The density in the shock layer should be of the order of 1.6×10^5 cm^{-3}. However, this density for the shell implies that the line-of-sight depth of the structure is less than 0.1 pc. This value is almost one order of magnitude lower than the observed width and seems to be incoherent. The problem we are facing can be seen in an other way. If we take the shock front 1, which has the highest column density, and make the assumption that it is a 1D structure, we get an upper bound for the density in the shock gas of 2×10^4 cm^{-3}. The corresponding maximum pressure is of the order of 4×10^5 K cm^{-3} that is rather low. *White et al.* (1999) estimated an electron density in the pillar area around 100-500 cm^{-3} that corresponds to a pressure for the ionized gas of $2-8\times10^6$ K cm^{-3}. The Rankine-Hugoniot conditions at the I-front impose that the pressure in the shock region is twice the pressure of the ionized region when the I-front is D-critical and decreases to be equal to the ionization pressure for a weak D-type front. This condition is far from being met here.

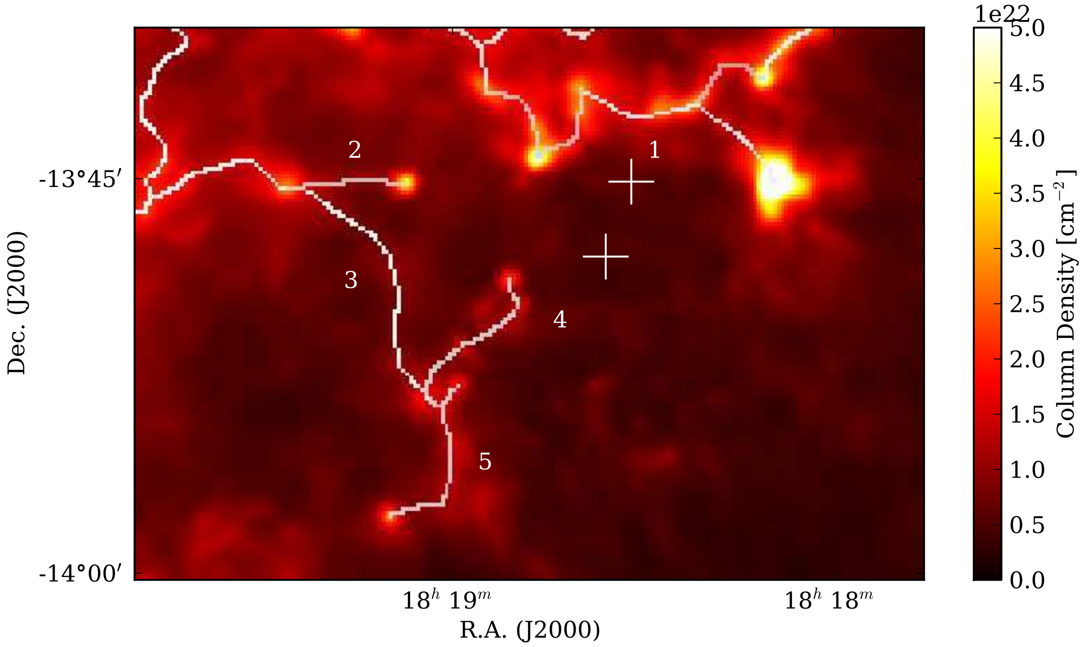

Figure 6.17: Column density map of the interface between the Eagle Nebula and the H II region around NGC 6611. The DisPerSe skeleton is drawn in white and each part of the shocked layer is labeled from 1 to 5. The position of the main ionizing sources (O stars) are indicated with the white crosses.

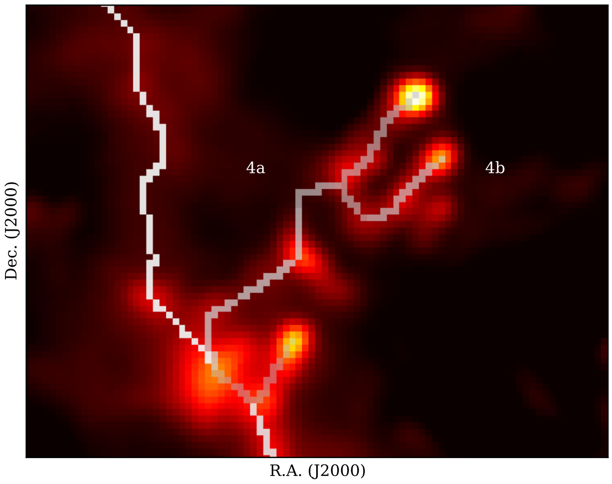

Figure 6.18: Column density map around the Pillars of Creation at a resolution of 18" (without 500 μm). The two pillars named Π_1 and Π_2 in *White et al.* (1999) are labeled 4a and 4b.

One (if not the only) solution of this problem is to suppose that the dense gas in the shell is at higher pressure and therefore at a higher temperature. This requirement is also supported by the *Spitzer* observations in *Flagey et al.* (2011) who proposed stellar winds or supernova remnant to be the source of this extra pressure. If we assume a temperature of 400 K for the shell, the initial density is of the order of 3.5×10^3 cm^{-3} and the H_2 density in the shock layer is 5×10^3 cm^{-3}. Then, the depth of the shell along the line of sight is of the order of 0.8 pc, that is much more in agreement with the observed thickness. The

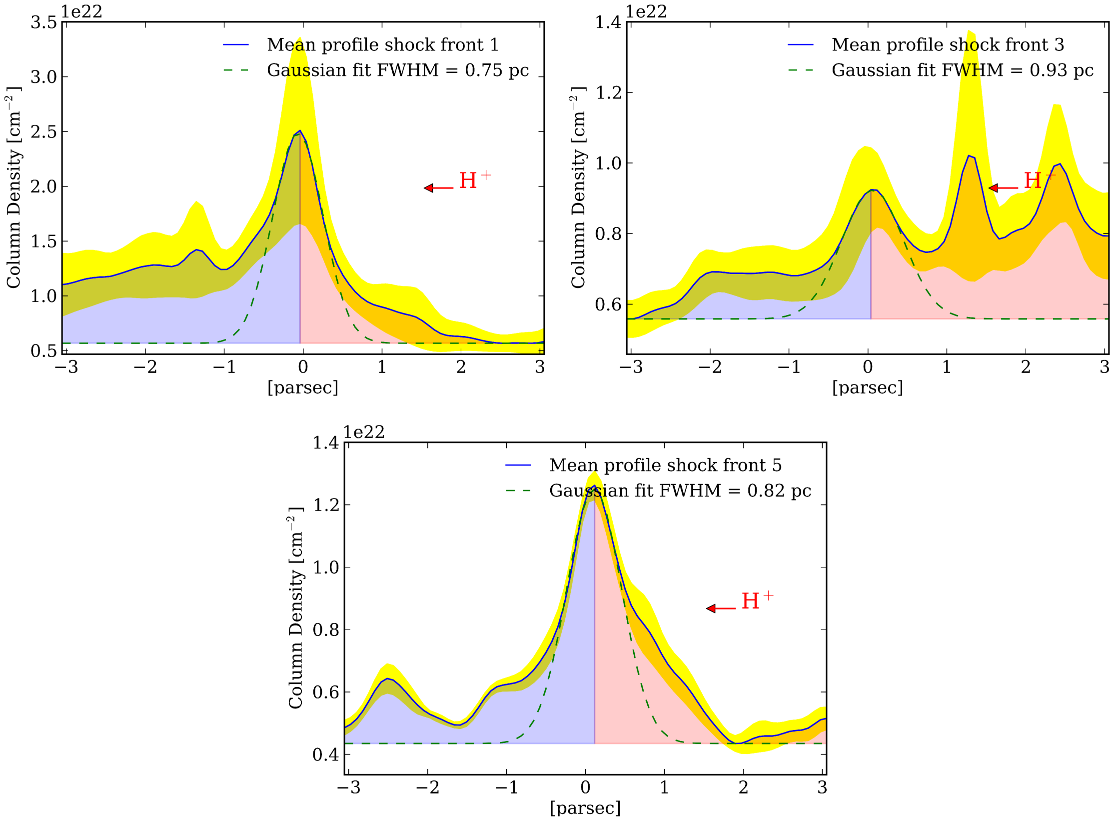

Figure 6.19: Profiles perpendicular to the shock fronts (1, 3 and 5) traced by DisPerSe. These fronts are perpendicular to the direction of propagation of the ionizing photons. The yellow shaded area represents the standard deviation of the profiles. The red arrows indicate on which side ionized gas is present (see also Fig. 6.21 and the Hα emission). The green-dashed curve is the Gaussian fit used to determine the FWHM width.

shock fronts seem to be 1D structure, similarly to what was found in Rosette, although more data are required to better constrain the model.

6.5.3 Velocity structure

There are not much spectral-line observations of the whole M16 nebula. The majority of the studies are concentrated on the Pillars of Creation and SFO30 at the north of them. We took public data taken from the James Clerk Maxwell Telescope (JCMT[7]) to get some information about the velocity structure of the pillars and the north area of the cavity. Figure 6.21 is a three-color (70/250 Herschel + Hα in blue) image around the ionized bubble on which we indicated the different areas studied thanks to these ^{12}CO 3-2 spectral-line data taken at JCMT. We divided the analysis in three main areas, pillar 1, pillars 2 and 3, and SFO30 and the spectra are shown in Fig. 6.22.

The SFO30 area presents a complex velocity structure with a gradient from east to west of 3 km/s (from +17.5 km/s (cyan spectrum) to 20.5 km/s (blue spectrum)). This gradient is very important compared to the typical velocity of the shell, 2 km/s from Eq. 6.2. It would suggest a change in orientation of more than 90° in a small area, unless there is a large confusion on the line of sight. The different spectra are also wide compared

---

[7] JCMT is operated by the Joint Astronomy Centre on behalf of the Science and Technology Facilities Council of the United Kingdom, the Netherlands Organisation for Scientific Research, and the National Research Council of Canada.

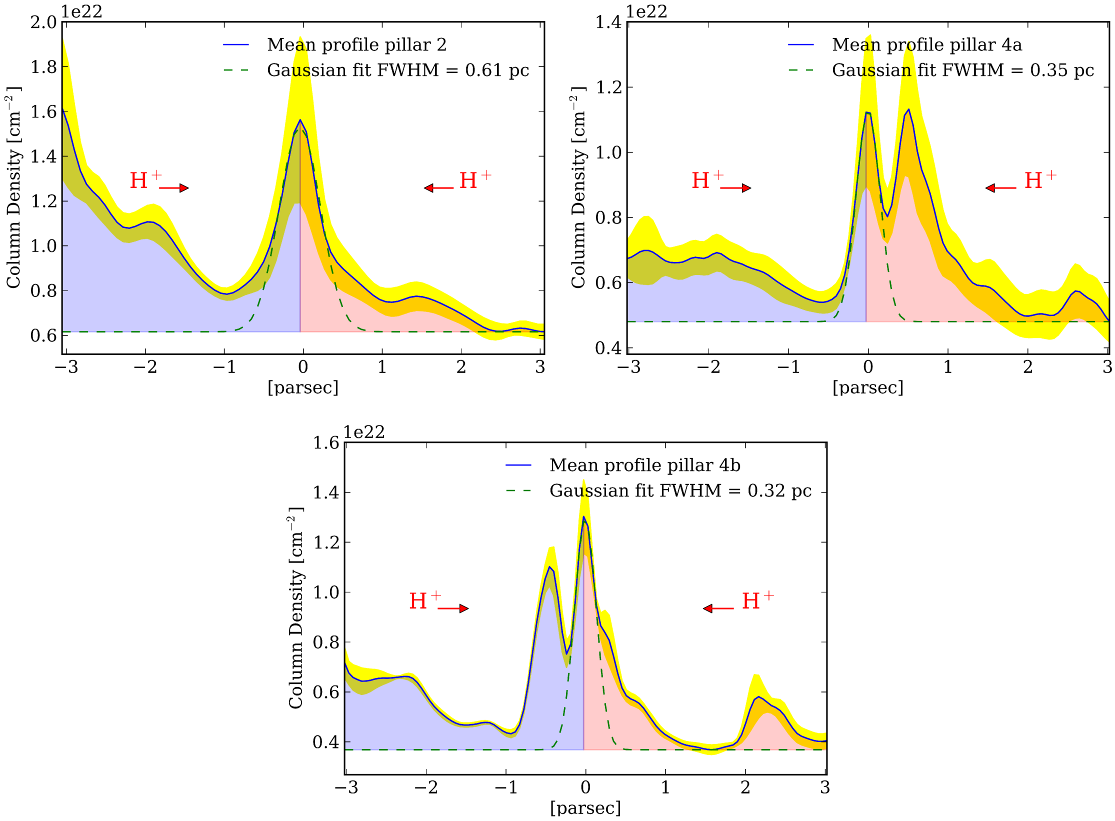

Figure 6.20: Profiles of the pillars fronts (2 (Spire), 4a (pillar of Creation Π_1) and 4b (pillar of Creation Π_2)) traced by DisPerSe. The yellow shaded area represents the standard deviation of the profiles. The red arrows indicate on which side ionized gas is present (see also Fig. 6.21 and the Hα emission). The green-dashed curve is the Gaussian fit used to determinate the FWHM width (red, green cyan for pillar 4).

to the pillar areas. All these properties suggest that the SFO30 region is more complex than a collect phase on a homogeneous medium, with two possibilities: there are density inhomogeneities and the region is closer to the cluster than the 7 pc calculated above; or there are initial velocity fluctuations that caused these gradients. Both cases suggest that the turbulence in the initial medium may be important here and limits the possibility to predict the properties of the shell with the models we used for Rosette. Despite these limits, we will apply the same analysis to the pillars of Creation whose velocity structures seem less influenced by the initial turbulence.

The area named pillar 2 and 3 contains two of the Pillars of the Creation. The blue and cyan spectra are integrated around the heads of the pillars and the black and green are integrated along pillar 2. The pillar 1 area contains the biggest of the three pillars of Creation and the base under the pillars (from which the pillars seem disconnected in almost all the data (see *White et al.*, 1999)). The blue spectrum is integrated around the head of the pillar, the black around the middle and the green and cyan around the base. The first thing to notice is that the pillar 1 has a velocity around +26 km/s while the pillars 2 and 3 have a velocity around +22.5 km/s. This difference was already seen by *White et al.* (1999) and can be interpreted as a difference of orientation and location of the pillars. Indeed, in the *Hubble* image of *Hester et al.* (1996), the pillar 1 and the base appear illuminated while the pillars 2 and 3 appear dark. Therefore the pillar 1 and the base are behind the ionizing source, at the back of the cavity while the pillars 2 and 3 are

Shock front	FWHM	σ_{FWHM}	Asymmetry	σ_{asym}
1	0.73	0.25	2.45	1.55
2 (pillar)	0.55	0.19	2.64	1.26
3	0.89	0.17	0.63	0.48
4a (pillar)	0.36	0.08	1.01	0.44
4b (pillar)	0.32	0.07	1.80	0.43
5	0.83	0.15	1.12	0.31

Table 6.6: Deconvolved FWHM width and asymmetric parameter for the averaged profiles of the 5 shock fronts.

between the ionizing source and us.

The three spectra that are integrated around the heads of the pillars (blue for pillar 1, blue and cyan for pillars 2 and 3) also show a small component at 30 km/s. However, this component is not related to the pillars since it can also be observed away from them. The black spectra in the pillar 1 is enlarged towards velocities around +23 km/s. This is probably caused by a line-of-sight projection of the material connecting the pillars 1 and 2 (already suggested in *White et al.* (1999)).

Age and initial size of the pillars with stretching: It is interesting to note that the pillars 1 and 2 present velocity gradients. For the pillar 1 ($l_{\rm obs} = 1.6$ pc), the head is blue-shifted at 0.3 km/s compared to the base and for the pillar 2 ($l_{\rm obs} = 1$ pc) the head is red-shifted at 0.5 km/s. Because of the observed orientation, the head of the pillar 1 is between the base and us therefore the pillar is in extension and the opposite orientation of the pillar 2 also leads to a pillar in extension. Note that the fact that pillars are observed in extension is in good agreement with all the models we proposed in Chap. 4 and 5 that predict growing pillars. The half-maximum column density along the pillars 1 and 2 is 4×10^{21} cm^2 and the width of the pillars are respectively 0.36 and 0.32 pc (see Sect. 6.5.2). The averaged mass per unit length of the pillars deduced from the fits are 32 and 29 M$_\odot$ pc^{-1}. With these values, the stretching on the pillar 1 is negligible if $i \leq 19°$ and the initial structure will be negligible if $i \geq 87°$, with a limit for the initial size at 5 % of the observed size. For the pillar 2 the stretching is negligible if $i \leq 7°$ and the initial structure is negligible if $i \geq 80°$, with a limit for the initial structure that is also around 4 % of the observed size. In both cases the limit on the angles suggest that both stretching and initial size of the structure are important in their formation.

6.6 RCW 36

RCW 36, at a distance of 700 pc from the Sun (*Murphy and May*, 1991), is one hourglass-shaped environment. At the centre, an embedded cluster, 2-3 Myr old, has 350 members with the most massive star being a type O8 or O9 (*Baba et al.*, 2004). The cluster extends over a radius of 0.5 pc, with a stellar surface number density of 3000 stars pc^{-2} within the central 0.1 pc. FIR emission and radio continuum emission are reported to be consistent with the presence of an H II region (*Verma et al.*, 1994). The star cluster has probably inflated the G265.151+1.454 H II region (*Caswell and Haynes*, 1987) that is responsible for the Hα emission originally observed by *Rodgers et al.* (1960). Looking at larger scales, RCW 36 is located within the Vela C molecular cloud that consists of an apparent network of column density filaments (*Hill et al.*, 2011). Such filaments are star formation sites. Herschel observations of low-mass star-forming molecular clouds (e.g. *Arzoumanian et al.*, 2011) show that stars form in supercritical filaments while *Schneider et al.* (2012a) propose that massive star cluster-formation sites correlate with filament network junctions. Among

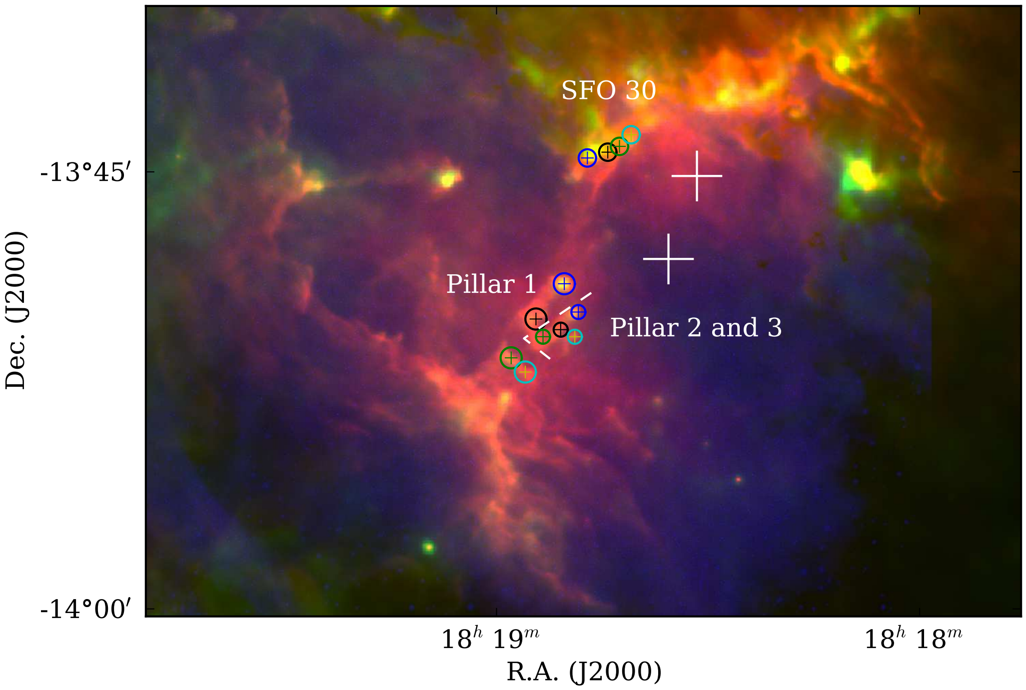

Figure 6.21: Three color image of the interface between the Eagle Nebula cloud and the H II region around NGC 6611 (red: PACS 70 μm, green: SPIRE 250 μm, blue: Hα). The white crosses indicate the O stars. Each spectrum in Fig. 6.22 is integrated inside the corresponding colored circle.

the networks of filaments in Vela C, there is a more prominent and elongated interstellar dust structure of $\approx$ 10 pc in length that is named the Centre-Ridge by *Hill et al.* (2011). It encompasses RCW 36, which is at its Southern end. In subsect. 6.6.1, we investigate the large-scale structure of the cloud around RCW 36 thanks to the PDF of the gas, in function of the distance from the ionizing source. In subsect. 6.6.2, we investigate the column density structure of the edge of the molecular cloud and in subsect. 6.6.3, we concentrate on the velocity structure of the dense gas around the H II region. We finally investigate in subsect. whether the dense clumps around RCW 36 were pre-existing or were triggered by the ionizing source, thanks to dedicated numerical simulations.

6.6.1 Probability density function

We study the large scale structure of the region around RCW 36. Figure 6.23 is a *Herschel* column density map of the Vela C molecular cloud overlapped with the different regions used for the PDFs. All the disks include the smaller ones. The first region corresponds to the extension of the ionized gas. Note that this region is not well sampled here because of the lack of resolution (only 6000 pixels). Despite of this limit, the PDF presents two components. The high-density component consists of the dense region close to the cluster, and the low-density one corresponds to the voids that are present around the Centre-Ridge. When the radius of the area increases, the low-density component remains and the high-density shifts to lower densities. This is because the dense area close to the cluster is only present there and as the radius increases, its relative weight in the distribution decreases while the weight of the all ridge increases. At high radius, the PDFs have two components but cannot be interpreted as the compression of the cluster. The high-density

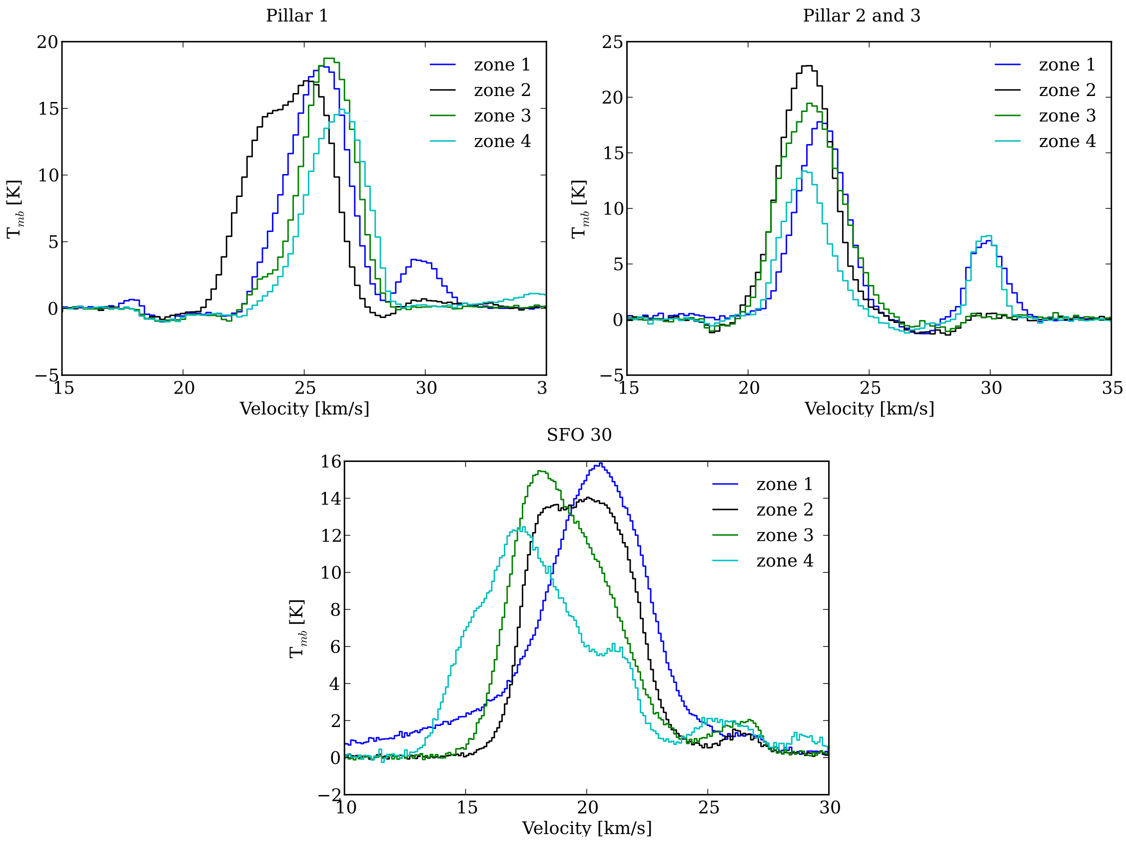

Figure 6.22: ^{12}CO 3→2 integrated spectra in the three sub-regions of the interface . The spectra are spatially integrated in the colored circles showed in Fig. 6.21.

component consists of the ridge-like molecular cloud, while the low-density corresponds to the low-dense hot and neutral interstellar medium that is around the ridge-like molecular cloud. Therefore the double log-normal shape is a nice signature of a bistable ISM and the PDF is very similar to the simulations of *Audit and Hennebelle* (2010) (see Fig. 1.4). Note that *Herschel* sensitivity towards low-density is impressive and can be used to study both phases of the ISM, and therefore can be used to constrain the thermal instability. The possible compressed region is only present in region 1, and its relative weight in the PDFs is too low to be able to conclude. However, a small-scale study of the column density can help to constrain the physical properties of this region.

6.6.2 Column density structure

The Vela C molecular cloud shows an elongated structure running approximately North-South, with a size of about 30 pc. RCW 36 is located close to the centre of Vela C. Focusing on the RCW 36 area, interstellar matter appears to have been cleared up to 1.5 pc away on each side of the star cluster, where high-mass stars have already formed during the last few millions years, revealing the dense filamentary structure: the Centre-Ridge (*Hill et al.*, 2011). The shape of the ridge is much more complex than a single filament. The column density image, as represented in Fig. 6.25 to emphasize low densities, exhibits a ring-like morphology that could define the dense gas contours of a H II region cavity (*Minier et al.*, 2012 submitted). Hα emission is observed toward RCW 36 and traces an ionized gas shell of ≈ 1.8 pc in extent. The Hα emission falls within an ellipse with an East-West major axis (Fig. 6.25). The corresponding radio continuum emission with a total flux of ≈ 26 Jy at 4.8 GHz, derived from the PMN survey map, is consistent with an ionizing photon

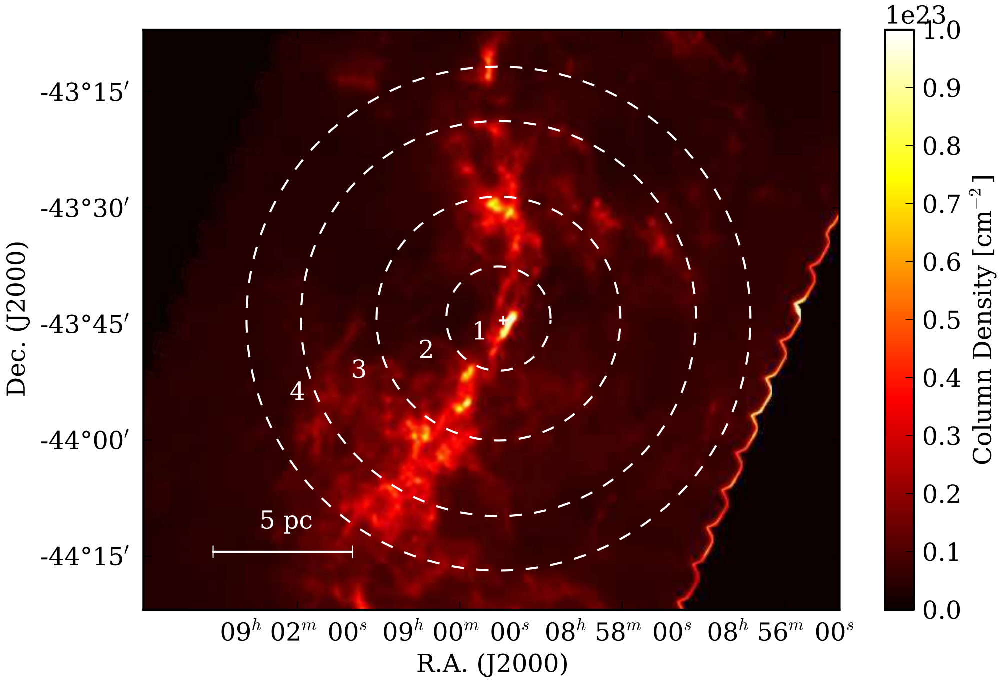

Figure 6.23: RCW 36 *Herschel* column density map. The circles indicate the different regions used for the PDFs. The regions are inclusive (region 2 contains region 1 ...). The white cross indicates the position of the main ionizing source. The first region indicates the limit of the Hα emission and the limit of the H II region.

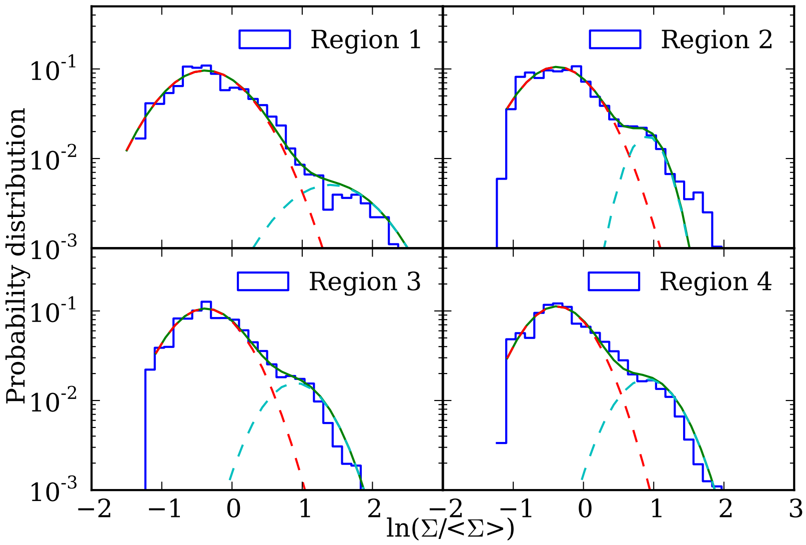

Figure 6.24: RCW 36 PDFs on the four regions indicated in Fig. 6.23. The multi-component fit is done using log-normal distributions.

flux of 6×10^{47} s^{-1} (i.e. a O9.5 star in *Panagia* (1973)) and an electronic density of ≈ 200 cm^{-3} assuming a temperature of 8000 K (see *Martín-Hernández et al.*, 2005, for detailed equations used for the calculation).

Figure 6.26 shows a column density map around RCW 36 with the DisPerSe skeleton. We labeled 1 and 2 the two parts of the ring-like structure. Note that, it is possible to

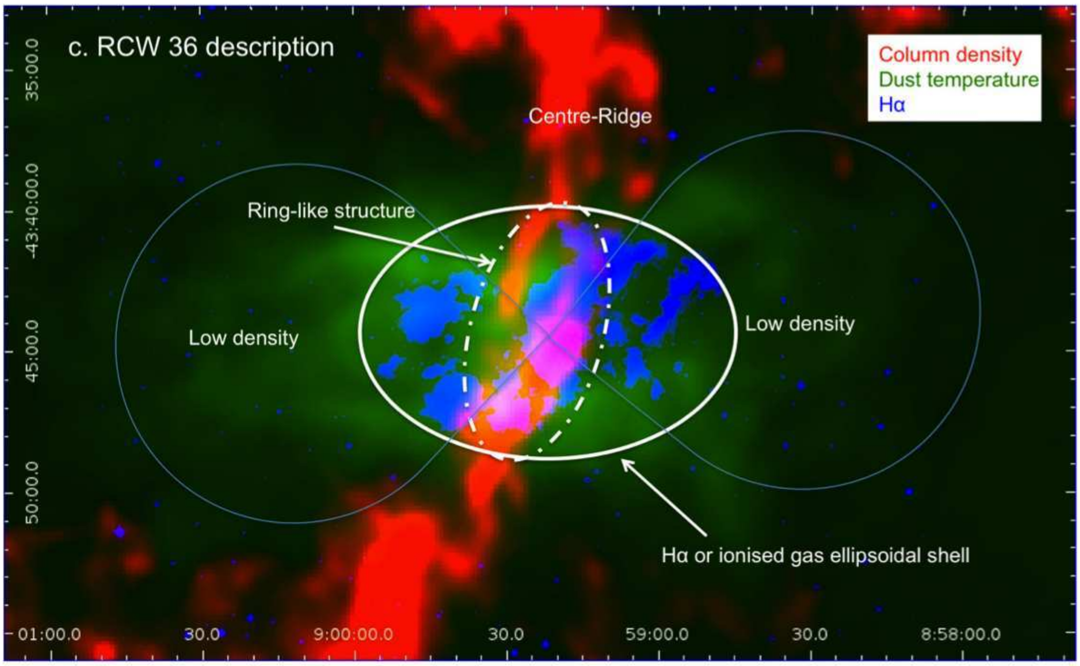

Figure 6.25: RCW 36 morphology on a three color image (column density, temperature, Hα).

deduce from the Hα data that the front labeled 1 is behind the cluster (seen in emission in Hα in Fig. 6.25), and the front labeled 2 is between the cluster and the observer (seen in extinction in Hα in Fig. 6.25). The profiles of the two fronts are shown in Fig. 6.27 and the deconvolved FWHM of these profiles is around 0.1 pc (0.10±0.02 pc for the front 1 at a resolution 12” and 0.20±0.02 pc for the front 2 at a resolution of 36”).

Comparison with the Collect and Collapse model: The parameters of a compressed shell around the ionized bubble can be determined thanks to Eq. 6.2. The input parameters are the ionizing flux of the cluster (6×10^{47} s^{-1}), the initial H I density (3.4×10^4 cm^{-3}), and the observed radius of the shell (0.9 pc). These values give a shell thickness of 0.11 pc, and an electron density of 170 cm^{-3}. These estimations are very close to the observations. Furthermore, we can estimate a shell H_2 density of 5×10^4 cm^{-3}. For an average column density of 3×10^{22} cm^{-2} for the front 1 and 2 (without the dense clumps), we get a depth of 0.2 pc. The dense structure around the ionized bubble is indeed a “ring”.

Since the shell is in fact a ring, the validity of the collect model in a homogeneous medium can be questioned. The mass of ionized gas is of the order of 25 M$_\odot$. At the initial density, this mass is contained in a sphere with a radius of 0.17 pc. Therefore if the initial medium is a sheet of thickness 0.5 pc confined by the hot low-dense neutral phase of the ISM (see PDFs), the ionized bubble can form with the final density around 200 cm^{-3} while a ring of dense material will form only in the plane of the sheet. In that case, the collect formalism is still a good approximation. The extension of the sheet has to be ≈ 2 pc to get the final ring. This means that we can estimate the initial dense ridge to have a H_2 column density of 10^{23} cm^{-2} and a thickness of 0.3 pc. Note that the pressure of the ionized gas is much bigger than the pressure in the hot ISM. Therefore, it is likely that the region will evolve into a blister-type H II region with a morphology that strongly deviate from the spherical shape to a ring like structure with bipolar cavities. We have employed HERACLES in spherical coordinates to simulate the ionization inside a initial ridge with

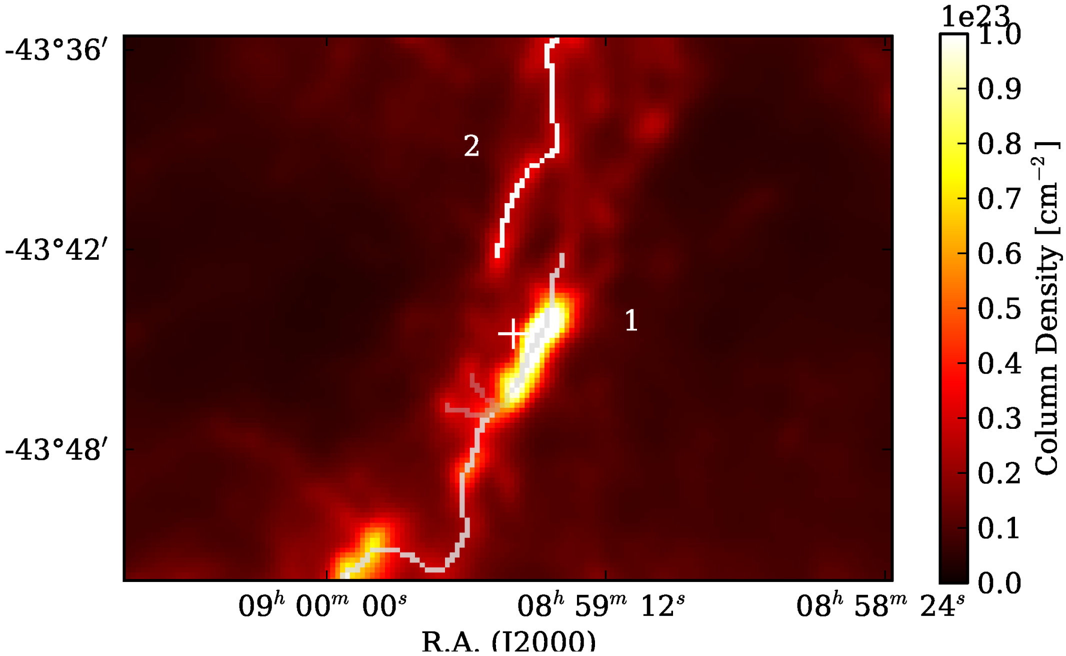

Figure 6.26: Column density map around RCW 36. The DisPerSe skeleton is drawn in white and each part of the shocked layer is labeled 1 and 2. The position of the main ionizing source is indicated with the white cross.

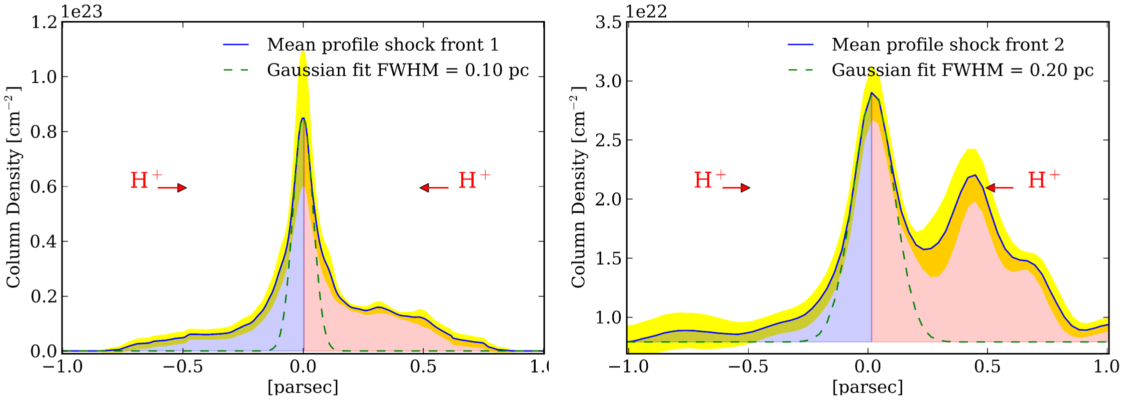

Figure 6.27: Left: profile of the front 1 traced by DisPerSe on a *Herschel*+P-ArTéMiS column density map at 12" resolution (see Sect. 6.6.4). Right: profile of the front 2 traced by DisPerSe on a *Herschel* column density map at 36" resolution. The yellow shaded area represents the standard deviation of the profiles. The red arrows indicate on which side ionized gas is present (see also Fig. 6.29 and the Hα emission). The green-dashed curve is the Gaussian fit used to determinate the FWHM width.

the properties deduced from the 1D analysis. The geometry of the mesh is spherical. The radius extents from 0.1 pc to 1.5 pc, the polar angle θ from 45° to 135°, and the azimuth angle ϕ between -45° and +45°. The number of cells is 100^3. The boundary conditions are reflexive at the inner radius, free flow at the outer radius, and periodic in the other directions. The adiabatic index γ is set to 1.01 allowing us to treat both the hot ionized gas and the cold unionized one as two different isothermal phases. The simulation is ran until the shocked layer reached a radius of 1 pc. A 3D view of the output of the simulation is shown in Fig. 6.28c,d. The density and the width of the ring as well as the density in the ionized region are in good agreement with the parameters that was deduced from the

1D analytical formulae. Another snapshot (Fig. 6.28e) illustrates the bipolar morphology of the H II region formed in the simulation, with the two lobes on each side of the dense ring. Interestingly, such a morphology would appear as a ridge or a filament on the sky if observed edge-on (Fig. 6.28f). The only difference with the 1D model in an homogeneous medium is the velocity of the shell and the time at which the radius of 1 pc is reached. In the 3D case, the velocity of the shell is around 1.4 km/s (1-pc radius reached in 600 ky) while it was only 0.6 km/s in the 1D case (1-pc radius reached in 750 ky). This difference can be easily understood in terms of rocket motion. The analytic formula gives a shell velocity that always decreases with time for the collect process in an homogeneous medium. In our 3D simulation, the ridge has a thickness that gives enough material to the ionized bubble to reach an electron density around 200 cm^{-3}. Nevertheless some ionized gas is evacuated from the 1-pc radius bubble through the extended lobes (see Fig. 6.28). Therefore the ionization at the front will increase and will accelerate the shell so that the velocity remains almost constant around 1.4 km/s.

6.6.3 Velocity structure

The dynamics of the region, such as the velocity information, is provided by the CS $1 \rightarrow 0$ line data mapped with the Mopra Telescope (CSIRO/CASS)[8].

We integrated the spectra at four different locations on the ring-like structure around RCW 36 (see Fig. 6.29). The corresponding spectra are shown in Fig. 6.30. The yellow and green spectra are integrated on the front 2 and the blue and cyan spectra on the front 1. The four zones present a component at +7 km/s that we interpret as the systematic velocity of the ridge area. In addition to that component, the yellow spectrum on the front 2 has a blue-shifted component at 5 km/s and the blue spectrum on the front 1, a red-shifted component at 8 km/s. Recall that from the Hα emission (see Fig. 6.25), it is possible to infer that the front 1 is behind the cluster and the front 2 in front of it. Therefore the velocity shifts are not the signature of an in-fall and can be interpreted as the outward expansion of the ring at a velocity between 1 and 2 km/s. The green and cyan areas expand on the north-south axis that is perpendicular to the line of sight. Therefore their velocity spectra are coherent with an expansion. The velocity of the shell obtained in the 3D simulation is 1.4 km/s and is in relatively good agreement with the velocity inferred from the CS data.

6.6.4 Triggered formation of clumps in the ring

Complementary and unpublished data at 450 μm for the RCW 36 area were obtained with the p-ArTéMiS bolometer camera (*André et al.*, 2008) on the APEX telescope during May 2008. This has allowed us to improve the angular resolution of the derived column density map in this area from 36" in *Hill et al.* (2011) to 12", by combining the Herschel 160 and 250 μm data with the P-ArTéMiS 450 μm data (see Fig. 6.31). To produce this column density map, a temperature map at the 18" resolution of the SPIRE 250 μm observations was first derived based on the ratio of Herschel 160 and 250 μm data. The PACS 160 μm data (12" resolution) and a slightly smoothed version of the P-ArTéMiS 450 μm data were then converted to a column density map at 12" resolution, assuming optically thin dust emission at a fixed temperature given by the temperature map at each pixel and the same dust opacity law as in *Hill et al.* (2011) and *Arzoumanian et al.* (2011). This procedure is

---

[8] as part of the continuing Vela C multi-molecular line mapping project at 3, 7 and 12 mm wavebands (PI: Cunningham, Maria). The RCW 36 region observations were carried out in 2009 and 2010 using the 8 GHz bandwidth UNSW-MOPS digital filterbank backend and the Monolithic Microwave Integrated Circuit (MMIC) receiver, at 48 GHz the velocity resolution is 0.2 km s^{-1} and the FWHM beam size is 76".

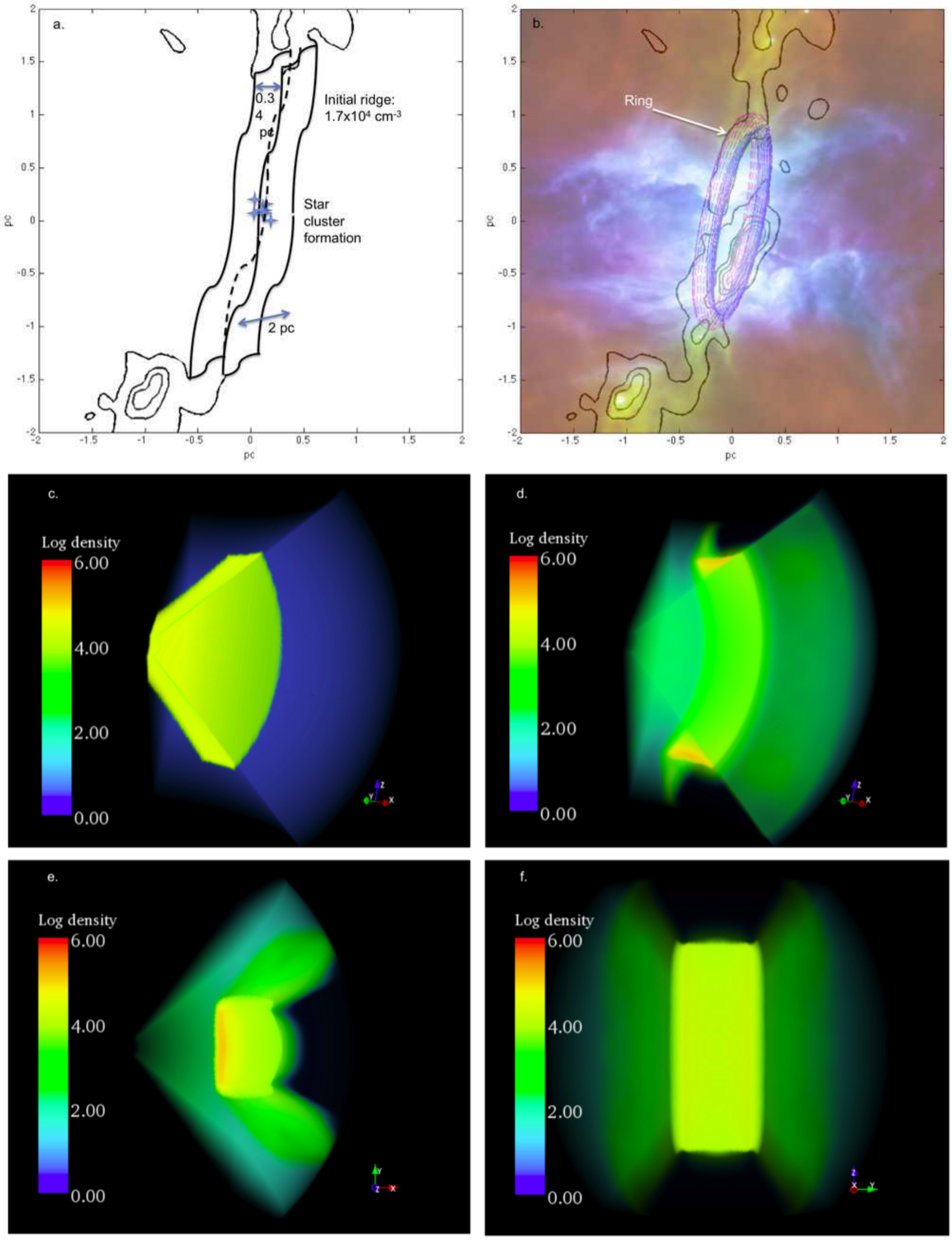

Figure 6.28: Illustration of the proposed scenario. Observations: a. Schematic view of the initial ridge. b. Modelled ring superimposed on the Herschel 3-colour image. Numerical simulations: c. View through the plane of the initial ridge. The radius of the yellow circular section is 1 pc. The density is given in H I cm^{-3}. d. View through the plane of the ridge after ionization reshaped it and formed a ring. e: View of d from above, The bipolar shape clearly appears. f: View of d. from the backside. The ridge/filament projected shape clearly appears. The orientation of each view is given by x, y, z axes on each image.

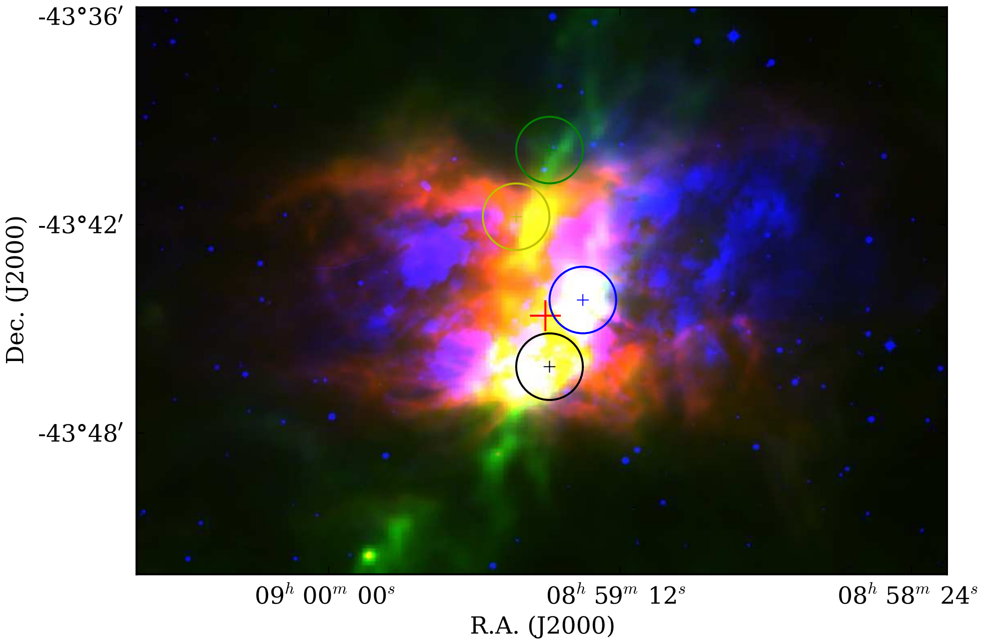

Figure 6.29: Three color image of the interface between the Vela C molecular cloud and RCW 36 (red: PACS 70 μm, green: SPIRE 250 μm, blue: Hα). The white crosses indicate the ionizing source. Each spectrum in Fig. 6.30 is integrated inside the corresponding colored circle.

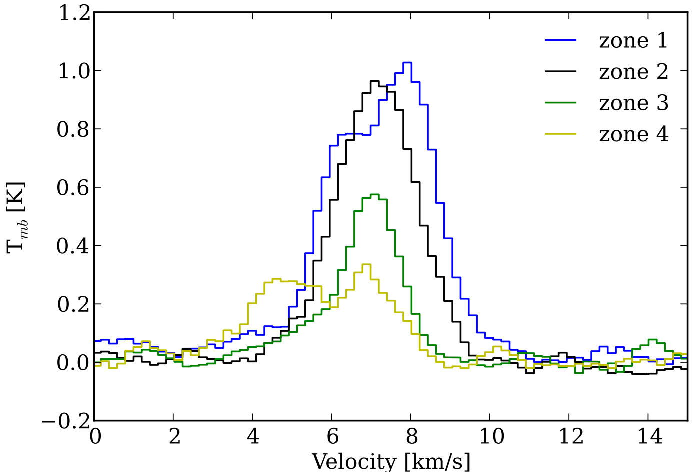

Figure 6.30: CS 1→0 integrated spectra around RCW 36. The spectra are spatially integrated in the colored circles showed in Fig. 6.29.

only approximate as it neglects any temperature variation on angular scales smaller than 18" in the plane of the sky, as well as any temperature variation along the line of sight.

The *Herschel*+P-ArTéMiS and *Spitzer* IRAC observations allow the examination of the various structures of interstellar matter that comprise the environment of the RCW 36 at smaller scales ($\approx$ 0.1-0.2 pc). We focus here on objects that are associated with clumps and bright rims. Seven areas with enhanced emission clearly stand out at the outer border of the "ring" formed around the star cluster in Fig. 6.31. These clumps are identified in those figures by their number and are associated in position with the observed bright-rims

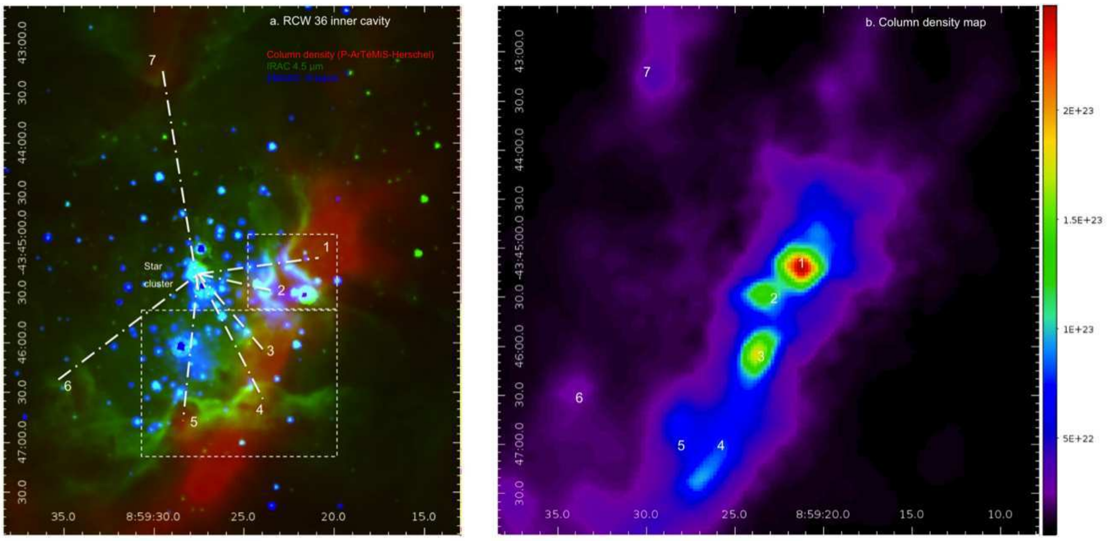

Figure 6.31: a. Three colour image of the RCW 36 cavity corresponding to the field mapped by P-ArTéMiS. Red is the column density that is shown for values between 3×10^{21} and 5×10^{22} cm^{-2} to limit the dynamics and emphasize low density features. The peak column density is 1.7×10^{23} cm^{-2}. Green is the IRAC 4.5 μm image that shows structures due to extinction or emission near the star cluster. Blue is the 2MASS K-band image that shows the young stars. The 7 clumps as described in the text are numbered from 1 to 7 on this image. b. Column density map combining Herschel and p-ArTéMiS observations.

in NIR. The bright-rims reveal that the clumps are surrounded by ionization that penetrates in large gaps between them (e.g. between clump 5 and 6, between clump 1 and 4, and around clump 7). There is no doubt that these clumps are under the influence of the ionization coming from the cluster. However, the question whether they were pre-existing or triggered by the compression remains.

We have employed the simulations to test the two possibilities. Fig. 6.32a shows the first assumption that clumps existed before the impact of ionization on the filament. A dense and small spherical clump (0.1 pc in diameter, $3{\times}10^{5}$ cm^{-3}, 20 times the density in the initial filament) was embedded in the slab of interstellar gas. Such physical conditions corresponded to those observed in the Herschel map where the clump column density reached 10^{23} cm^{-2} within 0.1 pc. Fig. 6.32b shows the result after 0.6 Myr, the ionizing front pushed away the gas by 1 pc and an elongated pillar formed due to the dense clump resistance inducing a curvature in the shock front. We discussed in Chap. 4 the role of shock curvature in forming pillars. The pillar head was nearly at the location of the clump in this model. Fig. 6.32c illustrates the second situation, where the spherical clump was wider (0.1 pc in diameter) and less dense ($5{\times}10^{4}$ cm^{-3}), i.e. 3 times the density in the initial filament. Instead of forming an elongated pillar, the ionization front produced a more compact structure than in the first situation. Large gaps on each side of the compact clump were also formed (Fig. 6.32d), which are consistent with the large gaps observed in Fig. 6.31. The perturbation, caused by ionization, triggered local curvature of the ionization and shock fronts. This process was already identified in Chap. 4 as the key process to form pillars, i.e., when the induced curvature is sufficient to make the shell collapse on itself. When the clumpy inhomogeneity is large in size and at a lower density, however, the curvature is not sufficient to trigger a collapse, but rather leads to gas flows in the shell perpendicular to the propagation of the ionizing flux. These flows are accelerated with the shell and will form dense clumps and gaps that will remain in the shell during the

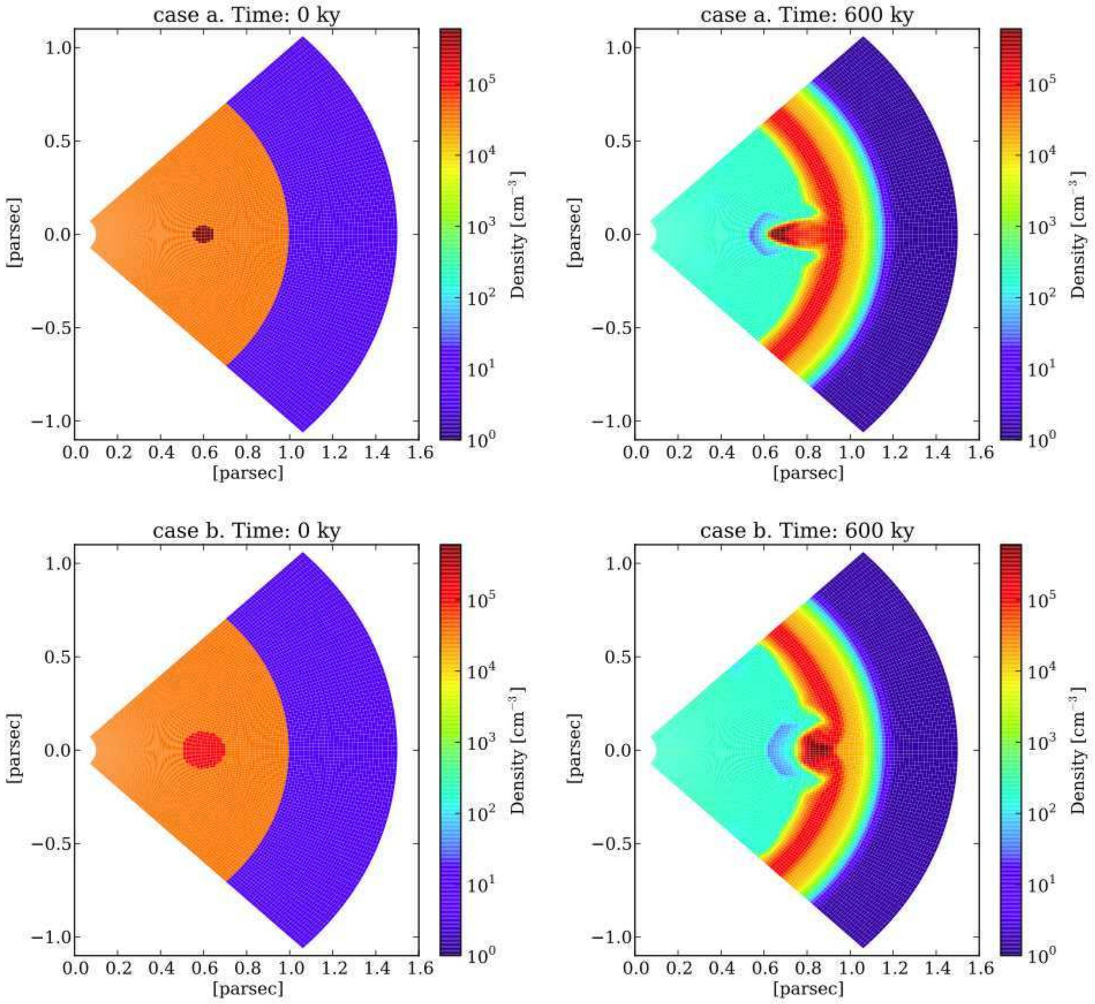

Figure 6.32: Numerical simulations. Each box shows a cut of the density map (ϕ=0) before or after the ionization of a slab of interstellar gas. a. A clump with a density of 3×10^5 cm^{-3} is embedded in the slab of interstellar gas. Radiation from the O9.5 star comes from the position (0,0). b. After 0.6 Myr, the ionization has led to the formation of a pillar. The base of the pillar is located within the compressed shell, in between the ionization and shock fronts. The head of the pillar remains nearly at the position of the initial clump. c. A larger clump with a lower density is ionized by the O9.5 photon flux. d. A clump is formed within the compressed shell with a hole around it.

0.6 Myr of expansion. In summary, the second set of numerical hydrodynamic simulations (Fig. 6.32b) suggest that an ionized filament of gas with inhomogeneities in density could lead to the formation of small structures with dense clumps surrounded by gaps at the edge of a H II region. Such structures are consistent with the morphologies seen in the Herschel and Spitzer images (Fig. 6.25 and 6.31).

6.7 Conclusions

Thanks to the *Herschel* column density maps, we showed that the compression from the ionized gas can be seen on the PDF of the gas in most of the regions studied here. The weight of the compressed gas in the PDF decreases when the radius of the studied region around the ionizing source increases as suggested in Chap. 5.

The small-scale structure of the shells around the studied H II regions are in a good agreement with the analytical model derived from the collect and collapse scenario. A good estimation of the shocked-gas density, ionized-gas density, velocity and width of the shell can be derived from the model and compared with a wide-range of observations (*Herschel* column density maps, electronic density from VLA data, velocity information from molecular lines, etc). The modeling also confirms that the gas around the Eagle Nebula is relatively hot as suggested by *Flagey et al.* (2011) from *Spitzer* observations.

The globules in Rosette and Cygnus X do present a large bulk-velocity dispersion that confirms their turbulent origin proposed in Chap. 5.

A triple point on the DisPerSe skeleton points out the presence of a nascent pillar in the Rosette Nebula whose velocity structure suggests that it is formed by the collapse of the shell of itself as proposed in Chap. 4.

Assuming that pillars are indeed formed by the collapse of the shell, we derived an analytical formulation to predict the initial size and the age of a pillar with and without stretching. This model was tested on the pillars in Rosette and the Eagle Nebula whose stretching can be evaluated thanks to the velocity shift between the head and the base of the pillars.

We used dedicated simulations in RCW 36 to test whether clumps at the edge of the ionized gas are pre-existing or triggered. If they are pre-existing, these clumps present a large density contrast with the rest of the medium that prevent them from being accelerating with the shell, therefore they cannot remains at the edge of the ionized gas. The simulations show that a perturbation of the initial medium with a low-density contrast is needed to form these clumps and accelerate them with the shell so that they are observed at the edge of the ionized gas. Therefore the formation of the clumps have to be triggered if they are observed at the edge of the ionized gas.

Bibliography

Allen, L. E., M. G. Burton, S. D. Ryder, M. C. B. Ashley, and J. W. V. Storey (1999), Fluorescent molecular hydrogen in the Eagle nebula, *MNRAS*, *304*(1), 98–108. 108

Anderson, L. D., et al. (2010), The physical properties of the dust in the RCW 120 H II region as seen by Herschel, *A&A*, *518*, L99. 93

André, P., et al. (2008), First 450 μm dust continuum mapping of the massive star-forming region NGC 3576 with the P-ArTéMiS bolometer camera, *A&A*, *490*(3), L27–L30. 120

André, P., et al. (2010), From filamentary clouds to prestellar cores to the stellar IMF: Initial highlights from the Herschel Gould Belt Survey, *A&A*, *518*, L102. 92

Arzoumanian, D., et al. (2011), Characterizing interstellar filaments with Herschel in IC 5146, *A&A*, *529*, L6. 93, 100, 114, 120

Audit, E., and P. Hennebelle (2010), On the structure of the turbulent interstellar clouds . Influence of the equation of state on the dynamics of 3D compressible flows, *A&A*, *511*, 76. 116

Baba, D., et al. (2004), Deep Near-Infrared Imaging toward the Vela Molecular Ridge C. I. A Remarkable Embedded Cluster in RCW 36, *ApJ*, *614*(2), 818–826. 114

Bonatto, C., J. F. C. J. Santos, and E. Bica (2006), Mass functions and structure of the young open cluster NGC 6611, *A&A*, *445*(2), 567–577. 108

Bontemps, S., et al. (2010), The Herschel first look at protostars in the Aquila rift, *A&A*, *518*, L85. 93

Caswell, J. L., and R. F. Haynes (1987), Southern H II regions - an extensive study of radio recombination line emission, *A&A*, *171*, 261–276. 114

Celnik, W. E. (1985), The Rosette nebula. II - Radio continuum and recombination line observations, *A&A*, *144*, 171–178. 102

Cox, P., L. Deharveng, and A. Leene (1990), IRAS observations of the Rosette nebula complex, *A&A*, *230*, 181–192. 97

de Graauw, T., et al. (2010), The Herschel-Heterodyne Instrument for the Far-Infrared (HIFI), *A&A*, *518*, L6. 92

Deharveng, L., A. Zavagno, F. Schuller, J. Caplan, M. Pomarès, and C. De Breuck (2009), Star formation around RCW 120, the perfect bubble, *A&A*, *496*(1), 177–190. 93

Di Francesco, J., et al. (2010), Small-scale structure in the Rosette molecular cloud revealed by Herschel, *A&A*, *518*, L91. 93

Flagey, N., F. Boulanger, A. Noriega-Crespo, R. Paladini, T. Montmerle, S. J. Carey, M. Gagné, and S. Shenoy (2011), Tracing the energetics and evolution of dust with Spitzer: a chapter in the history of the Eagle Nebula, *A&A*, *531*, 51. 108, 111, 125

Giannini, T., et al. (2012), The Herschel view of the on-going star formation in the Vela-C molecular cloud, *A&A*, *539*, 156. 93

Griffin, M. J., et al. (2010), The Herschel-SPIRE instrument and its in-flight performance, *A&A*, *518*, L3. 92

Hennemann, M., et al. (2010), Herschel observations of embedded protostellar clusters in the Rosette molecular cloud, *A&A*, *518*, L84. 93

Hennemann, M., et al. (2012), The spine of the swan: a Herschel study of the DR21 ridge and filaments in Cygnus X, *A&A*, *543*, L3. 93, 97

Hester, J. J., et al. (1996), Hubble Space Telescope WFPC2 Imaging of M16: Photoevaporation and Emerging Young Stellar Objects, *Astronomical Journal v.111*, *111*, 2349. 108, 113

Heyer, M. H., J. P. Williams, and C. M. Brunt (2006), Turbulent Gas Flows in the Rosette and G216-2.5 Molecular Clouds: Assessing Turbulent Fragmentation Descriptions of Star Formation, *ApJ*, *643*(2), 956–964. 97, 102, 104

Hill, T., et al. (2011), Filaments and ridges in Vela C revealed by Herschel: from low-mass to high-mass star-forming sites, *A&A*, *533*, 94. 93, 114, 115, 116, 120

Hill, T., et al. (2012), The M 16 molecular complex under the influence of NGC 6611. Herschel's perspective of the heating effect on the Eagle Nebula, *A&A*, *542*, 114. 92, 93, 108

Hora, J. L., et al. (2009), The Spitzer Survey of Cygnus-X and Infrared Dark Clouds, *American Astronomical Society*, *213*, 498. 96

Knödlseder, J. (2000), Cygnus OB2 - a young globular cluster in the Milky Way, *A&A*, *360*, 539–548. 96

Könyves, V., et al. (2010), The Aquila prestellar core population revealed by Herschel, *A&A*, *518*, L106. 93

Linsky, J. L., M. Gagné, A. Mytyk, M. McCaughrean, and M. Andersen (2007), Chandra Observations of the Eagle Nebula. I. Embedded Young Stellar Objects near the Pillars of Creation, *ApJ*, *654*(1), 347–360. 108

Martín-Hernández, N. L., R. Vermeij, and J. M. van der Hulst (2005), High spatial resolution radio continuum observations of compact H II regions in the Magellanic Clouds, *A&A*, *433*(1), 205–216. 117

Men'shchikov, A., et al. (2010), Filamentary structures and compact objects in the Aquila and Polaris clouds observed by Herschel, *A&A*, *518*, L103. 93

Miville-Deschênes, M.-A., et al. (2010), Herschel-SPIRE observations of the Polaris flare: Structure of the diffuse interstellar medium at the sub-parsec scale, *A&A*, *518*, L104. 93

Motte, F., et al. (2010), Initial highlights of the HOBYS key program, the Herschel imaging survey of OB young stellar objects, *A&A*, *518*, L77. 92

Murphy, D. C., and J. May (1991), Molecular clouds in VELA, *A&A*, *247*, 202–214. 114

Nguyen-Luong, Q., et al. (2011), The Herschel view of massive star formation in G035.39-00.33: dense and cold filament of W48 undergoing a mini-starburst, *A&A*, *535*, 76. 93

Panagia, N. (1973), Some Physical parameters of early-type stars, *Astronomical Journal*, *78*, 929–934. 117

Peretto, N., et al. (2012), The Pipe Nebula as seen with Herschel: formation of filamentary structures by large-scale compression?, *A&A*, *541*, 63. 93, 100, 101

Pilbratt, G. L., et al. (2010), Herschel Space Observatory. An ESA facility for far-infrared and submillimetre astronomy, *A&A*, *518*, L1. 92

Poglitsch, A., et al. (2010), The Photodetector Array Camera and Spectrometer (PACS) on the Herschel Space Observatory, *A&A*, *518*, L2. 92

Poulton, C. J., T. P. Robitaille, J. S. Greaves, I. A. Bonnell, J. P. Williams, and M. H. Heyer (2008), A Spitzer survey of young stellar objects in the Rosette Molecular Cloud, *MNRAS*, *384*(4), 1249–1262. 98

Pound, M. W. (1998), Molecular Gas in the Eagle Nebula, *Astrophysical Journal Letters v.493*, *493*, L113. 108

Reipurth, B., and N. Schneider (2008), Star Formation and Young Clusters in Cygnus, *Handbook of Star Forming Regions*, *I*, 36. 96

Rodgers, A. W., C. T. Campbell, and J. B. Whiteoak (1960), A catalogue of Hα-emission regions in the southern Milky Way, *MNRAS*, *121*, 103. 93, 114

Román-Zúñiga, C. G., and E. A. Lada (2008), Star Formation in the Rosette Complex, *Handbook of Star Forming Regions*, *I*, 928. 103

Sadavoy, S. I., et al. (2012), Herschel observations of a potential core-forming clump: Perseus B1-E, *Astronomy & Astrophysics*, *540*, 10. 93

Schneider, N., J. Stutzki, G. Winnewisser, and D. Block (1998a), The Rosette Molecular Complex. I. CO observations, *A&A*, *335*, 1049–1069. 98

Schneider, N., J. Stutzki, G. Winnewisser, A. Poglitsch, and S. Madden (1998b), The Rosette molecular complex. II. [CII] 158 μm observations, *A&A*, *338*, 262–272. 98

Schneider, N., et al. (2010), The Herschel view of star formation in the Rosette molecular cloud under the influence of NGC 2244, *A&A*, *518*, L83. 92, 93, 98

Schneider, N., et al. (2012a), Cluster-formation in the Rosette molecular cloud at the junctions of filaments, *A&A*, *540*, L11. 93, 98, 114

Schneider, N., et al. (2012b), Globules and pillars seen in the [CII] 158 μm line with SOFIA, *A&A*, *542*, L18. 97

Sousbie, T. (2011), The persistent cosmic web and its filamentary structure - I. Theory and implementation, *MNRAS*, *414*(1), 350–383. 91

Urquhart, J. S., G. J. White, G. L. Pilbratt, and C. V. M. Fridlund (2003), ISOCAM-CVF imaging of M 16, *A&A*, *409*, 193–203. 108

Verma, R. P., R. S. Bisht, S. K. Ghosh, K. V. K. Iyengar, T. N. Rengarajan, and S. N. Tandon (1994), Far-infrared observations of three galactic star-forming regions: RCW 36, IRAS 10361-5830 and IRAS 10365-5803, *A&A*, *284*, 936–948. 114

Ward-Thompson, D., et al. (2010), A Herschel study of the properties of starless cores in the Polaris Flare dark cloud region using PACS and SPIRE, *A&A*, *518*, L92. 93

White, G., et al. (1999), The Eagle Nebula's fingers - pointers to the earliest stages of star formation?, *A&A*, *342*, 233–256. 108, 110, 111, 113, 114

Williams, J. P., E. J. de Geus, and L. Blitz (1994), Determining structure in molecular clouds, *ApJ*, *428*, 693–712. 97

Zavagno, A., M. Pomarès, L. Deharveng, T. Hosokawa, D. Russeil, and J. Caplan (2007), Triggered star formation on the borders of the Galactic H ii region RCW 120, *A&A*, *472*(3), 835–846. 93, 94, 95, 96

Zavagno, A., et al. (2010), Star formation triggered by the Galactic H II region RCW 120. First results from the Herschel Space Observatory, *A&A*, *518*, L81. 93

Conclusions and future works

A conclusion is the place where you got tired thinking.
Martin H. Fischer

Thanks to numerical simulations and observations, we have studied how the ionization from massive stars impacts the molecular gas of an interstellar cloud. In Chap. 4, we have presented a new scenario for the formation of pillars and clumps at the edge of H II regions. We have shown that a shell forms a pillar if it is sufficiently curved to collide laterally on itself. At low curvature, a dense clump is formed in the shell.

In Chap. 5, we have shown that the same mechanisms are at work in simulations with a turbulent medium. Furthermore, because of turbulence, hot ionized gas can get into the shadow of cold dense gas, leading to a very long recombination time for the gas. This gas can only be treated with a non-equilibrium model for ionization. Up to 20 % of the box can get into that state. Globules are formed preferentially when the turbulence in the cold gas dominates the ionized-gas pressure. Bubbles of dense gas have sufficient kinetic energy to penetrate into the H II regions to form cometary globules.

Different diagnostics for the observations have been derived to test these scenarii:

i If pillars are formed by the collapse of the dense shell on itself, the velocity spectrum of a nascent pillar is large, with a red-shifted and a blue-shifted components that are caused by the foreground and background parts of the shell that collapse on the line of sight.

ii If cometary globules emerge because of the turbulence of the molecular cloud, the velocity spectrum of these globules is shifted at different velocities than the velocity of the shell, pillars and clumps that follow the global expansion of the H II region.

iii Probability density functions of the cold gas are double peaked when the turbulent ram pressure is low compared to the ionized-gas pressure. This is the signature of the compression caused by the expansion of the ionized bubble. When the turbulence is high, the two peaks merge and the compression can still be identified although the signature is less clear.

Furthermore, analytical models based on the collect and collapse scenario and new analytical models of the properties of pillars were used to compare the theoretical properties of the H II regions to observations:

i The shocked-gas density, ionized-gas density, velocity and width of the shell can be derived from the collect and collapse model.

ii Assuming that pillars are formed by the collapse of the shell, an analytical formulation of the age and initial size of the pillars can be derived as well as the evolution of its density and width in time. The stretching of the pillars between the head and the base was taken into account.

All these diagnostics were tested on observations of RCW 120, RCW 36, Cygnus X, the Rosette and Eagle Nebulae. We used *Herschel* column density maps and molecular-line data to estimate the density and velocity structure of the interface between the ionized and molecular gas. We have shown that:

i The small-scale structures of the shells around the studied H II regions are in a good agreement with the analytical models. The modeling also confirms that the gas around the Eagle Nebula is relatively hot as suggested by *Spitzer* observations.

ii The globules in Rosette and Cygnus X do present a large bulk-velocity dispersion that confirms their turbulent origin.

iii A triple point on the DisPerSe skeleton points out the presence of a nascent pillar in the Rosette Nebula whose velocity structure suggests that it is formed by the collapse of the shell of itself.

iv Assuming that pillars are indeed formed by the collapse of the shell, we used an analytical formulation of the properties of such pillars to derive the age and initial size of the ones present in the Rosette and Eagle Nebulae (including two of the Pillars of Creation) in function of their angle with the line of sight.

Thanks to the *Herschel* column density maps, we showed that the compression from the ionized gas can be seen on the PDF of the gas in most of the regions studied here. This result is important for the link between the initial mass function (IMF) and the global properties of the cloud. If the IMF can be derived from the probability density function of a cloud, the impact of the massive stars on the PDF has to be taken in account.
Recently, *Hennebelle and Chabrier* (2008) proposed an analytical theory to derive the CMF/IMF from the PDF of a gravo-turbulent molecular cloud. The central idea is that the typical shape of the Chabrier IMF (see *Chabrier*, 2003) is set by the shape of the PDF of the gravo-turbulent cloud: a log-normal distribution (from the turbulence) and a high-density power-law tail (from the gravitational instabilities). One direct consequence of the present work is that this typical shape is not preserved around the ionized gas. H II regions are present in a vast number of molecular clouds, even in low-mass star-forming regions (e.g. the Cocoon Nebula in IC 5146, *Arzoumanian et al.* (2011)). As a feedback from massive stars, it is also thought to be one of the most important processes in order to disperse molecular clouds in our galaxy (see *Whitworth*, 1979; *Matzner*, 2002). Considering the typical lifetime of molecular clouds ($\approx$ 10 My) and the typical time of the development of H II regions ($\approx$ 1 My), the clouds should spend almost all this time in a state where the ionized gas is present and compress the cold gas to form a double-peaked PDF. It is therefore unlikely that the dispersion of the molecular gas by ionization is sufficiently rapid to safely ignore its impact on the PDF of the gas. It is also unlikely that any feedback processes (radiation pressure, supernovae, stellar winds...) is sufficiently rapid to ignore the compression phase that will disperse the gas to get a gas-free cluster with a given IMF.

Multiple H II regions are susceptible to develop but it is rather unlikely that a sufficient number is produced to restore a log-normal shape with the statistical argument of Kevlahan & Pudritz (2009). In all the observations presented here, only one or two H II region is present in the cloud. However it could be sufficient to enlarge the PDF in order to get wide PDF with a rather small initial Mach number for the cloud. For example, the width of the PDF of the ionized Mach-1 simulation in Chap. 5 is equivalent to the width of the Mach-4 simulation. Therefore we propose that the feedback processes such as the ionization could account for the relatively large PDF that are needed in *Hennebelle and Chabrier* (2008) to have a good agreement with the computed and observed IMF. Since other processes could also enlarge the PDF (e.g. the equation of state (see *Hennebelle and Chabrier*, 2009)), the relative importance of the physical phenomena leading to these large

PDF in molecular clouds remains a relatively open question although the present work supports observationally the role of ionization.

Finally, we used dedicated simulations in RCW 36 to test whether clumps at the edge of the ionized gas are pre-existing or triggered. If they are pre-existing, these clumps present a large density contrast with the rest of the medium that prevent them from being accelerating with the shell, therefore they cannot remains at the edge of the ionized gas. The simulations show that a perturbation of the initial medium with a low-density contrast is needed to form these clumps and accelerate them with the shell so that they are observed at the edge of the ionized gas. Therefore the formation of the clumps have to be triggered if they are observed at the edge of the ionized gas. This suggests that the origin of the large fraction of massive young stellar objects, that is seen at the edge of the H II regions, is probably triggered and not pre-existing.

This thesis tried to shed some light on the different formation mechanisms of pillars and globules. This work can be extended in various ways. In chap. 6, we develop an analytic model for the evolution of pillars after they are formed by the collapse of the shell. This model can be compared to the numerical simulations performed in Chap. 4. In Chap. 5, we looked at the structures formed in three turbulent simulations with different mean Mach numbers. An interesting follow-up is to look at the difference between solenoid and compressible forcing on the morphology of these structures. The shape of the compressed peak in the PDF could also be better characterized (e.g., log-normal width...). Finally, an interesting property to investigate is the rotation pattern of globules and pillars that are formed in the simulations. Preliminary works, in collaboration with J. Pety (IRAM/Grenoble), indicate that the final structures could get a significant angular momentum because of the stretching and compression amplification of the vorticity (similar to a tornado in the incompressible case). These rotation patterns could be directly compared to observations, for instance the Horsehead Nebula.

A longer term perspective is the inclusion of the winds coming from the massive stars and a study of their effects on the structures. An important point is to look at the mixing between the molecular gas and the winds in order to constrain the efficiency of the heavy-element injection. A direct application could be the enrichment of the Solar Nebula with aluminum-26 coming from massive stars that could better constrain the models on the origin of the Solar system.

Finally, an important work is to follow the formation of the young stellar objects in these simulations in order to constrain the star formation activity with and without feedback. This relatively small-scale simulations could give important constraints for simulations at the scale of the molecular cloud or at the scale of the galaxy. These simulations could also give indications on how the impact of the massive stars has to be taken into account in the link between the IMF and the global property of the cloud, especially when ionization is responsible for the final cloud destruction. In this way, the picture of star formation in the life cycle of molecular clouds could be greatly clarified.

Bibliography

Arzoumanian, D., et al. (2011), Characterizing interstellar filaments with Herschel in IC 5146, *A&A*, *529*, L6. 130

Chabrier, G. (2003), Galactic Stellar and Substellar Initial Mass Function, *PASP*, *115*(8), 763–795. 130

Hennebelle, P., and G. Chabrier (2008), Analytical Theory for the Initial Mass Function: CO Clumps and Prestellar Cores, *ApJ*, *684*(1), 395–410. 130

Hennebelle, P., and G. Chabrier (2009), Analytical Theory for the Initial Mass Function. II. Properties of the Flow, *ApJ*, *702*(2), 1428–1442. 130

Matzner, C. D. (2002), On the Role of Massive Stars in the Support and Destruction of Giant Molecular Clouds, *ApJ*, *566*(1), 302–314. 130

Tremblin, P., E. Audit, V. Minier, W. Schmidt, and N. Schneider (2012), Three-dimensional simulations of globule and pillar formation around HII regions: turbulence and shock curvature, *A&A*, *546*, 33.

Whitworth, A. P. (1979), The erosion and dispersal of massive molecular clouds by young stars, *MNRAS*, *186*, 59–67. 130

Appendix A

Antarctica site testing

> *The last thing I have to say is that ice is the past tense of water. I've always wanted to write that sentence and now I have.*
>
> *Rita Mae Brown*

Over the past few years a major effort has been put into the exploration of potential sites for the deployment of submillimetre astronomical facilities. Amongst the most important sites are Dome C and Dome A on the Antarctic Plateau, and the Chajnantor area in Chile. In this context, we report on measurements of the sky opacity at 200 μm over a period of three years at the French-Italian station, Concordia, at Dome C, Antarctica. We also present some solutions to the challenges of operating in the harsh polar environment. The 200-μm atmospheric opacity was measured with a tipper. The forward atmospheric model MOLIERE (Microwave Observation LIne Estimation and REtrieval) was used to calculate the atmospheric transmission and to evaluate the precipitable water vapour content (PWV) from the observed sky opacity. These results have been compared with satellite measurements from the Infrared Atmospheric Sounding Interferometer (IASI) on Metop-A, with balloon humidity sondes and with results obtained by a ground-based microwave radiometer (HAMSTRAD). In addition, a series of experiments has been designed to study frost formation on surfaces, and the temporal and spatial evolution of thermal gradients in the low atmosphere.

Dome C offers exceptional conditions in terms of absolute atmospheric transmission and stability for submillimetre astronomy. Over the austral winter the PWV exhibits long periods during which it is stable and at a very low level (0.1 to 0.3 mm). Higher values (0.2 to 0.8 mm) of PWV are observed during the short summer period. Based on observations over three years, a transmission of around 50% at 350 μm is achieved for 75% of the time. The 200-μm window opens with a typical transmission of 10% to 15% for 25% of the time. Dome C is one of the best accessible sites on Earth for submillimetre astronomy. Observations at 350 or 450 μm are possible all year round, and the 200-μm window opens long enough and with a sufficient transparency to be useful. Although the polar environment severely constrains hardware design, a permanent observatory with appropriate technical capabilities is feasible. Because of the very good astronomical conditions, high angular resolution and time series (multi-year) observations at Dome C with a medium size single dish telescope would enable unique studies to be conducted, some of which are not otherwise feasible even from space.

A.1 Introduction

Submillimetre (submm) astronomy is one of the most important techniques for the study of the cold Universe and for unveiling the birth and early evolution of planets, stars, and galaxies. Submm continuum observations are particularly powerful for the measurement of luminosities, temperatures, and masses of cool, dusty objects because dust enshrouded star-forming regions emit the bulk of their energy between 60 and 500 μm. The submm range of the spectrum (or THz regime in frequency) is also rich in the atomic and molecular lines that offer the only means of studying the kinematic structure of the interstellar medium of galaxies. Observations at these wavelengths with medium to large telescopes should lead to breakthroughs in the study of star-formation at all scales, and to a better understanding of its history back to the early Universe—thus leading to a better understanding of galaxy evolution. Asteroids, debris disks, planet formation, dust origin in evolved stars, interstellar dust and polarisation of dust in the Universe are also potential science drivers for submm astronomy (see *Minier et al.*, 2009, for details).

A.1.1 Dome C, a potential site

A major obstacle to ground-based observations in the submm range (and specifically at wavelengths shorter than 500 μm) is the atmosphere. This part of the electromagnetic spectrum is normally the preserve of space telescopes such as the Herschel space observatory (*Pilbratt et al.*, 2010) although large submm facilities such as ALMA will be able to operate down to 420 μm and possibly below in the future (*Hills et al.*, 2010). However, submm observations in the 200-μm window with ground-based instruments will always require exceptional conditions (see *Marrone et al.*, 2005; *Oberst et al.*, 2006). A very good, high-altitude site like Chajnantor is usable for less than 25% of the time in winter (i.e. at least 40% transmission) in the 350/450 μm windows, and probably for less than 5% of the time at 200 μm (*Peterson et al.*, 2003). *Matsushita et al.* (1999) reported a more optimistic estimate, operational experience with APEX, ALMA, and other telescopes will tell.

While ground-based observations are limited by the atmosphere, space telescopes remain limited in size and thus can offer only modest angular resolution: from $\sim 6''$ to $37''$ at 70 to 500 μm, respectively for the Herschel space observatory, implying a fairly high extragalactic confusion limit and preventing the study of individual protostars in all but the nearest star-forming clusters of our Galaxy (e.g. *Schneider et al.*, 2010; *André et al.*, 2010). In this context, large (> 10 m) single-dish telescopes operating at 200-450 μm, can provide a better angular resolution than Herschel, and wider-field mapping capabilities than ALMA. This appears to satisfy a clear need in submm astronomy (e.g. Radford et al. 2008). As a result, an intensive study of new sites is currently underway.

Although the average altitude of the Antarctic plateau, ∼3000m, is less than that of the Chajnantor plateau (∼5000m), Antarctica might nevertheless offer better conditions for submm astronomy because of its peculiar geography and climate. The very low atmospheric precipitable water vapour content (PWV) in Antarctic results from the low sun elevation, isolation by the circumpolar vortex , and the high optical reflectivity of ice combined with its high emissivity in the infrared—leading to intense radiative cooling of the ice at night. These phenomena make Antarctica the coldest continent on Earth. Snow precipitation is very low on the Antarctic plateau and low pressure fronts rarely penetrate into the inner plateau, instead staying at the coastline. In fact, the inland part of the continent is a true desert: across an area of 5 million km^2, snow precipitation is about 5 cm annually, and often less than 2 cm at the highest regions (called Domes). As a consequence, the average PWV above the Antarctic plateau is expected to be lower than at Chajnantor (*Minier et al.*, 2009, and references therein).

These high plateau Antarctic sites (Domes A, C, F) are therefore potential locations for astronomical facilities (for Dome A see *Yang et al.*, 2010). The relative merits of the sites have been presented in *Saunders et al.* (2009). These studies follow the development of astronomy at the South Pole, where submm facilities have already been deployed by US astronomers. The atmospheric transmission at 225 GHz has been measured there in

1992 with an NRAO radiometer (*Chamberlin*, 2004).The pathfinder for Antarctic submm-astronomy was AST/RO, a 1.7 m dish (*Stark et al.*, 2001) installed at the South Pole and operational from 1995. Recently, a 10m submm dish has been built at the South Pole (South Pole Telescope SPT, *Carlstrom et al.*, 2011).

Dome C is the location of the French-Italian Concordia station, accessible from both the Dumont-d'Urville and Mario Zucchelli coastal stations by either light plane or, for transporting heavy material, motorised ground expeditions. Concordia station hosts a crew of people during winter and thus allows experiments all year round. Monitoring of the atmosphere characteristics and qualification of the site for optical and near-infrared astronomy have been conducted for many years by French, Italian, and Australian teams (e.g. *Aristidi et al.*, 2005; *Lawrence et al.*, 2004). However, little effort has so far been put into evaluation of the quality of the atmosphere, the meteorological constraints, or the specific advantages of Dome C for a potential submm/FIR telescope. Preliminary meteorological studies and atmospheric transmission models (*Schneider et al.* (2009) and Fig. A.1) suggest that Dome C might offer atmospheric conditions that open the 200-μm window (*Valenziano and Dall'Oglio*, 1999; *Tomasi et al.*, 2006; *Minier et al.*, 2008) for a significant amount of time. *Calisse et al.* (2004) undertook measurements of the atmospheric opacity at 350 μm during a summer campaign and found that it is comparable, but consistently better than, that at South Pole. However, no direct assessment of the wintertime atmospheric transmission has so far been performed.

The stability of the atmosphere is an equally important parameter when comparing different sites, and Dome C may turn out to be far more stable than the Chilean sites (*Minier et al.*, 2008). Determining whether a telescope facility at Dome C in Antarctica might be able to operate in all atmospheric windows between 200 μm and 1 mm, and routinely at 350 and 450 μm throughout the year, has been the main objective of our site testing activities since 2008, as reported in the ARENA[1] European conference proceedings.

A.1.2 Prerequisites for a large submm telescope at Dome C

A study of the necessary pre-requirements for the future deployment of a large, submm telescope has been carried out between 2007 and 2010 at Concordia. Besides the atmospheric transmission in all windows in the far-infrared and submillimetre parts of the spectrum, complementary site testing has focused on the polar constraints and their potential impact on instruments. This work includes a study of the removal and prevention of frost formation, and a study of the temperature gradient in the ground layer.

A.2 Ground-based measurement of atmospheric transmission

The sky opacity at submillimetre wavelengths depends critically on the amount of water vapour in the atmosphere. SUMMIT08 (SUbMilliMetre Tipper version 2008) is an in-situ instrument measuring sky transparency at 200 μm. It consists of a motorised mirror collecting atmospheric radiation at different elevations. This flux is then measured by a photometer behind a 200-μm filter. The previous prototype, SUMMIT, was installed in 2000 at Concordia by the University of New South Wales (UNSW) and performed measurements during the Austral summer between December 2000 and January 2001 (*Calisse et al.*, 2004). SUMMIT has then been refurbished in Saclay and was installed at Concordia in February 2008 under the responsability of CEA/Irfu in collaboration with UNSW (*Durand et al.*, 2008). The instrument then worked almost continuously between April 2008 and December 2008, and has been in full operation since June 2009.

---

[1] Antarctic Research, a European Network for Astrophysics: http://arena.unice.fr

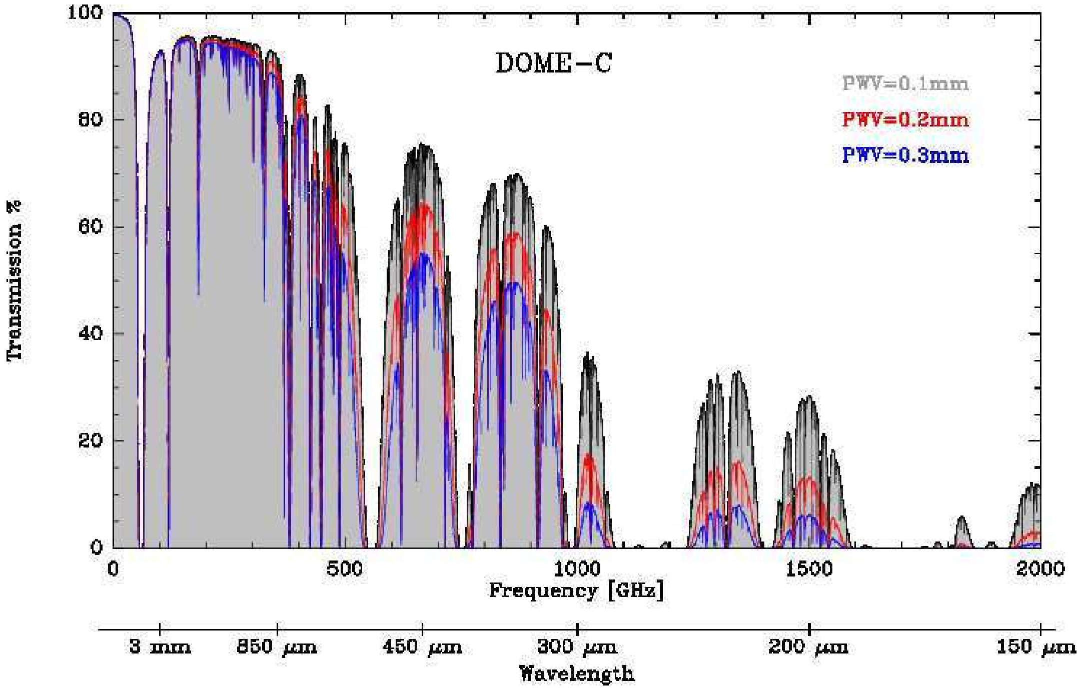

Figure A.1: Atmospheric transmission at 0.1, 0.2, and 0.3mm PWV between 0–2 THz (≈3mm to ≈150 μm) at Dome C calculated with the atmospheric model MOLIERE.

A.2.1 The atmospheric model MOLIERE

MOLIERE (Microwave Observation and LIne Estimation and REtrieval) is a forward and inversion atmospheric model (*Urban et al.*, 2004), developed for atmospheric science applications. The code calculates the absorption of radiation in the mm- to mid-IR wavelength range (equivalent from 0 to 10 THz in frequency) as a result of several effects: (i) spectroscopic lines such as those of atmospheric water (H_2O), oxygen (O_2), and ozone (O_3) absorb strongly at short wavelengths, while (ii) collisions of H_2O with O_2 and nitrogen (N_2) result in continuous absorption across all wavelengths. For the line absorption, a radiative transfer model including refraction and absorption by major and minor atmospheric species is included (H_2O, O_2, O_3, NO_2, HNO_3, CO and other lines up to 10 THz). Spectroscopic parameters are taken from HITRAN[2] and the JPL[3] database. The pseudo-continuum water vapour absorption and collisionally-induced dry absorption are included as a quadratic frequency term according to *Pardo et al.* (2001) for f<1 THz and *Borysow and Frommhold* (1986) for f>1 THz.

This model has previously been used to calculate the atmospheric transmission up to 2000 GHz (∼150 μm) for a large number of astronomical sites (*Schneider et al.*, 2009). The results can be found on a dedicated website[4]. For those studies, approriate temperature and pressure profiles (for example Antarctic profiles for Dome C) of the sites were used (*Schneider et al.*, 2009). The colder Antarctic atmosphere preferentially populates the low-lying energy state of water, leading to a greater absorption for a given PWV than that of a non-polar site. This effect is included in the model.

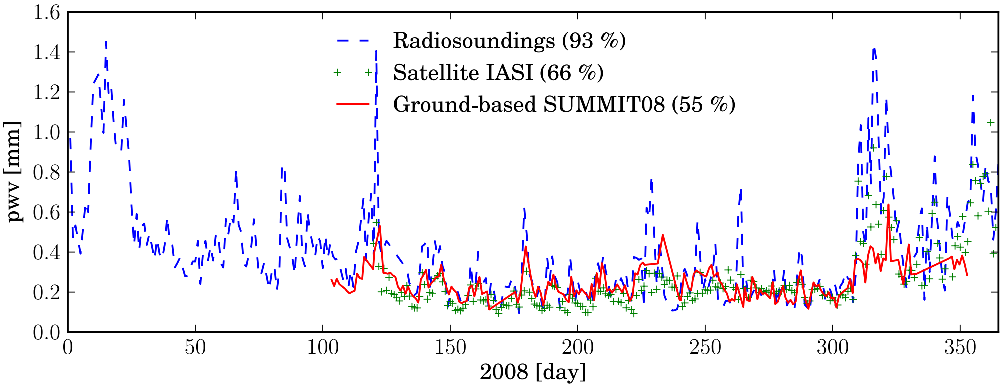

Figure A.2: Precipitable Water Vapour (PWV) in [mm] in 2008 at the Concordia Station measured in-situ by SUMMIT08 (red line), by radiosoundings (blue line) and from space by IASI (green line). Percentages indicate the fraction of time that each of the instruments worked during the year.

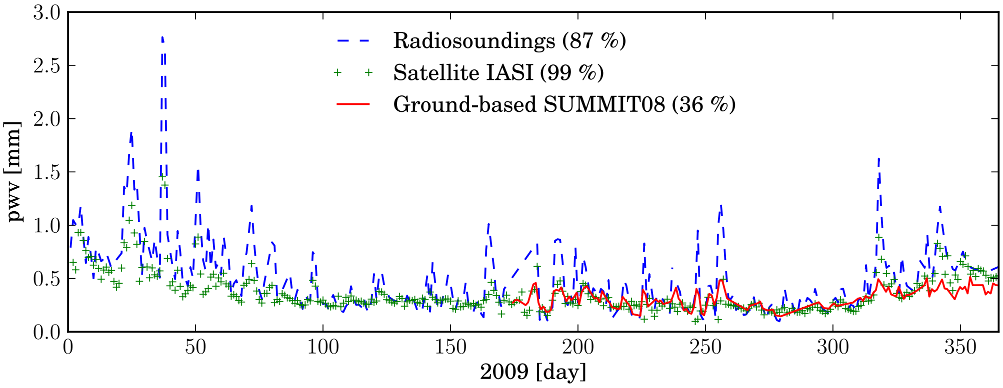

Figure A.3: PWV in 2009 at the Concordia Station measured in-situ by SUMMIT08 (red line), by radiosoundings (blue line) and from space by IASI (green line).

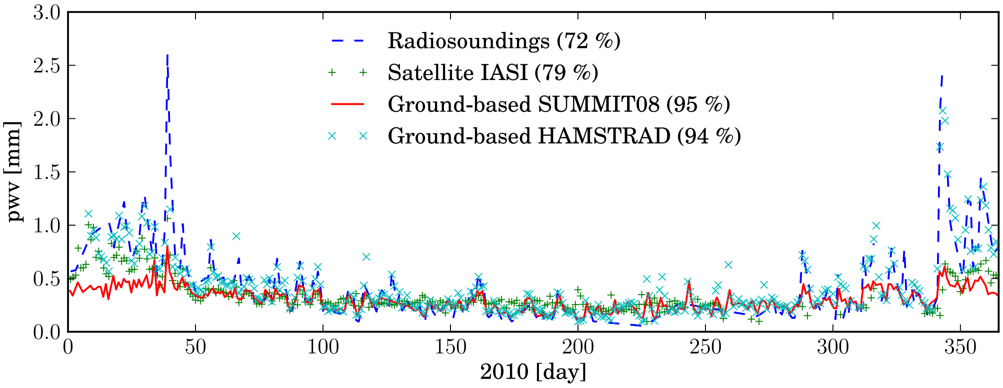

Figure A.4: PWV in 2010 at the Concordia Station measured in-situ by SUMMIT08 (red line), by radiosoundings (blue line), by HAMSTRAD (turquoise line) and from space by IASI(green line).

A.2.2 Measurements, data analysis and results

The atmospheric emission at 200 μm $S(X)$ is a function of zenith opacity τ_{200}, airmass X and atmospheric temperature T_{atm} (see Eq. A.1). G and T_{ref} are the gain and the offset of the detector determined by an internal "hot-cold" calibration. a_{eff} is the transmission of an effective grey body at temperature T_{eff} which takes in account all the noise contributions (e.g. the instrument window, see *Calisse et al.*, 2004); these parameters were determined by an external calibration performed during the two summer campaigns. The two unknown variables τ_{200} and T_{atm} can be extracted from Eq. A.1 by a non linear regression of S as function of the airmass.

$$S(X) = -G(a_{eff}(1 - e^{-X\tau_{200}})T_{atm} + (1 - a_{eff})T_{eff} + T_{ref}) \tag{A.1}$$

The 200-μm filter has a bandwidth (FWHM) of 9 μm. The measured zenith transmission is an average over the bandwidth of the filter. Using the atmospheric model MOLIERE (Sect. A.2.1), we characterize the atmospheric window at a given PWV, i.e. the transmission of the atmosphere as a function of the wavelength. For example, in Fig. A.1, the average value of the transmission over the bandwdith of the atmospheric window around 200 μm is less than the transmission at the peak. We can convolve the transmission spectra of the filter with that of the atmospheric window and thereby evaluate how much the peak transmission is under-estimated. On average, a relative under-estimation of 25% was calculated for the zenith transmission (i.e. an average transmission of 10% implies a peak transmission of 12.5%).

MOLIERE is used to relate the opacity at any wavelength to the atmospheric PWV. For the 200-μm window, for example, we extract from the transmission curves (Fig. A.1) the 200-μm transmission for a given PWV. Then, we convert the transmission into an opacity and perform a linear regression of the PWV as a function of this opacity. The relation is given by equation A.2 with a correlation coefficient of 0.9999.

$$PWV = 0.13 \times \tau_{200} - 0.06 \tag{A.2}$$

SUMMIT08 works on a two-hour cycle, performing a measurement at airmass X=1 and 2 as well as two full skydips with ten pointing angles from horizon to zenith. The transmission at 350 μm and the PWV were deduced using MOLIERE, with the method described above.

The points in Figs. A.2, A.3, and A.4 are average values per day, for 2008, 2009, and 2010 respectively. Quartiles of transmission at zenith for 200 and 350 μm ($\mathrm{Trans}_{200/350} = \exp(-\tau_{200/350})$), and PWVs are indicated in Table. A.1. Quartiles represent the distribution function of PWV content, e.g. there is less than 0.19 mm of PWV at Dome C, 25% of the time that SUMMIT08 was working in 2008.

The quartiles indicate that there was a degradation of the transmission between 2008 and 2009 as the amount of PWV increased significantly in one year.

Opacity variations based on a one-day avearges are plotted in Fig. A.5. The standard deviation of the opacity distribution is 0.45, which corresponds to variations of only 37% in transmission. Atmospheric conditions are very stable during winter in Antarctica, where the polar night avoids the strong diurnal variations of water vapour induced by the solar radiation in non-polar regions.

---

[2] High Resolution Transmission molecular absorption database

[3] Jet Propulsion Laboratory

[4] http://transmissioncurves.free.fr

Table A.1: Quartiles of SUMMIT08 measurements in 2008, 2009, 2010 and cumulated on the three years. PWV and transmission at 350 μm are derived using the MOLIERE model.

Time % 2008	PWV (mm)	$Trans_{200}$	$Trans_{350}$
25 %	0.19	0.15	0.60
50 %	0.22	0.11	0.56
75 %	0.29	0.07	0.50
Time % 2009	PWV (mm)	$Trans_{200}$	$Trans_{350}$
25 %	0.25	0.09	0.54
50 %	0.32	0.05	0.48
75 %	0.39	0.03	0.42
Time % 2010	PWV (mm)	$Trans_{200}$	$Trans_{350}$
25 %	0.22	0.12	0.57
50 %	0.28	0.07	0.51
75 %	0.38	0.03	0.43
Time % cumulated	PWV (mm)	$Trans_{200}$	$Trans_{350}$
25 %	0.21	0.12	0.58
50 %	0.27	0.08	0.52
75 %	0.35	0.04	0.45

A.3 Comparisons between instruments

A.3.1 Satellite measurements : IASI

IASI (Infrared Atmospheric Sounding Interferometer) is an atmospheric interferometer working in the infrared, launched in 2006 on the METOP-A satellite (*Phulpin et al.*, 2007; *Pougatchev et al.*, 2008). The data are available at the website of the Centre for Atmospheric Chemistry Products and Services[5]. IASI was developed by the French Space Agency CNES[6] in collaboration with EUMETSAT[7]. The satellite is in a polar orbit such that each point on Earth is seen at least once a day by the detector. IASI is a Fourier Transform Spectrometer (FTS) working between 3.7 and 15.5 μm. It is associated with an infrared imager, operating between 10.3 and 12.5 μm. Each pixel of the instrument corresponds to a spatial extent of 12 km at nadir, and vertical profiles of humidity at ninety altitude levels are retrieved with a typically 10% accuracy. The amount of precipitable water vapour is given by the integral of these vertical profiles. We took all the measurements in a zone of 110 km^2 around Concordia. The results for 2008, 2009, and 2010 are plotted together with the SUMMIT08 data in Fig. A.2, A.3, and A.4 together with the correlation of the data in Fig. A.6. There is a small negative bias for SUMMIT08 (SUMMIT08 values are lower than the ones for IASI) at low PWV (less than 0.4 mm), and a significant negative bias at high PWV (more than 0.4 mm). This bias occurs during the summer period, when the PWV is high. An analysis of the skydips shows that the fluxes received at different elevations are highly variable during the summer and do not fit the exponential profile given by equation A.1. Therefore we conclude that there are atmospheric temperature or PWV variations at the scale of Summit field of view that pollute the analysis and prevent us to extract an accurate value for the PWV during summer periods.

---

[5] http://ether.ipsl.jussieu.fr

[6] Centre National d'Etudes Spatiales

[7] European organisation for meteorological satellites http://www.eumetsat.int

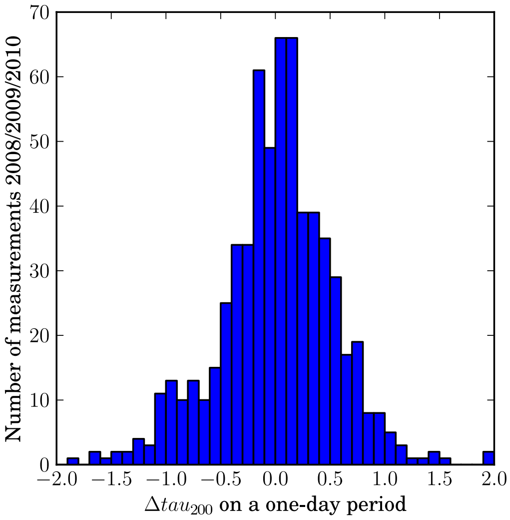

Figure A.5: Distribution of 200-μm opacity variations on a one-day statistic for 2008/2009/2010

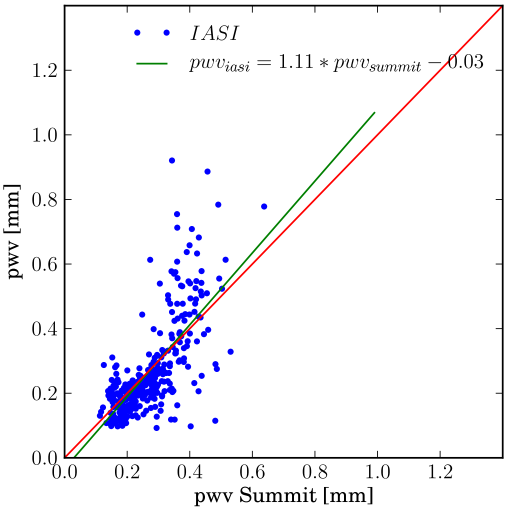

Figure A.6: Correlation between in-situ measurement (SUMMIT08) and satellite measurments(IASI) between 2008 and 2010

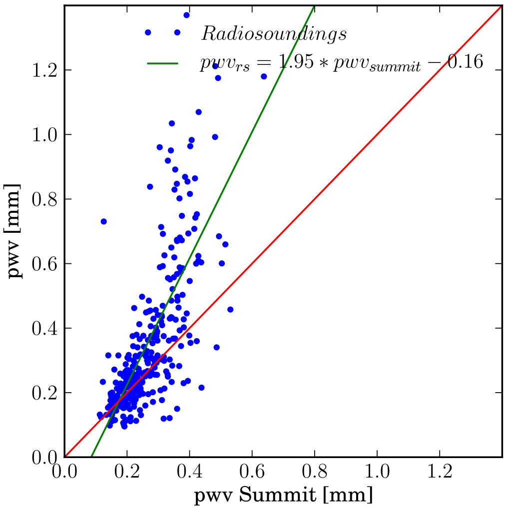

Figure A.7: Correlation between in-situ measurements SUMMIT08 and radiosoundings between 2008 and 2010

A.3.2 In-situ measurements: Radiosoundings & HAMSTRAD

An atmospheric radiosounding station was installed at Concordia Station in 2005. Radiosonde balloons are launched twice a day, and reach an altitude of 25-30 km. The vertical profile of the atmospheric pressure, temperature and relative humidity is measured during the ascent. PWV is calculated by integrating this vertical profile. The data and additional information were obtained from IPEV/PNRA Project "Routine Meteorological Observation at Station Concordia [8]" (see *Tomasi et al.*, 2006). The results from these measurements are plotted in Fig. A.2, A.3, and A.4 and the correlation of the data with SUMMIT08 data in Fig. A.7.

HAMSTRAD is a microwave instrument operating at 60 and 183 GHz, measuring temperature and water vapour profiles between 0 and 10 km with a time resolution of 7 minutes (*Ricaud et al.*, 2010). The instrument has been fully operating since the beginning of 2010. PWV derived from the vertical profile is plotted in Fig. A.4, and the correlation of these data with the SUMMIT08 data in Fig. A.8. The SUMMIT08 measurements and radiosonde or HAMSTRAD data are well correlated at low PWV (less than 0.4 mm), but less so at high PWV (more than 0.4 mm), probably due to temperature or PWV spatial variations during summer skydips of SUMMIT08.

A.3.3 Instrument and site comparison

Low PWV periods mainly occur during the austral winter (from March to October) and high PWV periods are concentrated during austral summer periods (from November to February). In contrast to, for example, the Chilean sites where strong day-to-day variations are found, there is a very long and stable period of high transparency at submillimetre wavelengths at Dome C. This will be the subject an upcoming paper, in which we study a large number of locations using satellite data to characterize the quality of the sites in an unbiased way. The stable periods at Dome C are identified as *winter periods* in the quartiles (Fig. A.9). *Summer period* quartiles are plotted in Fig. A.10, and total quartiles per period in Fig. A.11. The time fractions used for these quartiles are based on the time the instruments were in operation. The quartiles of SUMMIT08 are slightly biased because

---

[8] http://www.climantartide.it

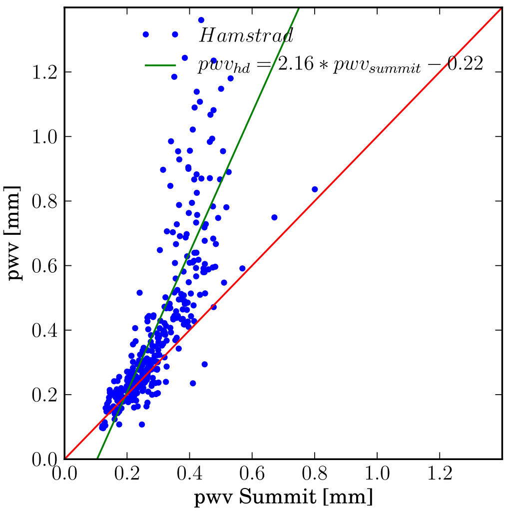

Figure A.8: Correlation between in-situ measurements SUMMIT08 and HAMSTRAD in 2010

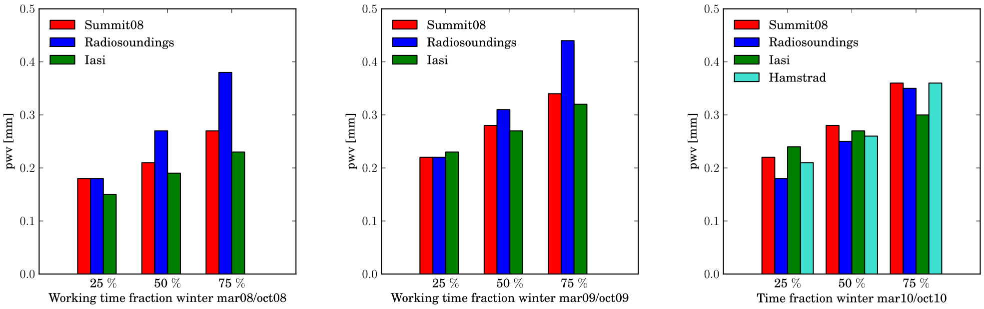

Figure A.9: Winter quartile during the working time of the instruments between March 2008 and October 2010.

it was not functional all the time during these periods (between 36% and 95%), while the satellite and radiosounding quartiles are less biased (IASI was operational between 85% and 100% of the time during these periods).

The SUMMIT08 campaign allows validation of the satellite measurements. There is a very good correlation during winter periods between IASI, SUMMIT08, HAMSTRAD, and radiosonde data. However the correlation is not so good during summer periods, or more generally when PWV is high (more than 0.4 mm). HAMSTRAD is well correlated with the radiosonde data but there is a dry bias for IASI data. This bias was previously identified by *Ricaud et al.* (2010) and could be attributed to the influence of the surface emission parameter over Antarctica. In order to further improve the effectiveness of satellites for measuring temperature and humidity over the White Continent, a consortium (see *Rabier et al.*, 2010) was created to collect ground-based data for comparison; in particular to understand why measurements differ at high PWV.

Nevertheless, for astronomical observations, we are only interested in PWV values below about 0.3 mm (50% transmission at 350 μm wavelength), and the disparity between measurements at high PWV disappears for the median and 25% winter time fraction (Fig. A.9 and Fig. A.11).

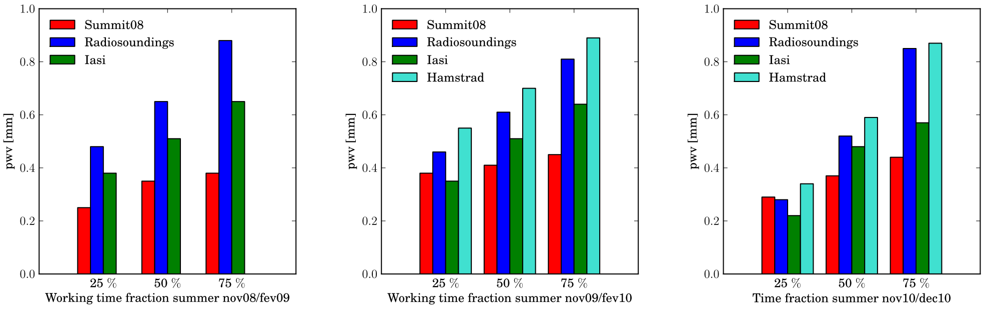

Figure A.10: Summer quartile during the working time of the instruments between March 2008 and December 2010.

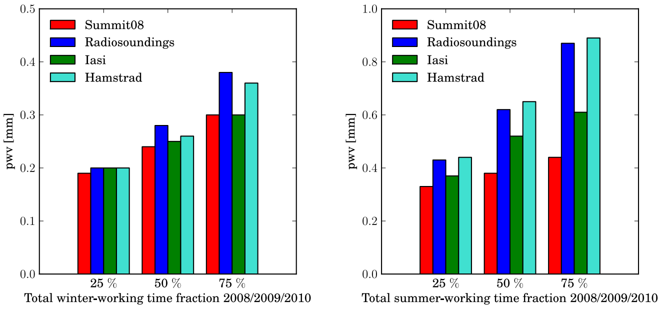

Figure A.11: Total quartile per summer/winter periods during the working time of the instruments between March 2008 and December 2010.

A.4 Polar Constraints

A.4.1 Frost Formation

The GIVRE experiment was designed in 2006 to study frost formation (*Durand et al.*, 2008). It consists of a series of twelve probes of different shapes and colors: five black and two bright cylinders, two black and two bright disks, and an aluminium plate. The probes are divided in two groups, which were placed at different altitudes on a fifty meter tower. They can all be warmed by heaters except for the plate, which instead can have dry air (from near the ground) blown over it. In 2007, building upon the results from the first year of tests, an antifrost system was installed on the COCHISE telescope (*Sabbatini et al.*, 2009) at Concordia. Three different techniques are used : heaters at the rear of the mirror, an infrared lamp, and an air blowing system.

Table A.2: Water vapour partial pressure for saturated air as a function of atmospheric temperature.

Temperature (°C)	Partial Pressure Of Water Vapour (Pa)
-40	12.84
-50	3.94
-60	1.08
-70	0.26

During the summer season, the mean temperature at Concordia is of the order of -30°C and no frost appears on instruments during this period. However during winter, the temperature can fall to -70°C and the partial pressure of water vapour is two orders of magnitude lower (see Table A.2). At -70°C, a partial pressure of water vapour of 0.26 Pa

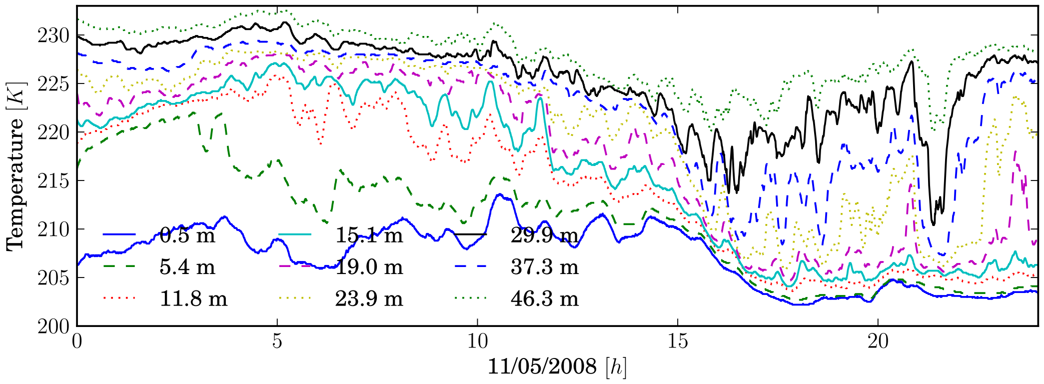

Figure A.12: Typical temperature variation at altitudes between 0.5 m and 46.3 m during a winter day. Each curve is the temperature in Kelvin measured at a given altitude on the 50m tower

corresponds to an absolute humidity of 1 mg of water per m^3; i.e., a hundred times smaller than a drop of water. In such conditions, however, the relative humidity is very high, nearly 100 %. If the temperature decreases by 5°C, the relative humidity will increase by almost a factor of two and can become much higher than 100 %, leading to ice nucleation and frost formation. Frost can also appear due to snow precipitation on surfaces.

Three systems can be used against frost formation and snow deposit:

- Warming up the probes by three or four degrees is enough to prevent frost. It is also the most efficient way to prevent frost formation on the mirror of a telescope.
- Taking dry air at snow surface level and blowing it over the probes is effective; it is also a useful method because it does not require warm optics (which can introduce undesirable temperature gradients).
- Explosive air blowing can be used to physically remove the snow deposit.

Frost mainly forms as a result of the cooling of a surface radiating towards the sky. Close to these surfaces, the maximum amount of water vapour that the atmosphere can hold is lower and frost appears. Warming up these surfaces by three or four degrees is sufficient to compensate for the heat loss due to radiation. Blowing dry air taken from close to the ground is an also effective way to dehumidify the local environment.

A.4.2 Temperature gradient in the boundary layer

The large temperature gradient in the first thirty meters above the snow limits the choice of materials that can be used to build large instruments in a polar environment. The MAST experiment, installed in 2007 at Concordia, consists of sixteen temperature probes placed on a fifty-meter tower (*Durand et al.*, 2008) with a logarithmically increasing spacing bewteen the probes The probes are Pt1000 sensors sandwiched between two bright plates to protect them from solar radiation. GIVRE and MAST can be controlled from the station, and data are automatically sent daily to the station and thence to Europe via the station's communication system.

Close to the ground, the atmosphere is cooled by contact with the snow surface. The temperature increases with altitude up to a point of inversion, above which the atmosphere has the usual tropospheric profile, decreasing by 6.5 °C per kilometre. The atmosphere between the ground and the point of inversion is called the boundary layer. The thickness of this layer can be very low, leading to very good astronomical seeing in the visible (see *Fossat*, 2005). However this thickness is variable and is responsible for strong (vertical and temporal) temperature gradients close to the ground. These gradients can be extreme, as shown in Fig. A.12 and A.13. The typical variations during a winter day can result in a vertical gradient of 30°C over 50 meters, and variations of 15°C in one hour have been recorded. However, the engineering issues this creates can be readily overcome by using materials with low thermal expansion.

A.5 Discussion and conclusions

The necessary requirements for the future deployment of a large (10–25 m) telescope have been explored between 2007 and 2010. The atmospheric opacity at 200 μm was monitored for three years, making this the first extended study at this wavelength and providing the first multi-year statistics. Based on these atmospheric opacity measurements and the derived PWV, we can conclude that the submm/THz atmospheric windows open during a relatively large and stable fraction of time, and particularly for all windows down to 350 μm. The 200-μm window opens for somewhat less than 25% of the time (PWV$<$ 0.2 mm). These findings are based upon a $\sim$3 year study in which we noticed significant variations from one year to another.

Comparisons between Dome C and other sites (e.g. Dome A, Chajnantor) should be made over the same period of time to be directly comparable. In addition, the issue of calibration (window transmission, filter bandwdith,. etc see *Radford*, 2009) usually complicates comparisons between sites where measurements are made with different instruments. However, although non-polar sites can offer very good conditions for submillimetre observations (e.g. Chajnantor *Radford et al.* (2008)), Antarctica provides not only better transmission, but also extremely good stability that is invaluable for time-series studies at submillimetre wavelengths.

In addition to the measurement of the atmospheric opacity, a knowledge of the polar constraints is an equally necessary prerequisite for operating in the harsh Antarctic plateau environment. The thermal gradient in the boundary layer and the problem of ice formation have been extensively monitored. Techniques for preventing or removing ice have also been implemented on site. Solutions for preventing and removing icing and frost proved to be useful on probes and on the surface of a 2.5-m diameter telescope, which could scale-up for installations on larger and more complex instruments. Another polar constraint of importance is the thermal gradient that was measured in a 46-m high layer above the ground. *Radford* (2009) pointed out the possible lack of surface accuracy of mirrors due to thermal gradients arising from both the vertical gradient and iced surface of the telescope. Tests of image quality while removing frost will be done on the IRAIT telescope (*Tosti*, 2006) that is currently deployed at Dome C. Further studies of the polar constraints based on the thermal gradient and variation will be discussed in technical reports. For the scope of this paper, we may conclude that any instrument in the boundary layer should be built with materials whose thermal expansion coefficient is low at temperatures around -70°C. In addition, materials must be able to be cooled rapidly to very low temperature without internal stresses being created.

In conclusion, Dome C is currently one of the best accessible sites on Earth in terms of transmission in the FIR/submm. The 200-μm window opens at a level of 10-15% for slightly less than 25% of the time. Further analysis indicates that observations at 350 and 450 μm would be possible all year round. These very good astronomical conditions in terms of atmospheric transmission and stability offer a unique opportunity for high angular resolution and time series observations at Dome C with medium size instruments.

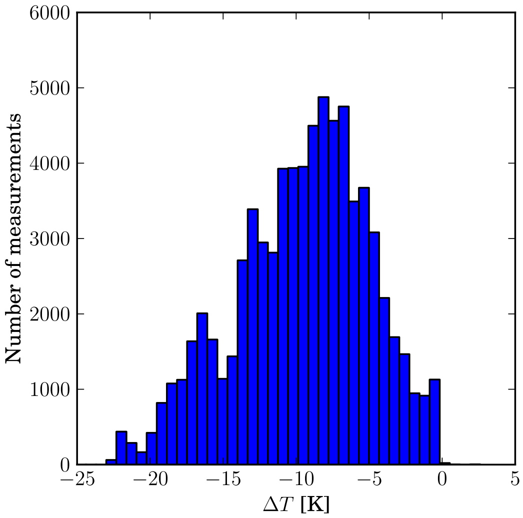

Figure A.13: Distribution of temperature gradient between 0.5 m and 46.3 m between 01/2010 and 04/2010.

Bibliography

André, P., et al. (2010), From filamentary clouds to prestellar cores to the stellar IMF: Initial highlights from the Herschel Gould Belt Survey, *A&A*, *518*, L102, doi:10.1051/0004-6361/201014666. 134

Aristidi, E., et al. (2005), An analysis of temperatures and wind speeds above Dome C, Antarctica, *A&A*, *430*(2), 739–746, doi:10.1051/0004-6361:20041876. 135

Borysow, A., and L. Frommhold (1986), Collision-induced rototranslational absorption spectra of N2-N2 pairs for temperatures from 50 to 300 K, *ApJ*, *311*, 1043, doi:10.1086/164841. 136

Calisse, P. G., M. C. B. Ashley, M. G. Burton, M. A. Phillips, J. W. V. Storey, S. J. E. Radford, and J. B. Peterson (2004), Submillimeter Site Testing at Dome C, Antarctica, *PASA*, *21*(3), 256–263, doi:10.1071/AS03018. 135, 138

Carlstrom, J. E., et al. (2011), The 10 Meter South Pole Telescope, *PASP*, *123*(903), 568–581, doi:10.1086/659879. 135

Chamberlin, R. A. (2004), Reanalysis of the 1992 South Pole Millimetre-Wavelength Atmospheric Opacity Data, *PASA*, *21*(3), 264–274, doi:10.1071/AS03012. 135

Durand, G. A., et al. (2008), Toward a large telescope facility for submm/FIR astronomy at Dome C, *SPIE*, *7012*, 70,122B–70,122B–11, doi:10.1117/12.789337. 135, 143, 144

Fossat, E. (2005), The Concordia station on the Antarctic plateau: The best site on earth for the 21st century astronomers, *JApA*, *26*(2-3), 349–357, doi:10.1007/BF02702343. 145

Hills, R. E., R. J. Kurz, and A. B. Peck (2010), ALMA: status report on construction and early results from commissioning, *SPIE*, *7733*, 773,317–773,317–10, doi:10.1117/12.857017. 134

Lawrence, J. S., M. C. B. Ashley, A. Tokovinin, and T. Travouillon (2004), Exceptional astronomical seeing conditions above Dome C in Antarctica., *Nature*, *431*(7006), 278–81, doi:10.1038/nature02929. 135

Marrone, D. P., R. Blundell, E. Tong, S. N. Paine, D. Loudkov, J. H. Kawamura, D. Lühr, and C. Barrientos (2005), Observations in the 1.3 and 1.5 THz Atmospheric Windows with the Receiver Lab Telescope, *STT*. 134

Matsushita, S., H. Matsuo, J. R. Pardo, and S. J. E. Radford (1999), FTS Measurements of Submillimeter-Wave Atmospheric Opacity at Pampa la Bola II : Supra-Terahertz Windows and Model Fitting, *PASJ*. 134

Minier, V., et al. (2008), Submm/FIR Astronomy in Antarctica: Potential for a large telescope facility, *EAS*, *33*, 21–40, doi:10.1051/eas:0833005. 135

Minier, V., et al. (2009), The Antarctic Submillimetre Telescope, *EAS*, *40*, 269–273, doi: 10.1051/eas/1040039. 134

Oberst, T. E., et al. (2006), Detection of the 205 um [N ii] Line from the Carina Nebula, *ApJ*, *652*(2), L125–L128, doi:10.1086/510289. 134

Pardo, J., J. Cernicharo, and E. Serabyn (2001), Atmospheric transmission at microwaves (ATM): an improved model for millimeter/submillimeter applications, *ITAP*, *49*(12), 1683–1694, doi:10.1109/8.982447. 136

Peterson, J., S. Radford, P. Ade, R. Chamberlin, M. O'Kelly, K. Peterson, and E. Schartman (2003), Stability of the Submillimeter Brightness of the Atmosphere above Mauna Kea, Chajnantor, and the South Pole, *PASP*, *115*(805), 383–388, doi:10.1086/368101. 134

Phulpin, T., D. Blumstein, F. Prel, B. Tournier, P. Prunet, and P. Schlüssel (2007), Applications of IASI on MetOp-A: first results and illustration of potential use for meteorology, climate monitoring, and atmospheric chemistry, *SPIE*, *6684*, 66,840F–66,840F–12, doi:10.1117/12.736816. 139

Pilbratt, G. L., et al. (2010), Herschel Space Observatory, *A&A*, *518*, L1, doi:10.1051/0004-6361/201014759. 134

Pougatchev, N., T. August, X. Calbet, T. Hultberg, O. Oduleye, P. Schlüssel, B. Stiller, K. St. Germain, and G. Bingham (2008), Validation of the IASI temperature and water vapor profile retrievals by correlative radiosondes, *SPIE*, *7081*, 70,810J–70,810J–9, doi: 10.1117/12.795382. 139

Rabier, F., et al. (2010), The Concordiasi Project in Antarctica, *BAMS*, *91*(1), 69, doi: 10.1175/2009BAMS2764.1. 142

Radford, S. J. E. (2009), Submillimeter Astronomy, *EAS*, *40*, 405–410, doi:10.1051/eas/1040056. 145

Radford, S. J. E., R. Giovanelli, G. E. Gull, and C. P. Henderson (2008), Submillimeter observing conditions on Cerro Chajantor, *SPIE*, *7012*, 70,121Z–70,121Z–7, doi:10.1117/12.789335. 145

Ricaud, P., B. Gabard, S. Derrien, J.-P. Chaboureau, T. Rose, A. Mombauer, and H. Czekala (2010), HAMSTRAD-Tropo, A 183-GHz Radiometer Dedicated to Sound Tropospheric Water Vapor Over Concordia Station, Antarctica, *ITGRS*, *48*(3), 1365–1380, doi:10.1109/TGRS.2009.2029345. 141, 142

Sabbatini, L., G. Dall'Oglio, L. Pizzo, A. Miriametro, and F. Cavaliere (2009), COCHISE: a 2.6 meter millimetric telescope at Concordia, *EAS*, *40*, 319–325, doi:10.1051/eas/1040045. 143

Saunders, W., J. S. Lawrence, J. W. V. Storey, M. C. B. Ashley, S. Kato, P. Minnis, D. M. Winker, G. Liu, and C. Kulesa (2009), Where Is the Best Site on Earth? Domes A, B, C, and F, and Ridges A and B, *PASP*, *121*(883), 976–992, doi:10.1086/605780. 134

Schneider, N., J. Urban, and P. Baron (2009), Potential of radiotelescopes for atmospheric line observations: I. Observation principles and transmission curves for selected sites, *P&SS*, *57*(12), 1419–1433, doi:10.1016/j.pss.2009.07.002. 135, 136

Schneider, N., et al. (2010), The Herschel view of star formation in the Rosette molecular cloud under the influence of NGC 2244, *A&A*, *518*, L83, doi:10.1051/0004-6361/201014627. 134

Stark, A. A., et al. (2001), The Antarctic Submillimeter Telescope and Remote Observatory (AST/RO), *PASP*, *113*(783), 567–585, doi:10.1086/320281. 135

Tomasi, C., et al. (2006), Characterization of the atmospheric temperature and moisture conditions above Dome C (Antarctica) during austral summer and fall months, *JGR*, *111*(D20), doi:10.1029/2005JD006976. 135, 141

Tosti, G. (2006), The International Robotic Antarctic Infrared Telescope (IRAIT), *SPIE*, *6267*, 62,671H–62,671H–12, doi:10.1117/12.670302. 145

Urban, J., P. Baron, N. Lautié, N. Schneider, K. Dassas, P. Ricaud, and J. De La Noë (2004), Moliere (v5): a versatile forward- and inversion model for the millimeter and sub-millimeter wavelength range, *JQSRT*, *83*(3-4), 529–554, doi:10.1016/S0022-4073(03)00104-3. 136

Valenziano, L., and G. Dall'Oglio (1999), Millimetre astronomy from the High Antarctic Plateau: Site testing at Dome C, *PASA*, *16*, 167–174. 135

Yang, H., et al. (2010), Exceptional Terahertz Transparency and Stability above Dome A, Antarctica, *PASP*, *122*(890), 490–494, doi:10.1086/652276. 134

Appendix B

Sites comparison for submillimetre astronomy

The most important limitation for ground-based submillimetre (submm) astronomy is the broad-band absorption of the total water vapour in the atmosphere above an observation site, often expressed as the Precipitable Water Vapour (PWV). A long-term statistic on the PWV is thus mandatory to characterize the quality of an existing or potential site for observational submm-astronomy. In this study we present a three-year statistic (2008–2010) of the PWV for ground-based telescope sites all around the world and for stratospheric altitudes relevant for SOFIA (Stratospheric Observatory for Far-infrared astronomy). The submm-transmission is calculated for typical PWVs using an atmospheric model.

We used data from IASI (Infrared Atmospheric Sounding Interferometer) on the Metop-A satellite to retrieve water vapour profiles for each site (11 in total, comprising Antarctica, Chile, Mauna Kea, Greenland, Tibet). The use of a single instrument to make the comparison provides unbiased data with a common calibration method. The profiles are integrated above the mountain/stratospheric altitude to get an estimation of the PWV. We then applied the atmospheric model MOLIERE (Microwave Observation and LIne Estimation and REtrieval) to compute the corresponding atmospheric absorption for wavelengths between 150 μm and 3 mm.

We present the absolute PWV values for each site sorted by year and time percentage. The PWV corresponding to the first decile (10%) and the quartiles (25%, 50%, 75%) are calculated and transmission curves between 150 μm and 3 mm for these values are shown. The Antarctic and South-American sites present very good conditions for submillimetre astronomy. The 350 μm and 450 μm atmospheric windows are open all year long whereas the 200 μm atmospheric window opens reasonably for 25 % of the time in Antarctica and the extremely high-altitude sites in Chile. Potential interesting new facilities are Macon in Argentinia and Summit in Greenland that show similar conditions as for example Mauna Kea (Hawaii). For SOFIA, we present in more detail transmission curves for different altitudes (11 to 14 km), PWV values, and higher frequencies (up to 5 THz). Though the atmosphere at these altitude is generally very transparent, the absorption at very high frequencies becomes more important, partly caused by minor species. In conclusion, the method presented in this paper could identify sites on Earth with a great potential for submillimetre astronomy, and guide future site testing campaigns *in situ*.

B.1 Introduction

Despite its large interest for astronomy, the submillimetre (submm) to far-infrared (FIR) wavelength range is mostly limited by the pressure-broadened absorption of tropospheric water vapour present in the Earth's atmosphere (see, e.g. *Minier et al.*, 2010, for a summary of astronomy projects). The water vapour profile, and thus also the integrated column of water expressed in Precipitable Water Vapour (PWV), depends on the geographical location. The PWV generally decreases with altitude, so that high-lying sites are best suited for submm-astronomy. Airborne astronomy, now possible on a regular base using SOFIA, is much less limited by water vapour and due to the lower atmospheric pressure, spectral broadening is less important. However, there is still absorption close to major and minor species (e.g., O_3, N_2O, CO) as well as collision induced non-resonant continuum absorption. SOFIA can now access the very high frequency range (>2 THz), definitely closed for ground-based sites, but line intensities and abundances of the major and minor species need to be known precisely. First spectroscopic observations performed with SOFIA (see A&A special issue) showed that small-scale atmospheric variations in the troposphere/stratosphere layer are very difficult to assess (*Guan et al.*, 2012)

For ground-based sites, previous studies (e.g. *Schneider et al.*, 2009; *Tremblin et al.*, 2011; *Matsushita et al.*, 1999; *Peterson et al.*, 2003) already showed that a few sites are well-suited for submm/mid-IR, and FIR-astronomy and their transmission properties are rather well determined (for example by Fourier Transform Spectrometer obervations in the 0.5–1.6 THz range at Mauna Kea/Hawaii (*Pardo et al.*, 2001)). The high-altitude (>5000 m) Chilean sites are known for dry conditions (see *Matsushita et al.*, 1999; *Peterson et al.*, 2003), and site testing is now carried out at the driest place on Earth, Antarctica (see *Chamberlin et al.*, 1997; *Yang et al.*, 2010; *Tremblin et al.*, 2011). Comparisons between Antarctic and Chilean sites are difficult and uncertain since they rely on ground-based instruments that use different methods and calibration techniques (see *Peterson et al.*, 2003, for example). The working conditions are also an important issue, a single instrument moved from Chile to Antarctica will have a different behavior in the harsh polar environment (-70°C in winter at Dome C). A meaningful comparison is possible if several independent instruments are used at each place. An example of such a study is the one of *Tremblin et al.* (2011) that obtained transmission data at Dome C thanks to radio-soundings and the radiometers HAMSTRAD (*Ricaud et al.*, 2010) and SUMMIT08. However, it is rare to have many instruments at one site. The best solution is to use satellite data, which also enables to investigate any location on Earth. Thanks to the IASI (Infrared Atmospheric Sounding Interferometer) on the Metop-A satellite, it is now possible to conduct such a comparison over several years with no instrument bias and with the same working conditions for the detectors. We present here a 3-year study of the PWV of a selection of existing and upcoming submm-sites in Antarctica, Chile, Tibet, and Argentina, as well as for two SOFIA stations, Palmdale/California and Christchurch/New Zealand. A direct comparison is enabled by comparing the individual and cumulated quartiles of PWV and the transmission is given, using these PWV values and the atmospheric model MOLIERE-5 (*Urban et al.*, 2004). The paper is organized as follows: After introducing all the sites that are considered in the present study (Sect. 2), we first show the PWV extraction from the satellite data and the comparison of the PWV statistics between all the sites (Sect. 3). Then we present the method to extract transmission curves with the MOLIERE atmospheric model and perform a site comparison for the 250 μm and 350 μm transmission (Sect. 4) The ratio of the monthly-averaged transmission to its fluctuations is then used to compare the stability of the transmission at 200 μm between all the sites at the end of Sect. 4. Section 5 deals with the results for SOFIA and Sect. 6 discusses and summarizes the results.

B.2 Sites of interest

We selected eleven representative sites around the world that can be grouped as follows:

Antarctic sites
Dome C: Concordia station (http://arena.oca.eu) with several telescopes, e.g. IRAIT (International Robotic Antarctic Infrared Telescope)
Dome A: new site in exploration,
http://www.chinare.gov.cn
South pole: SPT (South Pole Telescope),
http://astro.uchicago.edu/research/south-pole-telescope

South-American sites
Chajnantor Plateau in Chile: ALMA (Atacama Large Millimetre Array) site,
http://www.almaobservatory.org
Cerro Chajnantor in Chile: CCAT (Cornell Caltech Atacama Telescope),
http://www.ccatobservatory.org
Cerro Macon in Argentinia

Northern-hemisphere sites
Mauna Kea in Hawaii: JCMT (James Clerk Maxwell Telescope),
http://www.jach.hawaii.edu
Summit in Greenland: http://www.geosummit.org
Yangbajing in Tibet: KOSMA (Cologne Observatory for submm-astronomy),
http://www.astro.uni-koeln.de/kosma

"Stratospheric" sites
SOFIA over Palmdale (USA) and Christchurch (New Zealand), http://www.sofia.usra.edu

The location of the different sites are resumed in Fig. B.1. Our selection includes known sites in Antarctica and North/South America plus northern-hemispheric sites that could be of interests (Summit in Greenland, Yangbajing in Tibet) to have a complete sky coverage. The geographical location, altitude, and related existing/planned telescopes are listed in Table B.1.

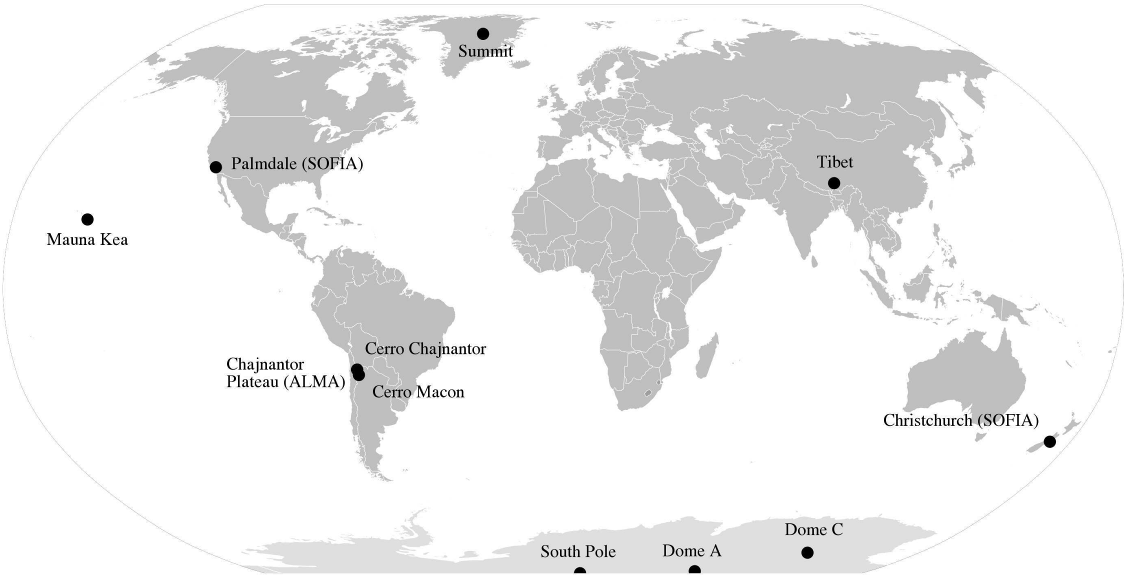

Figure B.1: Location of the different sites of interest.

Table B.1: Location, altitude and telescopes for the different sites. Future telescopes are indicated in parenthesis.

Site	Latitude	Longitude	Alt. [m]	Tel.
Dome C	75°06′s	123°23′e	3233	IRAIT
Dome A	80°22′s	77°21′e	4083	
South pole	90°s	0°e	2800	SPT
Cerro Chajnantor	22°59′s	67°45′w	5612	(CCAT)
Cerro Macon	24°31′s	67°21′w	5032	
Chaj. Plateau	23°00′s	67°45′w	5100	ALMA
Mauna Kea	19°45′n	155°27′w	4207	JCMT
Summit (Greenland)	72°35′n	38°25′w	3210	
Yangbajing (Tibet)	30°05′n	90°33′e	4300	KOSMA
Palmdale	34°37′n	118°05′w	12000	SOFIA
Christchurch	43°31′s	172°38′e	12000	SOFIA

B.3 PWV extraction from satellite data

B.3.1 Method and results

IASI (Infrared Atmospheric Sounding Interferometer) is an atmospheric interferometer working in the infrared, launched in 2006 on the METOP-A satellite (*Phulpin et al.*, 2007; *Pougatchev et al.*, 2008; *Herbin et al.*, 2009; *Clerbaux et al.*, 2009). The data are available at the website of the Centre for Atmospheric Chemistry Products and Services[1]. IASI was developed by the French Space Agency CNES[2] in collaboration with EUMETSAT[3]. The satellite is on a polar orbit so that each point on Earth is seen at least once per day by the detectors. IASI is a Fourier Transform Spectrometer (FTS) working between 3.7 and 15.5 μm. It is associated with an infrared imager, operating between 10.3 and 12.5 μm. Each pixel of the instrument corresponds to a spatial extent of 12 km at nadir, and vertical profiles of tropospheric humidity at ninety altitude levels (resolution 1 km) are retrieved with a typically 10% accuracy (*Pougatchev et al.*, 2008). The amount of precipitable water vapour is given by the integral of these vertical profiles. We averaged on a daily base all measurements whose central position falls in a zone of 110 km^2 around each site to derive PWV statistics between 2008 and 2010. This method was validated in *Tremblin et al.* (2011) in which we compared IASI satellite data with ground-based instruments (HAMSTRAD and SUMIT08) and radio-sounding data over the French-Italian base Concordia at Dome C in Antarctica. All instruments have a good correlation at low PWV which is precisely the range we are interested in for submillimetre astronomy.

The use of vertical satellite profiles is slightly trickier for a mountain site. Since we take all measurements in a zone of 110 km^2, we sometimes get profiles that do not contain mountain altitude but include lower ones. This would bias the retrieved PWV to high values. To overcome this difficulty, we generally truncated the profiles at the pressure level of the site of interest. This method was already used by *Ricaud et al.* (2010) to compare IASI measurements with the HAMSTRAD radiometer, over the Pyrenees mountains. They showed a very good correlation for the integrated PWV. We also determined in this way the PWV content at high altitudes (>11 km) over Palmdale, USA and Christchurch, New Zealand for the on-going and future flights of SOFIA. During a typical flight, SOFIA will range hundreds of kilometers from its base and the water vapour depends on local weather conditions at the position of the plane. Since the profiles are averaged on a 110-km^2

---

[1] `http://ether.ipsl.jussieu.fr`

[2] Centre National d'Etudes Spatiales

[3] European organization for meteorological satellites `http://www.eumetsat.int`

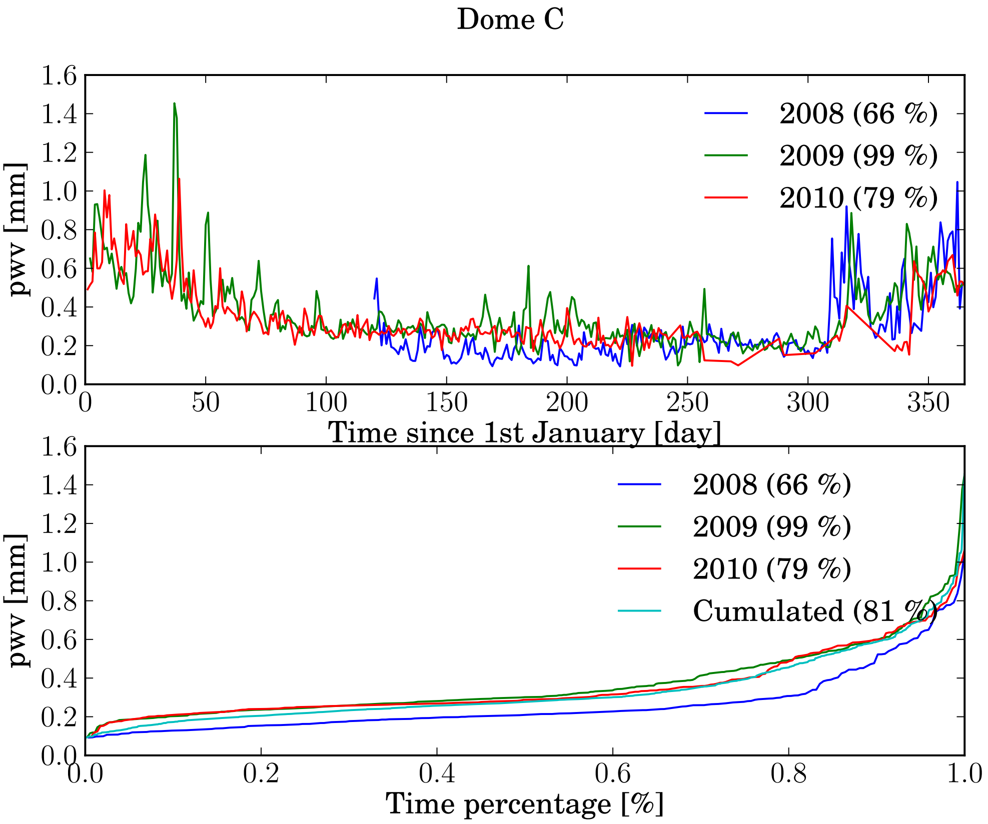

Figure B.2: Top: PWV content measured at Dome C, Antarctica over the French Italian base Concordia between 2008 and 2010. The percentage indicates the fraction of days of the year on which we were able to extract the data from the satellite measurements. Bottom: function of repartition of the PWV for each year and for the whole period.

Table B.2: First decile and quartiles of the PWV for all the studied sites.

Time frac. 2008-2010	SOFIA (Palm./Christ.)	Dome C	Dome A	South Pole	Cerro Chajn.
0.10	0.006/0.004	0.17	0.11	0.15	0.27
0.25	0.006/0.005	0.22	0.16	0.21	0.37
0.50	0.007/0.006	0.28	0.21	0.30	0.61
0.75	0.009/0.007	0.39	0.26	0.49	1.11

Time frac. 2008-2010	Chajn. Plat.	Cerro Macon	Summit	Yang- -bajing	Mauna Kea
0.10	0.39	0.47	0.36	1.21	0.62
0.25	0.53	0.66	0.51	2.47	0.91
0.50	0.86	1.02	0.94	inf	1.44
0.75	1.63	1.66	1.96	inf	2.57

area and the time statistics done on three years, the results given here will represent the averaged conditions under which SOFIA is operating. Precise local measurements of the PWV useable for calibration are much more difficult to perform (see *Guan et al.*, 2012).

Note that the water vapour profiles are measured in function of the pressure by IASI. Therefore it is important to get the correct pressure level at the altitude of the sites. We used as much as we could, in-situ measurements to get the local averaged pressure level. When it was not possible (for Yangbajing, Cerro Macon and SOFIA), we used the pressure

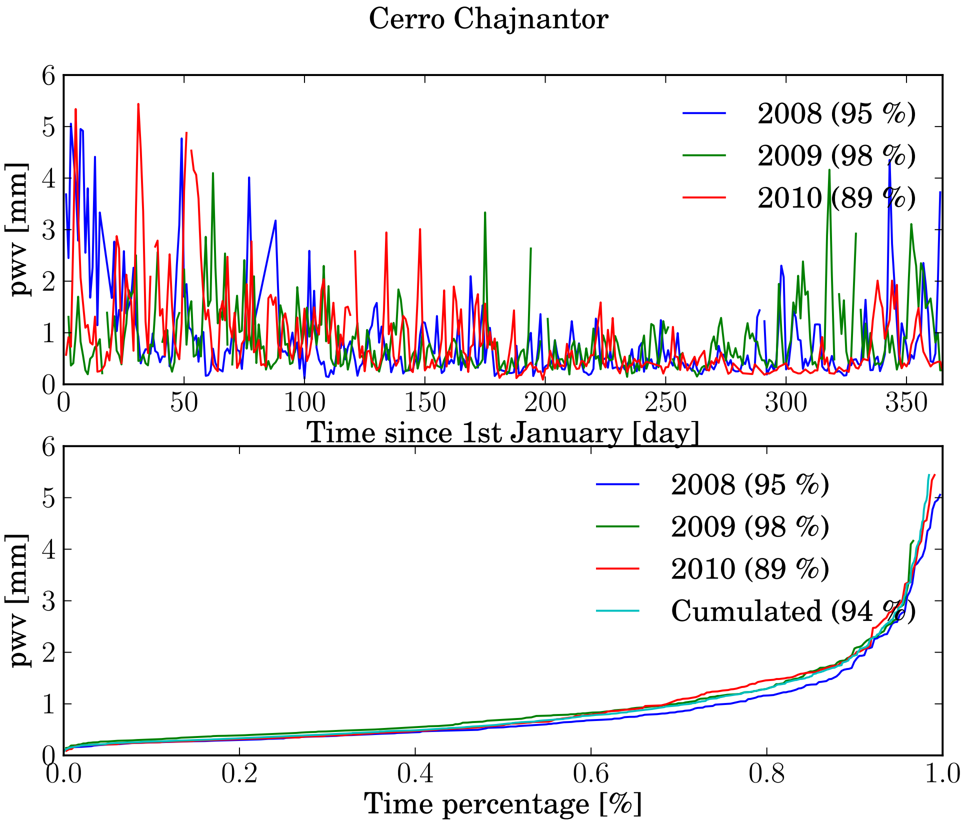

Figure B.3: Same as Fig. B.2 for Cerro Chajnantor in Chile. The satellite profiles were truncated at the altitude of the mountain summit. Note the different scale range of PWV compared to Fig. B.2.

level of the US standard atmosphere (1976) computed at the altitude of the site. However we observed on the other sites that this method can lead to a wrong pressure level that will bias the retrieved PWVs.

Figure B.2 presents the PWV measurements for the Antarctic site of Dome C and Fig. B.3 the measurements for the Chilean site of Cerro Chajnantor. The corresponding figures for all other sites are found in the Appendix and on a dedicated website[4]. Since on Antarctic domes (expression for the mountains in Antarctica), the difference in height is small over 100 km, we do not need to truncate the profiles, whereas it has to be done for a mountain site like Cerro Chajnantor. Some ground measurements are available for different sites and can be compared to our results. Cerro Chajnantor and Chajnantor Plateau were extensively studied (see *Giovanelli et al.*, 2001) and the PWV quartiles between 2006 and 2010 can be found in *Radford* (2011). The values deduced from opacity measurements at 225 GHz are 0.61 mm (25 %), 1.08 mm (50 %), and 2.01 mm (75 %) for the plateau; and 0.33 mm (25 %), 0.61 mm (50 %), and 1.36 mm (75 %) for Cerro Chajnantor. The quartiles for Cerro Chajnantor are in a good agreement with our satellite measurements (between 10 and 20 % difference). Note that the studied periods are not the same and can explain partly the difference. Furthermore, a scale height of the water vapour profiles on the Chajnantor area can be deduced from the quartiles of the plateau and the "Cerro". With the satellite measurements, we computed a 1/e scale height h_e of the order of 1.1 km that is in a good agreement with measurements from *Giovanelli et al.* (2001). The PWV quartiles at the South Pole were computed at saturation from radio-sounding bal-

---

[4] `http://submm.eu`

loons over a period of 40 years (see *Chamberlin*, 2002). They estimated that the PWV should be at 90 % saturated, thus the saturation level can be used as a proxy for the real PWV. They found averaged quartiles of 0.25 mm (25 %), 0.33 mm (50 %), and 0.44 mm (75 %); the difference with our satellite measurements is around 10 %. A radiometer at 225 GHz is operating at the CSO[5] on Mauna Kea. PWV quartiles between 1997 and 2001 can be found in *Otárola et al.* (2010); *Radford* (2011), 1.08 mm (25 %), 1.82 mm (50 %), and 3.32 mm (75 %). The difference with the satellite measurements is around 15-20 % and could be easily caused by variations between the period 1997-2001 and 2008-2010.

The effect of seasons are clearly visible in the Figures. Obviously, the PWV during winter is lower than in summer, i.e. below 0.3 mm at Dome C and below 0.6 mm at Cerro Chajnantor. The Chilean site presents a strong day-to-day variation compared to the Antarctic site. This is caused by the dayily variation of the PWV, that is not present in Antarctica with the long polar night/winter. This may cause a slight bias in the non-polar site data because only one or two measurements per day are available, thus we do not sample very well these day-night variations. Nevertheless, we expect these statistics to represent well the trends over years. The functions of repartition in Fig. B.3 are very similar from 2008 and 2010, therefore the year-to-year statistics are not too much affected by the lack of the day-night variation sampling. In 2008 the PWV was slightly lower than in 2009-2010. This effect was seen in Antarctica (see Fig. B.2) also with the in-situ measurements (radio-soundings, HAMSTRAD, SUMMIT08). Possible explanations were discussed in *Tremblin et al.* (2011) and should not be interpreted as a possible effect of the day-night variations.

B.3.2 Site comparison

Figure B.4 shows the comparison between all sites as a function of repartition of the PWV over the period 2008-2010. Obviously, the air-borne SOFIA stratospheric instrument encounters the lowest PWV, lower than 0.01 mm most of the time and much lower than any ground-based sites. The Antarctic sites follow then as the driest places on Earth, with Dome A, and then Dome C and the South Pole. These sites have PWVs lower than 0.5 mm most of the time (75 % of the time between 2008 and 2010). Chilean and Argentinian sites are next with a PWV lower than 1.5 mm most of the time, followed by Hawaii and Summit in Greenland with a PWV lower than 2 mm, and finally Yangbajing in Tibet which presents a high level of water vapour. The satellite measurements saturate over the Tibet site with high values of the PWV (around 10 mm), this is clearly visible in the figure in the appendix.
These results are presented quantitatively in Table B.2 with the first decile and the quartiles for each site. The difference caused by the truncation for mountain sites can be seen by comparing Cerro Chajnantor to Chajnantor Plateau. The mountain (Cerro) is close to the ALMA site, therefore the profiles that are extracted from the satellite are the same, the difference in the PWV retrieved is mostly caused by the altitude truncation of the profiles. The first decile and the quartiles again clearly show that Antarctic sites are the driest sites followed by South-American sites and then northern-hemisphere sites. Remarkable, our long-term satellite statistic of PWV shows that the site of Summit in Greenland offers comparable observing conditions (PWV and altitude) like on Mauna Kea which opens a new perspective for submm astronomy in the northern hemisphere.

---

[5] Caltech Submillimeter Observatory

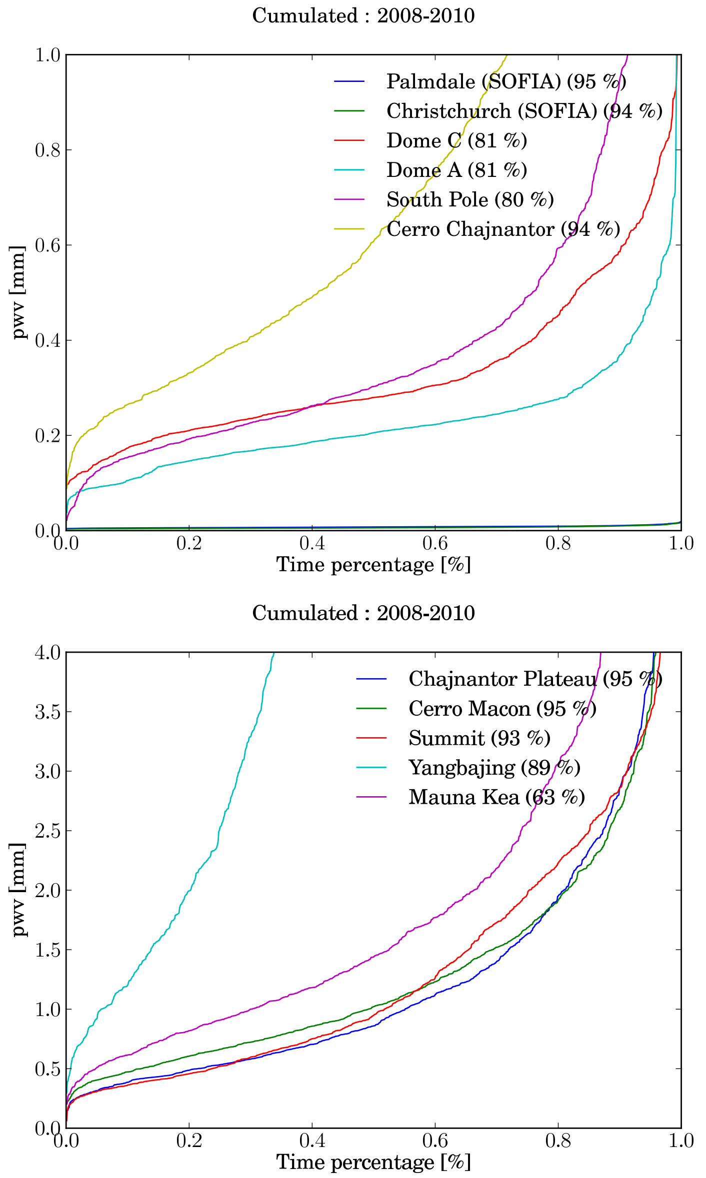

Figure B.4: Comparison of the functions of repartition of the PWV for all sites between 2008 and 2010. The percentage of days over this period on which we achieved the data extraction is indicated in parenthesis. The time percentage (x-axis) is made over the total number of days on which we achieved the data extraction. Note that in the upper panel, the curves for Palmdale (dark blue) and Christchurch (green) are blended and very close to the 0.0 mm level.

B.4 Atmospheric transmission from PWV and MOLIERE

B.4.1 Method

For the determination of the tropospheric transmission corresponding to the PWVs of the various deciles and quartiles for each site, we use *MOLIERE-5.7* (Microwave Observation and LIne Estimation and REtrieval), a forward and inversion atmospheric model (*Urban et al.*, 2004), developed for atmospheric science applications. It has previously been used to calculate the atmospheric transmission up to 2000 GHz (∼150 μm) for a large number of

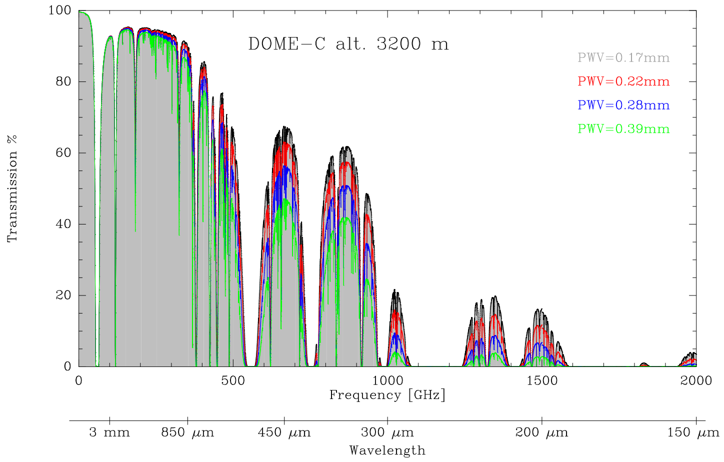

Figure B.5: Transmission curves between 150 μm and 3 mm corresponding to the first decile (grey) and the quartiles (red: 25 %, blue: 50 %, green: 75 %) of PWV between 2008 and 2010 at Dome C.

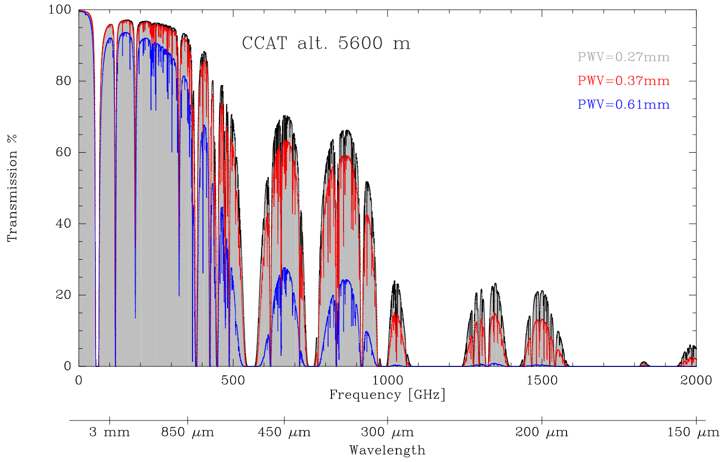

Figure B.6: Transmission curves between 150 μm and 3 mm corresponding to the first decile (grey) and the quartiles (red: 25 %, blue: 50 %) of PWV between 2008 and 2010 at Cerro Chajnantor.

astronomical sites. The results are published in *Schneider et al.* (2009) and on a website[6].

The code calculates the absorption of radiation in the mm- to far-IR wavelength range (equivalent from 0 to 10 THz in frequency) considering the wet- and dry-air components of atmospheric absorption. Spectroscopic lines such as those of atmospheric water (H_2O), oxygen (O_2), and ozone (O_3) absorb strongly at short wavelengths, while collisions of H_2O with O_2 and nitrogen (N_2) result in continuous absorption across all wavelengths. For the line absorption, a radiative transfer model including refraction and absorption by major and minor atmospheric species is included (H_2O, O_2, O_3, NO_2, HNO_3, CO and other lines up to 10 THz). Spectroscopic parameters are taken from HITRAN[7] and the JPL[8] database. The pseudo-continuum water vapour absorption and collisionally-induced dry absorption are included as a quadratic frequency term according to *Pardo et al.* (2001) for f<1 THz and *Borysow and Frommhold* (1986) for f>1 THz (see *Schneider et al.*, 2009). Temperature and pressure profiles of the sites were determined using the compilation described in *Schneider et al.* (2009). The colder Antarctic atmosphere preferentially populates the low-lying energy

---

[6] `http://submm.eu`

[7] High Resolution Transmission molecular absorption database

[8] Jet Propulsion Laboratory

state of water, leading to a greater absorption for a given PWV than that of a non-polar site. This effect is included in the model.

We present here the transmission curves corresponding to the first decile and the quartiles of PWV for two sites of currently large interest, Dome C (Fig. B.5) and Cerro Chajnantor (Fig. B.6) while transmission curves for the other sites are found in the appendix. From Table B.2 we extract that Dome C shows generally lower PWV values than Cerro Chajnator for longer time periods. Comparing the transmission curves at the same PWV (for example 0.28/0.27 mm which corresponds to 50 % of the time at Dome C (blue curve) and 10 % of the time at Cerro Chajnator (grey line)) indicates, however, that the transmission is slighhtly higher at Cerro Chajnator. It corresponds to 20 (65) % at 200 μm (350 μm) for Cerro Chajnator with regard to ~10 (60) % at 200 μm (350 μm) for Dome C. The difference becomes more important for high frequencies (shorter wavelengths) because the absorption by water vapour and the dry-air component are both a function of the altitude. See *Schneider et al.* (2009) for more details on the different absorption characteristics depending on altitude and wavelength. In any case, observations at 350 and 450 μm are possible all year long for both observatories.

B.4.2 Sites comparison

Table B.3: First decile and quartiles of the 350-μm (top) and 200-μm (bottom) transmissions for all the studied sites.

Time frac. 2008-2010	Dome C	Dome A	South Pole	Cerro Chaj.	Chaj. Plat.	Cerro Macon	Mauna Kea	Sum- -mit	Yang- -bajing
0.10	0.62	0.72	0.61	0.65	0.56	0.49	0.40	0.42	0.19
0.25	0.57	0.67	0.56	0.58	0.46	0.41	0.27	0.31	0.02
0.50	0.51	0.62	0.47	0.44	0.31	0.29	0.14	0.15	0.00
0.75	0.41	0.57	0.34	0.24	0.12	0.15	0.03	0.02	0.00

Time frac. 2008-2010	Dome C	Dome A	South Pole	Cerro Chaj.	Chaj. Plat.	Cerro Macon	Mauna Kea	Sum- -mit	Yang- -bajing
0.10	0.17	0.32	0.16	0.20	0.09	0.05	0.03	0.03	0.00
0.25	0.11	0.22	0.11	0.12	0.04	0.02	0.01	0.01	0.00
0.50	0.07	0.16	0.05	0.04	0.01	0.00	0.00	0.00	0.00
0.75	0.03	0.11	0.01	0.00	0.00	0.00	0.00	0.00	0.00

Using the method described in *Tremblin et al.* (2011), we use MOLIERE to calculate the transmissions at 200 μm and 350 μm. We do not compute here the transmissions for SOFIA because it is by far superior compared to all ground based sites. Its transmission curves will be discussed in a dedicated section (Sect. 5).

Figure B.7 shows the functions of repartition of the 350- and 200- μm transmissions for all the other sites. In Table B.3, we give the first decile and the quartiles of 200- and 350-μm transmissions. 25 % of the time, a transmission better than 55-65 % (10-20 %) at 350 μm (200 μm) can be found in Antarctica. For the first quartile, Cerro Chajnantor catches up the Antarctic sites thanks to its high altitude. However for the second and third quartiles Antarctic sites have a better transmissions based on the long term statistics, especially at 350 μm. For the three sites, Chajnantor Plateau, Cerro Macon and Mauna Kea, the transmission window at 350 μm opens significantly while it is only rarely possible to observe at 200 μm.

The extreme stability of the Antarctic sites is clearly visible in Fig. B.7. There is a stable plateau for the transmission between the first and third quartiles that allows long time series and surveys to be conducted on these sites. This is the direct consequence of the stability of the PWV that was previously identified at Dome C in Fig. B.2. With its higher altitude, Dome A presents the best conditions on Earth for submillimetre astronomy in terms of transmission and day-to-day stability.

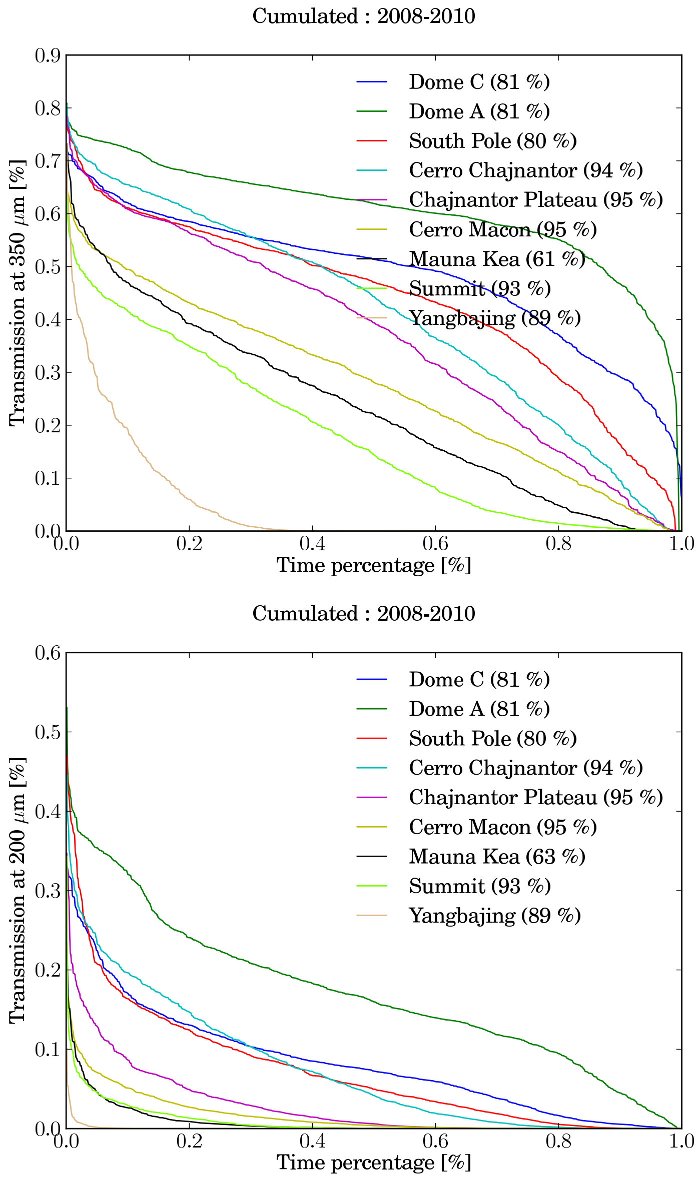

Figure B.7: Comparison of the functions of repartition of the 350-μm (top) and 200-μm (bottom) transmissions for all the sites between 2008 and 2010. The x-axis time percentage is done over the period on which the data extraction for the sites was possible, the actual percentage of data we got is indicated for each site in parenthesis.

B.4.3 Transmission stability at 200 μm

The stability of the transmission is an important parameter for large surveys and time-series studies. The PWV of Chilean Sites is highly variable from one day to another whereas Antarctic sites are much more stable (see Figs. B.2 and B.3). The stability of the transmission leads to a high transmission even at long time fraction in the repartition functions of Fig. B.7. In order to quantify and compare the stability, we used the indicator introduced by *De Gregori et al.* (2012), the site photometric quality ratio (SPQR). It consists in the ratio of the monthly averaged transmission to its monthly standard deviation, on a daily time-scale

$$\mathrm{SPQR} = \langle T \rangle / \sigma_T \tag{B.1}$$

The variations of this ratio for the transmission at 200 μm between 2008 and 2010 are plotted in Fig. B.8. A first look at the figure shows that all temperate sites have a SPQR ratio lower than 1 while Antarctic sites have a ratio greater than 1. Therefore, the fluctuations of the transmission are greater than the averaged transmission, on temperate sites. This quantifies the high variability of the transmission at these sites. Note that the Arctic site on the Summit mountain is also highly variable, hence Antarctica is really unique even among polar environments. On the Antarctic plateau, Dome A has the best SPQR ratio with a monthly-averaged transmission that is typically 3-4 times higher than the fluctuations. Dome C achieves also very good conditions with a ratio of the order of 2-3 while the South Pole has a monthly-averaged transmission of the same order of the fluctuations comparable to the conditions reached at Cerro Chajnantor.

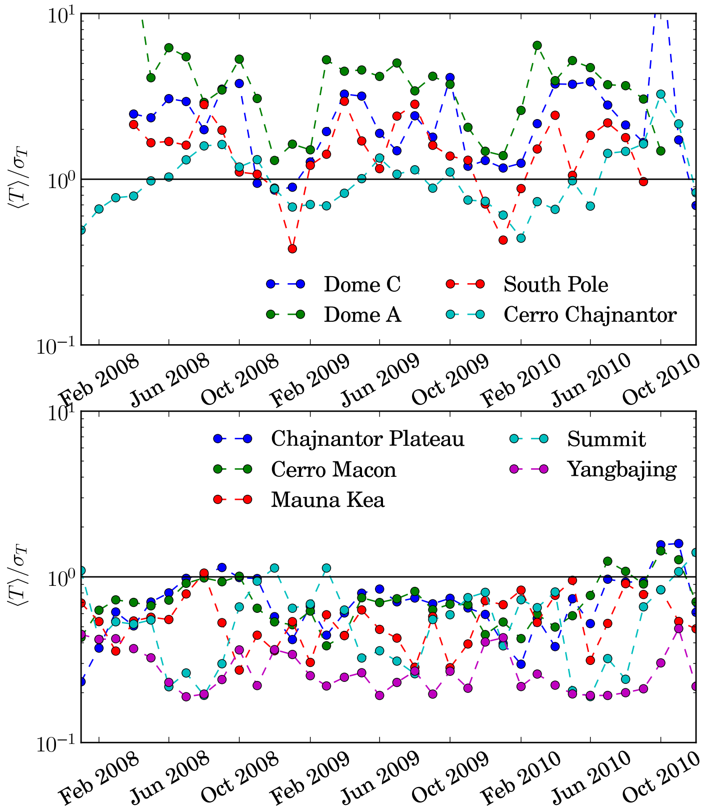

Figure B.8: SPQR ratio for the 200-μm transmission for all the sites between 2008 and 2010. The mean values between 2008 and 2010 are Dome A 3.6, Dome C 2.7, South Pole 1.3, Cerro Chajnantor 1.1, Chajnantor Plateau 0.7, Cerro Macon 0.7, Mauna Kea 0.6, Summit (Greenland) 0.6, Yangbajing (Tibet) 0.3.

B.5 Atmospheric transmission for SOFIA

The first successfull science flights with SOFIA were carried out in 2011 and summarized in special issues of A&A (2012, Vol. 542, spectroscopic observations with GREAT) and ApJ (2012, Vol. 749, continuum imaging). In particular the spectroscopic observations at high frequencies (e.g. the [CII] line at 1.9 THz) showed that although the transmission is very high at these frequencies (typical PWVs are in the range of a few μm up to 50 μm for altitudes between 11 and 14 km), the calibration of the data using atmospheric models is not straightforward and requires a more detailed understanding of the atmospheric processes at the troposphere/stratosphere border. As pointed out in *Guan et al.* (2012), atmospheric models are particularly important because atmospheric absorption lines are more narrow at these altitudes and their small-scale variation is very difficult to measure. In *Guan et al.* (2012), three atmospheric models are compared: AM (*Paine*, 2011), ATRAN (Lord 1992, priv. comm.) and MOLIERE (*Urban et al.*, 2004). Special emphasize is given seperately to the wet- and dry-component. While all models agree well for the wet component, ATRAN does not include the collision-induced absorption by N_2 and O_2, and AM calculates a two times lower opacity than MOLIERE. Results of versatile models like MOLIERE depend much on choices made by the user. At this stage, it is not clear which models fits best for the data calibration and studies to compare the AM and MOLIERE codes are under way.

In this paper, we present selected model results of MOLIERE calculated for 4 different altitudes (11 to 14 km in steps of 1 km), three PWVs (3, 10 and 20 μm), and a frequency range of 1800 to 2000 GHz. We chose this frequency range because it includes the astronomically very important atomic finestructure emission line of ionized carbon at 1900 GHz. Figure B.9 shows the transmission curves for the 4 altitudes at a PWV of 10 μm. Generally, the transmission is high (>80 %) except of the deep and broad water absorption features and line absorption of minor species. Only in these ranges, the atmosphere is opaque even at those high altitudes. Figure B.10 shows a zoom into the frequency range around the [CII] 1.9 THz line for different PWVs. The transmission remains high (∼75 %) even for a PWV of 20 μm.

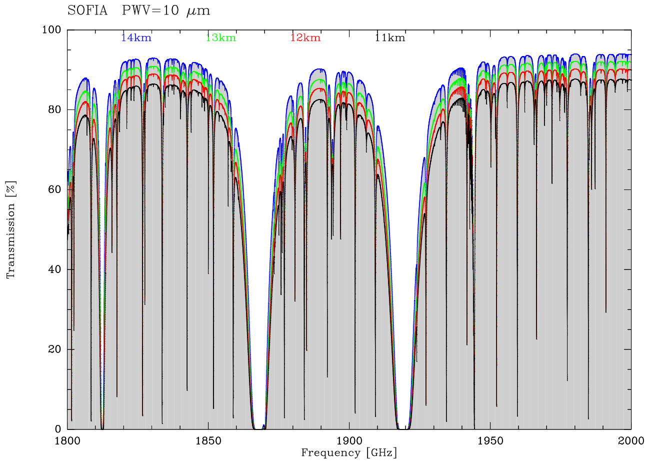

Figure B.9: Atmospheric transmission curve for 4 flight altitudes of SOFIA calculated with MOLIERE at a PWV of 10 μm.

B.6 Summary and conclusions

We presented PWV statistics and the corresponding transmission curves for potential and existing submillimetre observational sites all around the world. Thanks to satellite measurements (IASI) it is possible for the first time to conduct a comparison which is not biased by the different calibration techniques of ground-based instruments that have very different behaviors caused by their working conditions. This is particularly true for comparison between polar and non-polar sites because of the harsh environmental conditions at the poles.

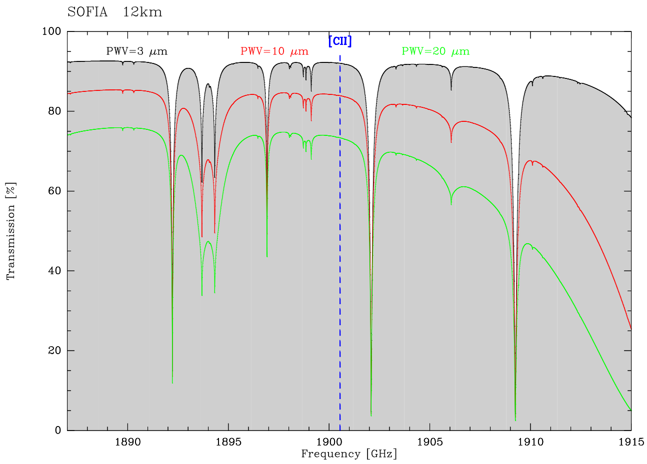

Figure B.10: Zoom into the transmission curve for the frequency range containing the [CII] 1.9 THz for 3 different PWV at an altitude of 12 km calculated with MOLIERE. The [CII] line is indicated by a dashed blue line.

Comparisons were done for the PWV statistics and for the transmissions using the atmospheric model MOLIERE. For astronomical purposes, a comparison using the transmissions is mandatory since the altitude of the site has also a strong influence on the resulting transmission. For a percentage of 25 % of the year, Cerro Chajnantor presents very good transmissions that are comparable to Antarctic sites. However on the long term, only Antarctic sites provide a stable transmission that will allow unique science cases to be studied there. Observations at 350 μm and 450 μm are possible all year long while the 200 μm window opens significantly for at least 25 % of the year. Furthermore, Antarctic sites are free of day-night variations thanks to the long polar night. All the other sites studied here have a highly-variable transmission. The typical monthly-averaged transmission at 200 μm is lower than its fluctuations on all the sites except for Dome A and Dome C. Therefore, these two sites will be unique for surveys and time-series studies in the submm range.

The method used to compare the different sites is robust and based on only one instrument, IASI, and the atmospheric model MOLIERE. We derived in this paper the PWV and atmospheric transmission on well-known sites for submillimetre astronomy and showed that it is possible to retrieve statistics that are in a good agreement with in-situ measurements. A calculator to show these PWV statistics and to compute the corresponding transmission at any given wavelength is available to the community[9] for all the sites presented here and for the three year 2008, 2009 and 2010. The year 2011 will be added to the calculator. Other potential sites could be investigated upon request [10].

In conclusion, this method could identify sites on Earth with a great potential for submillimetre astronomy, and guide future site testing campaigns *in situ*.

B.7 PWV statistics and transmission curves

---

[9] `http://irfu.cea.fr/submm` and `http://submm.eu`

[10] Contact: pascal.tremblin@cea.fr

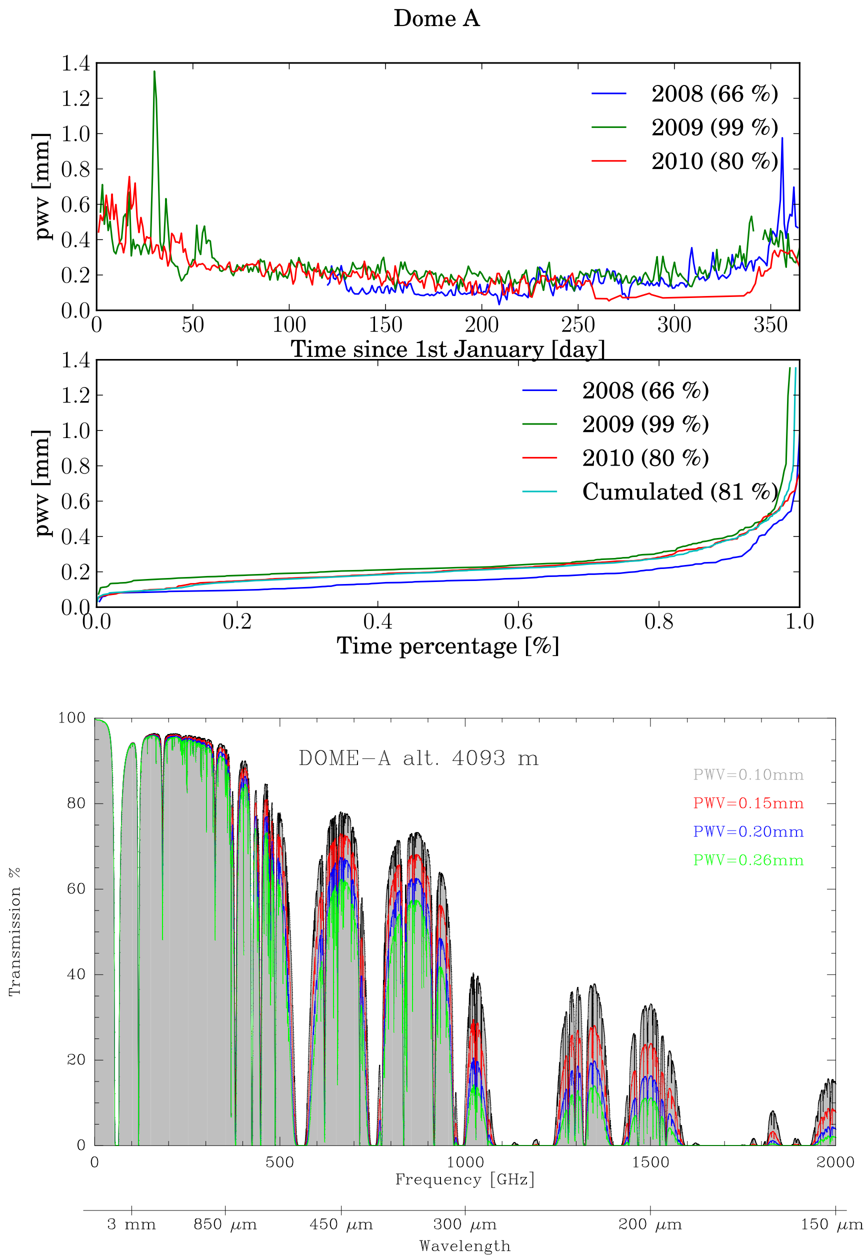

Figure B.11: PWV statistics (top) and transmission curves (bottom) for Dome A. The transmission curve for the first decile of PWV is in grey and the quartiles of PWV are given by red: 25 %, blue: 50 %, green: 75 %.

Bibliography

Borysow, A., and L. Frommhold (1986), Theoretical collision-induced rototranslational absorption spectra for modeling Titan's atmosphere - H2-N2 pairs, ApJ, 303, 495–510. 157

Chamberlin, R. (2002), Comparisons of saturated water vapor column from radiosonde, and mm and submm radiometric opacities at the South Pole, in Astronomical Site Evaluation in the Visible and Radio Range. ASP Conference Proceedings, p. 172. 155

Chamberlin, R. A., A. P. Lane, and A. A. Stark (1997), The 492 GHz Atmospheric Opacity at the Geographic South Pole, ApJ, 476, 428. 150

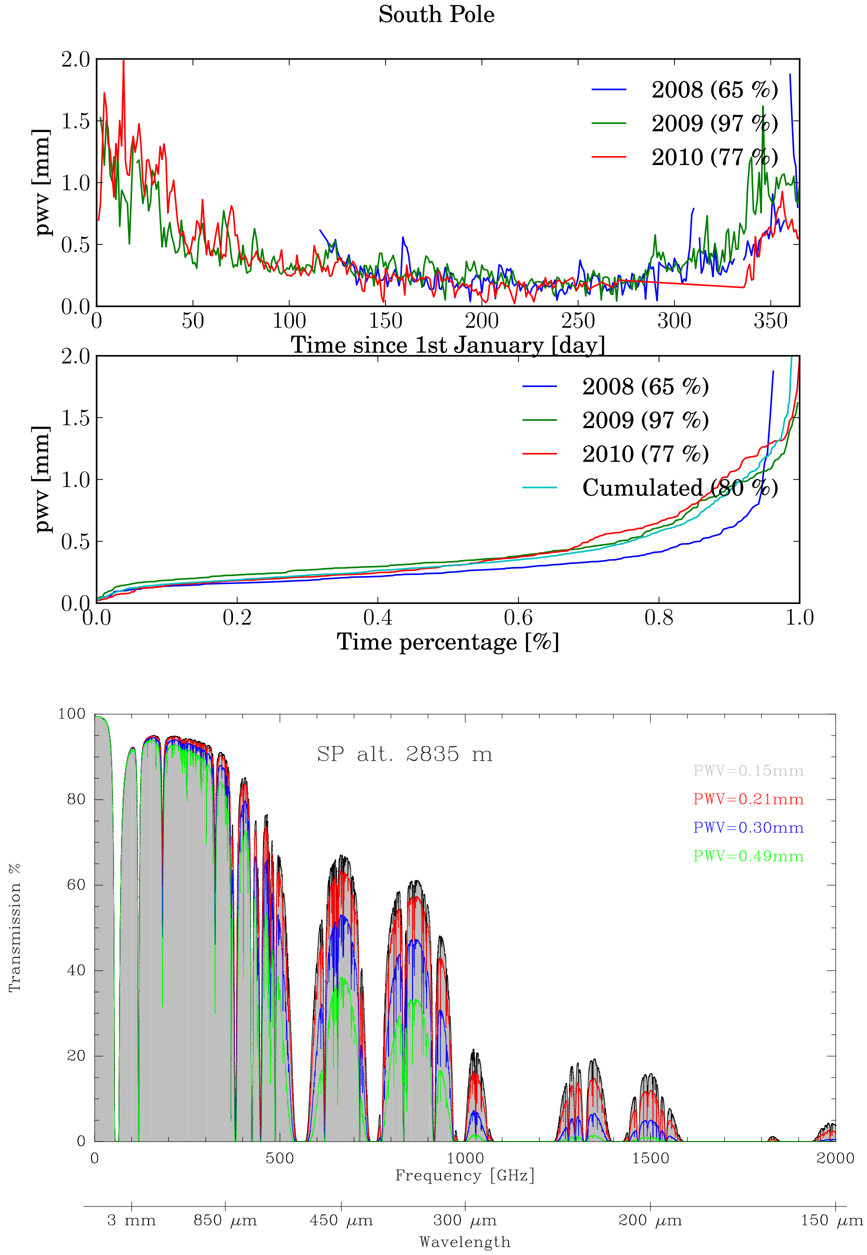

Figure B.12: PWV statistics (top) and transmission curves (bottom) for the South Pole. The transmission curve for the first decile of PWV is in grey and the quartiles of PWV are given by red: 25 %, blue: 50 %, green: 75 %.

Clerbaux, C., et al. (2009), Monitoring of atmospheric composition using the thermal infrared IASI/MetOp sounder, Atmospheric Chemistry and Physics, 9(1), 6041–6054. 152

De Gregori, S., M. de Petris, B. Decina, L. Lamagna, J. R. Pardo, B. Petkov, C. Tomasi, and L. Valenziano (2012), Millimetre and submillimetre atmospheric performance at Dome C combining radiosoundings and ATM synthetic spectra, MNRAS, 425(1), 222–230. 159

Giovanelli, R., et al. (2001), The Optical/Infrared Astronomical Quality of High Atacama Sites. I. Preliminary Results of Optical Seeing, The Publications of the Astronomical Society of the Pacific, 113(7), 789–802. 154

Guan, X., J. Stutzki, U. U. Graf, R. Güsten, Y. Okada, M. A. R. Torres, R. Simon, and

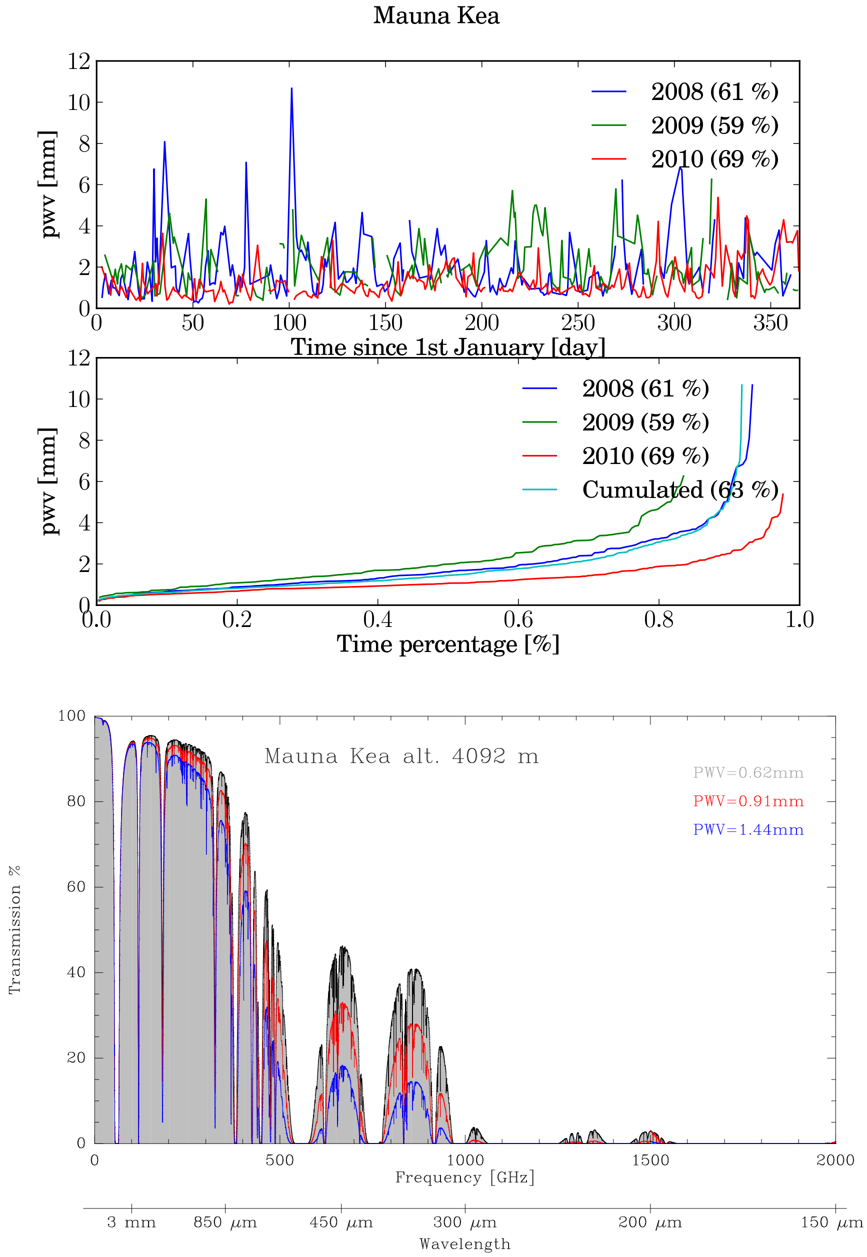

Figure B.13: PWV statistics (top) and transmission curves (bottom) for Mauna Kea. The transmission curve for the first decile of PWV is in grey and the quartiles of PWV are given by red: 25 %, blue: 50 %.

H. Wiesemeyer (2012), GREAT/SOFIA atmospheric calibration, arXiv, astro-ph.IM, L4. 150, 153, 161

Herbin, H., D. Hurtmans, C. Clerbaux, L. Clarisse, and P. F. Coheur (2009), H216O and HDO measurements with IASI/MetOp, Atmospheric Chemistry and Physics, 9(2), 9433–9447. 152

Matsushita, S., H. Matsuo, J. R. Pardo, and S. J. E. Radford (1999), FTS Measurements of Submillimeter-Wave Atmospheric Opacity at Pampa la Bola II : Supra-Terahertz Windows and Model Fitting, Publications of the Astronomical Society of Japan, 51, 603. 150

Minier, V., et al. (2010), The Antarctic Submillimetre Telescope, in EAS Publications

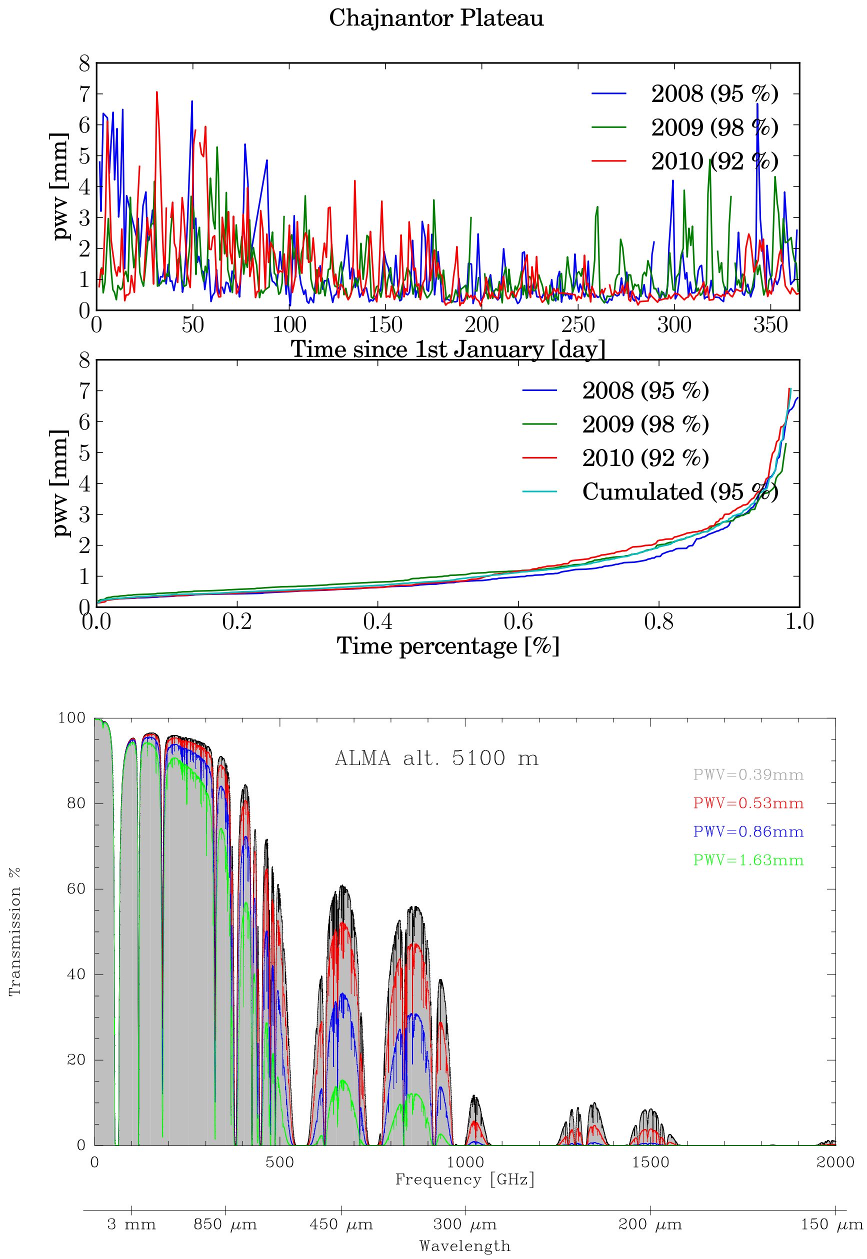

Figure B.14: PWV statistics (top) and transmission curves (bottom) for Chajnantor Plateau. The transmission curve for the first decile of PWV is in grey and the quartiles of PWV are given by red: 25 %, blue: 50 %.

Series, pp. 269–273, CEA Saclay, Laboratoire AIM, Service d'Astrophysique/Irfu, France vincent.minier@cea.fr. 149

Otárola, A., T. Travouillon, M. Schöck, S. Els, R. Riddle, W. Skidmore, R. Dahl, D. Naylor, and R. Querel (2010), Thirty Meter Telescope Site Testing X: Precipitable Water Vapor, PASP, 122, 470–484. 155

Paine, S. (2011), SMA Technical Memo, 152(7.2). 161

Pardo, J. R., J. Cernicharo, and E. Serabyn (2001), Atmospheric transmission at microwaves (ATM): an improved model for millimeter/submillimeter applications, IEEE Transactions on Antennas and Propagation, 49, 1683–1694. 150, 157

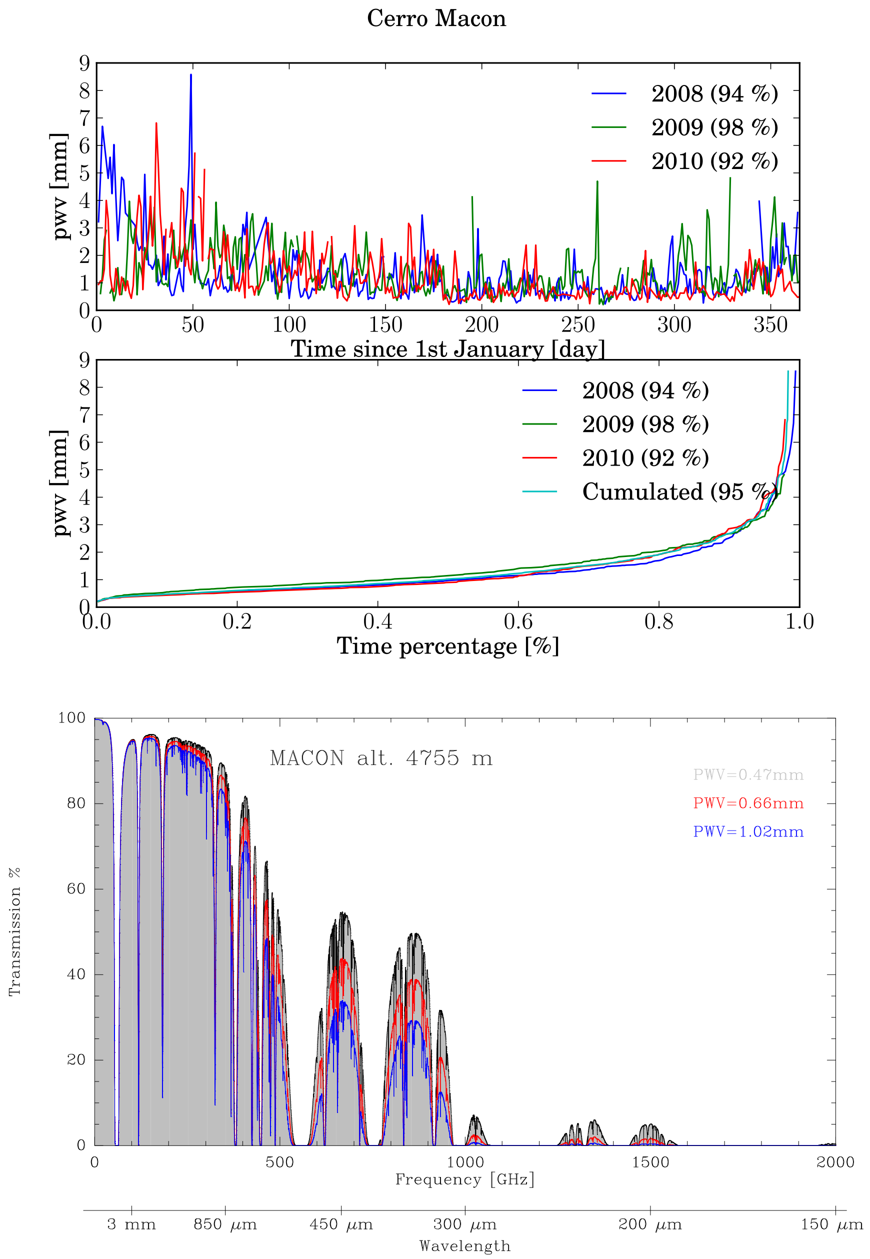

Figure B.15: PWV statistics (top) and transmission curves (bottom) for Cerro Macon. The transmission curve for the first decile of PWV is in grey and the quartiles of PWV are given by red: 25 %, blue: 50 %.

Peterson, J. B., S. J. E. Radford, P. Ade, R. A. Chamberlin, M. J. O'Kelly, K. M. Peterson, and E. Schartman (2003), Stability of the Submillimeter Brightness of the Atmosphere above Mauna Kea, Chajnantor, and the South Pole, PASP, 115(8), 383–388. 150

Phulpin, T., D. Blumstein, F. Prel, B. Tournier, P. Prunet, and P. Schlüssel (2007), Applications of IASI on MetOp-A: first results and illustration of potential use for meteorology, climate monitoring, and atmospheric chemistry, Atmospheric and Environmental Remote Sensing Data Processing and Utilization III: Readiness for GEOSS. Edited by Goldberg, 6684, 12. 152

Pougatchev, N., T. August, X. Calbet, T. Hultberg, O. Oduleye, P. Schlüssel, B. Stiller,

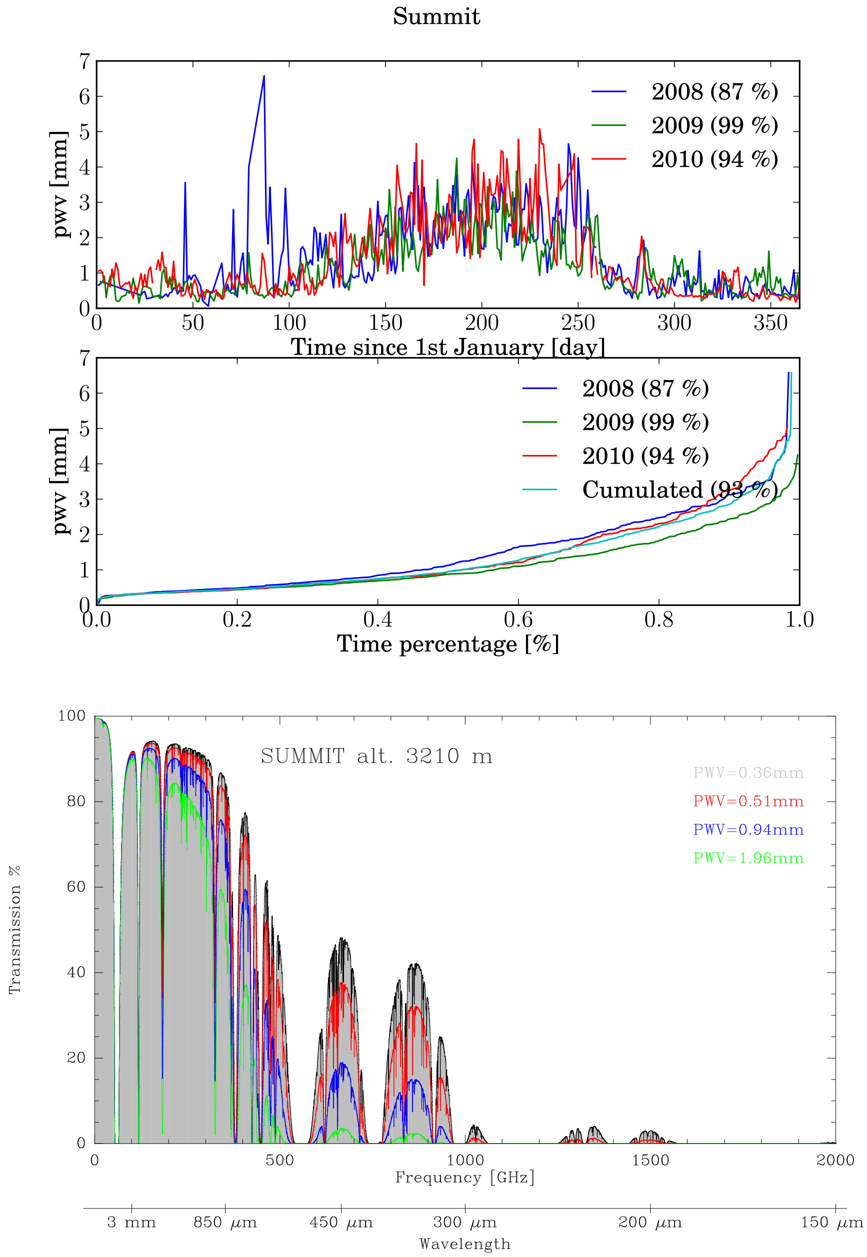

Figure B.16: PWV statistics (top) and transmission curves (bottom) for Summit (Greenland). The transmission curve for the first decile of PWV is in grey and the quartiles of PWV are given by red: 25 %, blue: 50 %, green: 75 %.

K. St Germain, and G. Bingham (2008), Validation of the IASI temperature and water vapor profile retrievals by correlative radiosondes, Earth Observing Systems XIII. Edited by Butler, 7081, 18. 152

Radford, S. J. E. (2011), Observing Conditions for Submillimeter Astronomy, Astronomical Site Testing Data in Chile (Eds. M. Curé, 41, 87–90. 154, 155

Ricaud, P., B. Gabard, S. Derrien, J.-L. Attie, T. Rose, and H. Czekala (2010), Validation of Tropospheric Water Vapor as Measured by the 183-GHz HAMSTRAD Radiometer Over the Pyrenees Mountains, France, ITGRS, 48, 2189–2203. 150, 152

Schneider, N., J. Urban, and P. Baron (2009), Potential of radiotelescopes for atmospheric

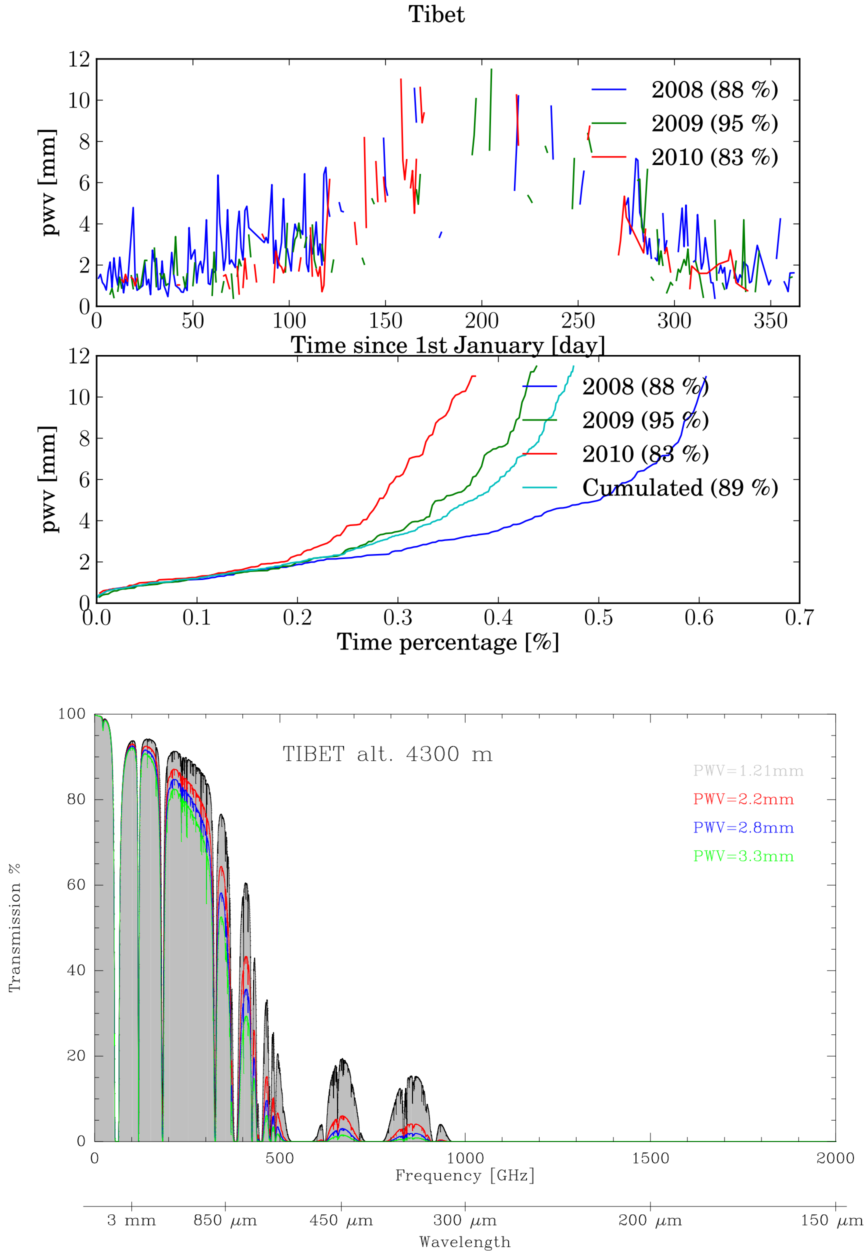

Figure B.17: PWV statistics (top) and transmission curves (bottom) for Yangbajing (Tibet). The transmission curve for the first decile of PWV is in grey and the quartiles of PWV are given by red: 25 %, blue: 50 %, green: 75 %.

line observations I. Observation principles and transmission curves for selected sites, PSS, 57(12), 1419–1433. 150, 157, 158

Tremblin, P., et al. (2011), Site testing for submillimetre astronomy at Dome C, Antarctica, A&A, 535, 112. 150, 152, 155, 158

Urban, J., P. Baron, N. Lautié, N. Schneider, K. Dassas, P. Ricaud, and J. De La Noë (2004), Moliere (v5): a versatile forward- and inversion model for the millimeter and sub-millimeter wavelength range, Journal of Quantitative Spectroscopy and Radiative Transfer, 83, 529–554. 150, 156, 161

Yang, H., et al. (2010), Exceptional Terahertz Transparency and Stability above Dome A, Antarctica, PASP, 122, 490–494. 150

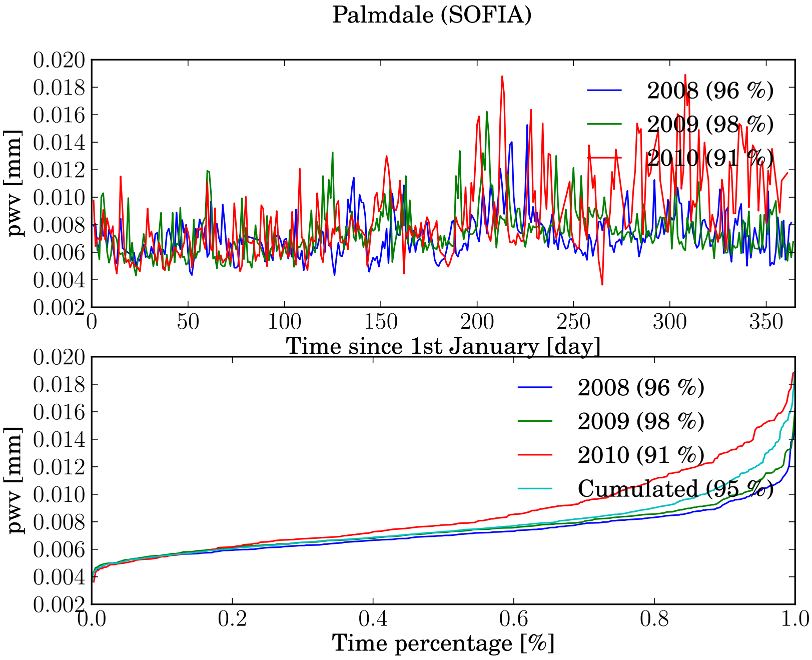

Figure B.18: PWV statistics for Palmdale USA, at a stratospheric altitude of 12km.

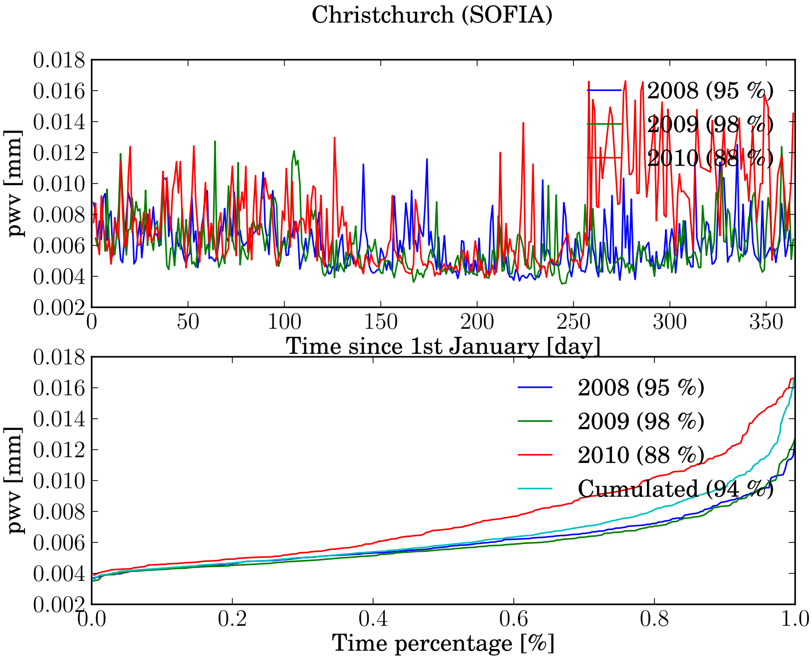

Figure B.19: PWV statistics for Christchurch New Zealand, at a stratospheric altitude of 12 km.

Appendix C

Colliding Planetary and Stellar Winds

> *If the only tool you have is a hammer, you tend to see every problem as a nail.*
> *Abraham Maslow*

When transiting their host stars, hot Jupiters absorb about 10% of the light in the wings of the stellar Lyman-alpha emission line. Surprisingly, the absorption occurs at wavelengths Doppler-shifted from line center by ±100 *km/s—much larger than the speeds with which partially neutral, 7000 K hydrogen escapes from hot Jupiter atmospheres. It has been proposed that the absorption arises from* 10^6 *K hydrogen from the host stellar wind, made momentarily neutral by charge exchange with planetary H I. To test this proposal, we perform 2D hydrodynamic simulations of colliding hot Jupiter and stellar winds, augmented by a chemistry module to compute the amount of hot neutral hydrogen produced by charge exchange. We observe the contact discontinuity where the two winds meet to be Kelvin-Helmholtz unstable. The Kelvin-Helmholtz instability mixes the two winds; in the mixing layer, charge exchange reactions establish, within tens of seconds, a chemical equilibrium in which the neutral fraction of hot stellar hydrogen equals the neutral fraction of cold planetary hydrogen (about 20%). In our simulations, enough hot neutral hydrogen is generated to reproduce the transit observations, and the amount of absorption converges with both spatial resolution and time. We provide physical scaling relations that describe how the absorption varies with stellar and planetary wind properties; in particular the absorption scales positively but weakly with both the stellar and planetary wind densities. Our calculations support the idea that charge transfer between colliding winds correctly explains the Lyman-alpha transit observations—modulo the effects of magnetic fields, as yet unmodeled. How hot stellar hydrogen cools when it collides with cold planetary hydrogen is briefly considered; a more careful treatment of how the mixing layer thermally equilibrates might explain the recent detection of Balmer Hα absorption in transiting hot Jupiters.*

C.1 Introduction

Gas-laden planets lose mass to space when their upper atmospheres are heated by stellar ultraviolet (UV) radiation. Ubiquitous in the Solar System, thermally-driven outflows modify the compositions of their underlying atmospheres over geologic time (e.g., Weissman et al. 1999). Thanks to the Hubble Space Telescope (HST), escaping winds are now observed from extrasolar hot Jupiters: Jovian-sized planets orbiting at distances $\lesssim 0.05$ AU *from their host stars and bathed in intense ionizing fields. Spectroscopy with HST reveals absorption depths of ∼2–10% in various resonance transitions (H I, O I, C II, Si III and Mg II) when* *the planet transits the star, implying gas outflows that extend for at least several planetary radii (e.g., Vidal-Madjar et al. 2003, VM03; Vidal-Madjar et al. 2004; Ben-Jaffel 2007; Ben-Jaffel 2008; Vidal-Madjar et al. 2008; Lecavelier Des Etangs et al. 2010; Fossati et al. 2010; Linsky et al. 2010). These data promise to constrain the compositions of hot Jupiter atmospheres and the degrees to which they are vertically mixed (Liang et al. 2003; Moses et al. 2011).*

The HST observations of hot Jupiter winds are accompanied by theoretical studies that model planetary outflows starting from first principles (e.g., Yelle 2004; Tian et al. 2005; García Muñoz 2007; Murray-Clay, Chiang, & Murray 2009, M09). These 1D hydrodynamic models generally agree that hot Jupiters like HD 209458b and HD 189733b are emitting $\dot{M} \sim 10^{10}$–10^{11} *g/s in mostly hydrogen gas.*

Do the models agree with the observations? Linsky et al. (2010) find that their observations of C II absorption in HD 209458b can be made consistent with modeled mass loss rates, assuming the carbon abundance of the wind is not too different from solar. More comparisons between observation and theory would be welcome—particularly for hydrogen, the dominant component of the wind. But the observations of H I absorption have proven surprisingly difficult to interpret. On the one hand, the original measurements by VM03 indicate substantial (∼10%) absorption at Doppler shifts of ± 100 *km/s from the center of the H I Lyman-*α *line. On the other hand, theory (e.g., M09) indicates that planetary outflows, heated by photoionization to temperatures* $T \lesssim 10^4$ *K, blow only at ∼10 km/s. How can such slow planetary winds produce significant absorption at* ± 100 *km/s?*

Holmström et al. (2008, H08) propose that the observed energetic neutral H atoms arise from charge exchange between planetary H I and protons from the incident stellar wind. In this interpretation, the ±100 km/s velocities correspond to the thermal velocities of 10^6 *K hydrogen from the star—hydrogen which is made neutral by electron-exchange with planetary H I. The situation is analogous to that of the colliding winds of O star binaries (Stevens et al. 1992; Lamberts et al. 2011, and references therein). The H I Lyman-*α *absorption arises from the contact discontinuity where the two winds meet, mix, and charge exchange to produce hot neutral hydrogen.*

The calculations of H08, and those of the follow-up study by Ekenbäck et al. (2010, E10), are based on a Monte Carlo algorithm that tracks individual "meta-particles" of neutral hydrogen launched from the planet. The meta-particles collide and charge exchange with stellar wind protons outside a presumed planetary magnetosphere, which is modeled as an "obstacle" in the shape of a bow shock. Good agreement with the Ly-α *observations is obtained for a range of stellar and planetary wind parameters, and for a range of assumed obstacle sizes.*

In this work we further test the hypothesis of charge exchange first explored by H08 and E10. Our methods are complementary: instead of adopting their kinetic approach, we solve the hydrodynamic equations. We do not prescribe any obstacle to deflect the stellar wind, but instead allow the planetary and stellar winds to meet and shape each other self-consistently via their ram and thermal pressures. Some aspects of our solution are not realistic—we ignore the Coriolis force, the centrifugal force, stellar tidal gravity, and magnetic fields.[1] *Our goal is to develop a first-cut hydrodynamic-chemical model of the contact discontinuity between the two winds where material mixes and charge exchanges. Simple and physically motivated scaling relations will be developed between the amount of H I absorption and the properties of the stellar and planetary winds.*

The plan of this paper is as follows. In §C.2 we describe our numerical methods, which involve augmenting our grid-based hydrodynamics code to solve the chemical reactions of charge exchange, and specifying special boundary conditions to launch the two winds. In

---

[1] No simulation of a hot Jupiter wind of which we are aware treats magnetic forces explicitly; the obstacle introduced by H08 and E10 is a stand-in for the planet's magnetosphere.

§C.3 we present our results, including a direct comparison with the H I Ly–α transit spectra of VM03, and a parameter study to elucidate how the absorption depth varies with stellar and planetary wind properties. A summary is given in §C.4, together with pointers toward future work.

C.2 Numerical methods

In §C.2.1 we describe the hydrodynamics code used to simulate the colliding planetary and stellar winds. In §C.2.2 we detail the charge exchange reactions that were added to the code. In §C.2.3, we outline our post-processing procedure for computing the Lyman-α transmission spectrum. As a convenience to readers, in §C.2.4 we re-cap the differences between our treatment of colliding winds and that of E10/H08.

C.2.1 Hydrodynamics: Code and Initial Conditions

Our simulations are performed with **`HERACLES`** *(González et al., 2007),*[2] *a grid-based code using a second-order Godunov scheme to solve the Euler equations:*

$$\begin{aligned} \frac{\partial \rho}{\partial t} + \nabla \cdot (\rho \boldsymbol{V}) &= 0 \\ \frac{\partial \rho \boldsymbol{V}}{\partial t} + \nabla \cdot [\rho \boldsymbol{V} \otimes \boldsymbol{V} + pI] &= 0 \\ \frac{\partial E}{\partial t} + \nabla \cdot [(E+p)\boldsymbol{V}] &= 0 \\ \frac{\partial \rho x_i}{\partial t} + \nabla \cdot (\rho x_i \boldsymbol{V}) &= 0 \quad . \end{aligned} \tag{C.1}$$

Here ρ, $\boldsymbol{V}$, p, and E are the mass density, velocity, pressure, and total energy density, respectively (e.g., Clarke and Carswell 2003). The code tracks abundances of individual species: x_i is the mass fraction of the $i^{\rm th}$ species of hydrogen, where $i \in \{1,2,3,4\}$ to cover four possible combinations of ionization state (either neutral or ionized) and temperature (either "hot" because it is arises from the star or "cold" because it arises from the planet). The outer product is denoted $\otimes$, and I is the identity matrix.

All our simulations are 2D Cartesian in the dimensions x (stellocentric radius) and y (height above the planet's orbital plane). Equivalently the simulations may be regarded as 3D, but with no rotation and with a star and a planet that are infinite cylinders oriented parallel to the z-axis. At fixed computational cost, two-dimensional simulations enjoy better spatial resolution than three-dimensional simulations and thus better resolve the fluid instabilities at the interface of the two winds. The standard box size is $(L_x, L_y) = (40R_p, 60R_p)$, where $R_p = 10^{10}$ cm is the planet radius. The number of grid points ranges up to $(N_x, N_y) = (6400, 9600)$; see Table 1.

The star and its wind are modeled after the Sun and the Solar wind. The stellar wind is injected through the left edge of the simulation box; the densities, velocities, and temperatures in the vertical column of cells at the box's left edge are fixed in time. Stellar wind properties as listed in Table C.1 are given for a stellocentric distance $r = r_{\rm launch,*} = 5R_\odot$, near the box's left edge. Here the stellar wind density, temperature, sound speed, and flow speed are set to $n_* = 2.9 \times 10^4$ cm^{-3}, $T_* = 10^6$ K, $c_* = 129$ km/s (computed for a mean molecular weight equal to half the proton mass, appropriate for an $f_*^+ = 100\%$ ionized hydrogen plasma), and $v_* = 130$ km/s (Sheeley et al. 1997; Quémerais et al. 2007; see also Lemaire 2011), respectively. Our stellar wind parameters are such that the implied spherically symmetric (3D) mass loss rate is 1×10^{12} g/s or $2 \times 10^{-14} M_\odot$/yr.

---

[2] http://irfu.cea.fr/Projets/Site_heracles/index.html

Our stellar wind parameters are similar to those of the "slow" Solar wind in the Sun's equatorial plane. Compare our choices with those of Ekenbäck et al. (2011), who adopt a stellar wind speed of 450 km/s. Their speed is closer to that of the "fast" Solar wind which emerges from coronal holes. At Solar minimum, the fast wind tends to be confined to large heliographic latitudes (polar regions), but at Solar maximum, the coronal holes migrate to lower latitudes and the fast wind can more readily penetrate to the ecliptic (Kohl et al. 1998; McComas et al. 2003; S. Bale 2012, personal communication). Evaporating hot Jupiters like HD 209458b and HD 189733b have orbit normals that are nearly aligned with the spin axes of their host stars (Winn et al. 2005; Winn et al. 2006). Because such planets reside near their stellar equatorial planes, the slow equatorial Solar wind seems a better guide than the fast, more polar wind; nevertheless, as noted above, the fast wind is known to extend to low latitudes, and the speeds and densities of both winds vary by factors of order-unity or more with time.

The stellar wind velocity at the left boundary is not plane-parallel but points radially away from the central star (located outside the box). The density, velocity, and temperature in each cell at the boundary are computed by assuming that the central star emits a spherical isothermal wind whose velocity grows linearly with stellocentric distance r *and whose density decreases as* $1/r^3$*. These scalings, which are modeled after empirical Solar wind measurements (e.g., Sheeley et al. 1997) and which maintain constant mass loss rate with* r*, are used only to define the left-edge boundary conditions and are not used in the simulation domain. Outflow boundary conditions are applied at the top, bottom, and right edges of the box.*

As a final comment about our choice of stellar wind parameters, we note that they are valid for the left-edge boundary at $r = r_{\rm launch,*} = 5R_\odot$*—not for the planet's orbital radius of* $r = 10R_\odot$*. The left-edge boundary must be far enough away from the planet that the stellar wind properties at the boundary are well-approximated by their "free-stream" values in the absence of any planetary obstacle. We will see in §C.3 that the stellar wind slows considerably between* $r = 5R_\odot$ *and* $r = 10R_\odot$ *as a consequence of the oncoming planetary wind. This region of deceleration is absent from the models of H08 and E10.*

A circle of radius $d_{\rm launch,p} = 4R_{\rm p}$*, centered at position* $(l_x, l_y) = (30R_{\rm p}, 30R_{\rm p})$ *(where the origin is located at the bottom left corner of the domain), defines the boundary where the assumed isotropic and radial planetary wind is launched. The properties of our simulated planetary wind, which are similar to those of the standard supersonic models of HD209458b by García-Muñoz (2007) and Murray-Clay et al. (2009), are listed in Table C.1, and are constant in time along the circular boundary. The density and velocity of the planetary wind at this boundary are such that if the wind were spherically symmetric, the mass loss rate would be* 1.6×10^{11} *g/s. This value lies within the range estimated from observations by Linsky et al. (2010). Note that* $1 - f_p^+ = 20\%$ *of the planetary wind at launch is neutral (Murray-Clay et al., 2009) and available for charge exchange. The planetary and stellar winds are barely supersonic at launch (Mach numbers* $M_p = 1.2$ *and* $M_* = 1.01$*).*

Gravity is neglected, as are all rotational forces. The pressure p *is related to the internal energy density* $e = E - \rho V^2/2$ *via* $p = (\gamma - 1)e$*, where* $\gamma = 1.01$*. That is, gas is assumed to behave nearly isothermally. This isothermal assumption should not be taken to mean that the temperature is the same across the simulation domain; the temperature of the stellar wind at injection is* $T_* = 10^6$ *K, while that of the planetary wind is* $T_p = 7000$ *K. Rather, the two winds, as long as they remain unmixed, tend to maintain their respective temperatures as they rarefy and compress. In reality, the stellar wind can keep, in and of itself, a near-isothermal profile on length scales of interest to us because thermal conduction times (estimated, e.g., using the Spitzer conductivity) are short compared to dynamical times. Treating the planetary wind as an isothermal flow is less well justified, as cooling by adiabatic expansion can be a significant portion of the energy budget (García-Muñoz 2007;*

Table C.1: Parameters of the winds at launch, and of the simulation box

Stellar Wind	Planetary Wind
$r_{\mathrm{launch},*} = 5R_\odot$	$d_{\mathrm{launch},p} = 4R_p$
$n_* = 2.9\mathrm{E}4/\mathrm{cm}^3$	$n_p = 3.9\mathrm{E}6/\mathrm{cm}^3$
$T_* = 1\mathrm{E}6$ K	$T_p = 7000$ K
$v_* = 130$ km/s	$v_p = 12$ km/s
$f_*^+ = 1$	$f_p^+ = 0.8$
$c_* = 129$ km/s	$c_p = 10$ km/s
$M_* = 1.01$	$M_p = 1.2$
radial (x) direction	vertical (y) direction
$\mathrm{L}_x/\mathrm{R}_p = 40$	$\mathrm{L}_y/\mathrm{R}_p = 60$
$\mathrm{N}_x = 50, 100, 200,400, 800, 1600, 3200, 6400$	$\mathrm{N}_y = 75, 150, 300, 600, 1200, 2400, 4800, 9600$

M09). Nevertheless the error incurred by assuming the planetary wind is isothermal is small for our standard model because the planetary wind hardly travels beyond its launch radius of $4R_p$ before it encounters a shock; thus rarefaction factors are small. Furthermore, as noted above, shock compression factors are modest because the speed of the planetary wind is only marginally supersonic. Where the stellar and planetary winds meet and mix, the code ascribes an intermediate temperature $10^4\,\mathrm{K} < T < 10^6\,\mathrm{K}$. This temperature, as computed by ***HERACLES****, is used only for the hydrodynamic evolution; it is not used for computing either the charge exchange reactions (§C.2.2) or the transmission spectrum (§C.2.3).*

Each simulation is performed in two steps. First only the planetary wind is launched from its boundary and allowed to fill the entire domain for 2×10^5 seconds. Second the stellar wind is injected through the left side of the box, by suitable assignment of ghost cells. This two-step procedure was found to minimize transients. The simulations typically run for 2×10^6 s, which corresponds to ~60 box-crossing times for the stellar wind in the horizontal direction.

C.2.2 Charge Exchange

Charge exchange consists of the following forward and reverse reactions:

$$H_h^+ + H_c^0 \;\rightleftarrows\; H_h^0 + H_c^+ \tag{C.2}$$

Hot (subscript h) ionized (superscript $+$) hydrogen emitted by the star can collide with cold (subscript c) neutral (superscript 0) hydrogen emitted by the planet, neutralizing the former and ionizing the latter while preserving their kinetic energies. The reverse reaction occurs with an identical rate coefficient β (units of cm^3/s; β is the cross section multiplied by the relative velocity).

We have added reaction (C.2) to ***HERACLES*** *by integrating the following equations in* *every grid cell (we refer to this portion of the calculation as the "chemistry step"):*

$$\begin{aligned}\frac{d(n_H x_h^+)}{dt} &= \beta n_H^2 (x_h^0 x_c^+ - x_h^+ x_c^0)\\ \frac{d(n_H x_c^0)}{dt} &= +\frac{d(n_H x_h^+)}{dt}\\ \frac{d(n_H x_c^+)}{dt} &= -\frac{d(n_H x_h^+)}{dt}\\ \frac{d(n_H x_h^0)}{dt} &= -\frac{d(n_H x_h^+)}{dt}\\ x_h^+ + x_h^0 + x_c^+ + x_c^0 &= 1\,. \end{aligned} \tag{C.3}$$

Here n_H is the total hydrogen number density (regardless of ionization state or temperature), and $x_{(c,h)}^{(0,+)}$ is a number fraction (equivalently a mass fraction because the only element treated in the simulation is hydrogen). The rate coefficient $\beta = 4 \times 10^{-8}$ cm^3/s is calculated by combining the energy-dependent cross section of Lindsay and Stebbings (2005) with a Maxwellian distribution for the relative velocity between hydrogen atoms at the two (constant) temperatures T_* and T_p. The finite-difference forms of equations (C.3) are

$$\begin{aligned} x_h^{+(n+1)} - x_h^{+(n)} &= b\left(x_h^{0(n+1)} x_c^{+(n+1)} - x_h^{+(n+1)} x_c^{0(n+1)}\right)\\ x_c^{0(n+1)} - x_c^{0(n)} &= x_h^{+(n+1)} - x_h^{+(n)}\\ x_c^{+(n+1)} - x_c^{+(n)} &= -x_h^{+(n+1)} + x_h^{+(n)}\\ x_h^{0(n+1)} - x_h^{0(n)} &= -x_h^{+(n+1)} + x_h^{+(n)}\\ x_h^{+(n)} + x_h^{0(n)} + x_c^{+(n)} + x_c^{0(n)} &= 1 \end{aligned} \tag{C.4}$$

*where the superscript (n) refers to the n^{th} time step, $b \equiv \beta n_H \Delta t$, and Δt is the integration time step of **HERACLES**. Because the righthand side of the first of these equations is evaluated at step $(n+1)$ instead of step (n), our scheme is implicit. The first equation combines with the others to yield*

$$x_h^{+(n+1)} = \frac{\left[x_h^{+(n)} + b\left(x_h^{+(n)} + x_h^{0(n)}\right)\left(x_h^{+(n)} + x_c^{+(n)}\right)\right]}{1+b} \tag{C.5}$$

from which the remaining number fractions at time step $(n+1)$ are derived. Because our solution is implicit, the dimensionless timestep b can exceed unity (as it does for our runs at low spatial resolution), and the system will still relax to its correct equilibrium. This chemical equilibrium is discussed further in §C.3.2.

Note that in contrast to H08 and E10, our calculations account for the reverse reaction $H_h^0 + H_c^+ \rightarrow H_h^+ + H_c^0$. Accounting for the reverse reaction helps us to avoid overestimating the amount of hot neutral hydrogen. Our calculations of n_h^0 are still overestimated, however, because we neglect thermal equilibration, i.e., cooling of hot hydrogen by collisions with cold hydrogen. In §C.4.1 we estimate the error incurred to be on the order of unity.

C.2.3 Lyman-α Absorption

*The transmission spectrum in the Lyman-α line is post-processed, i.e., calculated after **HERACLES** has finished running. Both hot and cold neutral hydrogen (n_h^0 and n_c^0) contribute to the Lyman-α optical depth. It is assumed that the hot and cold neutral hydrogen do not thermally equilibrate (see §C.4.1 where we question this assumption). Thus in computing the opacity due to hot hydrogen, we adopt a kinetic temperature of $T_* = 10^6$ K, and in* *computing the opacity due to cold hydrogen we take* $T_p = 7000$ *K. In each grid cell, the wavelength at line center is Doppler shifted according to the horizontal component of the bulk velocity (the observer is to the far right of the simulation box). Voigt line profiles are used with a damping constant (Einstein A coefficient) equal to* $\Gamma = 6.365 \times 10^8$ s^{-1} *(e.g., Verhamme et al., 2006).*

For each wavelength λ*, the line-of-sight optical depth* $\tau_\lambda(y)$ *is evaluated along each horizontal row of cells pointing to the star (lying between the white dashed lines in Figures C.1 and C.2). The total absorption is then computed as*

$$A(\lambda) = \langle 1 - \exp(-\tau_\lambda) \rangle \tag{C.6}$$

where $\langle\rangle$ *denotes a 1-dimensional spatial average over* y*. Of course the star actually presents a circular disc, but because the simulation is only 2D, our simple 1D average seems fair. The absorption profile* $A(\lambda)$ *can be computed for every snapshot (timestep) of the simulation.*

C.2.4 Differences Between This Work and E10/H08

The main difference between our methods and those of E10/H08 is that we numerically solve the equations of hydrodynamics in a 2D geometry, whereas E10/H08 simulate collisions of hydrogen "meta-particles" in a more kinetic, 3D treatment. Neither we nor they compute magnetic forces explicitly.

E10 include forces arising from the orbit of the planet about the star, including the Coriolis force, the centrifugal force, and stellar tidal gravity. We do not. Our focus is on resolving mixing and charge exchange in the interface between the two winds. To that end, we solve for both the forward and reverse reactions of charge exchange (equations C.2–C.3), whereas E10/H08 solve only for the forward reaction. Our equations permit a chemical equilibrium to be established in the mixing layer; see §C.3.2. Furthermore, the structure and geometry of the interaction region between the two winds are direct outcomes of our simulations, whereas the shape of the interface layer is imposed as a fixed "obstacle" in the simulations of E10.

Other differences include our treatments of the planetary and stellar winds. We account for both the neutral and ionized components of the planetary wind; E10 assume the planetary outflow is purely neutral. We draw our parameters of the stellar wind from those of the slow equatorial Solar wind, which blows at ∼130 km/s at a stellocentric distance of $r = 5R_\odot$ *(Sheeley et al. 1997; Quémerais et al. 2007). E10 take the stellar wind to blow at 450 km/s, while H08 take the stellar wind to blow at 50 km/s. Neither work accounts for how the stellar wind decelerates due to its interaction with the planetary wind, whereas in our simulations the deceleration zones are well-resolved.*

C.3 Results

Results for Lyman-α absorption by the mixing layer, including numerical convergence tests and a direct comparison with observations, are given in §C.3.1. A parameter study is described in §C.3.2.

C.3.1 Absorption vs. Spatial Resolution and Time

In Figures C.1 and C.2, we present results at our lowest (50×75) *and near-highest* (3200×4800) *spatial resolutions, respectively. The simulations agree on the basic properties of the flow. The planetary wind is launched from the red circle and encounters a bow shock, visible in the left panels as a curved boundary separating orange (unshocked planetary wind) from*

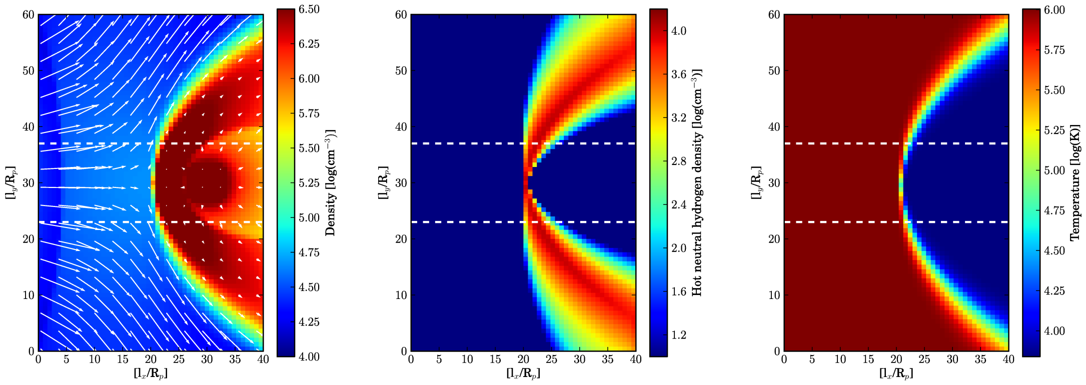

Figure C.1: Snapshots of total density and velocity (left panel), density of hot neutral hydrogen (n_h^0, middle panel), and temperature (right panel) of the 50x75 simulation, with parameters listed in Table C.1. Snapshots are taken at $t = 2 \times 10^6$ s. The temperature map shown in the right panel is computed by `HERACLES` and used only to compute the hydrodynamic evolution; it is not used to compute the charge exchange reactions or the Lyman-α spectrum (see §C.2.2–C.2.3). The two dashed white lines represent sightlines to the stellar limbs.

red (shocked planetary wind). The radius of curvature of the planetary wind shock is roughly $\sim 6R_p$. *Outside, the red region of thickness* $\sim 5R_p$ *contains shocked planetary wind.*

The stellar wind encounters a weak shock—visible as a near-vertical line separating dark blue from lighter blue in the left-hand panels of Figures C.1 and C.2—at a distance of $\sim 5R_p$ *from the left edge of the box. The shocked stellar wind is diverted around the planet by the pressure at the stagnation point where the two winds collide head on.*

We observe that both winds accelerate somewhat before they encounter shocks. For our standard model, $M_* \lesssim 1.3$ *and* $M_p \lesssim 1.5$ *(for the parameter study simulations of §C.3.2,* M_p *can grow up to 2–3). Density enhancements are thus modest—less than a factor of 2.*

The contact discontinuity between the stellar and planetary winds separates light blue from dark red in the left panels. It is laminar at low resolution but breaks up into turbulent Kelvin-Helmholtz rolls at high resolution (cf. Stone & Proga 2009 whose spatial resolution was probably too low to detect the Kelvin-Helmholtz instability). The middle panels plot the density of hot neutral hydrogen produced by charge exchange in the mixing layer. The "head" of the mixing layer, located near the stagnation point, spans only one or two grid cells in the low resolution simulation. The high resolution simulation resolves much better the head of the mixing layer. Zoomed-in snapshots of the head will be presented in §C.3.2.

In Figure C.3, the star-averaged absorption A at an equivalent Doppler velocity of +100 km/s (redshifted away from the observer) is plotted against time for a range of spatial resolutions. From $t = 0$ *to* 2×10^5 *s, the planetary wind fills the simulation domain; the absorption quickly settles down to a value of* $\sim 2\%$. *At these early times, only cold (*$T_p = 7000$ *K) neutral hydrogen from the planet is available to absorb in Ly-*α*, and it is clearly insufficient to explain the absorption observed with HST.*

Starting at $t = 2 \times 10^5$ *s, the stellar wind is injected into the box. The absorption attains a first peak when the planetary and stellar winds reach a rough momentum balance and a mixing layer containing hot (*$T_* = 10^6$ *K) neutral hydrogen is established. The height of the first peak decreases with each factor of 2 improvement in grid resolution until a resolution of 3200x4800 is reached. Encouragingly, all of the absorption values calculated in the various simulations converge at late times.*

The 3200x4800 run is the best behaved, with the absorption holding steady at $A \approx 9\%$

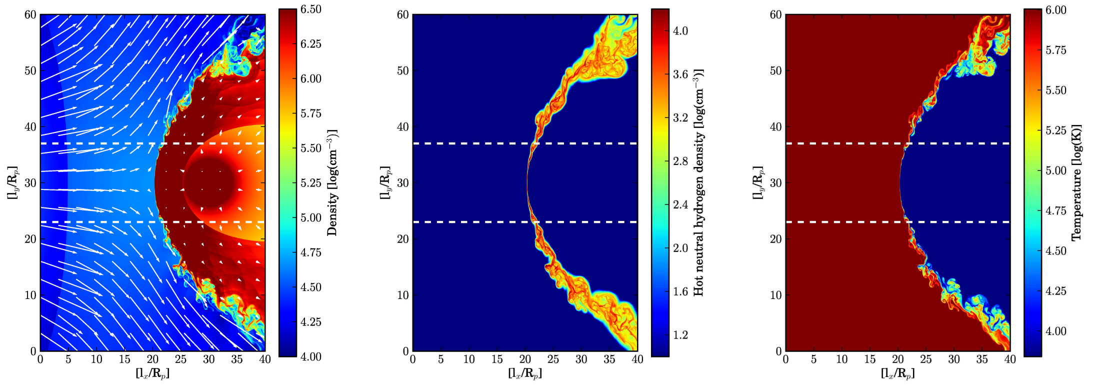

Figure C.2: Same as Figure C.1 and for the same simulation parameters but at a grid resolution of 3200x4800. Kelvin-Helmholtz rolls at the contact discontinuity first appear at this resolution. An even higher resolution of 6400x9600 yields the same star-averaged absorption; see Figure C.3.

for 10^6 *s. Compared to all other simulations at lower resolution, the 3200x4800 run is the only one in which Kelvin-Helmholtz rolls appear (more on the Kelvin-Helmholtz instability in §C.3.2).*

We further tested the convergence of the 3200x4800 run by performing an even higher resolution simulation with 6400x9600 grid cells. Because of the expense of such a simulation, the initial conditions of the 6400x9600 run were taken from the 3200x4800 run at $t = 10^6$ *s, and integrated forward for only* 3×10^5 *s (approximately 9 box crossing times for the stellar wind in the horizontal direction). The absorption values versus time for the 6400x9600 run are overlaid in Figure C.3 and are practically indistinguishable from those of the 3200x4800 run. Having thus satisfied ourselves that the 3200x4800 run yields numerically convergent results, we will utilize this grid resolution* ($0.0125R_p$ *per grid cell length) for further experiments to understand the dependence of the absorption on input parameters, as described in §C.3.2.*

Figure C.4 plots the absorption spectrum for our standard 3200x4800 simulation at $t = 2 \times 10^6$ *s. The absorption* A *is evaluated at wavelengths offset from the central rest-frame wavelength of the Lyman-α transition by 9 Doppler-shift velocities* Δv*. Absorption at -50 km/s is stronger than at +50 km/s, a consequence of neutral, charge-exchanged hydrogen from the star accelerating from the stagnation point toward the observer. At larger velocities* $|\Delta v| > 100$ *km/s, the spectrum is more nearly reflection-symmetric about* $\Delta v = 0$*, because the broadening is purely thermal at* $T_* = 10^6$ *K.*

Figure C.5 displays the same information as in Figure C.4 but in the full context of the Hubble Space Telescope observations. The agreement between the modeled and observed in-transit spectra is encouraging.

C.3.2 Scaling Relations for Absorption in the Mixing Layer

To understand how absorption in the mixing layer depends on input parameters, we performed 3 additional simulations varying the launch properties n_p, n_*, v_p *and* T_p*. The altered parameters are listed in Table C.2. For all 3 simulations, the box size was maintained at* $(L_x, L_y) = (40R_p, 60R_p)$ *and the grid resolution was* $(N_x, N_y) = (3200, 4800)$*.*

Note that our parameter study is not exhaustive. For example, none of the simulations listed in Table C.2 varies the Mach number at launch of either the planetary or stellar wind. Actually we have performed simulations varying the Mach number of the stellar

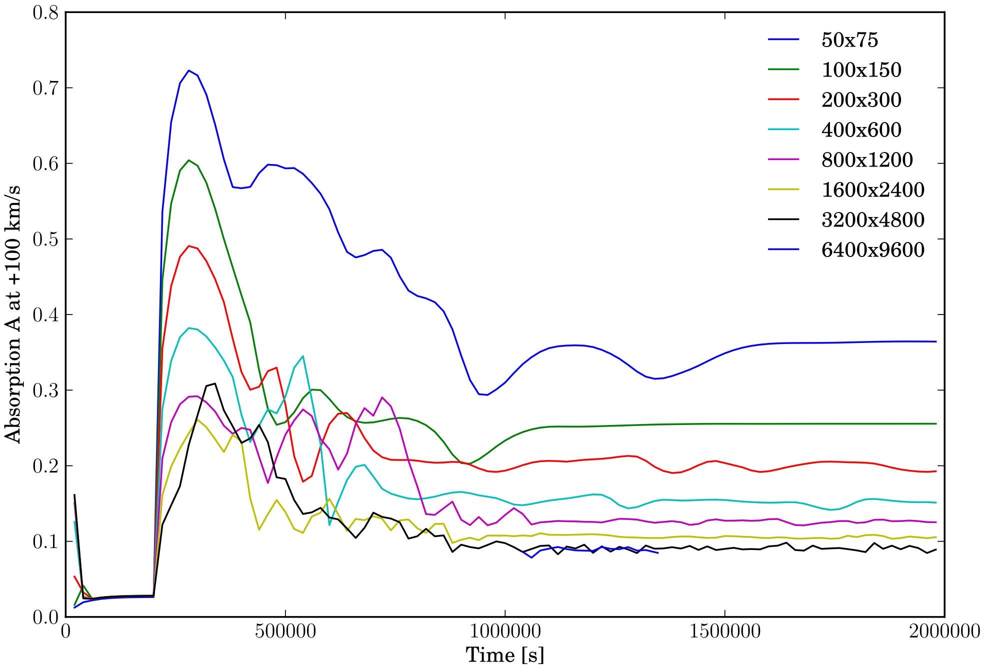

Figure C.3: Lyman-α absorption A (equation C.6), evaluated at a Doppler-shift velocity of +100 km/s from line center, versus time and spatial resolution. The absorption converges in time for all simulations, but only for grid resolutions of 3200x4800 or greater does a unique value for the absorption emerge. The 3200x4800 simulation is also the lowest resolution run to resolve Kelvin-Helmholtz billows; see Figure C.2.

wind. These behave as we would expect—in particular, increasing M_* increases the amount of absorption because of the increased compression in the stellar shock. Nevertheless we elect not to include these extra simulations in our parameter study below. Magnetic fields, neglected by our simulations but certainly present in the stellar wind if not also the planetary wind, would stiffen the gas and prevent the kind of compression that we see when we raise M_*.

In the following subsections, we explain our numerical results on the properties of the mixing layer with order-of-magnitude scaling relations. The mixing layer's location is analyzed in §C.3.2; its thickness in §C.3.2; the densities of its constituent species in §C.3.2; and the column density and absorptivity of hot neutral hydrogen in §C.3.2.

Table C.2: Launch parameters for the 3 additional $40R_p \times 60R_p$ simulations at 3200×4800 resolution. The stellar parameters v_* and T_* are kept at their nominal values from Table C.1. Note that none of the Mach numbers change.

	Nominal	$n_p \uparrow$	$n_* \downarrow$	v_p,$T_p \uparrow$
n_*	2.9E4/cm^3	2.9E4/cm^3	9.7E3/cm^3	2.9E4/cm^3
n_p	3.9E6/cm^3	1.2E7/cm^3	3.9E7/cm^3	3.9E6/cm^3
v_p	12 km/s	12 km/s	12 km/s	$\sqrt{3}\times 12$ km/s
T_p	7000 K	7000 K	7000 K	21000 K
$\mathcal{R}$	$\mathcal{R}_0 = 0.11$	$3 \times \mathcal{R}_0$	$3 \times \mathcal{R}_0$	$3 \times \mathcal{R}_0$

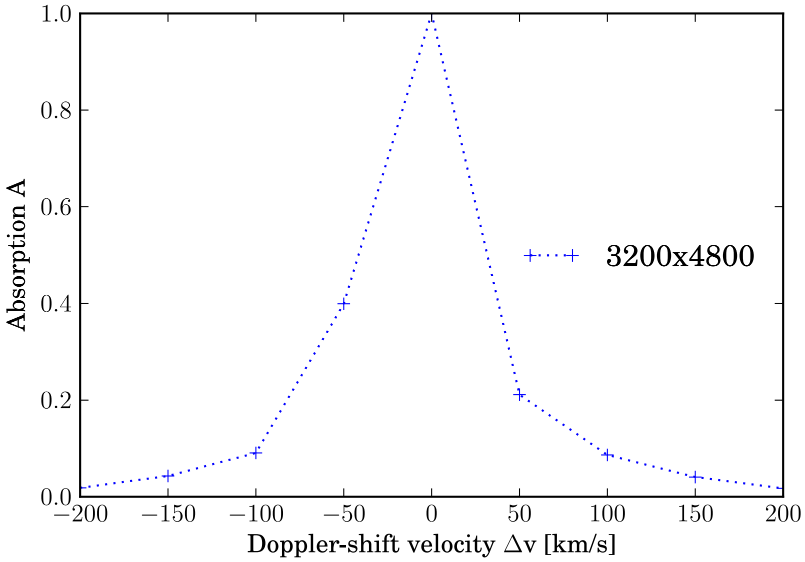

Figure C.4: Lyman-α absorption A versus Doppler-shift velocity Δv from line center, evaluated for our standard 3200x4800 simulation at $t = 2 \times 10^6$ s. Absorption at -50 km/s is stronger than at +50 km/s because of the bulk motion of charge-exchanged neutral hydrogen streaming from the star toward the observer. The line wings at larger Doppler shifts are primarily thermally broadened at $T_* = 10^6$ K. The absorption $A \approx 9\%$ at $\Delta v = \pm 100$ km/s, in accord with *HST* observations; see Figure C.5.

Location of the mixing layer

Along the line joining the planet to the star, the mixing layer—equivalently, the contact discontinuity—is located approximately where the two winds reach pressure balance:

$$\rho_*(v_*^2 + c_*^2) = \rho_p(v_p^2 + c_p^2)\,. \tag{C.7}$$

In equation (C.7), quantities are evaluated near the mixing layer, not at launch. Note further that in equation (C.7) and in equations to follow, we ignore the distinction between shocked and unshocked gas, as wind Mach numbers are near unity. Idealizing each wind velocity as constant, we substitute $\rho_p = \dot{M}_p/(2\pi v_p d_p)$ *and* $\rho_* = \dot{M}_*/(2\pi v_* d_*)$ *into equation (C.7), as appropriate for the 2D circular winds in our simulations. Here* d_p *measures distance from the planet, and* d_* *measures distance from the star. Then the distance from the planet to the mixing layer—i.e., the approximate radius of curvature of the mixing layer—is given by*

$$d_p = d_* \mathcal{R} \tag{C.8}$$

where

$$\mathcal{R} \equiv \frac{\dot{M}_p(v_p^2 + c_p^2)/v_p}{\dot{M}_*(v_*^2 + c_*^2)/v_*}\,. \tag{C.9}$$

For our standard model, $\mathcal{R} = \mathcal{R}_0 \approx 0.11$. *For 3D spherical winds,* $d_p = d_*\sqrt{\mathcal{R}}$ *(Stevens et al., 1992).*

The parameters in Table C.2 were chosen to increase $\mathcal{R}$ *by a factor of 3 compared to its value in our fiducial model. By equation (C.8), when* $\mathcal{R} = 3\mathcal{R}_0$, *the mixing layer should be displaced* 3× *farther away from the planet compared to its location in our standard model, assuming the star is far enough away that* d_* *is essentially fixed at the star-planet separation. Figure C.6 displays zoomed-in snapshots of the mixing layers for all simulations*

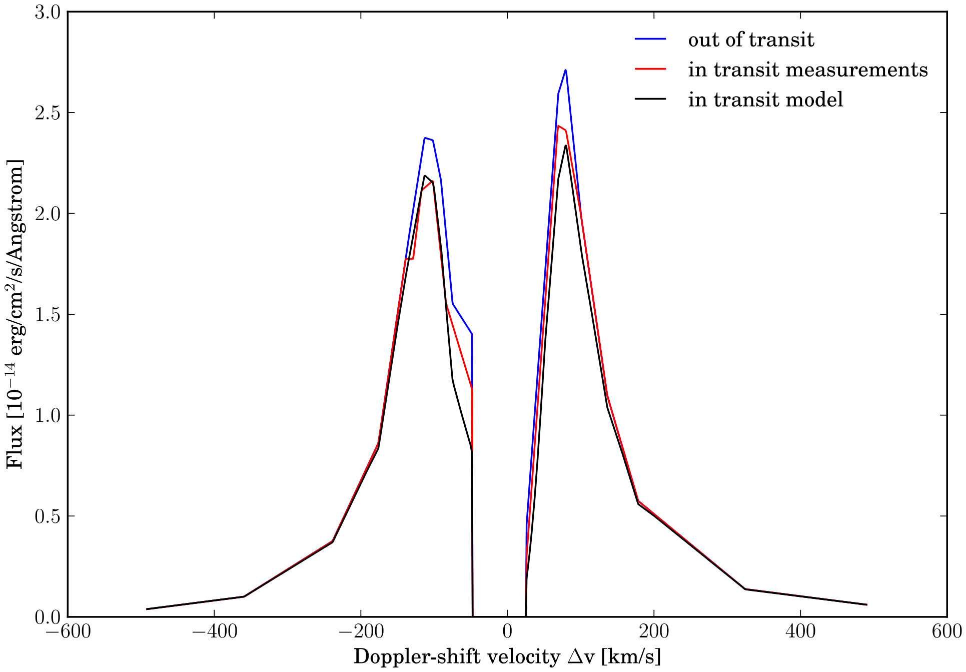

Figure C.5: Observed out-of-transit (highest blue curve) and observed in-transit (green curve) Lyman-α spectra, reproduced from Figure 2 of Vidal-Madjar et al. (2003). In the line "core" from -42 to +32 km/s, where interstellar absorption is too strong to extract a planetary transit signal, the flux is set to zero. Our theoretical in-transit spectrum (red curve) is computed by multiplying the observed out-of-transit spectrum by $1 - A$, where A is plotted in Figure C.4. The agreement between the theoretical and observed in-transit spectra is good, supporting the idea that charge exchange between the stellar and planetary winds correctly explains the observed absorption at Doppler-shift velocities around ±100 km/s.

in Table C.2. Looking at the l_x-positions of the mixing layers, and recalling that the planet sits at $l_x = 30R_p$, we find that the layer is displaced $(30-8)/(30-21) \approx 2.4\times$ farther away in the three new simulations as compared to the standard model. We consider this close enough to our expected factor of 3, given our neglect of the rather thick layers of shocked gas surrounding the mixing layer.

Figure C.7 shows density profiles for hot neutral hydrogen in the mixing layer for the three simulations plus our standard model. Densities are averaged over l_y and plotted against l_x. The fact that the mixing layers in the simulations having $\mathcal{R} = 3\mathcal{R}_0$ align in position confirms that $\mathcal{R}$ is the dimensionless parameter controlling the location of the mixing layer.

Thickness of the mixing layer

Figure C.7 also indicates that the thickness of the mixing layer, $L_{\rm mix}$, varies when we change input parameters. Empirically, we find that the variations are consistent with the relation

$$L_{\rm mix} \sim 0.1 R_p \left(\frac{n_p}{n_*}\right)^{0.5} \tag{C.10}$$

where, as before, the distinction between shocked and unshocked gas densities is ignored.

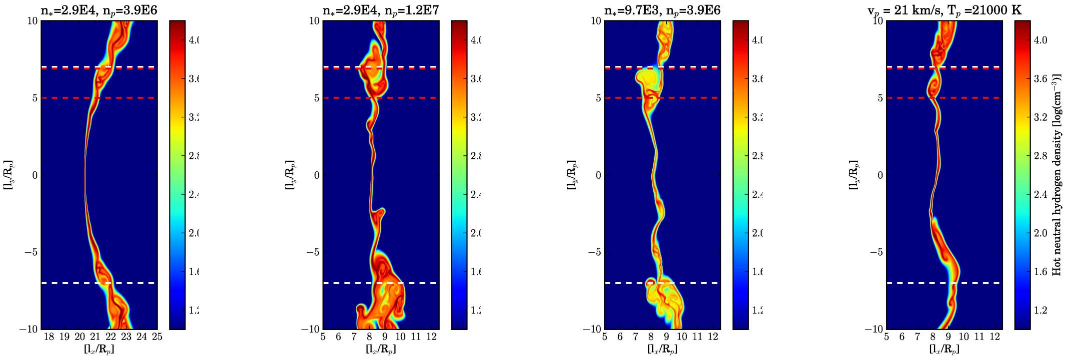

(a) Standard case (b) n$_p$ increased (c) n$_*$ decreased (d) v$_p$,T$_p$ increased

Figure C.6: Zoomed-in snapshots of hot neutral hydrogen in the four simulations used to study how the properties of the mixing layer depend on input parameters; see Table C.2. Snapshots are taken near $t = 2 \times 10^6$ for the standard model, and near $t = 1 \times 10^6$ s for the others. The bottom white dashed line is the line of sight to the lower stellar limb. The upper two red dashed lines bracket the "sampling interval" over which the hot neutral hydrogen density is vertically averaged to produce the density profiles shown in Figure C.7 (the uppermost red dashed line is also the sightline to the upper stellar limb). In cases (b), (c), and (d), the mixing layer is located farther from the planet (centered at $l_x = 30R_p$) than is the case in (a). In cases (b) and (c), the horizontal thickness of the mixing layer is greater than in cases (a) and (d). And in case (c), the density of hot neutral hydrogen is lowest. See §C.3.2 for explanations.

We can rationalize (C.10) as follows. The timescale for a mode of wavelength $\lambda_{\rm KH}$ *to grow exponentially by the linear Kelvin-Helmholtz instability (KHI) is given by*

$$t_{\rm KH} \sim \frac{\lambda_{\rm KH}}{v_* - v_p} \frac{\rho_p + \rho_*}{2\pi(\rho_p \rho_*)^{1/2}} \sim \frac{\lambda_{\rm KH}}{2\pi v_*} \sqrt{\frac{\rho_p}{\rho_*}} \qquad \text{(C.11)}$$

(e.g., Chandrasekhar 1961). We assume that the thickness of the mixing layer saturates when a certain mode first becomes nonlinear. Near saturation, the velocity perpendicular to the background shear flow becomes comparable to the shear flow velocity: $v_\perp \sim v_* - v_p \sim v_*$*. Thus when the mode becomes nonlinear, the mixing layer has thickness* $L_{\rm mix} \sim v_\perp t_{\rm KH} \sim (\lambda_{\rm KH}/2\pi)\sqrt{\rho_p/\rho_*}$*. This result matches (C.10), if we assume the initial disturbance that develops into the mixing layer has a characteristic lengthscale that is fixed at* $\lambda_{\rm KH} \sim R_p$*. Our description of mode saturation can only apply to locations not too far downstream from the stagnation point; far away, the flows are too strongly perturbed to be described by the linear growth timescale (C.11).*

Density of hot neutral hydrogen in the mixing layer

The density of hot neutral hydrogen in the mixing layer is set by chemical equilibrium. Suppose that within the layer, the total density $n_{\rm H,mix}$ *is approximately the average of the planetary wind density and the stellar wind density:*

$$n_{\rm H,mix} \sim \frac{n_p + n_*}{2} \sim \frac{n_p}{2} \,. \qquad \text{(C.12)}$$

The densities in (C.12) are those of shocked gas, but as is the case for all of §C.3.2, we ignore for simplicity the difference in density between pre-shock and post-shock gas (see §C.3.2). Because $n_p \gg n_*$*, charge exchange hardly alters the ionization state of the*

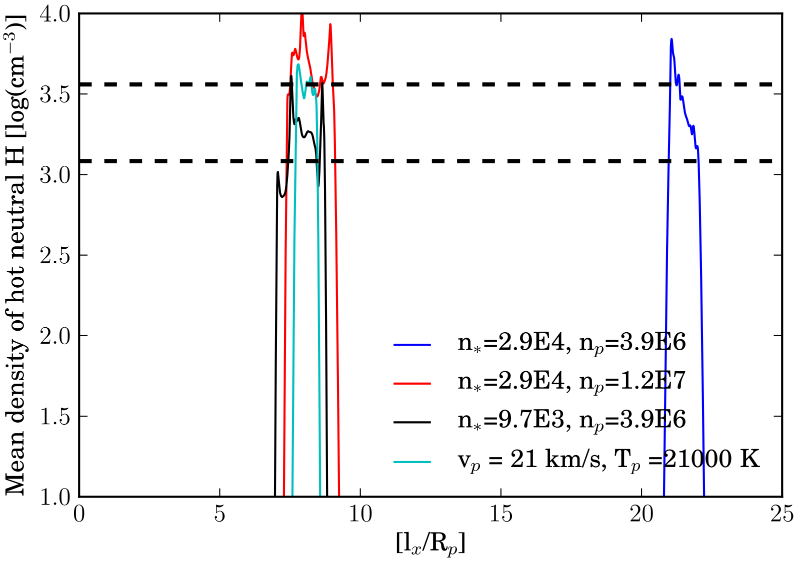

Figure C.7: Density profiles of charge-exchanged hot neutral hydrogen in the mixing layer, averaged vertically (between the dashed red lines in Figure C.6) and plotted against horizontal position. The planet is located to the right at $l_x = 30R_p$. The mixing layers of the three non-standard simulations are all displaced farther from the planet than in the standard model, a consequence of increasing the ratio $\mathcal{R}$ of the momentum carried by the planetary wind to that of the stellar wind (§C.3.2). The thicknesses of the mixing layers as shown by the red and green curves are larger than those shown by the blue and cyan curves, a consequence of changing the growth rate for the Kelvin-Helmholtz instability (§C.3.2). The two dashed lines are predictions of equation (C.16) based on considerations of chemical equilibrium; the blue, green, and cyan curves correctly intersect the upper dashed line, while the red curve correctly intersects the lower dashed line (§C.3.2).

shocked—and still cold—planetary wind. That is, the values of x_c^0 *and* x_c^+ *do not change as the dense planetary wind mixes with the dilute stellar wind. In particular, the ratio* x_c^0/x_c^+ *is fixed at its initial value of* $(1-f_p^+)/f_p^+ = 1/4$.

The timescale for charge exchange is $(n_{\mathrm{H,mix}}\beta)^{-1} \sim 10$ *s, much shorter than the hours required for stellar-occulting gas to travel from the stagnation point to regions off the projected stellar limb. Thus nearly all of the gas seen in transit is driven quickly into chemical equilibrium, which from equation (C.3) demands that:*

$$\frac{x_h^0}{x_h^+} = \frac{x_c^0}{x_c^+} \tag{C.13}$$

$$= \frac{1-f_p^+}{f_p^+} = \frac{1}{4}\,. \tag{C.14}$$

In other words, in the mixing layer, the ionization fraction of stellar wind material quickly slaves itself to the ionization fraction of planetary wind material. Now all of the hot hydrogen (both neutral and ionized) in the mixing layer originates from the stellar wind; from (C.12), we have

$$\left(x_h^0 + x_h^+\right) n_{\mathrm{H,mix}} \sim \frac{n_*}{2}\,. \tag{C.15}$$

Combining (C.14) with (C.15) yields

$$n_h^0 = x_h^0 n_{\mathrm{H,mix}} \sim \frac{1}{2}\left(1-f_p^+\right) n_*\,. \tag{C.16}$$

Equation (C.16) is approximately confirmed by our numerical results in Figure C.7; the horizontal dashed lines predicted by (C.16) roughly match the densities from our numerical simulations.

Column density and absorptivity of hot neutral hydrogen

Combining (C.10) with (C.16) gives the total column density of hot neutral hydrogen:

$$N_h^0 \sim n_h^0 L_{\rm mix} \sim 0.05\left(1-f_p^+\right)\left(n_p n_*\right)^{1/2} R_p\,. \tag{C.17}$$

For our standard model, $N_h^0 \sim 3\times10^{13}$ *cm*$^{-2}$*.*

During planetary transit, the hot absorbing gas that covers the face of the star is located near the stagnation point. As such, the bulk line-of-sight velocity of transiting gas is much less than its thermal velocity, which is of order 100 km/s. Assuming that the gas is only thermally broadened, and that the gas is optically thin at wavelengths Doppler-shifted from line center by velocities Δv*, we construct an approximate, semi-empirical formula for the absorption:*

$$A(\Delta v) \sim N_h^0 \sigma_{\rm line-ctr} \exp[-m_H(\Delta v)^2/2kT_*] \tag{C.18}$$

$$\sim 0.1\left(\frac{1-f_p^+}{0.2}\right)\left(\frac{n_p}{4\times10^6\,{\rm cm}^{-3}}\right)^{1/2}\left(\frac{n_*}{3\times10^4\,{\rm cm}^{-3}}\right)^{1/2}$$

$$\times\left(\frac{10^6\,{\rm K}}{T_*}\right)^{1/2}\left(\frac{\exp[-m_H(\Delta v)^2/2kT_*]}{0.5}\right) \tag{C.19}$$

where $\sigma_{\rm line-ctr} = 6\times10^{-15}(10^6\,{\rm K}/T_*)^{1/2}\,{\rm cm}^2$ *is the line-center cross section for the Lyman-*α *transition,* m_H *is the mass of the hydrogen atom, and* k *is Boltzmann's constant. Strictly speaking, the quantities in equation (C.19) should be evaluated in the vicinity of the contact discontinuity, but we have instead normalized equation (C.19) to the wind properties at launch (evaluated at* $d_{\rm launch,p} = 4R_p$ *and* $r_{\rm launch,*} = 5R_\odot$*). We have verified in our simulations that the launch properties differ only by factors of order unity from the values at the contact discontinuity, and so equation (C.19) may be used to predict the absorption by inserting only the launch properties. The exponential in equation (C.19) is evaluated for nominal parameters* $\Delta v = 100$ *km/s and* $T_* = 10^6$ *K.*

As a further check, we show in Figure C.8 the absorption values A *to which the four simulations converge. They compare well with the values predicted by (C.19) using only the launch properties.*

Had we kept the dependence of the mixing layer properties on the stellar wind Mach number M_**, equation (C.16) would be modified such that* $n_h^0 \propto M_*^2 n_*$*—where* n_* *is the pre-shock (launch) density—in accord with the usual Rankine-Hugoniot jump condition that states that the density increases by the square of the Mach number across a plane-parallel isothermal shock. And equations (C.17)–(C.19) would be modified such that* $A \propto N_h^0 \propto M_*$*. Indeed our numerical simulations (not shown) confirm this linear dependence of* A *on* M_**. We mention this result only in passing because it is not likely to remain true once we account for the real-life magnetization of the stellar wind. Magnetic fields stiffen gas and reduce the dependence of* A *on* M_**.*

C.4 Summary and Discussion

Using a 2D numerical hydrodynamics code, we simulated the collisional interaction between two winds, one emanating from a hot Jupiter and the other from its host star. The winds were assumed for simplicity to be unmagnetized. Properties of the stellar wind were drawn

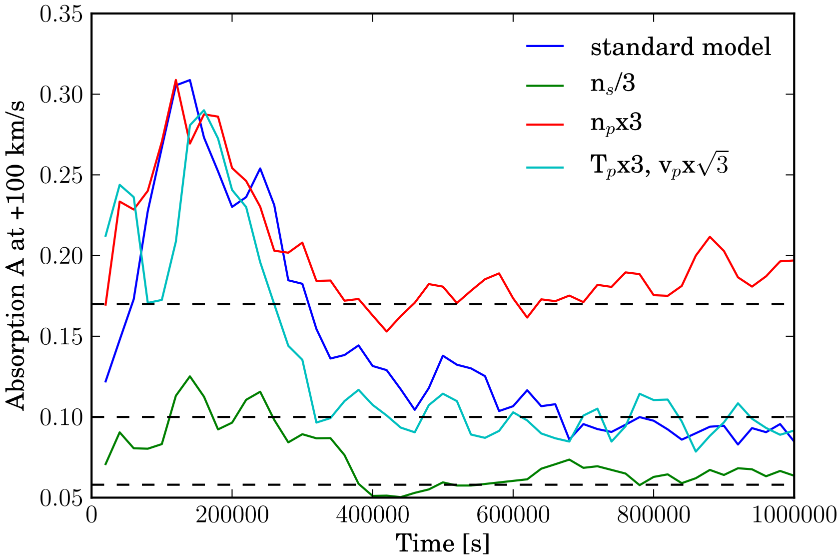

Figure C.8: Lyman-α absorption A versus time, evaluated at a Doppler-shift velocity of $+100$ km/s from line center, for our standard model plus three additional models with different input parameters as indicated in the legend (see also Table C.2). The colored jagged lines are the results from our numerical simulations. The dashed black lines are the predictions from our physically motivated scaling relation (C.19); the simulations converge fairly well to the predicted values.

directly from observations of the equatorial slow Solar wind (Sheeley et al. 1997; Quémerais et al. 2007; Lemaire 2011), while those of the planetary wind were taken from hydrodynamic models of outflows powered by photoionization heating (García-Muñoz 2007; Murray-Clay et al. 2009). For our standard parameters, the mass loss rate of the star is $\dot{M}_* = 2 \times 10^{-14} M_\odot/yr = 10^{12}$ *g/s and the mass loss rate of the planet is* $\dot{M}_p = 1.6 \times 10^{11}$ *g/s* $= 2.7 \times 10^{-3} M_J/Gyr$*. At the relevant distances, each wind is marginally supersonic—the stellar wind blows at ∼130–170 km/s (sonic Mach number* $\mathcal{M}_* \lesssim 1.3$*) and the planetary wind blows at ∼12–15 km/s (Mach number* $\mathcal{M}_p \lesssim 1.5$*). Thus shock compression is modest, even without additional stiffening of the gas by magnetic fields.*

A strong shear flow exists at the contact discontinuity between the two winds. At sufficiently high spatial resolution, we observed the interfacial flow to be disrupted by the Kelvin-Helmholtz instability. The Kelvin-Helmholtz rolls mix cold, partially neutral planetary gas with hot, completely ionized stellar gas. Charge exchange in the mixing layer produces observable amounts of hot (10^6 *K) neutral hydrogen. Upon impacting the planetary wind, the hot stellar wind acquires, within tens of seconds, a neutral component whose fractional density equals the neutral fraction of the planetary wind (about* $1 - f_p^+ = 20\%$*). Seen transiting against the star, hot neutral hydrogen in the mixing layer absorbs ∼10% of the light in the thermally broadened wings of the stellar Lyman-*α *emission line, at Doppler shifts of ∼100 km/s from line center. Just such a transit signal has been observed with the Hubble Space Telescope (Vidal-Madjar et al. 2003).*

Our work supports the proposal by Holmström et al. (2008) and Ekenbäck et al. (2010) that charge exchange between the stellar and planetary winds is responsible for the Ly-α *absorption observed by HST. Our ability to reproduce the observations corroborates the first-principles calculations of hot Jupiter mass loss on which we have relied (e.g., Yelle 2004; García-Muñoz 2007; Murray-Clay et al. 2009). Time variations in Ly-*α *absorption are expected both from the variable stellar wind—the Solar wind is notoriously gusty—and* *from the variable planetary wind, whose mass loss rate tracks the time-variable ultraviolet stellar luminosity.*

C.4.1 Directions for Future Research

Although the general idea of photoionization-powered planetary outflows exchanging charge with their host stellar winds seems correct, details remain uncertain. One issue is the exact dependence of the Ly-α *absorption* A *on the planetary wind density* n_p. *We found empirically that* $A \propto n_p^{1/2}$, *and argued that this result arose from the Kelvin-Helmholtz growth timescale. Ekenbäck et al. (2010) found a much weaker dependence: increasing* n_p *by a factor of 100 only increases* A *in their models by a factor of ∼2 at -100 km/s and even less at positive velocities—see their Figures 8 and 9. The results of Ekenbäck et al. (2010) depend on a kinetic description of the two winds in which Lorentz forces by magnetic fields are not explicitly calculated. Our results also neglect magnetic fields, which can suppress Kelvin-Helmholtz mixing (Frank et al. 1996). The effects of magnetic fields, and the question of whether the hydrodynamic equations provide an adequate description of the wind-wind interaction,*[3] *remain unresolved issues.*

Our calculations overestimate the amount of hot neutral hydrogen produced by charge exchange because they neglect thermal equilibration. A hot neutral hydrogen atom cools by colliding with cold gas, both ionized and neutral, from the planetary wind. The concern is that hot neutral gas cools before it transits off the face of the star. Starting from where the mixing layer is well-developed (say the lower red dashed line in Figure C.6), hot neutral gas is advected off the projected stellar limb in a time

$$t_{\rm adv} \sim 2R_p/v_* \sim 2\times10^3\,{\rm s}\,. \tag{C.20}$$

By comparison, the cooling time is of order

$$t_{\rm cool} \sim \frac{1}{n_c^+\sigma v_{\rm rel}} \sim 500\left(\frac{2\times10^6\,{\rm cm}^{-3}}{n_c^+}\right)\left(\frac{10^{-16}\,{\rm cm}^2}{\sigma}\right)\left(\frac{100\,{\rm km/s}}{v_{\rm rel}}\right)\,{\rm s} \tag{C.21}$$

where n_c^+ *is the density of cold ionized hydrogen in the mixing layer,* $v_{\rm rel}$ *is the relative speed between hot and cold hydrogen, and* σ *is the H-H*$^+$ *cross section for slowing down fast hydrogen, here taken to be the "viscosity" cross section calculated by Schultz et al. (2008).*[4] *Our estimate of* $t_{\rm cool}$ *in (C.21) neglects cooling by neutral-neutral collisions, but we estimate the correction to be small, as* n_c^0 *is lower than* n_c^+ *by a factor of* $1/(1-f_p^+)\sim 5$, *and the cross section for H-H collisions is generally not greater than for H-H*$^+$ *collisions (A. Glassgold 2012, personal communication; see also Swenson et al. 1985; note that Ekenbäck et al. (2010) take the relevant H-H cross section to be* 10^{-17} *cm*^{2} *but do not provide a reference).*

That $t_{\rm cool} \sim t_{\rm adv}$ *indicates our simulated column densities of hot neutral hydrogen may be too large, but hopefully not by factors of more than a few. Keeping more careful track of the velocity distributions—and excitation states—of neutral hydrogen in the mixing layer would not only improve upon our calculations of Lyman-*α *absorption, but would also bear upon the recent detection of Balmer H*α *absorption in the hot Jupiters HD 209458b and HD 189733b (Jensen et al. 2012).*

---

[3] See, e.g., comments on the kinetic vs. hydrodynamic debate for modeling the interaction of the Solar wind with cometary outflows by *Biermann et al.* (1967). Plasma instabilities are invoked to justify fluid treatments of collisionless, magnetized matter.

[4] For slowing down fast H in a sea of cold H$^+$, there may also be a contribution to σ from "momentum transfer" in "elastic" (non-charge-exchange) collisions. This contribution increases σ over the viscosity cross section by only ∼30%; compare Figures 6 and 7 of *Schultz et al.* (2008).

Acknowledgments

This project was initiated during the 2011 International Summer Institute for Modeling in Astrophysics (ISIMA) program hosted by the Kavli Institute for Astronomy and Astrophysics (KIAA) at Beijing University. We thank Pascale Garaud and Doug Lin for organizing this stimulating workshop, and Edouard Audit, Stuart Bale, Andrew Cumming, Sebastien Fromang, Pascale Garaud, Astrid Lamberts, Eliot Quataert, and Jim Stone for helpful exchanges. We are indebted to Al Glassgold for his guidance in helping us understand H-H and H-H^+ collisions. ISIMA is funded by the American and Chinese National Science Foundations, the Center for the Origin, Dynamics and Evolution of Planets and the Center for Theoretical Astrophysics at the University of California at Santa Cruz, the Silk Road Project, and the Excellence Cluster Universe at TU Munich. Support for EC was provided by NASA through a Hubble Space Telescope Theory grant. This work was granted access to the HPC resources of [CCRT/CINES/IDRIS] under the allocations c2011042204 and c2012042204 made by GENCI (Grand Equipement National de Calcul Intensif).

Bibliography

Ben-Jaffel, L. (2007), Exoplanet HD 209458b: Inflated Hydrogen Atmosphere but No Sign of Evaporation, The Astrophysical Journal, 671(1), L61–L64, doi:10.1086/524706. 172

Ben-Jaffel, L. (2008), Spectral, Spatial, and Time Properties of the Hydrogen Nebula around Exoplanet HD 209458b, ApJ*, 688, 1352–1360, doi:10.1086/592101.* 172

Biermann, L., B. Brosowski, and H. U. Schmidt (1967), The interactions of the solar wind with a comet, Solar Physics, 1, 254–284, doi:10.1007/BF00150860. 187

Chandrasekhar, S. (1961), Hydrodynamic and hydromagnetic stability, Dover Publications. 183

Clarke, C. J., and R. F. Carswell (2003), Principles of Astrophysical Fluid Dynamics, Cambridge University Press, doi:10.2277/0521853311. 173

Ekenbäck, A., M. Holmström, P. Wurz, J.-M. Grießmeier, H. Lammer, F. Selsis, and T. Penz (2010), Energetic Neutral Atoms Around HD 209458b: Estimations of Magnetospheric Properties, ApJ*, 709, 670–679, doi:10.1088/0004-637X/709/2/670.* 172, 187

Fossati, L., et al. (2010), Metals in the Exosphere of the Highly Irradiated Planet WASP-12b, ApJ Letters*, 714, L222–L227, doi:10.1088/2041-8205/714/2/L222.* 172

Frank, A., T. W. Jones, D. Ryu, and J. B. Gaalaas (1996), The Magnetohydrodynamic Kelvin-Helmholtz Instability: A Two-dimensional Numerical Study, ApJ*, 460, 777, doi:10.1086/177009.* 187

García Muñoz, A. (2007), Physical and chemical aeronomy of HD 209458b, Planetary and Space Science, 55(10), 1426–1455, doi:10.1016/j.pss.2007.03.007. 172

González, M., E. Audit, and P. Huynh (2007), HERACLES: a three-dimensional radiation hydrodynamics code, Astronomy and Astrophysics, 464(2), 429–435, doi:10.1051/0004-6361:20065486. 173

Holmström, M., A. Ekenbäck, F. Selsis, T. Penz, H. Lammer, and P. Wurz (2008), Energetic neutral atoms as the explanation for the high-velocity hydrogen around HD 209458b., Nature, 451(7181), 970–2, doi:10.1038/nature06600. 172

Jensen, A. G., S. Redfield, M. Endl, W. D. Cochran, L. Koesterke, and T. Barman (2012), A Detection of Hα in an Exoplanetary Exosphere, ApJ*, 751, 86, doi:10.1088/0004-637X/751/2/86.* 187

Kohl, J. L., et al. (1998), UVCS/SOHO Empirical Determinations of Anisotropic Velocity Distributions in the Solar Corona, ApJ Letters*, 501, L127, doi:10.1086/311434.* 174

Lamberts, A., S. Fromang, and G. Dubus (2011), High-resolution numerical simulations of unstable colliding stellar winds, MNRAS*, 418, 2618–2629, doi:10.1111/j.1365-2966.2011.19653.x.* 172

Lecavelier Des Etangs, A., et al. (2010), Evaporation of the planet HD 189733b observed in H I Lyman-α, A&A*, 514, A72, doi:10.1051/0004-6361/200913347.* 172

Lemaire, J. F. (2011), Determination of coronal temperatures from electron density profiles, ArXiv e-prints. 173

Liang, M.-C., C. D. Parkinson, A. Y.-T. Lee, Y. L. Yung, and S. Seager (2003), Source of Atomic Hydrogen in the Atmosphere of HD 209458b, ApJ Letters*, 596, L247–L250, doi:10.1086/379314.* 172

Lindsay, B. G., and R. F. Stebbings (2005), Charge transfer cross sections for energetic neutral atom data analysis, Journal of Geophysical Research, 110(A12), doi:10.1029/2005JA011298. 176

Linsky, J. L., H. Yang, K. France, C. S. Froning, J. C. Green, J. T. Stocke, and S. N. Osterman (2010), Observations of mass loss from the transiting exoplanet HD 209458b, The Astrophysical Journal, 717(2), 1291–1299, doi:10.1088/0004-637X/717/2/1291. 172

McComas, D. J., H. A. Elliott, N. A. Schwadron, J. T. Gosling, R. M. Skoug, and B. E. Goldstein (2003), The three-dimensional solar wind around solar maximum, Geophys. Res. Lett.*, 30(10), 1517, doi:10.1029/2003GL017136.* 174

Moses, J. I., et al. (2011), Disequilibrium Carbon, Oxygen, and Nitrogen Chemistry in the Atmospheres of HD 189733b and HD 209458b, ApJ*, 737, 15, doi:10.1088/0004-637X/737/1/15.* 172

Murray-Clay, R. A., E. I. Chiang, and N. Murray (2009), Atmospheric escape from hot jupiters, The Astrophysical Journal, 693(1), 23–42, doi:10.1088/0004-637X/693/1/23. 174

Quémerais, E., R. Lallement, D. Koutroumpa, and P. Lamy (2007), Velocity Profiles in the Solar Corona from Multi-Instrument Observations, ApJ*, 667, 1229–1234, doi:10.1086/520918.* 173, 177

Schultz, D. R., P. S. Krstic, T. G. Lee, and J. C. Raymond (2008), Momentum Transfer and Viscosity from Proton-Hydrogen Collisions Relevant to Shocks and Other Astrophysical Environments, ApJ*, 678, 950–960, doi:10.1086/533579.* 187

Sheeley, J., et al. (1997), Measurements of Flow Speeds in the Corona Between 2 and 30 Rsun, The Astrophysical Journal, 484(1), 472–478, doi:10.1086/304338. 173

Stevens, I. R., J. M. Blondin, and A. M. T. Pollock (1992), Colliding winds from early-type stars in binary systems, ApJ, 386, 265–287. 172, 181

Swenson, D., D. Tupa, and L. Anderson (1985), Spin exchange collision cross sections for fast hydrogen atoms incident on hydrogen or alkali atoms, Journal of Physics B: Atomic and Molecular Physics, 18, 4433–4444. 187

Tian, F., O. B. Toon, A. A. Pavlov, and H. De Sterck (2005), Transonic Hydrodynamic Escape of Hydrogen from Extrasolar Planetary Atmospheres, ApJ, *621, 1049–1060, doi: 10.1086/427204.* 172

Verhamme, A., D. Schaerer, and A. Maselli (2006), 3D Lyα radiation transfer, Astronomy and Astrophysics, 460(2), 397–413, doi:10.1051/0004-6361:20065554. 177

Vidal-Madjar, A., A. L. Des Etangs, J.-M. Désert, G. E. Ballester, R. Ferlet, G. Hébrard, and M. Mayor (2003), An extended upper atmosphere around the extrasolar planet HD209458b., Nature, 422(6928), 143–6, doi:10.1038/nature01448. 172

Vidal-Madjar, A., A. Lecavelier des Etangs, J.-M. Désert, G. E. Ballester, R. Ferlet, G. Hébrard, and M. Mayor (2008), Exoplanet HD 209458b (Osiris): Evaporation Strengthened, ApJ Letters, *676, L57–L60, doi:10.1086/587036.* 172

Vidal-Madjar, A., et al. (2004), Detection of Oxygen and Carbon in the Hydrodynamically Escaping Atmosphere of the Extrasolar Planet HD 209458b, ApJ Letters, *604, L69–L72, doi:10.1086/383347.* 172

Weissman, P. R., L.-A. McFadden, and T. V. Johnson (1999), Encyclopedia of the solar system, Academic Press. 171

Winn, J. N., et al. (2005), Measurement of Spin-Orbit Alignment in an Extrasolar Planetary System, ApJ, *631, 1215–1226, doi:10.1086/432571.* 174

Winn, J. N., et al. (2006), Measurement of the Spin-Orbit Alignment in the Exoplanetary System HD 189733, ApJ Letters, *653, L69–L72, doi:10.1086/510528.* 174

Yelle, R. V. (2004), Aeronomy of extra-solar giant planets at small orbital distances, Icarus, *170, 167–179, doi:10.1016/j.icarus.2004.02.008.* 172